




5-2017

## Remote Neutron Spectroscopy on Mars

Christopher Gayle Tate

*University of Tennessee, Knoxville, ctate10@vols.utk.edu*

Follow this and additional works at: [https://trace.tennessee.edu/utk\\_graddiss](https://trace.tennessee.edu/utk_graddiss)

 Part of the [Instrumentation Commons](#), [Nuclear Commons](#), [Other Physical Sciences and Mathematics Commons](#), and the [The Sun and the Solar System Commons](#)

---

### Recommended Citation

Tate, Christopher Gayle, "Remote Neutron Spectroscopy on Mars. " PhD diss., University of Tennessee, 2017.

[https://trace.tennessee.edu/utk\\_graddiss/4501](https://trace.tennessee.edu/utk_graddiss/4501)

This Dissertation is brought to you for free and open access by the Graduate School at TRACE: Tennessee Research and Creative Exchange. It has been accepted for inclusion in Doctoral Dissertations by an authorized administrator of TRACE: Tennessee Research and Creative Exchange. For more information, please contact [trace@utk.edu](mailto:trace@utk.edu).

To the Graduate Council:

I am submitting herewith a dissertation written by Christopher Gayle Tate entitled "Remote Neutron Spectroscopy on Mars." I have examined the final electronic copy of this dissertation for form and content and recommend that it be accepted in partial fulfillment of the requirements for the degree of Doctor of Philosophy, with a major in Physics.

Jeffrey E. Moersch, Major Professor

We have read this dissertation and recommend its acceptance:

Yuri Kamyshkov, Mike Guidry, Josh Emery, Kate Jones

Accepted for the Council:

Dixie L. Thompson

Vice Provost and Dean of the Graduate School

(Original signatures are on file with official student records.)

**Remote Neutron Spectroscopy on Mars**

**A Dissertation Presented for the**

**Doctor of Philosophy**

**Degree**

**The University of Tennessee, Knoxville**

**Christopher Gayle Tate**

**May 2017**

Copyright © 2017 by Christopher G. Tate.

All rights reserved.

## **DEDICATION**

This dissertation is dedicated my parents, Dr. Gayle Tate and Karen Tate, who are the best parents anyone could ask for.

## ACKNOWLEDGEMENTS

There are many people I would like to acknowledge and say my thanks to. First and foremost I'd like to thank my parents, Gayle and Karen, who taught me to work hard for anything I deem worth accomplishing and for always supporting me through the endeavor that is graduate school. I would also like to thank the rest of my family, Nick, Whitney, Orion and Keeper for their support as well. Next, I have to recognize my advisor and my thanks to him for giving me the opportunity to work on projects like the Mars Science Laboratory. I would also like to thank my committee members for numerous helpful discussions, which have helped shape this work and at times point me in the right direction for approaching specific problems. Dr. Yuri Kamyshkov especially has my gratitude for helping me get started in research during my undergraduate education. I would also like to thank Dr. Stephen Daunt and Dr. Craig Hardgrove for similar friendly, helpful discussions. Lastly, I would like to mention some of the friends I have made during my time in graduate school here who were also pursuing their own degrees in Chad Mitchell, Maria Flores, Nick Sirica, and Josh Braverman. If you're not mentioned here, you have no less of my appreciation. Thank you for all the work related discussions, class study groups, and the many Appalachian Mountain adventures to relax and blow off steam, among other things. Graduate school was much more fun and fulfilling thanks to our adventures. Finally, as always, Go Vols!

## ABSTRACT

Remote neutron spectroscopy is an important technique in planetary science that allows for classification of the amount of light elements in a planetary regolith. It is especially suited for studying hydrogen abundances and elements with high thermal neutron absorption cross sections in the top ~1 meter of regolith. The Mars Science Laboratory rover Curiosity carries the first rover based neutron spectrometer Dynamic Albedo of Neutrons (DAN) in Gale crater, Mars. As the DAN instrument operates in passive mode, it is sensitive to neutrons produced through Galactic Cosmic Ray interactions and neutrons generated by the rover's Multi-Mission Radioisotope Thermoelectric Generator. In this work, we develop an appropriate simulation strategy and data analysis methods to interpret passive data from the DAN instrument. Furthermore, the methods are used to estimate water equivalent hydrogen abundances in the shallow regolith of Gale crater along the traverse route of *Curiosity* from landing to the base of Mt. Sharp. Hydrogen is shown to have large variability on a scale of a few meters, much smaller than the spatial footprint of previous orbital investigations. Strong correlations between WEH content and surface properties are not observed. While in passive operation, DAN also observes diurnal variations in the martian neutron leakage fluxes. These diurnal variations are investigated and shown to possibly be a consequence of a combination of instrumental effects and environmental effects, most notably preferential shielding of alpha particles by the martian atmosphere leading to increased neutron production in the regolith as the surface atmospheric pressure changes throughout the sol.

# TABLE OF CONTENTS

CHAPTER I Introduction .....	1
Background .....	4
Literature Review .....	8
References .....	20
CHAPTER II Water equivalent hydrogen estimates from the first 200 sols of <i>Curiosity's</i> traverse (Bradbury Landing to Yellowknife Bay): results from the Dynamic Albedo of Neutrons (DAN) passive mode experiment .....	23
Abstract .....	24
Introduction .....	26
Methods .....	31
Data .....	49
Dan Passive Measurements at Fixed Locations .....	49
DAN Passive Data along Traverse Segments .....	55
Ancillary Data .....	55
Sources of Uncertainty .....	61
Results .....	64
WEH Estimates for Fixed Locations .....	64
WEH Estimates for Traverse Segments .....	68
Discussion .....	76
Fixed Locations .....	76
Comparison with DAN Active Results .....	83
Traverse Segments .....	86



Statistical Distribution of WEH Estimates within Geologic Units .....	89
Clay Mineral Water Equivalent Hydrogen .....	92
Conclusions.....	96
Acknowledgments .....	98
References.....	99
Appendix.....	105
CHAPTER III Investigation of water equivalent hydrogen abundances and variations within the shallow subsurface of the Gale crater floor .....	
	119
Abstract.....	120
Introduction.....	122
Methods .....	125
Data.....	131
Fixed Location Data.....	132
Traverse Data .....	151
Ancillary Data.....	155
Sources of Uncertainties .....	156
Results.....	157
Fixed Location WEH Estimates.....	157
Traverse WEH Estimates .....	167
Discussion.....	171
Fixed Location WEH Estimates.....	171
Traverse WEH Estimates .....	174
DAN Passive Geochemical Index.....	176

Geologic Units .....	183
Conclusions.....	185
Acknowledgements.....	186
References.....	187
Appendix.....	192
CHAPTER IV Observed diurnal variations in MSL Dynamic Albedo of Neutrons passive mode data .....	202
Abstract.....	203
Introduction.....	205
Data.....	206
DAN Passive Data .....	206
Data From Other MSL Instruments .....	212
Engineering Data .....	212
Hypotheses Tested .....	212
Subsurface Temperature .....	215
Atmospheric Pressure Variations.....	219
Instrumental Effects .....	227
Diurnal Water Cycle .....	236
Discussion.....	237
Conclusions.....	245
Acknowledgements.....	247
References.....	248
CHAPTER V Conclusion .....	252

VITA..... 258

## LIST OF TABLES

Table 2.1. Fixed locations where the rover acquired DAN passive data within the first 200 sols. .....	50
Table 2.2. WEH estimates for fixed locations along the traverse from Bradbury Landing to John Klein.....	66
Table 2.3. Summary of WEH estimates derived from fixed and traverse segment DAN passive data.....	90
Table 3.1. The observational circumstances, DAN passive measurements, and constraints from other measurements .....	135
Table 3.2. WEH estimates for fixed locations derived from DAN passive data. ....	159
Table 4.1. Table of hypotheses investigated showing the modeled peak to peak amplitude in CTN count rates, modeled time of extrema in the CTN count rates, the correlation coefficients between the modeled CTN count rates and the data, and the amount of contribution to the observed diurnal variations.....	243

## LIST OF FIGURES

Figure 2.1. An illustration of the simulation process whereby the DAN instrument response is calculated. ....	33
Figure 2.2. RAD normalized penetrating counter average count rates (top) have been used in conjunction with our in situ calibration to constrain the GCR environment and produce GCR scale factors (bottom) on a sol by sol time scale that are useable with our MCNPX results. ....	42
Figure 2.3. Simulated thermal neutron counts per second for differing values of both H <sub>2</sub> O and AEC.....	44
Figure 2.4. Simulated thermal and epithermal neutron counts per second for a range of values of WEH and a fixed (typical) AEC abundance of 1 wt. %. ....	45
Figure 2.5. Simulated epithermal neutron count rates are shown separately for those sourced from the MMRTG (x symbols) and those induced by the GCR (circles) (with the same average scale factor applied for the period,) versus WEH content of the regolith. ....	46
Figure 2.6. DAN passive total neutron count rates (gray circles), thermal neutron count rates (black circles), and epithermal neutron count rates (gray squares) versus time during the first 200 sols of the mission. ....	53
Figure 2.7. Average thermal neutron count rate .....	54
Figure 2.8. DAN passive data acquired during rover traverse segments during the first 200 sols. ....	56
Figure 2.9. Passive thermal neutron count rates collected along the rover traverse during sol 48. ....	57

Figure 2.10. Passive thermal neutron count rates collected along the rover traverse during sol 102.....	58
Figure 2.11. Normalized count rates for RAD penetrating particle counter daily averages and DAN passive daily windowed averages at Rocknest.....	59
Figure 2.12. WEH estimates along <i>Curiosity's</i> traverse from Bradbury Landing to John Klein (sol 0 - 200).....	65
Figure 2.13. WEH estimates from DAN passive data acquired along all rover traverse segments. ....	70
Figure 2.14. WEH estimates along the sol 48 rover traverse.....	71
Figure 2.15. WEH estimates along the sol 102 rover traverse, exiting the Rocknest area. ....	72
Figure 2.16. Sol 48 traverse WEH estimates using AEC abundances interpolated from DAN active measurements .....	74
Figure 2.17. Sol 102 traverse WEH estimates using AEC abundances interpolated from DAN active measurements .....	75
Figure 2.18. Rear hazard camera photograph of the DAN measurement location on sol 52. ....	78
Figure 2.19. Fixed location WEH estimates from Shaler to John Klein.....	80
Figure 2.20. Percentage of thermal neutron count rate attributed to MMRTG-sourced thermal neutrons at fixed locations along the traverse. ....	82
Figure 2.21. Scatter plot of DAN passive WEH versus DAN active (60 cm weighted average) WEH for co-located, fixed location measurements. ....	84
Figure 2.22. Distribution of all WEH measurements during the first 200 sols of the mission for the hummocky plains unit (bottom) and the bedded fractured unit (top). ....	91

Figure 2.23. Estimated Na-exchanged and Ca-exchanged saponite water equivalent hydrogen (NaSWEH, CaSWEH) from DAN passive measurements at fixed locations within the Sheepbed member of Yellowknife Bay. ....	95
Supplementary Figure A.2.1. DAN passive WEH estimates for fixed locations plotted as a function of odometry.....	106
Supplementary Figure A.2.2. DAN passive WEH estimates for rover traverse on sol 38. ....	106
Supplementary Figure A.2.3. DAN passive WEH estimates for rover traverse on sol 49. ....	107
Supplementary Figure A.2.4. DAN passive WEH estimates for rover traverse on sol 50. ....	107
Supplementary Figure A.2.5. DAN passive WEH estimates for rover traverse on sol 52. ....	108
Supplementary Figure A.2.6. DAN passive WEH estimates for rover traverse on sol 53. ....	108
Supplementary Figure A.2.7. DAN passive WEH estimates for rover traverse on sol 55. ....	109
Supplementary Figure A.2.8. DAN passive WEH estimates for rover traverse on sol 56. ....	109
Supplementary Figure A.2.9. DAN passive WEH estimates for rover traverse on sol 57. ....	110
Supplementary Figure A.2.10. DAN passive WEH estimates for rover traverse on sol 59. ....	110
Supplementary Figure A.2.11. DAN passive WEH estimates for rover traverse on sol 100. ....	111
Supplementary Figure A.2.12. DAN passive WEH estimates for rover traverse on sol 111. ....	111
Supplementary Figure A.2.13. DAN passive WEH estimates for rover traverse on sol 120. ....	112
Supplementary Figure A.2.14. DAN passive WEH estimates for rover traverse on sol 122. ....	112
Supplementary Figure A.2.15. DAN passive WEH estimates for rover traverse on sol 123. ....	113
Supplementary Figure A.2.16. DAN passive WEH estimates for rover traverse on sol 124. ....	113
Supplementary Figure A.2.17. DAN passive WEH estimates for rover traverse on sol 125. ....	114
Supplementary Figure A.2.18. DAN passive WEH estimates for rover traverse on sol 127. ....	114
Supplementary Figure A.2.19. DAN passive WEH estimates for rover traverse on sol 130. ....	115

Supplementary Figure A.2.20. DAN passive WEH estimates for rover traverse on sol 133. ....	115
Supplementary Figure A.2.21. DAN passive WEH estimates for rover traverse on sol 147. ....	116
Supplementary Figure A.2.22. DAN passive WEH estimates for rover traverse on sol 151. ....	116
Supplementary Figure A.2.23. DAN passive WEH estimates for rover traverse on sol 152. ....	117
Supplementary Figure A.2.24. DAN passive WEH estimates for rover traverse on sol 159. ....	117
Supplementary Figure A.2.25. DAN passive WEH estimates for rover traverse on sol 163. ....	118
Supplementary Figure A.2.26. DAN passive WEH estimates for rover traverse on sol 166. ....	118
Figure 3.1. The focus of this paper is on DAN passive data along the RTR, which covers locations between Yellowknife Bay and Amargosa Valley.....	124
Figure 3.2. Normalized RAD penetrating counter data from the start of the mission up through sol 753 are shown on the top panel. ....	130
Figure 3.3. DAN thermal neutron count rates acquired at fixed locations for sols 0 through 753. .....	133
Figure 3.4. DAN thermal neutron count rates are shown for fixed locations, averaged by location and plotted versus traverse distance in meters. ....	134
Figure 3.5. DAN passive thermal neutron count rates from traverse measurements acquired along <i>Curiosity's</i> ~9.5 km route from Bradbury Landing to Amargosa Valley. ....	152
Figure 3.6. DAN passive thermal neutron count rates acquired during <i>Curiosity's</i> traverse on sol 424.....	154
Figure 3.7. WEH estimates derived from DAN passive data acquired at fixed locations along <i>Curiosity's</i> traverse from Bradbury Landing to Amargosa Valley. ....	158
Figure 3.8. WEH estimates along <i>Curiosity's</i> traverse from Bradbury Landing (traverse distance 0 m) to Amargosa Valley (traverse distance ~9435 m). ....	168



Figure 3.9. WEH estimates from sol 424 traverse showing an example of the small-scale anomalies observed in the continuously-acquired DAN passive traverse data. ....	169
Figure 3.10. DAN Passive WEH estimates versus DAN Active WEH estimates.....	172
Figure 3.11. DAN passive geochemical indices (DPGI) for all fixed and traverse measurement locations. ....	179
Figure 3.12. Histogram of DAN passive geochemical index (DPGI) values .....	180
Figure 3.13. Simulated DPGI values are calculated using the assumed “generic Mars” background regolith composition.....	181
Figure 3.14. Normalized histograms of WEH estimates from each unit traversed over during sols 0 to 753. ....	184
Figure A.3.1. Uncorrected thermal and epithermal neutron count rates acquired during the sol 683 traverse of a large, sandy ripple. ....	193
Figure A.3.2. Averaged uncorrected and corrected epithermal neutron count rates versus average DAN DE range acquired on sol 683 in the vicinity of the ripple.....	197
Figure A.3.3. Corrected thermal and epithermal neutron count rates from sol 683 as a function of traverse distance and averaged by odometry location. ....	198
Figure A.3.4. Histogram of the calculated average DAN DE ranges for the mission through sol 753.....	200
Figure A.3.5. Histogram of induced $\Delta$ WEH values between WEH estimates produced with the geometric correction applied and not applied. ....	201
Figure 4.1. DAN passive data from Rocknest acquired over sols 60 through 99, plotted as a function of Local Mean Solar Time (irrespective of sol number). ....	208

Figure 4.2. DAN passive data from John Klein acquired over sols 166 through 271, plotted as a function of Local Mean Solar Time (irrespective of sol number). .....	209
Figure 4.3. Rocknest power spectrum of DAN passive measured thermal neutron count rates from Fourier analysis showing 1 sol periodicity.....	210
Figure 4.4. John Klein power spectrum of DAN passive measured thermal neutron count rates from Fourier analysis showing 1 sol periodicity.....	211
Figure 4.5. Average atmospheric pressure at Rocknest (solid line) and John Klein (dashed line), plotted as a function of Local Mean Solar Time.....	213
Figure 4.6. Average REMS surface temperature measured at Rocknest (solid line) and John Klein (dashed line), plotted as a function of Local Mean Solar Time. ....	214
Figure 4.7. Simulation results for Rocknest showing the effect that subsurface temperature profiles for thermal skin depths of 6 cm and 10 cm have on total neutron count rates. ....	218
Figure 4.8. Modeled CTN count rates for the Rocknest location showing the effect that pressure variations in the martian atmosphere have on the measured count rates.....	223
Figure 4.9. Modeled CTN measured count rates for the John Klein location showing the effect that pressure variations in the martian atmosphere have on the measured count rates.....	224
Figure 4.10. Modeled thermal neutron measured count rates for the Rocknest location showing the effect that pressure variations in the martian atmosphere have on the measured count rates. ....	225
Figure 4.11. Modeled thermal neutron measured count rates for the John Klein location showing the effect that pressure variations in the martian atmosphere have on the measured count rates. ....	226
Figure 4.12. Average Rocknest detector temperature through sol.....	228

Figure 4.13. Average John Klein detector temperature throughout sol.....	229
Figure 4.14. Average CETN channel hourly count rate for channels 3, 4, 5, 8, 10, and 13 measured at Rocknest. ....	231
Figure 4.15. Average CETN channel hourly count rate for channels 3, 4, 5, 8, 10, and 13 measured at John Klein. ....	232
Figure 4.16. Average CTN channel hourly count rate for channels 3, 4, 5, 8, 10, and 13 measured at Rocknest.....	233
Figure 4.17. Average CTN channel hourly count rate for channels 3, 4, 5, 8, 10, and 13 measured at John Klein. ....	234
Figure 4.18. Modeled CTN count rates for the Rocknest location combining effects due to subsurface temperature variations, atmospheric pressure variations, and an empirically- derived correction for instrumental effects. ....	239
Figure 4.19. Modeled CTN count rates for the John Klein location combining effects due to subsurface temperature variations, atmospheric pressure variations, and detector temperature variations.....	240
Figure 4.20. Modeled thermal neutron count rates (squares) throughout the sol at Rocknest. ..	241
Figure 4.21. Modeled thermal neutron count rates (squares) throughout the sol at John Klein.	242

**CHAPTER I**  
**INTRODUCTION**

Neutron spectroscopy is the technique of using neutrons and their interactions with nuclei in order to study the light element composition, specifically hydrogen and elements with high thermal neutron absorption cross sections, of bodies within the solar system. In this context, spectroscopy refers to the broad energy discrimination between high energy and low energy neutrons used in this technique. Neutron spectroscopy can trace its heritage back to a technique on Earth that uses neutron interactions with matter as a means to find pore space within rock formations for oil drilling purposes. As well, before standing on its own as a planetary science technique, it was coupled to gamma-ray spectroscopy measurements as a means of constraining the gamma-ray flux intensities when converting to chemical concentrations. As such, many computational modeling endeavors involved calculating both planetary gamma-ray fluxes and neutron fluxes. In this way neutron spectroscopy techniques were developed in conjunction with gamma-ray spectroscopy techniques. Eventually, neutron spectroscopy became a singular useful measurement technique in its own right. While it is still actively used in conjunction with gamma-ray spectroscopy today, it is also often found in use without a corresponding gamma-ray instrument.

Neutron spectroscopy is important when compared to other remote-sensing techniques that determine composition in planetary science, for example, visible/near-infrared spectroscopy or gamma ray spectroscopy, because it is sensitive to shallow regolith depths of approximately  $160 \text{ g/cm}^2$ , which is  $\sim 89 \text{ cm}$  for an example density of  $1.8 \text{ g/cm}^3$ . Other techniques are only sensitive to the surface of the body or penetration depths of a few microns. Neutron spectroscopy is also important in the determination of hydrogen content within planetary regoliths. Hydrogen is an important element in planetary science in that it can be an indicator of places where there is water or has been water in the past. Finding water is relevant in the search for extraterrestrial life

and habitable environments that could support microbial extraterrestrial life because terrestrial life as we know it requires water (*e.g.*, Rasool and De Bergh, 1970). As such, one guiding principle in the search for extraterrestrial life in recent decades has simply been "follow the water". Hydrogen is also important in the future of manned spaceflight as it will most likely be necessary for missions to acquire resources, such as hydrogen, from the body itself. This hydrogen can be used to create fuel or water on the surface of the body for mission use, but must be derived from the parent body as transporting large amounts of hydrogen on long term missions, such as what would be required for a manned mission to Mars or an asteroid, quickly becomes cumbersome and cost prohibitive. Landing near hydrogen deposits thus not only gives better chances at investigating locations that could be able to or at one time were able to support life, but will also help provide the necessary resources for such a mission to be successful.

Lastly, neutron spectroscopy is intricately linked to the radiation environment at a planetary body. Understanding the local neutron fluxes at the surface of a body requires knowledge of the radiation environment, specifically high energy ionizing radiation reaching the surface, which is harmful to astronauts. Relatively low energy neutrons contribute to an astronaut's expected dose rates as well, though, not as much as the high energy ionizing radiation. Modeling work to estimate planetary neutron fluxes requires modeling of the primary high energy radiation environment and its interactions with the planetary body which allows for insight into the radiation environment at the surface of the body. These types of results, while not replacing *in situ* radiation data, are useful in mission planning and design when conceptualizing radiation shielding strategies in order to protect astronauts and keep them under the lifetime allowed dose limits. In practice, neutron spectrometers can provide *in situ* low energy neutron data which can be used for verifying these models and calculating expected dose rate

contributions from this portion of the radiation environment.

## Background

The principles of neutron spectroscopy follow from the primary interactions of neutrons with the nuclei of the constituents of the planetary body. More specifically, the underlying principle is the moderation of neutron energies from fast to thermal energies when neutrons are interacting with the regolith of a planetary body. These neutrons are created by interactions between high energy particles called Galactic Cosmic Rays (GCRs) and the constituents of the planetary regolith and or atmosphere. GCRs consist of protons (~87 %), alpha particles (~12 %), and heavier ions and other particles (~1 %) (Simpson *et al.*, 1983) that have energies from 100 MeV per nucleon to  $\geq 1$  TeV per nucleon (Morthekai *et al.*, 2007). The origin of GCRs is not explicitly known, but, they do originate from outside of the solar system, and the most popular hypotheses are from the supernova paradigm involving GCRs being generated in supernova remnants (Blasi, 2008). Fortunately, understanding the origin of GCRs is not fundamentally necessary for understanding the role they play in neutron spectroscopy. As GCRs penetrate the solar system they isotropically impinge on the planetary bodies. In the case of Earth, where the atmospheric column density is an order of magnitude greater than the penetration depth of GCRs ( $\sim 160 \text{ g/cm}^2$ ), the planet's surface is effectively shielded by GCR interactions in the upper atmosphere which produce secondary electromagnetic particle showers. However, on bodies where the atmosphere is thin or negligible, *e.g.*, the moon or Mars, GCRs will penetrate the atmosphere or lack thereof and reach the regolith where they will interact with the nuclei of the constituent elements.

Neutrons are produced through GCR interactions through two mechanisms: direct

interactions and spallation collisions and neutron evaporation from excited residual nuclei produced during the prompt interactions (Drake *et al.*, 1988). For bodies with tenuous atmospheres, these interactions can take place in the atmosphere as well, but not nearly as often as in the regolith of the body (Drake *et al.*, 1988). Approximately 9 or 10 neutrons are produced per primary GCR spallation interaction in a body (Reedy and Arnold, 1972). The energy spectra of these neutrons can be divided into two groups. Neutrons produced through direct interactions and spallation collisions have a continuous energy distribution up to the energy of the incoming GCR particle (Drake *et al.*, 1988). Evaporation neutrons exhibit a Gaussian energy distribution centered on 1 MeV (Drake *et al.*, 1988).

These neutrons subsequently moderate in the surrounding regolith material and lose energy through interactions with the nuclei of the regolith until they are either captured or escape and contribute to the surface neutron leakage flux. Above 1 MeV inelastic and elastic scattering collisions are both important neutron energy-moderating interactions (Drake *et al.*, 1988). Below 1 MeV, elastic scattering is the dominant energy loss mechanism (Drake *et al.*, 1988). Once the neutrons reach thermal energies, moderation ceases because neutrons will gain as much energy from thermal motion of the nuclei as they lose from collisions (Drake *et al.*, 1988). The spectra of the surface neutron leakage flux depends heavily on the composition of the body. More specifically, it depends largely on the amount of hydrogen in the regolith of the body (Lingenfelter *et al.*, 1961). This is because hydrogen is the most efficient moderator of neutron energies as it is the only isotope with a mass comparable to the mass of the neutron. From the equation

$$E_A^{max} = \frac{4m_N M_A}{(m_N + M_A)^2} E_N' \quad (\text{Knoll, 2000}),$$

where  $E_A^{max}$  is the maximum recoil energy of the target nucleus A and  $m_N$  is the mass of the



neutron, a neutron can give up to the entirety of its initial kinetic energy ( $E_N$ ) in an elastic collision with a target nucleus of mass  $M_A$ . A neutron will therefore lose, on average,  $1/2$  of its initial kinetic energy per collision with a hydrogen nucleus in an elastic scattering event. For heavier nuclei,  $A$  increases and thus the average energy loss per collision decreases, leading to less efficient moderation of neutron energies. As neutrons are generated in the atmosphere or shallow regolith of the body, they will have an energy spectrum that extends up to the energy of the incoming primary GCR particle. Generated high energy neutrons are known as "fast" neutrons. As the fast neutrons interact with the surrounding nuclei their energies will moderate into the epithermal range and so forth until the neutrons reach the thermal energy range. This moderation of neutron energies manifests itself as decreases in the fast and epithermal neutron populations, while increasing the thermal neutron population. In effect, the escaping surface leakage flux will contain neutrons of all energies, but, the relative populations of each energy range will vary depending on just how much moderation has taken place. Neutron spectroscopy instruments can therefore correlate decreases in the fast or epithermal neutron populations or increases in the thermal neutron population with hydrogen content.

The neutron leakage flux is further complicated by the presence of elements which have high thermal neutron absorption cross sections, such as iron or chlorine (Hardgrove *et al.*, 2011). The effect of these elements is to remove thermal neutrons from the surface leakage flux, causing a complicating factor when considering the thermal neutron population. This effect, however, can be useful in obtaining information about such elements and their abundances in the regolith being studied.

The problem is further complicated by the fact that the source of the neutrons is not constant in time. This is because GCRs are modulated by solar activity and more specifically the

interplanetary magnetic field (IMF). At times of greater solar activity, the IMF is stronger and the GCR intensity is reduced by the interactions of the GCRs with the IMF. On the other hand, when solar activity is at a minimum, the GCR intensities are greater. This introduces not only a time dependence of the GCR intensity, but also a radial distance from the sun dependence that must be taken into account when estimating the surface neutron leakage flux for a body. While the solar cycle has a period of ~11 years, there are other shorter period variations and transient events related to the sun that also affect the GCR intensity. Particularly notable, these are the 27 day period heliospheric variations, Forbush decreases due to coronal mass ejections, and solar energetic particles events. These events modulate the GCR intensity in event specific ways depending on the nature and magnitude of each event and also whether or not a specific neutron spectrometer instrument may be sensitive to those effects is dependent on the nature of the specific instrument.

Making use of the neutron leakage flux at a planetary body requires extensive modeling of the neutron leakage flux for different parameters in an effort to understand how the neutron leakage flux responds to said parameters. Initially, deterministic methods were used to calculate planetary leakage fluxes (*e.g.*, Lingenfelter *et al.*, 1961). This involves solving the Boltzmann equation for neutron transport using numerical methods. Neutron transport work of this sort initially came about in order to understand neutron transport and interactions with regard to reactor design and operation and is still in use today. Understandably, it is difficult to solve this equation for complex geometries and continuous neutron energy distributions.

As computational resources have progressed, so too has the ability to simulate neutron transport and interactions in a medium. These methods involve Monte Carlo techniques, which allow for neutron transport and computation in 3 dimensional geometries and continuous energy

distributions. The downside is that these methods are extremely computationally intensive. The method used for determining a neutron flux within a medium depends on the nature of the problem at hand and the specific results needed. Currently, in the case of planetary neutron spectroscopy, Monte Carlo techniques far outweigh the Boltzmann equation and are the typical method of calculating planetary neutron leakage fluxes. This is mainly because of the need to simulate 3 dimensional geometries and many different neutron energies. Specific Monte Carlo techniques used in this work will be discussed in more detail in Chapter 1.

Neutron spectrometers employ a variety of detector materials and methods to measure the relevant neutron fluxes. These include  $^3\text{He}$  detectors, various scintillation detectors, and combinations of the two either together or with various shielding configurations. These detectors are sensitive to neutrons in different energy regions with different efficiencies and detection methods and are selected depending on the science goals and requirements of the instrument and mission.

## Literature Review

In 1961, Lingenfelter *et al.* calculated the lunar neutron flux through multigroup diffusion calculations in order to estimate the usefulness of neutron flux measurements in determining the composition of the lunar surface. It was determined that hydrogen has a large effect on the neutron leakage flux and so they proposed an experiment near the lunar surface to determine the hydrogen abundance (Lingenfelter *et al.*, 1961). Specifically, using a combination of two neutron detectors, one of which has an energy sensitivity of  $1/v$  and the other which has a flat response at higher energy, the ratio of counts of the two detectors could be used to infer the  $H/Si$  atomic ratio (Lingenfelter *et al.*, 1961). This effectively pioneered the idea of using stand alone neutron

detectors as a means to measure the hydrogen abundance in the regolith of planetary bodies. However, that is not to say that the techniques and methods have not improved greatly since that time.

In 1984, a paper by Haines and Metzger expanded greatly on the application of neutron measurements by pointing out that this technique need not be constrained just to the moon, but that other bodies in the solar system, such as Mars, asteroids, comet nuclei, and large planet satellites would be reasonable targets for this type of study as well. While they proposed a simple neutron detector could be used by way of a neutron-absorbing shield surrounding a gamma ray spectrometer, they also expanded on detector techniques, such as proposing a collimated neutron detector that would increase spatial resolution by 2 to 3 times that of an omnidirectional detector (Haines and Metzger, 1984). Applications they proposed for such detectors were creating maps of thermal neutron flux enhancements over the entire surface of the body. Such maps are still typical products for neutron spectrometers today.

From this point, significant advancements in various topics in the field would start to come about. The first notable paper is that by Drake *et al.* in 1986. The authors studied sensitivities of different fast neutron detectors designed to fly in space. These detectors included a  $^3\text{He}$  proportional counter surrounded by a scintillating plastic annulus and a boron loaded plastic scintillator (Drake *et al.*, 1986). It was found that the boron loaded plastic scintillator had better detection efficiency and required less mass to implement (Drake *et al.*, 1986). The most interesting conclusion from this paper, however, is that the author was able to use the "Monte Carlo code" at Los Alamos National Lab to simulate the response of various detector designs. The method of using Monte Carlo techniques is still incredibly useful today and is the typical method of approaching problems such as these. Furthermore, beyond detector response studies,

Monte Carlo methods are specifically used extensively in modeling and predicting neutron fluxes for planetary bodies.

One important example of such an endeavor is the work by Drake *et al.* in 1988. This work was an extensive computational effort to calculate the Martian neutron leakage spectra and how it responds to different factors. Such neutron leakage flux calculations had previously been done for the moon by solving the Boltzmann equation (Lingenfelter *et al.*, 1961), but not yet for Mars. A combination of Monte Carlo techniques and solving the Boltzmann equation with a one-dimensional diffusion transport code were used to simulate high energy GCR interactions and neutron production in the Martian atmosphere and regolith and transport and moderation of neutrons within the regolith (Drake *et al.*, 1988). Neutron leakage flux response to factors like different initial GCR spectra, the presence of an atmosphere, and varying regolith composition and stratigraphic layering were explored. Results showed that the shape of the produced neutron spectra in the regolith is not dependent on the initial GCR energies, but the intensity is (Drake *et al.*, 1988). It was also shown that the presence of the Martian atmosphere causes a significant increase in the amount of low energy neutrons escaping the surface, compared to the no atmosphere case (Drake *et al.*, 1988). Lastly, they showed how the individual thermal and epithermal neutron leakage fluxes responded to various water contents and stratigraphies containing buried water ice, showing how such a neutron spectrometer may be used to determine buried ice deposits in a shallow regolith (Drake *et al.*, 1988). These methods are still employed today to infer hydrogen stratigraphy in shallow regoliths.

The first planetary science mission to use neutron detectors was NASA's Lunar Prospector, which launched in 1998. The instrument is titled the Neutron Spectrometer (NS). The NS consisted of two  $^3\text{He}$  proportional counters, one of which had a cadmium shield (Feldman *et*

*al.*, 1999) so that it could measure thermal and epithermal neutrons. It was also capable of measuring fast neutrons through the use of the anticoincidence shield on the Lunar Prospector gamma-ray spectrometer. One of the first results were global maps of the thermal, epithermal, and fast neutron fluxes (Feldman *et al.*, 1998) such as was proposed by Haines and Metzger in 1984. These maps showed large scale unit correlations. Specifically, a high thermal and low fast neutron flux unit corresponded to the lunar highlands, which is consistent with feldspathic rocks (Feldman *et al.*, 1998). Intermediate thermal and fast neutron flux units correlated with the South Pole-Aitken Basin (Feldman *et al.*, 1998). Lastly, the lunar maria showed low thermal and high fast neutron fluxes, consistent with basaltic rocks (Feldman *et al.*, 1998). This work demonstrated firsthand the usefulness of the techniques that had been in development since the 1960s.

The next planetary science mission to use a neutron spectrometer was Mars Odyssey which launched in 2001 containing the Gamma-Ray Spectrometer (GRS) instrument suite. This was the first instance of such an instrument investigating Mars. The GRS contained a gamma-ray spectrometer, a neutron spectrometer (NS) and the High Energy Neutron Detector (HEND) (Boynton *et al.* 2004). The NS consisted of a cubical block of boron-loaded plastic scintillator (Boynton *et al.*, 2004). HEND combined three  $^3\text{He}$  proportional counters surrounded by polyethylene moderators inside cadmium can shields and a scintillation block with two scintillators (Boynton *et al.*, 2004). Results from Mars Odyssey GRS would shed light on the global distribution of hydrogen on Mars.

A paper in 2004 by Feldman *et al.* showed just that by comparing GRS neutron data to simulations of Martian neutron leakage fluxes using the Monte Carlo Neutral Particle eXtended code (MCNPX). Using the NS epithermal and fast neutron counting data, Feldman *et al.* showed

that poleward of  $\pm 50^\circ$  latitude there were hydrogen deposits of 20% to 100% water equivalent hydrogen by mass. In the equatorial regions, water equivalent hydrogen ranged from 2% to 10% by mass (Feldman *et al.*, 2004). Ultimately, this gives an estimated global water layer of ~14 cm thick if the thickness of the reservoir sampled from orbit by GRS is 1 m (Feldman *et al.*, 2004). HEND and or gale crater estimate for region 5 wt. %. More important to the work to be discussed here, the water equivalent hydrogen abundance in the Gale crater region is ~ 5 wt. % (Feldman *et al.*, 2004). While the spatial footprint of HEND is ~600 km, the diameter of Gale crater is only 154 km. Another important aspect of the work performed by Feldman *et al.* (2004) was the use of Monte Carlo techniques. While Monte Carlo techniques had been used before in conjunction with deterministic methods such as in Drake *et al.* (1988), Mars Odyssey GRS would also fully implement the Monte Carlo techniques (MCNPX) for use in data analysis and martian neutron leakage flux modeling (Feldman *et al.*, 2004) with no use of deterministic methods, *i.e.*, solving the Boltzmann equation. As stated, this is now the typical method of performing such analyses.

The next mission to include a neutron spectrometer was to a new target within the solar system, Mercury, onboard the Mercury, Surface, Space Environment, Geochemistry, and Ranging (Messenger) spacecraft which launched in 2004. This instrument was a part of the Messenger Gamma-Ray and Neutron Spectrometer (GRNS) and consisted of two GS20 Li-glass scintillators and a BC454 scintillator in order to cover the thermal, epithermal, and fast energy ranges (Goldsten *et al.*, 2007). Results from the Messenger GRNS would help in understanding the composition of Mercury which was poorly constrained up until this point.

A paper illustrating this is by Lawrence *et al.* (2010). The authors again used Monte Carlo techniques and specifically, MCNPX to model Mercury neutron leakage fluxes for

comparison to data. Results showed that Mercury has a macroscopic neutron absorption cross section similar to that of lunar basalts from Mare Crisium (Lawrence *et al.*, 2010). They also show that the absorbing elements are Fe and Ti with trace contributions from Gd and Sm, which was different from previous models of Mercury's compositions which had very low amounts of these elements (Lawrence *et al.*, 2010). Lastly, they showed that these data could be fit by Mercury's surface having an ilmenite abundance of 7-18 wt. %.

Implications for hydrogen abundance in Mercury's surface would come later in 2013 as described by Lawrence *et al.* (2013). By correlating decreases in the populations of epithermal and fast neutrons, it was shown that Mercury contained hydrogen rich deposits in the north polar region (Lawrence *et al.*, 2013). Further modeling, showed that the data are fit by a nearly pure water ice layer buried 10 to 30 cm below a layer that contains less than 25 wt. % water equivalent hydrogen which was consistent with bright radar backscattering in the region (Lawrence *et al.*, 2013). The total water mass at the poles is also consistent with delivery by comets and volatile-rich asteroids, while models of water migration and surface modification indicate that the water ice was emplaced during the last 18 to 70 My (Lawrence *et al.*, 2013), providing insight into the recent history of Mercury and its surface processes.

The Dawn mission launched in 2007 and carried a gamma-ray spectrometer and neutron spectrometer instrument (GR/NS) to the main-belt asteroids Ceres and Vesta. The GR/NS is able to detect fast, epithermal, and thermal neutrons using 4 BC454 scintillators and 2 GS20 scintillators owing its heritage to both Lunar Prospector and Mars Odyssey (Prettyman *et al.*, 2003). Dawn first arrived at Vesta in 2011, where the neutron spectrometer was used to great extent to make conclusions about the origins of the body.

Hydrogen abundances are shown to range from 0  $\mu\text{g/g}$  to 400  $\mu\text{g/g}$  with a total global



inventory of  $2.4 \times 10^{11}$  kg of hydrogen within the regolith at the depths sensed by GR/NS (Prettyman *et al.*, 2011). This is important because Vesta is thought to have accreted from volatile-poor materials and thus would have been very hydrogen-poor, leading to the conclusion that hydrogen on Vesta has been delivered by exogenous sources (Prettyman *et al.*, 2011). More specifically, because of the high-hydrogen contents of certain regions, implantation of solar wind hydrogen is ruled out and the infall and survival of hydrous materials from meteoroids is found to be consistent (Prettyman *et al.*, 2011). Furthermore, this paper shows novel work on how to separate neutron counting rate contributions from hydrogen and other elements, *i.e.* absorbers, by creating scatter plots of epithermal neutron counting rates versus thermal plus epithermal neutron counting rates. In the case of Vesta, this showed that neutron absorption is not uniform on the surface and specifically, the Rheasilvia Basin composition is consistent with cumulate eucrites and diogenites (Prettyman *et al.*, 2011).

The next planetary science mission to carry a neutron spectrometer was a return to the moon in 2009 with the spacecraft Lunar Reconnaissance Orbiter, which carried the Lunar Exploration Neutron Detector (LEND). The LEND instrument is the first and so far only example of a collimated neutron detector to fly on an orbital platform on a planetary science mission (Mitrofanov *et al.*, 2008) and as such the first major improvement of the neutron spectroscopy technique since the first iteration of such an instrument on Lunar Prospector. LEND consists of 9 sensors. The most novel part of the design are the Collimated Sensors of Epithermal Neutrons (CSETN) of which there are 4. These sensors are  $^3\text{He}$  proportional counters with cadmium shields to absorb thermal neutrons. Collimation is achieved by surrounding the detectors on all sides, except their nadir facing openings, with neutron absorbing material. This collimator is made of an inner layer  $^{10}\text{B}$ , which has a very high neutron capture cross-section,

and an outer layer of polyethylene in order to slow incoming neutrons to increase the efficiency of the  $^{10}\text{B}$  absorber (Mitrofanov *et al.*, 2008). Inside the collimator is also a sensor of high energy neutrons (SHEN) which is a stilbene scintillator which detects neutrons in energy range of 0.3 to 150 MeV (Mitrofanov *et al.*, 2008). The other detectors are uncollimated  $^3\text{He}$  proportional counters, 3 of which are unshielded and 1 which has a cadmium shield, which allow characterization of the neutron environment around the spacecraft (Mitrofanov *et al.*, 2008). The most important aspect of LEND is the ability to collimate the neutron sensors allowing for increases in spatial resolution ( $\sim 10$  km) (Mitrofanov *et al.*, 2010) compared to omnidirectional counters of Lunar Prospector ( $\sim 450$  km) (Feldman *et al.*, 1998).

Owing to the greatly increased spatial resolution of the LEND instrument, lunar hydrogen was mapped at never before seen spatial scales (Mitrofanov *et al.*, 2010). More interesting, is that these results also showed that permanently shadowed regions at the lunar poles, which were thought to harbor enhanced hydrogen abundance due to cold trapping, were not hydrogen-rich compared to surrounding sunlit areas as previously thought (Mitrofanov *et al.*, 2010). These results did, however, show that a location within Cabeus crater contained the highest hydrogen concentration in the south polar region and furthermore this was to be the LCROSS mission impact site based on these results (Mitrofanov *et al.*, 2010).

While the LEND instrument brought about a very large increase in the spatial resolution of neutron spectrometers investigating the moon, the Dynamic Albedo of Neutrons instrument (DAN) onboard the Mars Science Laboratory (MSL) would usher in an even greater increase in spatial resolution for neutron spectrometers investigating Mars. DAN is the first instance of a neutron spectrometer onboard a rover based platform (Litvak *et al.*, 2008). This means that the spatial resolution of the instrument is  $\sim 3$  m versus the 600 km of previous Mars Odyssey

investigations (Litvak *et al.*, 2008). DAN consists of two  $^3\text{He}$  one of which is shielded with cadmium so that the instrument is sensitive to neutrons up to 100 keV (Litvak *et al.*, 2008). It also makes use of a pulse neutron generator (PNG) which pulses  $10^7$  neutrons per pulse allowing for greatly improved counting statistics and shorter integration times (Litvak *et al.*, 2008). This is known as active neutron spectroscopy and creates what is known as a die-away curve, a novel technique as well in planetary neutron spectroscopy (Litvak *et al.*, 2008) as all instruments up unto this point had not included an active neutron source. The die-away curve allows for capturing the timing of the neutron leakage fluxes as neutrons return post-PNG pulse (Litvak *et al.*, 2008). This allows for nuanced investigations into the neutron leakage fluxes that can better reveal information about the subsurface composition and stratigraphy (Litvak *et al.*, 2008). The instrument can also be operated in a continuous passive mode, similar to orbital neutron spectrometers. The DAN instrument therefore allows for characterization of the small scale variability of hydrogen and also thermal neutron absorbing elements within the regolith of Gale crater. Results from the passive mode of this instrument are the subject of this work and thus will be discussed further in the following chapters.

One important paper by Hardgrove *et al.* (2011) showed the effects that thermal neutron absorbing elements would have on the DAN data in relation to DAN die-away curves. The effects of these elements on the neutron leakage fluxes were already known from previous instruments and studies, but, the particular magnitude of these effects on DAN die-away curves was unrealized. Specifically, varying amounts of these elements within the martian regolith would cause both shifts in the peak time and shape of the thermal neutron die-away curves, which could lead to misinterpretation of the hydrogen abundance or subsurface stratigraphy, if not accounted for as a parameter in the Monte Carlo models (Hardgrove *et al.*, 2011). This is

useful in that it allows DAN, in its active mode, to actually characterize not just hydrogen abundance, but also the amount of thermal neutron absorbing elements in the shallow subsurface (Hardgrove *et al.*, 2011).

Currently, planetary neutron spectroscopy is still an evolving field with many advances in detectors, spacecraft design, and modeling capabilities allowing for revisions to previous data sets and setting the stage for future missions and instruments to previous and new targets within the solar system. There are many neutron spectrometers in development that will fly on missions in the near future. Two of these instruments will go to Mars. One is the Fine Resolution Epithermal Neutron Detector (FREND), which will launch in 2018 on ExoMars. FREND is a collimated neutron detector very similar to LEND and will improve upon the spatial resolution of martian global neutron emission maps of by a factor of 10 (Malakhov *et al.*, 2012). In conjunction with the 2018 ExoMars orbiter, a rover will land and explore Mars on the local scale as well. This rover's payload will include a neutron spectrometer (ADRON-RM) that has the same conceptual design as the MSL DAN passive mode instrument (Nikiforov *et al.*, 2013). Another new instrument is the Mercury Gamma-Ray and Neutron Spectrometer (MGNS) onboard the mission BepiColombo, which will also launch in 2018. The MGNS derives its heritage from the HEND instrument that flew to Mars in 2001 (Mitrofanov *et al.*, 2010). New detectors are also being developed. Namely, a new scintillator material of  $Cs_2YLiCl_6:Ce$  will fly on the LunaH-Map mission also launching in 2018 (Hardgrove *et al.*, 2016). This mission is innovative as well for the fact that it is a CubeSat mission and will attempt to demonstrate that significant scientific returns can be made with CubeSat-sized spacecraft, in particular in planetary neutron spectroscopy (Hardgrove *et al.*, 2016).

From satellites to planets to asteroids, neutron spectroscopy has been used successfully

on bodies within the inner solar system for nearly 2 decades with many more instruments currently being prepared to fly on their respective missions. These instruments have measured neutrons from thermal up to fast energies in order to understand the global bulk composition of the shallow regolith of the bodies being investigated. Our understanding of how to correctly model such neutron leakage fluxes has progressed greatly in this time span as well, allowing for more realistic models and more accurate results.

The MSL DAN instrument is the next evolution of such instruments with its greatly increased spatial footprint on the surface of Mars. The Mars Exploration Program at NASA has been exploring Mars for many years. This is because Mars is special in the inner solar system not only because it is our nearest planetary neighbor, but because the possibility of a warm and wet ancient Mars (Pollack *et al.*, 1987) leads to Mars being an excellent choice to search for habitable environments and or extraterrestrial life. Mars will also very likely be the next destination that manned spaceflight will attempt to reach, and the better we understand the current environment and processes of Mars, the better we will be able to assess potential landing areas with the highest scientific return for such missions. Things like resource acquisition and understanding the radiation environment will also play extremely important roles in such a mission and as such, the more we can learn about these factors now, the more likely we are to be successful in the future. Neutron spectroscopy on the surface with MSL DAN is allowing both characterization of the variability of hydrogen in the shallow regolith and characterization of the low energy neutron radiation environment generated by GCRs by interactions with the regolith and atmosphere. In comparison to previous orbital studies at Mars with such spectrometers (*e.g.*, Feldman *et al.*, 2004), the DAN instrument will allow for greatly increased spatial resolution of WEH measurements at a specific location on Mars. This will allow for investigation of the small-

scale spatial distribution of WEH, specifically in Gale crater, which will support the instrument suite and primary mission goal of finding an environment on Mars that was habitable at some point in its past. The first chapter of this work will discuss from the ground up the modeling and analysis of DAN passive mode data from Gale Crater. The second chapter will focus on extending and improving the models developed in the first chapter and again be used for analysis of DAN passive mode data over the extent of the MSL traverse over the crater floor units of Gale. Lastly, the third chapter presented here will cover investigations into diurnal variations observed in the martian neutron leakage fluxes by the DAN instrument on the surface of Mars.

## References

- Blasi, P. (2008), Origin of high energy cosmic rays: A short review, *Nuclear Instruments and Methods in Physics A*, 588, 166-170.
- Boynton, W. V., W. C. Feldman, I. G. Mitrofanov, L. G. Evans, R. C. Reedy, S. W. Squyres, R. Starr, J. I. Trombka, C. D'uston, J. R. Arnold, P. A. J. Englert, A. E. Metzger, H. Wänke, J. Brückner, D. M. Drake, C. Shinohara, C. Fellows, D. K. Hamara, K. Harshman, K. Kerry, C. Turner, M. Ward, H. Barthe, K. R. Fuller, S. A. Storms, G. W. Thornton, J. L. Longmire, M. L. Litvak, and A. K. Ton'chev (2004), The Mars Odyssey Gamma-Ray Spectrometer Instrument Suite, *Space Science Reviews*, 110, 37-83.
- Drake, D. M., W. C. Feldman, and C. Hurlbut (1986), New Electronically Black Neutron Detectors, *Nuclear Instruments and Methods in Physics A*, 247, 576-582.
- Drake, D.M., W.C. Feldman, and B.M. Jakosky (1988), Martian Neutron Leakage Spectra, *Journal of Geophysical Research*, 93, 6353-6368.
- Feldman, W. C., B. L. Barraclough, S. Maurice, R. C. Elphic, D. J. Lawrence, D. R. Thomsen, A. B. Binder (1998), Major Compositional Units of the Moon: Lunar Prospector Thermal and Fast Neutrons, *Science*, 281, 1489-1493.
- Feldman, W. C., B. L. Barraclough, K. R. Fuller, D. J. Lawrence, S. Maurice, M. C. Miller, T. H. Prettyman, and A. B. Binder (1999), The Lunar Prospector gamma-ray and neutron spectrometers, *Nuclear Instruments and Methods in Physics Research A*, 422, 562-566.
- Feldman, W. C., T. H. Prettyman, S. Maurice, J. J. Plaut, D. L. Bish, D. T. Vaniman, M. T. Mellon, A. E. Metzger, S. W. Squyres, S. Karunatillake, W. V. Boynton, R. C. Elphic, H. O. Funsten, D. J. Lawrence, and R. L. Tokar (2004), Global Distribution of near-surface hydrogen on Mars, *Journal of Geophysical Research*, 109, 2156-2202.
- Goldsten, J. O., E. A. Rhodes, W. V. Boynton, W. C. Feldman, D. J. Lawrence, J. I. Trombka, D. M. Smith, L.G. Evans, J. White, N. W. Madden, P. C. Berg, G. A. Murphy, R. S. Gurnee, K. Strohhahn, B. D. Williams, E. D. Schaefer, C. A. Monaco, C. P. Cork, J. Del Eckels, W. O. Miller, M. T. Burks, L. B. Hagler, S. J. DeTeresa, and M. C. Witte (2007), The MESSENGER Gamma-Ray and Neutron Spectrometer, *Space Science Reviews*, 131, 339-391.
- Haines, E. L. and A. E. Metzger (1984), Measuring Planetary Neutron Albedo Fluxes By Remote Gamma-Ray Sensing, *Nuclear Instruments and Methods in Physics Research*, 226, 517-523.
- Hardgrove, C., J. Moersch, and D. Drake (2011), Effects of geochemical composition on neutron die-away measurements: Implications for Mars Science Laboratory's Dynamic Albedo of Neutrons experiment, *Nuclear Instruments and Methods in Physics Research A*, 659, 442-455.

- Hardgrove, C., J. Bell, R. Starr, T. Colaprete, M. Robinson, D. Drake, I. Lazbin, G. West, E. Johnson, J. Christian, A. Genova, D. Dunham, B. Williams, D. Nelson, A. Babuscia, P. Scowen, K. M. Cheung, A. Klesh, H. Kerner, A. Deran, R. J. Amzler, Z. Burnham, J. Lightholder, P. Wren, A. Godber, and M. Beasley (2016), The Lunar Polar Hydrogen Mapper (LunaH-Map) CubeSat Mission, Lunar and Planetary Science Conference, The Woodlands, Texas.
- Knoll, G. F. (2000), Radiation Detection and Measurement, New York: John Wiley and Sons, Inc.
- Lawrence, D. J., W. C. Feldman, J. O. Goldsten, T. I. McCoy, D. T. Blewett, W. V. Boynton, L.G. Evans, L. R. Nittler, E. A. Rhodes, and S. C. Solomon (2010), Identification and measurement of neutron-absorbing elements on Mercury's surface, *Icarus*, 209, 195-209.
- Lawrence, D. J., W. C. Feldman, J. O. Goldsten, S. Maurice, P. N. Peplowski, B. J. Anderson, D. Bazell, R. L. McNutt Jr., L. R. Nittler, T. H. Prettyman, D. J. Rodgers, S. C. Solomon, and S. Z. Weider (2013), Evidence for Water Ice Near Mercury's North Pole from MESSENGER Neutron Spectrometer Measurements, *Science*, 339, 292-296.
- Lingenfelter, R. E., E. H. Canfield, and W. N. Hess (1961), The Lunar Neutron Flux, *Journal of Geophysical Research*, 66, 2665-2671.
- Litvak, M.L., I. G. Mitrofanov, Yu. N. Barmakov, A. Behar, A. Bitulev, Yu. Bobrovniksky, E. P. Bogolubov, W. V. Boynton, S. I. Bragin, S. Churin, A. S. Grebennikov, A. Konovalov, A. S. Kozyrev, I. G. Kurdumov, A. Krylov, Yu. P. Kuznetsov, A. V. Malakhov, M. I. Mokrousov, V. I. Ryzhkov, A. B. Sanin, V. N. Shvetsov, G. A. Smirnov, S. Sholeninov, G. N. Timoshenko, T. M. Tomilina, D. V. Tuvakin, V. I. Tretyakov, V. S. Troshin, V. N. Uvarov, A. Varenikov, and A. Vostrukhin (2008), The Dynamic Albedo of Neutrons (DAN) experiment for NASA's 2009 Mars Science Laboratory, *Astrobiology*, 8, 605-613.
- Malakhov, A., I. Mitrofanov, A. Sanin, M. Litvak, A. Kozyrev, V. Tretyakov, M. Mokrousov, A. Vostrukhin, D. Golovin, and F. Fedosor (2013), European Geosciences Union General Assembly, Vienna, Austria.
- Mitrofanov, I. G., A. B. Sanin, D. V. Golovin, M. L. Litvak, A. A. Konovalov, A. S. Kozyrev, A. V. Malakhov, M. I. Mokrousov, V. I. Tretyakov, V. S. Troshin, V. N. Unarov, A. B. Varenikov, A. A. Vostrukhin, V. V. Shevchenko, V. N. Shvetsov, A. R. Krylov, G. N. Timoshenko, Y. I. Bobrovniksky, T. M. Tomilina, A. S. Grebennikov, L. L. Kazakov, R. Z. Sagdeev, G. N. Milikh, A. Bartels, G. Chin, S. Floyd, J. Garvin, J. Keller, T. McClanahan, J. Trombka, W. Boynton, K. Harshman, R. Starr, and L. Evans (2008), Experiment LEND of the NASA Lunar Reconnaissance Orbiter for the High-Resolution Mapping of Neutron Emission of the Moon, *Astrobiology*, 8, 793-804.
- Mitrofanov, I. G., A. S. Kozyrev, A. Konovalov, M. L. Litvak, A. A. Malakhov, M. I. Mokrousov, A. B. Sanin, V. I. Tret'yakov, A. V. Vostrukhin, Yu. I. Bobrovnikskij, T. M.



- Tomilina, L. Gurvits, and A. Owens (2010a), The Mercury Gamma and Neutron Spectrometer (MGNS) on board the Planetary Orbiter of the BepiColombo mission, *Planetary and Space Science*, 58, 116-124.
- Mitrofanov, I. G., A. B. Sanin, W. V. Boynton, G. Chin, J. B. Garvin, D. Golovin, L. G. Evans, K. Harshman, A. S. Kozyrev, M. L. Litvak, A. Malakhov, E. Mazarico, T. McClanahan, G. Milikh, M. Mokrousov, G. Nandikotkur, G. A. Neumann, I. Nuzhdin, R. Sagdeev, V. Shevchenko, V. Shvetsov, D. E. Smith, R. Starr, V. I. Tretyakov, J. Trombka, D. Usikov, A. Varenikov, A. Vostrukhin, and M. T. Zuber (2010b), Hydrogen Mapping of the Lunar South Pole Using the LRO Neutron Detector Experiment LEND, *Science*, 330, 483-486.
- Morthekai, P., M. Jain, L. Dartnell, A.S. Murray, L. Bøtter-Jensen, and L. Desorgher (2007), Modeling of the dose-rate variations with depth in the Martian regolith using GEANT4, *Nuclear Instruments and Methods in Physics Research A*, 580, 667-670.
- Nikiforov, S., I. Mitrofanov, A. Kozyrev, F. Fedosov, M. Litvak, M. Mokrousov, A. Sanin, V. Tret'yakov, A. Vostrukhin, and A. Konovalov (2013), European Geosciences Union General Assembly, Vienna, Austria.
- Pollack, J. B., J. F. Kasting, S. M. Richardson, and K. Poliakov (1987), *Icarus*, 71, 203-224.
- Prettyman, T. H., W. C. Feldman, F. P. Ameduri, B. L. Barraclough, E. W. Cascio, K. R. Fuller, H. O. Funsten, D. J. Lawrence, G. W. McKinney, C. T. Russell, S. A. Soldner, S. A. Storms, C. Szeles, and R. L. Tokar (2003), Gamma-Ray and Neutron Spectrometer for the Dawn Mission to 1 Ceres and 4 Vesta, *IEEE Transactions on Nuclear Science*, 50, 1190-1197.
- Prettyman, T. H., D. W. Mittlefehldt, N. Yamashita, D. J. Lawrence, A. W. Beck, W. C. Feldman, T. J. McCoy, H. Y. McSween, M. J. Toplis, T. N. Titus, P. Tricarico, R. C. Reedy, J. S. Hendricks, O. Forni, L. Le Corre, J. Li, H. Mizzon, V. Reddy, C. A. Raymond, and C. T. Russell (2011), Elemental Mapping By Dawn Reveals Exogenic H in Vesta's Regolith, *Science*, 338, 242-246.
- Rasool, S.I., and C. De Bergh (1970), The Runaway Greenhouse and the Accumulation of CO<sub>2</sub> in the Venus Atmosphere, *Nature*, 226, 1037-1039.
- Reedy, R. C. and J. R. Arnold (1972), Interaction of Solar and Galactic Cosmic-Ray Particles with the Moon, *Journal of Geophysical Research*, 77, 537-555.

**CHAPTER II**  
**WATER EQUIVALENT HYDROGEN ESTIMATES FROM THE FIRST**  
**200 SOLS OF *CURIOSITY'S* TRAVERSE (BRADBURY LANDING TO**  
**YELLOWKNIFE BAY): RESULTS FROM THE DYNAMIC ALBEDO OF**  
**NEUTRONS (DAN) PASSIVE MODE EXPERIMENT**

A version of this chapter was originally published by Christopher G. Tate *et al.*:

Tate, C.G., J. Moersch, I. Jun, D. W. Ming, I. Mitrofanov, M. Litvak, A. Behar, W.V. Boynton, L. Deflores, D. Drake, B. Ehresmann, F. Fedosov, D. Golovin, C. Hardgrove, K. Harshman, D. M. Hassler, A.S. Kozyrev, R. Kuzmin, D. Lisov, A. Malakhov, R. Milliken, M. Mischna, M. Mokrousov, S. Nikiforov, A.B. Sanin, R. Starr, A. Varenikov, A. Vostrukhin, and C. Zeitlin (2015), Water Equivalent Hydrogen Estimates from the first 200 sols of *Curiosity's* Traverse (Bradbury Landing to Yellowknife Bay): Results from the Dynamic Albedo of Neutrons (DAN) Passive Mode Experiment, *Icarus*, 262, 102-123.

The student (Christopher G. Tate) is the lead author and researcher of this work. This article was revised through peer review upon submission to the journal *Icarus*. All co-researchers listed are members of the Mars Science Laboratory team, Dynamic Albedo of Neutrons team, or Radiation Assessment Detector team and have varying levels of involvement in this work. Most only contributed directly through instrument pre-flight building, testing, and or surface operations. J. Moersch, I. Jun, B. Ehresmann, and D. W. Ming have the most involvement with this project, helping with simulation creation and verification and interpretation of results. References to the manuscript in the following chapter and subsequent appendix refer to the main text of Chapter II presented here. The text has not been altered except for formatting changes.

## **Abstract**

The Dynamic Albedo of Neutrons (DAN) experiment on the Mars Science Laboratory (MSL) rover Curiosity is designed to detect neutrons to determine hydrogen abundance within the subsurface of Mars (Mitrofanov *et al.*, 2012; Litvak *et al.*, 2008). While DAN has a pulsed neutron generator for active measurements, in passive mode it only measures the leakage spectrum of neutrons produced by the Multi-Mission Radioisotope Thermoelectric Generator (MMRTG) and Galactic Cosmic Rays (GCR). DAN passive measurements provide better spatial coverage than the active measurements because they can be acquired while the rover is moving.

Here we compare DAN passive-mode data to models of the instrument's response to compositional differences in a homogeneous regolith in order to estimate the water equivalent hydrogen (WEH) content along the first 200 sols of Curiosity's traverse in Gale Crater, Mars. WEH content is shown to vary greatly along the traverse. These estimates range from  $0.5 \pm 0.1$  wt. % to  $3.9 \pm 0.2$  wt. % for fixed locations (usually overnight stops) investigated by the rover and  $0.6 \pm 0.2$  wt. % to  $7.6 \pm 1.3$  wt. % for areas that the rover has traversed while continuously acquiring DAN passive data between fixed locations. Estimates of WEH abundances at fixed locations based on passive mode data are in broad agreement with those estimated at the same locations using active mode data. Localized (meter-scale) anomalies in estimated WEH values from traverse measurements have no particular surface expression observable in co-located images. However at a much larger scale, the hummocky plains and bedded fractured units are shown to be distinct compositional units based on the hydrogen content derived from DAN passive measurements. DAN passive WEH estimates are also shown to be consistent with geologic models inferred from other MSL instruments, which indicate that fluvial/lacustrine activity occurred at certain locations (*e.g.*, Yellowknife Bay).

## Introduction

The Dynamic Albedo of Neutrons experiment (DAN) on the Mars Science Laboratory (MSL) rover *Curiosity* is designed to detect neutrons to determine hydrogen abundance within the subsurface of Mars (Mitrofanov *et al.*, 2012; Litvak *et al.*, 2008). The search for water in planetary exploration is intertwined with the search for life because water is considered by to be a prerequisite for terrestrial life (*e.g.*, Rasool and De Bergh, 1970). DAN contributes to the MSL mission of exploring and quantitatively assessing the habitability and environmental history of the Gale crater field site (Grotzinger *et al.*, 2012) through its sensitivity to the presence of hydrogen concentrations, which can be used to infer the presence of hydrogen-bearing minerals and water in the shallow subsurface (~60 cm depth). *Curiosity* landed in Gale crater on August 12th, 2012. This large (154 km diameter) impact crater is located on the hemispherical dichotomy boundary. It hosts a 5.2 km-high central mound of material that is mostly sedimentary in origin and formed during the Noachian - Hesperian boundary (Thomson *et al.*, 2011). Orbital data reveal geomorphic and geochemical evidence for aqueous activity contained within the crater and sedimentary mound (Anderson and Bell., 2010; Milliken *et al.*, 2010; Thomson *et al.*, 2011) and indeed, MSL data support the presence of a previously habitable, fluvio-lacustrine environment within Gale (Grotzinger *et al.*, 2014).

While neutron spectroscopy from orbital platforms is a proven method in planetary science (*e.g.*, Feldman *et al.*, 1998, Feldman *et al.*, 2002; Mitrofanov *et al.*, 2002; Goldsten *et al.*, 2007; Prettyman *et al.*, 2011), DAN measurements of neutrons from a mobile platform are the first application of the technique on a planetary surface other than Earth's. There are differences between orbital neutron measurements and MSL surface neutron measurements that must be taken into account when evaluating DAN surface data. An obvious difference is the physical

scale of the measurements on the surface. In passive mode, DAN has a sensing “footprint” with a radius of ~1.5 m, whereas measurements from orbital instruments typically have effective spatial resolutions of hundreds of kilometers (i.e., comparable to the height of the orbit above the surface) (*e.g.*, Mitrofanov *et al.*, 2002). Another important difference is the presence of a second significant source of neutrons. DAN detects neutrons that are produced by Galactic Cosmic Rays (GCRs) interacting with the planet, just as orbital instruments do. However, DAN also senses neutrons that originate from the rover’s Multi-Mission Radioisotope Thermoelectric Generator (MMRTG). The MMRTG acts as a separate source of neutrons that is in close proximity to not only the surface, but also the body of the rover and the DAN detectors. It produces high energy neutrons as a byproduct of the decay of its Plutonium-238. These neutrons contribute significantly to the leakage flux of neutrons from the surface, complicating the interpretation of DAN measurements (particularly those acquired in passive mode) compared to orbital measurements. As discussed in Section 2 (Methods), epithermal neutron count rates acquired in this configuration behave significantly differently from those measured from orbit because of these effects.

DAN uses two  $^3\text{He}$  proportional counters to detect neutrons via the reaction (Knoll, 2000):



One of the counters, known as counter of total neutrons (CTN), is capable of detecting neutrons over a broad spectrum of energies ( $< 0.1 \text{ MeV}$ ), however, detection efficiency above 1 keV is very low (Litvak *et al.*, 2008). The other, known as counter of epithermal neutrons (CETN), is covered with a thin jacket of cadmium that absorbs neutrons with energies below ~0.4 eV and therefore counts only neutrons with energies above this “Cd cutoff” (Litvak *et al.*, 2008). DAN

has two modes of operation: an active mode that makes use of a pulsed neutron generator (PNG) source, and a passive mode in which the PNG is not used (Mitrofanov *et al.*, 2012; Litvak *et al.*, 2008). Results of observations made with DAN's active mode are discussed by Mitrofanov *et al.* (2014) and Litvak *et al.* (2014). While the intensity of neutrons emanating from the PNG in active mode is high ( $\sim 10^7$  neutrons in each pulse), the pulses are short in duration (2  $\mu$ s) and relatively infrequent (10 Hz) (Litvak *et al.*, 2008), so the time-integrated count rates at the detectors are only marginally higher ( $\sim 4$ x) than the count rates received in passive mode. Passive mode observations do offer additional flexibility in that they may be made while the rover is moving, whereas active measurements may only be made while the rover is stopped. Thus, the passive mode data set has significantly better spatial coverage at a modest cost in counting statistics relative to active mode.

As mentioned above, in DAN's passive mode there are two sources of neutron production. GCRs, which consist of  $\sim 87\%$  protons,  $\sim 12\%$  alpha particles, and  $\sim 1\%$  heavier nuclei (Simpson, 1983) at energies from 10 MeV to  $\geq 1$  TeV per nucleon (Morthekai *et al.*, 2007), propagate through the Martian atmosphere. Some GCR particles will interact with nuclei in the atmosphere producing secondary free neutrons through spallation, along with other particles (*e.g.*, Drake *et al.*, 1988). The majority of GCR particles, however, will reach the surface of the planet and penetrate the subsurface due to the thin Martian atmosphere of  $\sim 16$  g/cm<sup>2</sup> relative to the GCR penetration depth of  $\sim 160$  g/cm<sup>2</sup>. Surviving GCR particles interact with the regolith nuclei, producing neutrons through spallation reactions and neutron evaporation from excited nuclei produced during prompt interactions (Drake *et al.*, 1988). A separate neutron source is the MMRTG, which produces neutrons with a wide range of energies up to  $\sim 10$  MeV (*e.g.*, Jun *et al.*, 2013). Both GCR-sourced neutrons and MMRTG-sourced neutrons move

throughout the subsurface and can interact with nuclei in the regolith through both elastic and non-elastic scattering, or they can be absorbed by certain nuclei. Scattering interactions have the effect of moderating the neutrons' energies (Drake *et al.*, 1988). Neutrons that are not ultimately absorbed within the surface will escape from it, providing a leakage flux that can be measured by the DAN detectors. GCR's penetrate to depths of ~1 m, however, the majority of neutrons that escape the surface originate from depths of <60 cm (Jun *et al.*, 2013).

Hydrogen is, by far, the most effective moderator of neutron energies in scattering interactions because it is the only isotope with a mass comparable to that of a neutron. On average, a neutron will lose  $\frac{1}{2}$  of its kinetic energy in an elastic scattering event with a hydrogen nucleus. Other nuclei have an atomic mass much greater than that of a neutron, as a result the neutrons lose much less of their kinetic energy to the recoil of the target nucleus in elastic scattering events. Thus, the energy spectrum of leakage neutrons is highly sensitive to the amount of hydrogen in the regolith. This abundance is commonly reported in terms of water equivalent hydrogen (WEH), i.e., the percentage (by weight) of water that the subsurface material would contain if all of the detected hydrogen was present in the form of H<sub>2</sub>O.

There are a variety of definitions of thermal and epithermal neutron energy ranges, but for this paper and many other planetary studies that make use of neutron remote sensing, “thermal neutrons” are meant to be those with energies below the cadmium cutoff ( $E < \sim 0.4$  eV), and “epithermal neutrons” are those with energies above this, up to ~ 1 keV. Higher energy (non-thermal) neutrons are moderated into thermal neutrons by interactions with the constituents of the regolith, leading to an increase in the population of thermal neutrons. Thermal neutron count rates are derived from DAN measurements by subtracting the count rates in the Cd shielded <sup>3</sup>He tube (CETN) from the count rates in the unshielded <sup>3</sup>He tube (CTN). The term "thermal neutron



count rate" and variations thereof will refer to the difference of the count rates in the two DAN detectors for the purpose of this work.

Interpretation of the spectrum of neutrons leaked from the subsurface can be complicated by the presence of elements with large thermal neutron absorption cross sections, such as chlorine and iron, which have the effect of preferentially removing neutrons from the thermalized population through absorption (*e.g.*, Hardgrove *et al.*, 2011). This means that DAN passive mode measurements, taken in isolation, are under-constrained because they cannot distinguish the confounding effects of the presence of thermal neutron absorbing elements and the absence of hydrogen, both of which would lead to a relative dearth of thermal neutrons. External constraints must be applied to separate these effects. Fortunately, the application of DAN active-derived results allows for constraints to be placed on the abundance of thermal neutron absorbing elements.

We present results and interpretations of data from the first 200 sols of DAN passive mode operation. Jun *et al.* (2013) discussed the first 100 sols of DAN passive results in relation to the radiation environment on the Martian surface. In this paper, we present WEH estimates and geological interpretations made using DAN passive data. In Section 2 (Methods), we describe our analysis methods in detail. This is followed in Section 3 (Data) by a description of the data acquired in the first 200 sols of the mission. Section 4 (Sources of Uncertainty) presents a discussion of the sources of uncertainties associated with both the measurements and the analysis methods. Our results are presented in Section 5 (Results) and we conclude with a discussion of the broader meaning of these results in Section 6 (Discussion) and a summary of our work in Section 7 (Conclusions).

## Methods

WEH concentrations are estimated from DAN passive data via comparisons of measured DAN count rates to simulated count rates. The simulations, which use the Monte Carlo N-Particle Extended (MCNPX) program, account for varying WEH and absorption equivalent chlorine (AEC, described below) abundances. MCNPX simulates the transport and interactions of neutrons and other particles within a user-defined geometry and compositional distribution (McKinney et al., 2006). We use a parallelized version of MCNPX version 2.6.0.

A single, full-scale simulation of the neutron environment at the DAN detectors is not computationally reasonable because the detectors have negligible volume compared to the volume of Mars and its atmosphere. To address this, we have parsed the problem into three separate components at two different spatial scales that simulate individual neutron sources. Figure 2.1 is a flow chart that illustrates our process for simulating the total detector response. The result is the total counts in each detector due to both the GCR and MMRTG sources. To simulate the atmospheric component of the response due to GCR source particles, we first simulate GCR transport and interactions globally, from the top of the Martian atmosphere down to three meters above the surface, tracking all protons and neutrons. We use the same atmospheric model as Prettyman *et al.* (2004) with an initial GCR minimum spectrum from the Cosmic Ray Effects on Micro-Electrics 1996 code (CREME96) (Tylka *et al.*, 1997). Interactions are modeled using the Cascade-Exciton Model (CEM03) and the Los Alamos Quark-Gluon String Model (LAQGSM) for all high energy proton and neutron ( $E > 20 \text{ MeV}$ ) interactions (Mashnik, 2005), otherwise interaction cross sections are used. The Evaluated Nuclear Data File B (ENDF-B) version 6 (Dunford, 1992) is used for neutron cross sections at energies  $\leq 20 \text{ MeV}$ . The GCR local-scale component of our simulations use the downward flux of GCR and

secondary particles simulated in the atmospheric component as input to a local-scale simulation that extends vertically from three meters above the surface to a depth of five meters and horizontally to a radius of thirty five meters around the rover. This facilitates simulating particle interactions within the local ground and atmosphere, the mass of the rover, and the DAN detectors. For reasons of computational efficiency, our method does not account for the possibility that compositional differences outside the 35-m radius of the local simulation could influence our results via contribution of gravitationally-bound neutrons. The scaling strategy we have employed (discussed below) does account for all source particles, including these “returning neutrons,” by forcing the total simulated count rates to match the measured count rates. The only characteristic of these gravitationally bound neutrons that our simulation strategy does not take into account is the fact that they carry the compositional signature of an area around the rover with a radius of several to hundreds of kilometers (i.e., the ballistic range of thermal energy neutrons). This is not a critical compromise, however, as Feldman *et al.* (1989) showed that the component of thermal neutron flux at the surface due to gravitational infall is only around a few percent and only for those neutrons with kinetic energy less than the Martian gravitational binding energy of 0.132 eV. In the case of DAN passive measurements, this fraction is even less because a significant fraction of the neutrons detected originate from the MMRTG which provides very few gravitationally-bound neutrons to the thermal count rate as gravitationally bound neutrons leaving the regolith near the rover would be a negligible fraction of gravitationally bound neutrons returning to the DAN detectors near the originating location. Our method of accounting for this small contribution would be inaccurate if the leakage spectrum of neutrons from launch locations outside the local-scale simulation around the rover was significantly different from that within the local-scale simulation. However, this is likely to

**Figure 2.1. An illustration of the simulation process whereby the DAN instrument response is calculated. Boxes are processing steps, with the rounded boxes representing the three MCNPX simulation components described in the text. Arrows represent inputs and outputs for these steps. The left side of the flow chart represents the processing steps for GCR-sourced neutrons, while the right side represents the processing steps for MMRTG-sourced neutrons. Lastly, the simulation results must be properly scaled in order to combine them to produce total counts in the detectors.**

### Simulation Approach

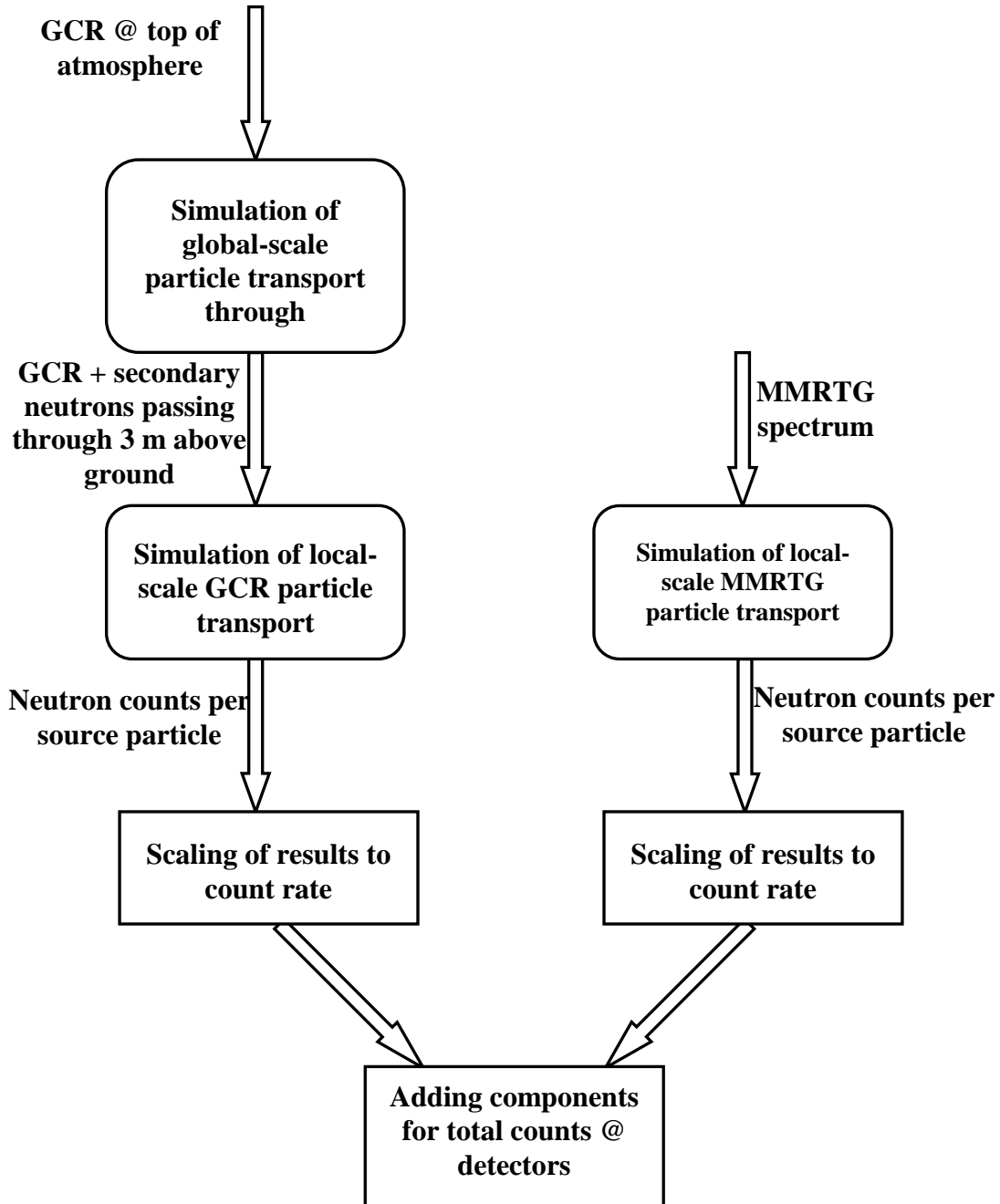


Figure 2.1 Continued.

be a second order effect, and the approach that we have taken carries significant computational advantage over any alternative assumptions.

In another local-scale component of our simulations, we simulate the transport and interactions of neutrons produced by the remaining source in the problem, the rover's MMRTG. For this we use the same local-scale geometry as in the previously described GCR local component. The energy spectrum of neutrons produced by the MMRTG is the same as the one presented in Jun *et al.* (2013).

Within both local-scale simulations, we use an idealized rover mass, developed for the purpose of DAN simulations by Jun *et al.* (2013). We use DAN detector models within MCNPX that have been developed and described by Mitrofanov *et al.* (2014). Neutron interactions within the detectors are modeled by the (n,p) reaction (Equation 1) with appropriate physical parameters for the counter volumes (Litvak *et al.*, 2008). Count rates for the two detectors are obtained from the Monte Carlo simulations using the method described below. Then, CETN count rates are subtracted from CTN count rates to get the final simulated thermal neutron count rate.

Our simulations use a reference Mars regolith composition derived from an average of compositions from the Mars Exploration Rovers (MER) Alpha Particle X-Ray Spectrometer (APXS) experiment (McSween *et al.*, 2010). We performed a series of simulations using this composition, modified to include a range of subsurface hydrogen and absorption equivalent chlorine abundances and to maintain a total stoichiometric sum of 100%. This approach is consistent with that of Hardgrove *et al.* (2011), Jun *et al.* (2013), and Mitrofanov *et al.* (2014). Following Mitrofanov *et al.* (2014), we account for variations in the total concentration of all thermal neutron absorbing elements by varying the chlorine concentration of the regolith. It is known that chlorine is not the only thermal neutron absorber present in the Mars' regolith,

however, one cannot use variable contents of all thermal neutron absorbing elements when analyzing DAN data (Mitrofanov *et al.*, 2014). A single parameter, absorption equivalent chlorine (AEC), has been used instead. AEC is the actual chlorine content plus additions due to the differences of fractions of other absorbing elements from their average values in the average MER APXS regolith composition (Mitrofanov *et al.*, 2014). In the case that other absorbing element abundances are equal to their abundances in the average MER APXS composition, the AEC value will equal the actual chlorine abundance (Mitrofanov *et al.*, 2014). It is also noted that the MER standard deviations of the abundances of the other most relevant neutron absorbers ( $^{56}\text{Fe}$ ,  $^{32}\text{S}$ , and  $^{48}\text{Ti}$ ) lead to small corrections to the expected AEC values, *i.e.*, small differences between the actual chlorine value and the AEC value (Mitrofanov *et al.*, 2014). While the expected differences between the actual chlorine and AEC are small, AEC is the more accurate parameter and thus what DAN active analysis calculates (Mitrofanov *et al.*, 2014).

Absorption equivalent chlorine values are better suited to our measurements and analysis than APXS or ChemCam measurements due to differences in the depth sensitivity of these instruments, the spot size contained within the instrument footprints, and the direct sensitivity of DAN passive and active measurements to all thermal neutron absorbers present (the other instruments are not sensitive to all absorbing elements). It should also be noted that, following Jun *et al.* (2013) and Mitrofanov *et al.* (2014), terrestrial isotopic ratios for each element were used in our composition models, and regolith density has been assumed to be  $1.8 \text{ g/cm}^3$ . Density is another factor that has the ability to affect the thermal neutron leakage flux, but the assumption of a fixed regolith density is necessary due to computational constraints. The effect of this assumption on the uncertainty in our results is discussed in Section 4 (Sources of Uncertainty).

MCNPX provides its output in terms of products per source particle. Combining the

results from the different simulation components (GCR-sourced and MMRTG-sourced) described above required the application of scale factors that are based on the intensities of the different sources. The appropriate scale factors will convert the MCNPX results to neutron counts per second so that the counts from each simulation can be combined. In the case of the MMRTG component, we used the scale factor derived by Jun *et al.* (2013) from Assembly, Test, and Launch Operations (ATLO) test data before the MSL launch. For a discussion on the relative contributions to thermal neutron count rates from each source, see Section 6.1 (Fixed Locations). However, note that for the following discussion, it is helpful to know that the MMRTG thermal neutron count rate contribution is very roughly  $50\% \pm 10\%$  and hence why so much effort has been put into correctly scaling the GCR-induced thermal neutron count rates.

The scale factor for the GCR component of the simulation is difficult to constrain because of inherent uncertainties in the GCR flux at the top of the Martian atmosphere (Ehresmann *et al.*, 2014; Mrigakshi *et al.*, 2012). Thus, it is desirable to use Radiation Assessment Detector (RAD) penetrating counter daily measurements to determine the appropriate GCR scale factor when combining the different components of our simulations. However, the RAD penetrating counter measurements are only sensitive to a subset of the particles that matter for DAN passive measurements. Specifically, RAD penetrating counter measurements are sensitive to high energy GCRs, but not secondary neutrons produced in the atmosphere that will contribute to DAN passive measurements. A strategy for scaling the RAD measurements to appropriate values for use with DAN passive simulations must be adopted. This strategy is described below.

First, in order to determine the overall magnitude of our GCR scale factors and their long-term variation during the time period, we have performed an *in situ* calibration of said



factors by the use of DAN active results. We accomplished this by carefully selecting calibration sites based on the criteria: 1) the site must have co-located passive and active measurements, 2) the site must have a "best-fit" model (the model with the highest probability of acceptance) of a homogeneous subsurface (as opposed to a layered subsurface) as a result from the active measurements, 3) the homogenous model must have a high probability of acceptance of the DAN active results based on the Pearson criteria described in Mitrofanov *et al.* (2014), and lastly, 4) the sites must be separated in time to give mathematical leverage on capturing any long duration temporal trends.

The calibration locations that met these criteria were those that *Curiosity* investigated on sols 0-15 (calibration site 1), sols 124-125 (calibration site 2), and sol 159 (calibration site 3). Analysis of the DAN active data for these sites resulted in a regolith composition that was homogenous with depth (Mitrofanov *et al.*, 2014). These were compositions of 1.6 wt. % WEH and 1.15 wt. % AEC, 1.7 wt. % WEH and 1.2 wt. % AEC, and 1.8 wt. % WEH and 0.9 wt. % AEC at calibration sites 1, 2, and 3, respectively (Mitrofanov *et al.*, 2014). Using the simulation approach described above and in Figure 2.1, we simulated the DAN passive mode count rates expected for these WEH and AEC abundances, assuming a homogeneous subsurface. MCNPX results for the MMRTG-sourced component were converted to count rates using the method of Jun *et al.* (2013). We then subtracted the simulated MMRTG-induced count rate from the measured passive count rate at these locations to get an estimate of the detector count rates that must have originally been stimulated by GCR. These results were then divided by the MCNPX results (in counts per source particle) from the simulated GCR sources for each location to derive a scale factor for the GCR component. Thus, we employed the following equation

$$f_{GCR,S} = \frac{C_{meas} - C_{sim}^{MMRTG}}{m_{sim}^{GCR}}, \quad (2)$$

where  $f_{GCR,S}$  is the GCR component scale factor specifically for calibration sites ( $S$ ) 1, 2, or 3 in source particles per second.  $C_{meas}$  is the measured neutron count rate from the unshielded detector (CTN) of the DAN instrument at the corresponding calibration site.  $C_{sim}^{MMRTG}$  is the simulated neutron count rate (CTN) calculated from the MMRTG component simulation of the location.  $m_{sim}^{GCR}$  is the MCNPX simulation result of counts per source particle from the GCR component simulation for the specific calibration location. CTN neutron counts are used here rather than thermal neutrons because CTN neutron counts are a direct measurement of the instrument, whereas thermal neutron counts are calculated by differencing count rates from the two counters. This calibration strategy scales both the GCR counts produced and the proportion of GCR counts to MMRTG counts. We then linearly fit the scale factor based on the three calibration sites for the time period. Because no suitable calibration site was found for sols 160-200, we extrapolate the line determined from the previous calibration sites to get scale factors during this time period. The determination of scale factors at the locations discussed gives us the overall magnitude and long-term trend of scale factors within the time period from landing to sol 159 due to solar modulation and seasonal atmospheric pressure changes. The linear increase in the GCR intensity during this time period is corroborated by data from the RAD instrument (Hassler *et al.*, 2014), and by (unpublished) data from the High Energy Neutron Detector (HEND) instrument on Mars Odyssey.

To account for higher frequency variations in the GCR environment, we modulate the long-term linear trend calculated as described above with an adjustment based on daily RAD measurements. This yields final GCR scale factors on a sol by sol time scale. By knowing the variation in the RAD daily measurements from sol 0 to 200 and the same in the DAN calibration factor ( $f_{GCR,S}$ ) described above, we can convert RAD daily measurements to the final GCR scale

factors necessary for DAN passive simulations for any given sol. This is done by linearly scaling the RAD data to the DAN calibration values, “pinning” the values of  $f_{GCR,S}$  at the calibration sites to the corresponding RAD values:

$$F_{GCR,RAD} = (R_{sol} - R_{13}) * \left( \frac{f_{GCR,159} - f_{GCR,13}}{R_{159} - R_{13}} \right) + f_{GCR,13}, \quad (3)$$

Here,  $R_{sol}$  is the RAD penetrating counter daily measurement for the sol being investigated.  $R_{13}$  and  $R_{159}$  are the RAD penetrating counter daily measurements on sols 13 and 159, respectively.  $f_{GCR,159}$ , and  $f_{GCR,13}$  are the DAN calibration values calculated with the trend established using equation 2 above.

Use of this empirically-derived scale factor provides a correction to account for the uncertainties associated with the magnitude of the GCR flux at the radial distance of Mars' orbit, the magnitude of the variability in GCR flux due to solar modulation through this time span the proportion of alpha particles present and their contribution to the neutron production in the subsurface, and seasonal variability due to changes in atmospheric column density. It also allows us to correct for transient GCR events, such as Forbush decreases. Forbush decreases are transient decreases in the GCR intensity due to interactions of coronal mass ejection-associated magnetic fields with the GCR environment (*e.g.*, Rao, 1971). Forbush decreases were identified by the RAD instrument during the surface mission on sols 50 and 97 (Hassler *et al.*, 2014). Thus, the effect of the sol 50 Forbush decrease (no DAN passive data were acquired on sol 97) and the subsequent rebound of the GCR environment in the sols following the sol 50 and 97 events are characterized and applied to our data analysis. However, measurements such as those on sol 50 should be viewed with caution because the time scale of the Forbush decrease is smaller than the integration time of the averaged RAD data we have used to characterize that sol. Thus our WEH estimates for sol 50 could be biased high or low, depending on the exact timing of the Forbush

decrease itself in relation to the DAN and RAD measurements. However, our discussion of sources of uncertainty (Section 4 (Sources of Uncertainty)) shows that the magnitude of such biases would be small. The major, multi-sol effects of such events are captured by the inclusion of the daily RAD data in our calibration approach.

Shown below (Figure 2.2) are the RAD penetrating particle counter data used to constrain the GCR environment and provide the ultimate product of our conversion to a scale factor usable with our MCNPX simulations. Two caveats must be considered regarding our scaling approach for the GCR-sourced neutrons. First, the vertical sensing depths of DAN's active and passive modes are different (~0.6 meters (Mitrofanov *et al.*, 2014) vs. ~ 1.0 meters, respectively, though the lower ~0.4 m of the passive sensing footprint is weakly weighted). Inherent in our *in situ* calibration approach is the assumption that the homogeneous composition observed at calibration sites 1, 2, and 3 in DAN's active mode extends to the depth sensed by DAN's passive mode. Second, as mentioned earlier, the GCR flux at the top of the atmosphere is time-variable (Rao, 1971; Hassler *et al.*, 2014). This is why recalculation of  $f_{GCR,S}$  is done at multiple locations. Though the GCR flux is anti-correlated with the solar cycle (Rao, 1971), which was increasing during sols 0 to 200 we see a relative increase in our GCR scale factor of 31% between the start of the landed mission and sol 200. This is because during this specific period of time the GCR flux was increasing due to a temporary decrease in the solar modulation constant (a departure from the nominal solar cycle trend), as inferred from RAD data during this period (Hassler *et al.*, 2014).

The simulation and scaling approach described above produces a suite of simulated count rates that may be compared to DAN passive measurements in order to interpret variations in the data in terms of changes in regolith composition. Because of computational constraints, we have

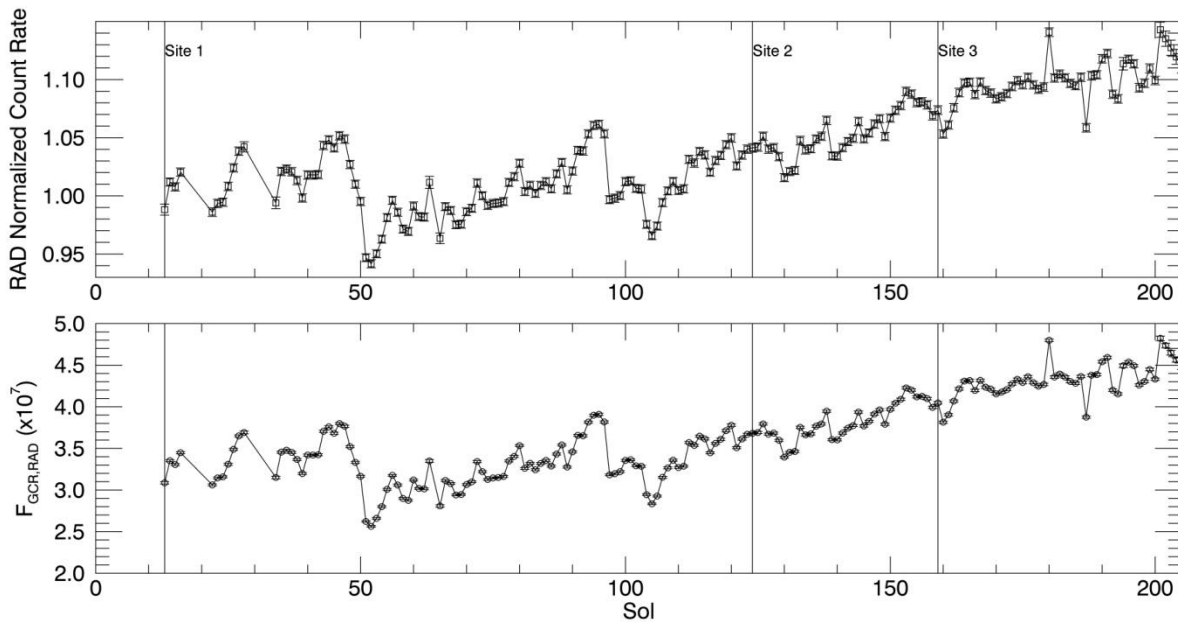


**Figure 2.2. RAD normalized penetrating counter average count rates (top) have been used in conjunction with our in situ calibration to constrain the GCR environment and produce GCR scale factors (bottom) on a sol by sol time scale that are useable with our MCNPX results. Calibration sites 1, 2, and 3 are marked by the vertical lines on their corresponding sols.**

simulated WEH in 1.0 wt. % increments from 0 wt. % up to 10.0 wt. %, and AEC contents at 0.5 wt. % increments from 0.5 wt. % up to 2.0 wt. %. The range of AEC values was selected based on previous studies (McSween *et al.*, 2010; Hardgrove *et al.*, 2011) in order to explore the parameter space.

Figures 2.3 and 2.4 show example simulation outputs of neutron count rates for differing values of WEH and AEC and specific scaling parameters. These count rates include contributions from both MMRTG-induced thermal neutron counts and GCR-induced thermal neutron counts, scaled using the methods discussed above. As expected, for a given WEH content the thermal neutron count rate decreases with increasing AEC content. Also as expected, for a given percentage of AEC, the thermal neutron count rate increases with increasing WEH content. Furthermore, as previously shown by Jun *et al.* (2013), the epithermal neutron count rate is relatively constant and insensitive to WEH content. While GCR-induced epithermal neutrons are known from orbital measurements to be anti-correlated with WEH content (*e.g.*, Drake *et al.*, 1988), MMRTG-induced epithermal neutrons are relatively constant to slightly positively correlated with WEH content. The reason for this, as discussed in Jun *et al.* (2013), is that the MMRTG emits mostly high-energy neutrons. As epithermal neutrons are moderated by hydrogen into thermal energies, so too are the high-energy MMRTG neutrons moderated into the epithermal range, resulting in a state of dynamic equilibrium (Jun *et al.*, 2013). Furthermore, it is estimated that ~40% of MMRTG-induced epithermal neutron count rates are detected directly from the MMRTG or scattered off of Curiosity, meaning that a significant fraction of measured epithermal neutrons do not interact with the ground before being detected (Jun *et al.*, 2013). These factors lead to the relatively constant epithermal neutron count rates observed both in the data (Section 3 (Data)) and simulation results (*e.g.*, Figure 2.4). Figure 2.5 shows simulated

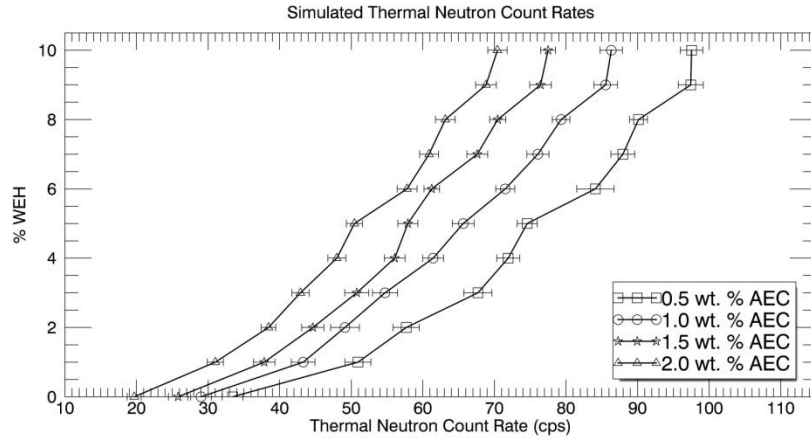


**Figure 2.3. Simulated thermal neutron counts per second for differing values of both H<sub>2</sub>O and AEC. For these examples, an average GCR scale factor ( $F_{GCR,RAD}$ ) has been used. Uncertainties are computed from MCNPX fractional standard deviations for simulations results.**

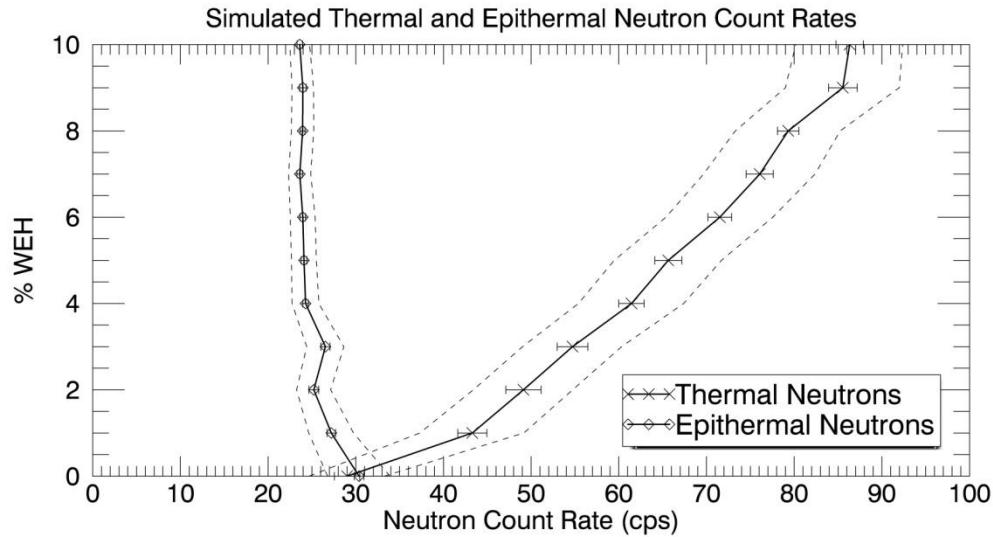


**Figure 2.4. Simulated thermal and epithermal neutron counts per second for a range of values of WEH and a fixed (typical) AEC abundance of 1 wt. %. Solid lines represent the count rates with the same average GCR scale factor applied as in Figure 2.3. Dashed lines represent the count rates with the minimum (taken from the time of the Forbush decrease on sol 50) and maximum GCR (taken from sol 200) scaling factors applied. These “envelopes” around the solid lines show the magnitude of the effect that the varying GCR can have on count rates within this time period.**



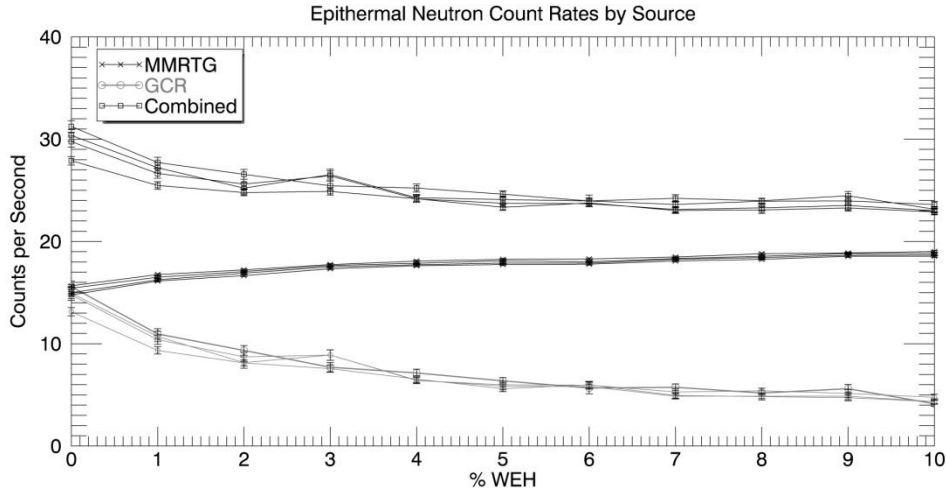


**Figure 2.5. Simulated epithermal neutron count rates are shown separately for those sourced from the MMRTG (x symbols) and those induced by the GCR (circles) (with the same average scale factor applied for the period,) versus WEH content of the regolith. The sum of those two curves simulates what DAN actually measures on the surface and it is shown as well (squares). The multiple curves for each source represent different abundances of AEC, ranging from 0.5% to 2.0%. The uncertainties shown are count rate uncertainties from simulations. Note that the combination of the two individual epithermal neutron count rate curves is essentially insensitive to WEH.**

epithermal neutron count rates separated according to their original sources (GCR vs. MMRTG). From this, the decrease in epithermal count rates seen in the simulation results at low WEH content is driven by the expected decrease in GCR-induced epithermal neutrons with WEH content. However, variations from both populations ultimately have a “canceling effect” on each other, leading to near-invariance when the two are combined.

Because epithermal neutron count rates show little variation, the bulk of the variability seen in total neutron count rates is driven by variability in the population of thermal neutrons. In the context of Figures 2.4 and 2.5, the epithermal neutron count rate curve will be degenerate for other values of AEC, however, the thermal neutron count rate curve will shift to greater or lesser values based on the amount of AEC present. Both the total neutron count rates and the ratio of thermal to epithermal neutron count rates are almost completely dependent on thermal neutron count rates because of the near invariance of epithermal neutron count rates. Thus, in analyzing DAN passive data, we avoid making compositional interpretations based on the ratio of thermal to epithermal neutron count rates. Instead, we base our compositional interpretations solely on thermal neutron count rates. Using the ratio of count rates would carry additional uncertainty with very little (if any) benefit in terms of compositional sensitivity. Note that this approach is different than that typically employed (using epithermal and fast neutrons) in the analysis of orbital neutron remote sensing data (*e.g.*, Feldman *et al.*, 2002; Mitrofanov *et al.*, 2002). When only GCR-sourced neutrons are present, epithermal neutron count rates vary inversely with WEH content. In fact, orbital epithermal count rates are more directly associated with WEH content than orbital thermal neutron count rates because the latter are also affected by the presence of variable amounts of high thermal neutron absorption cross section elements.

The final step in our method is to use these simulation results to produce WEH estimates

from the DAN measured count rates. Because of the ambiguities inherent in the thermal neutron count rate due to the presence of high thermal neutron absorption cross section elements (as seen in Figure 2.3), we use the AEC abundance taken from analyses of DAN active-mode results (Mitrofanov *et al.*, 2014) for every passive measurement that has a co-located active measurement. The additional information present in DAN active-mode die-away curves provides a means of constraining AEC abundances that is not possible with DAN passive data alone. The measured passive thermal neutron count rate is compared to a suite of simulated thermal neutron count rates for a range of WEH values that all have the same AEC abundance, derived from the co-located active measurement. Interpolating between the two closest simulated thermal neutron count rates provides the inferred WEH estimate for that passive measurement. Where DAN passive measurements do not have co-located DAN active measurements to provide AEC abundances, we have used the average of all AEC abundances from DAN active measurements in the first 200 sols, which is 1.05 wt. %. This situation typically occurs in passive measurements acquired while the rover was moving along traverse segments. An alternative assumption could have been to use a linear interpolation between AEC abundances obtained by DAN active measurements at the endpoints of each traverse segment. However, from a geologic standpoint it is likely that abundances of neutron absorbing elements vary up and down over a shorter length scale than the length of most traverses, so the assumption of a linear variations in AEC abundance between traverse endpoints is difficult to justify. Lacking any way to determine the true nature of AEC variations independently when there is no co-located active measurement, the simplest assumption is to use a constant, average AEC value, bearing in mind the caveat that some of the variability in our derived WEH values could actually be caused by variations in AEC abundances.

## Data

### *DAN Passive Measurements at Fixed Locations*

DAN passive measurements were acquired at 36 fixed locations during the first 200 sols of the surface mission, from Bradbury Landing to John Klein within Yellowknife Bay. By “fixed location,” we mean a place where the rover stopped that was not in the middle of a given sol’s traverse segment. The amount of time the rover spent at each of these fixed locations varied from one to many sols, with the total integration time of the measurements ranging from 740 seconds (sol 38) to 677900 seconds (sols 59-100, at the site called Rocknest). The acquired data are neutron counts per second from each of the two detectors, recorded in 20-second bins. The total integration time (number of bins) for each measurement is variable and determined by constraints on rover resources, *i.e.*, the instrument is not continuously on, which leads to gaps in the data. In Table 2.1 we present the observational circumstances and average neutron count rates for all of the DAN passive measurements at fixed locations analyzed in the present work. Table 2.1 also provides the AEC abundances (obtained from DAN active analyses presented in Mitrofanov *et al.* (2014)) and GCR component scale factors ( $F_{GCR,RAD}$ ) used in estimating WEH (Section 4 (Sources of Uncertainty)).

Figure 2.6 shows the thermal count rate data and epithermal count rate data for the locations listed above. Figure 2.7 shows the average count rate for those same locations. Detector count rates have been corrected for a so-called “efficiency curve”. This is an asymptotic count rate increase that occurs after the high voltage power turn on of the instrument and reaches a saturation level in approximately one hour (Jun *et al.*, 2013). Corrections are applied using the method discussed in Jun *et al.* (2013). This is done for each measurement and applied to each detector separately (Jun *et al.*, 2013). Thermal neutron count rates are produced by differencing

**Table 2.1. Fixed locations where the rover acquired DAN passive data within the first 200 sols. The GCR scale factors shown are averaged over the period of sols during which passive data were acquired at a location.**

Sols	Traverse Distance (m)	Latitude (S) (degrees)	Longitude (E) (degrees)	Average Thermal Count rate (neutrons/second)	Average Epithermal Count rate (neutrons/second)	Absorption Equivalent Chlorine Abundance Used (wt. %)	Average $F_{GCR,RAD}$ (source particles/second)	Comments
0-15	0.0	4.589467	137.441633	43.13 (0.06)	23.17 (0.03)	1.15	3.15E+07	Bradbury Landing
17-21	7.0	4.589465	137.441734	39.73 (0.08)	24.40 (0.04)	1.10	3.13E+07	
22-23	27.0	4.589403	137.441892	43.01 (0.09)	24.89 (0.05)	1.10	3.15E+07	
24-26	48.5	4.589447	137.442181	46.16 (0.12)	24.63 (0.06)	1.15	3.31E+07	
26-29	78.6	4.589750	137.442476	53.93 (0.08)	25.99 (0.04)	1.20	3.57E+07	Near Link
29-37	109.1	4.590137	137.442786	52.15 (0.04)	25.74 (0.02)	0.75	3.28E+07	CAP2
38	141.5	4.590244	137.443302	52.81 (0.37)	25.55 (0.19)	0.95	3.37E+07	Near Hottah
39	163.2	4.590319	137.443663	54.56 (0.20)	25.08 (0.10)	0.85	3.31E+07	
45	293.8	4.590435	137.445348	54.04 (0.05)	24.75 (0.03)	0.90	3.69E+07	
49	335.2	4.590306	137.446506	54.20 (0.14)	24.66 (0.07)	1.00	3.33E+07	
50	392.3	4.590176	137.447304	37.19 (0.14)	24.11 (0.07)	0.95	3.16E+07	Forbush decrease in GCR

**Table 2.1. Continued.**

Sols	Traverse Distance (m)	Latitude (S) (degrees)	Longitude (E) (degrees)	Average Thermal Count rate (neutrons/second)	Average Epithermal Count rate (neutrons/second)	Absorption Equivalent Chlorine Abundance Used (wt. %)	Average $F_{GCR,RAD}$ (source particles/second)	Comments
52	453.3	4.590062	137.447900	54.57 (0.14)	24.86 (0.07)	1.05	2.66E+07	
54	455.0	4.590066	137.447940	55.09 (0.06)	25.92 (0.03)	0.95	2.82E+07	
55	479.1	4.590063	137.448297	42.96 (0.09)	25.48 (0.05)	1.05	3.09E+07	Near Bathurst
57	485.1	4.590017	137.448351	40.01 (0.06)	24.36 (0.03)	0.90	3.12E+07	
59	486.9	4.590020	137.448339	39.87 (0.04)	24.62 (0.02)	0.90	2.94E+07	
59-100	490.0	4.589996	137.448342	37.34 (0.01)	24.49 (0.01)	0.80	3.30E+07	Rocknest
100-102	491.9	4.590022	137.448310	42.31 (0.04)	26.19 (0.02)	0.75	3.34E+07	
102-111	517.2	4.589948	137.448695	49.81(0.03)	25.30 (0.02)	1.35	3.16E+07	Near Point Lake
111-120	519.1	4.589922	137.448676	51.64 (0.02)	25.66 (0.01)	1.60	3.61E+07	Near Point Lake
120-121	553.7	4.590442	137.448828	43.01 (0.10)	25.36 (0.05)	1.20	3.64E+07	Near Shaler
121-122	577.9	4.590282	137.449107	44.63 (0.13)	26.61 (0.07)	1.10	3.56E+07	
122-123	578.9	4.590275	137.449120	41.72(0.09)	24.56 (0.05)	1.30	3.64E+07	
123-124	598.3	4.590054	137.449349	47.24 (0.11)	24.73 (0.06)	1.55	3.68E+07	
124-125	612.3	4.589866	137.449277	46.35 (0.07)	24.44 (0.03)	1.20	3.69E+07	

**Table 2.1. Continued.**

Sols	Traverse Distance (m)	Latitude (S) (degrees)	Longitude (E) (degrees)	Average Thermal Count rate (neutrons /second)	Average Epithermal Count rate (neutrons/ second)	Absorption Equivalent Chlorine Abundance Used (wt. %)	Average $F_{GCR,RAD}$ (source particles/ second)	Comments
125-127	638.4	4.589637	137.449331	53.48 (0.04)	25.98 (0.02)	1.00	3.72E+07	
127-130	671.2	4.589231	137.449383	50.99 (0.04)	25.33 (0.02)	1.00	3.59E+07	
130-133	676.8	4.589137	137.449388	52.43 (0.04)	25.47 (0.02)	1.15	3.52E+07	
133-147	698.8	4.589463	137.449258	55.23 (0.03)	25.29 (0.01)	1.00	3.76E+07	
147-151	701.5	4.589506	137.449235	53.40 (0.03)	24.82 (0.01)	0.95	3.94E+07	
151-152	702.2	4.589516	137.449231	56.64 (0.07)	27.22 (0.04)	1.10	4.07E+07	
152-159	704.6	4.589552	137.449223	61.79 (0.02)	26.32 (0.01)	1.20	4.11E+07	
159-162	705.9	4.589535	137.449238	55.28 (0.04)	25.59 (0.02)	0.90	3.96E+07	
162	714.9	4.589497	137.449218	63.94 (0.10)	26.87 (0.05)	0.95	4.07E+07	
163-166	716.8	4.589476	137.449120	56.89 (0.04)	25.96 (0.02)	0.90	4.26E+07	
166-200	723.4	4.589485	137.449129	56.06 (0.01)	26.16 (0.01)	1.00	4.33E+07	John Klein

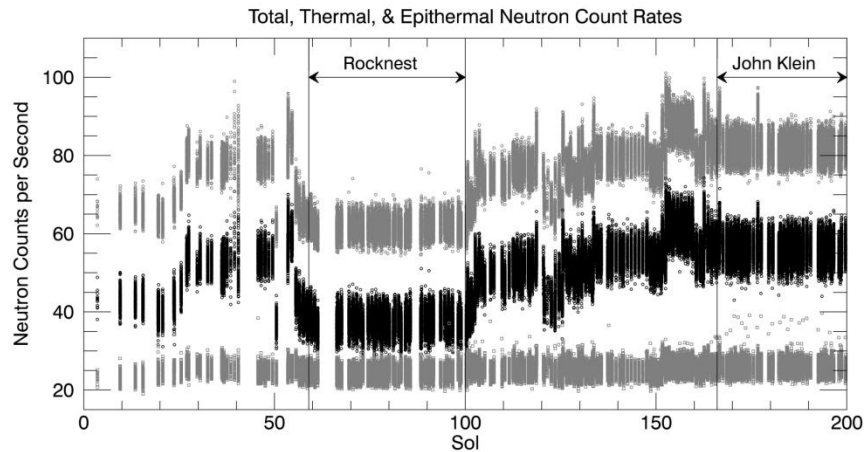


**Figure 2.6. DAN passive total neutron count rates (gray circles), thermal neutron count rates (black circles), and epithermal neutron count rates (gray squares) versus time during the first 200 sols of the mission. Note that variations in the total neutron count rates are almost exclusively driven by variations in the thermal neutron count rates. Variations in thermal count rates are attributed to changes in subsurface composition. The Rocknest and John Klein locations are marked by the drop lines denoting the range of sols the rover was parked at these locations. Curiosity spent sols 59 through 100 at Rocknest and sols 166 through the end of this time period at John Klein. Other locations featured multi-sol stays, but these two were the longest stops by a wide margin.**



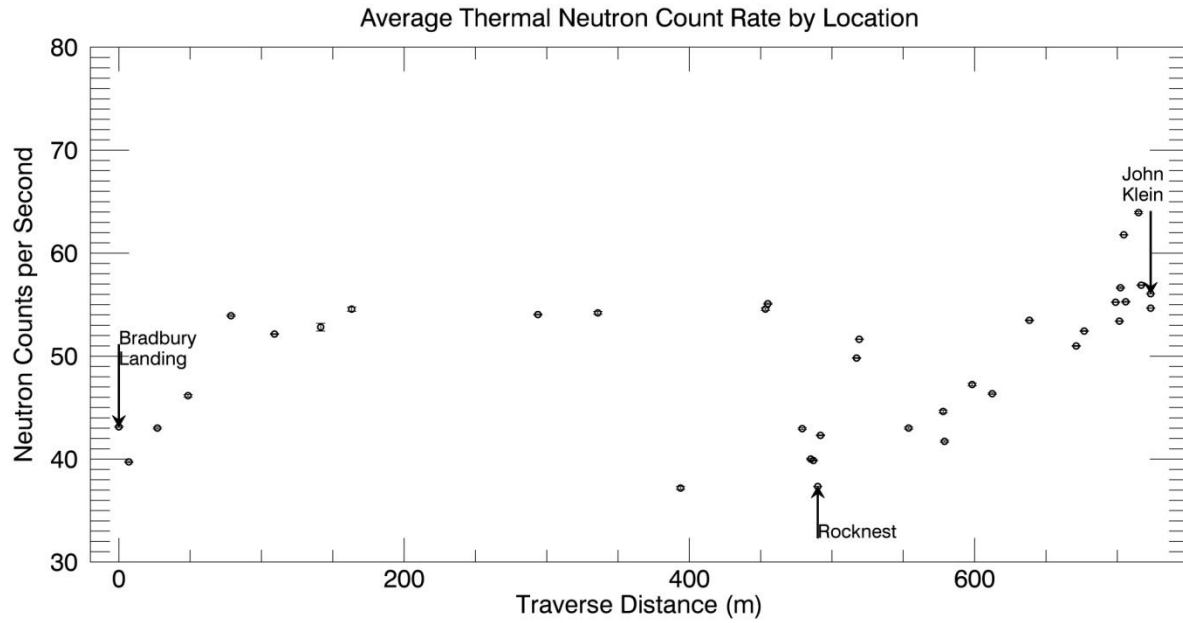


**Figure 2.7. Average thermal neutron count rate at each fixed location shown. The statistical uncertainty derived from Poisson statistics on the two measurements that make up the thermal neutron count rate is shown.**

the efficiency-corrected count rates of the CTN and CETN detectors for a given measurement.

### ***DAN Passive Data along Traverse Segments***

DAN passive data were also acquired along 27 rover traverse segments during sols 0 to 200. Figure 2.8 shows continuously-acquired passive data (thermal neutron count rates) from these traverse segments plotted as a function of rover traverse distance. Count rates from the same locations (at the same traverse distance) are averaged together. This is done because the rover travels at very low speeds and also stops periodically for navigation updates, but these mid-drive stops are distinct from the fixed locations in that they are still contained within rover traverse segments. Therefore, continuously-acquired DAN passive measurements are often separated by centimeters or less or are exactly co-located, in which case they are averaged together. Gaps are present in the traverse coverage because not all traverse segments included DAN passive data collection. Data from individual traverse segments can be expanded along the traverse distance axis to reveal small-scale variations of interest. The sol 48 traverse data and sol 102 traverse data are shown in Figures 2.9 and 2.10 as examples.

### ***Ancillary Data***

Several ancillary data sets were used when analyzing DAN passive measurements. RAD data from the penetrating counter (Ehresmann *et al.*, 2014) have been used to constrain the GCR environment at the times of DAN passive measurements, as described in Section 2 (Methods).

We have made a comparison between the RAD data mentioned above and DAN passive data in a location where the rover was stationary for over a month (Rocknest) in order to verify that the short term variations observed in DAN passive count rates are consistent with variations seen in the RAD data.

As seen in Figure 2.11, there is a correlation between the RAD and DAN passive data

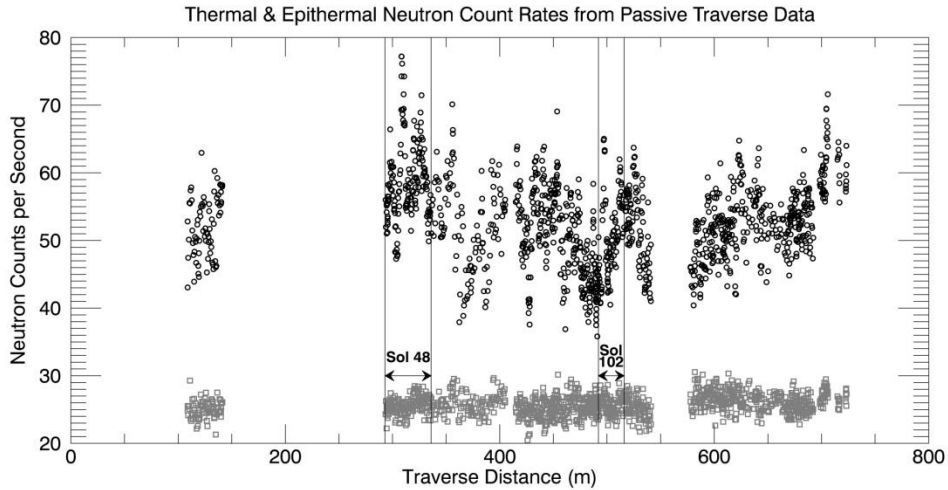


**Figure 2.8. DAN passive data acquired during rover traverse segments during the first 200 sols. All odometry values are relative to the starting point of the mission at Bradbury Landing. Thermal neutron counts per second (black circles) and epithermal neutron counts per second (gray squares) are shown versus traverse distance. Initial and final traverse distances for the example traverse segments shown in Figures 2.9 and 2.10 are marked with drop lines. Uncertainty bars are omitted for clarity, however, are of the same magnitude as seen in Figures 2.9 and 2.10.**

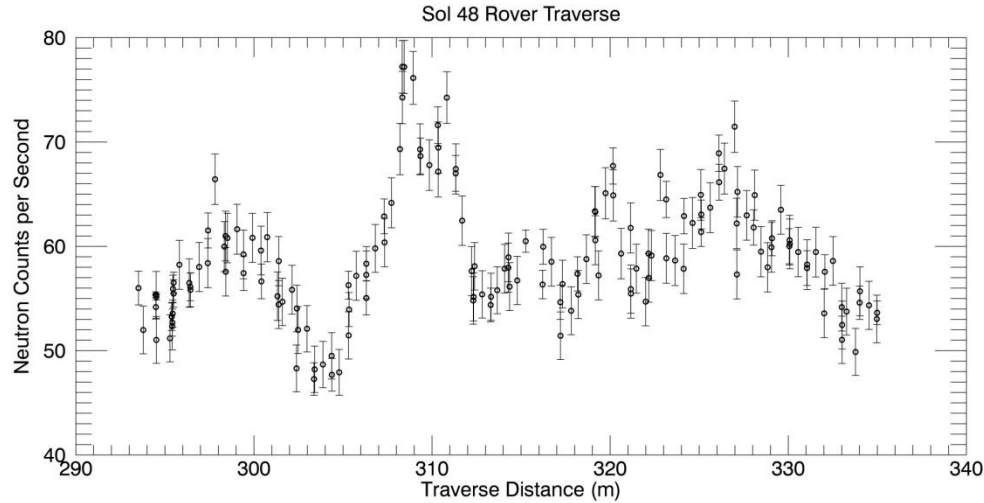


**Figure 2.9. Passive thermal neutron count rates collected along the rover traverse during sol 48. The statistical uncertainty derived from Poisson statistics on the two measurements that make up the thermal neutron count rate is shown. The sizes of the uncertainty bars are mostly related to the net speed of the rover because points where the rover lingered for various mobility-related procedures have been averaged together to improve counting statistics. The largest measured thermal neutron count rate observed during the sol 0 to 200 period can be seen at a traverse distance of ~308 m.**

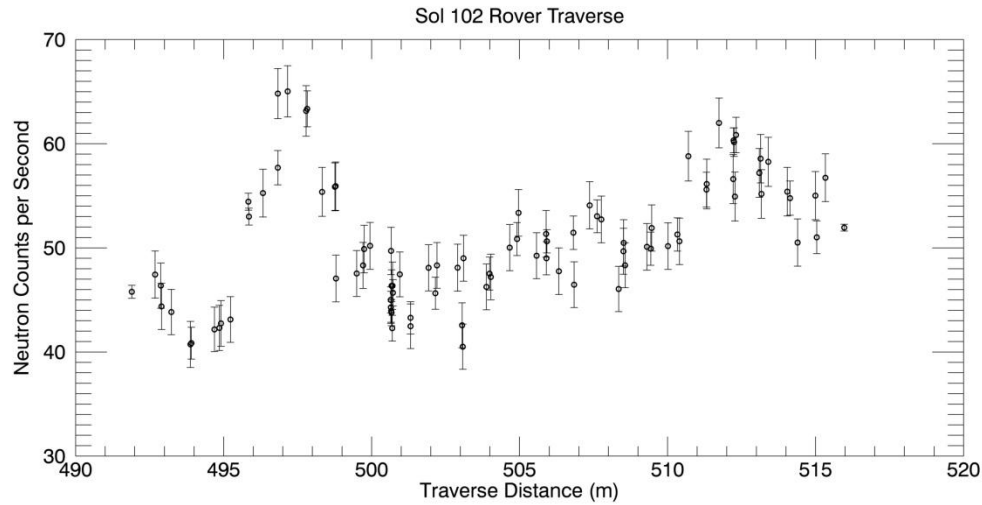


**Figure 2.10. Passive thermal neutron count rates collected along the rover traverse during sol 102. The statistical uncertainty derived from Poisson statistics on the two measurements that make up the thermal neutron count rate is shown. The sizes of the uncertainty bars are mostly related to the net speed of the rover because points where the rover lingered for various mobility-related procedures have been averaged together to improve counting statistics. Another large measured thermal neutron count rate can be observed at a traverse distance of ~497 m.**

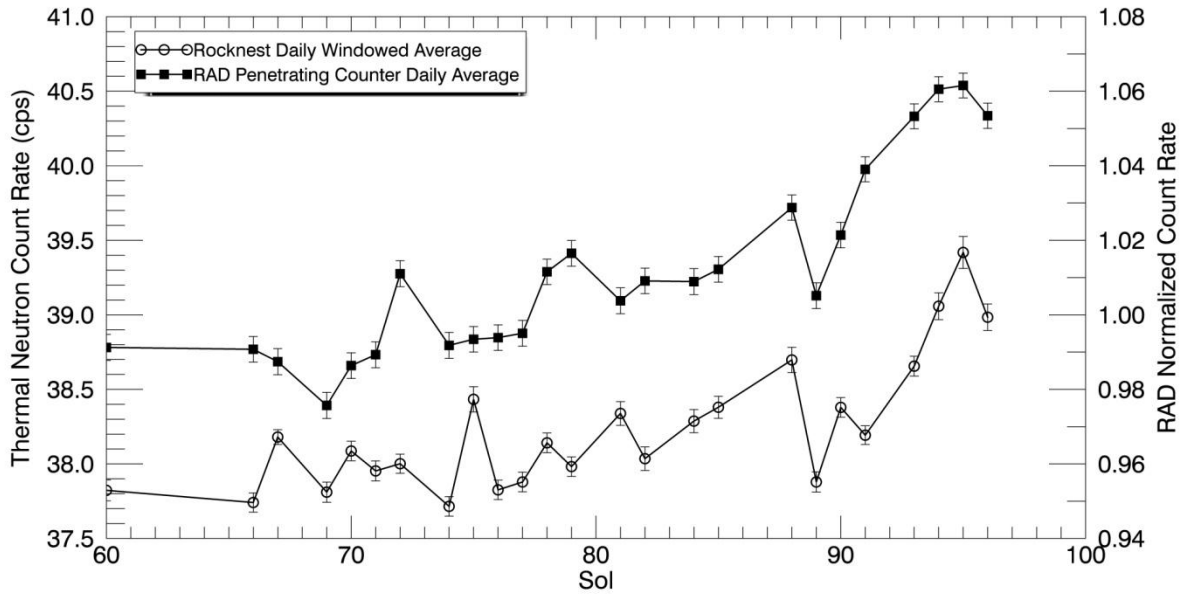


**Figure 2.11. Normalized count rates for RAD penetrating particle counter daily averages and DAN passive daily windowed averages at Rocknest are shown versus sol. As no compositional changes in the regolith are occurring, changes in the GCR flux due to variations in atmospheric pressure and solar modulation are the dominant source of the variation in DAN passive count rates over this period.**

acquired at Rocknest. For the sake of comparison, DAN passive data at Rocknest have been windowed to only afternoon measurements at the same time of each sol in order to isolate variations due only to the changing GCR environment. A linear regression shows a correlation coefficient of 0.84. This demonstrates that the changing primary GCR flux is the dominant source of variability in DAN passive count rates (at a given location) on a sol by sol basis and validates our use of RAD data in conjunction with our DAN active *in situ* calibration as a means of constraining the GCR environment.

Other ancillary data sets have also been used in our analysis. DAN active-derived WEH estimates and high thermal neutron absorption cross section element abundances for the mentioned calibration sites (Mitrofanov *et al.*, 2014), expressed in wt. % AEC, have been used to calibrate the GCR count rate simulations as discussed in Section 2 (Methods). All DAN active AEC results for the period of sol 0 to 200 have also been used to constrain WEH estimates at sites other than the calibration sites investigated by DAN passive measurements. Geologic maps made by the MSL team (Calef *et al.*, 2013) of the surface units traversed were used to search for correlations between DAN passive-derived WEH content and geologic units exposed at the surface. Images taken from the MSL navigation cameras, rear hazard avoidance cameras, and High Resolution Imaging Science Experiment on the Mars Reconnaissance Orbiter (HiRISE) have been used to look for correlations between DAN passive results and local variations in surface geology. Finally, results from the Chemistry and Mineralogy instrument (CheMin) (Vaniman *et al.*, 2014) and Sample Analysis at Mars instrument suite (SAM) (Ming *et al.*, 2014) from John Klein have been used in conjunction with DAN passive results to estimate variations in clay mineral abundance in the Yellowknife Bay Sheepbed member, as described in Section 6.5 (Clay Mineral Water Equivalent Hydrogen).

## Sources of Uncertainty

Some sources of uncertainty in our analysis of DAN passive measurements are known and understood, while others are difficult to quantify. Fortunately, the largest of these uncertainties fall into the former category. The formal uncertainties presented in our WEH results (Section 5 (Results)) include the statistical uncertainties associated with count rates from our measurements and simulations, uncertainties from DAN active mode-derived AEC abundances, and uncertainties associated with the RAD data used for scaling our simulation results.

Uncertainties quoted for measured DAN passive count rates are Poisson statistical uncertainties calculated from the total counts at a location. Uncertainties quoted for simulation results are MCNPX fractional standard deviations with the GCR and MMRTG scale factors (Section 2 (Methods)) applied. Uncertainties in the RAD penetrating counter count rates are ultimately manifested as an uncertainty in our simulated GCR count rates through incorporation as an uncertainty in the applied GCR scale factor.

Uncertainties in AEC abundances are taken from Mitrofanov *et al.* (2014). In the case of our traverse data, where we have used the average of all 51 DAN active-determined AEC abundances over the first 200 sols of the mission, we represent the uncertainty in the average AEC value as 1 standard deviation in the population of all the AEC abundances that went into the average. This uncertainty, which is  $\pm 0.19$  wt. % AEC, cannot be considered a formal uncertainty because of the way we use the abundance - *i.e.*, it is not derived from measurements at the same locations as the passive traverse measurements. However, it does provide a crude means of representing the variability of AEC throughout the first 200 sols of the traverse, which in turn propagates into increased uncertainty in the derived WEH values.



Other uncertainties that are also difficult to quantify include the assumed density of the regolith, uncertainties in detector height above the ground, and small diurnal variations that have been observed in the thermal neutron count rates (Tate *et al.*, 2015). Although formal uncertainties from these sources are difficult (if not impossible) to derive, a sense of their likely magnitudes may be gained by testing the sensitivity of derived WEH estimates to each of these parameters.

Density has been held constant in our simulations at  $1.8 \text{ g/cm}^3$ , which is consistent with the approach taken by Jun *et al.* (2013) and Mitrofanov *et al.* (2014). While  $1.8 \text{ g/cm}^3$  is consistent with loose regolith, it is expected that the materials the rover has driven over actually have a range of densities. Exposures of bedrock have been seen along the traverse where the density could easily be as high as  $\sim 2.8 \text{ g/cm}^3$ . Simulation results indicate that thermal neutron counts increase with the density of the regolith. An example thermal neutron count rate of  $\sim 55$  thermal neutron counts per second corresponds to a WEH estimate of 3 wt. % at an AEC abundance of 1 wt. % for a density of  $1.8 \text{ g/cm}^3$ . However, if the density is increased to  $2.8 \text{ g/cm}^3$ , the corresponding composition that produces the same thermal neutron count rate is only  $\sim 2.6$  wt. % WEH at 1 wt. % AEC.

Another source of uncertainty is the height of the DAN detectors and the MMRTG above the surface. Variations in these heights can occur along traverses as the rover's suspension system adapts to the terrain. As the detectors and MMRTG move closer to the ground, the intensity of MMRTG-sourced neutrons reaching the detectors increases. For fixed locations (i.e., overnight stops), the possible range of heights of the DAN detectors did not vary by more than  $\sim 2$  cm. Simulations indicate that a height difference of 2 cm will not change our derived WEH values significantly. However, along rover traverse segments, it is possible for the height

variability to be larger. Our simulations indicate that for a nominal regolith composition of 3 wt. % WEH and 1 wt. % AEC, a change of 10 cm closer to the ground will induce an increase of ~12%, or about 6 counts per second, in the thermal neutron count rate relative to that produced at the nominal height, and a 7% increase in the epithermal neutron count rate. Inverting the problem, if the 10-cm height difference were not taken into account, these count rates would cause an actual WEH abundance of 3 wt. % to be estimated as 3.8 wt. % WEH. For a height decrease of 5 cm, the same surface composition would be estimated as 3.4 wt. % WEH. Conversely, increases in the distance from detector to the regolith will lead to a decrease in the thermal neutron count rates and would cause comparable underestimates of the actual WEH content of the regolith. While there were localized “spikes” in the thermal neutron count rates along the traverse of the magnitude suggested by these simulations (and in some cases, much larger), there were not corresponding increases in the epithermal count rates of a magnitude that would be expected if changes in detector height were the cause. Realistically, changes in the detector height more than 10 cm from the nominal height would have occurred rarely, if at all. Future work will further explore the possibility of applying a refinement to the results presented here by using engineering telemetry to derive detector heights for each measurement.

Lastly, small diurnal variations in the thermal neutron count rates have been identified at two locations during the traverse where the rover was stopped for many sols (Tate *et al.*, 2015). As an example, at Rocknest the change in WEH estimates produced by these variations is only  $\sim\pm 0.1$  wt. %. The origins of these variations are the topic of ongoing work, but they are not yet considered to be understood well enough to apply a generalized diurnal correction to all DAN passive data.

In summary, the sources of uncertainty in our WEH estimates include formal statistical

uncertainties from our measurements and simulations along with formal uncertainties in assumed AEC abundances and GCR intensities. Sources of uncertainty that are less quantifiable include the density of the regolith, the height of the detectors and MMRTG above the ground, and diurnal variations in thermal neutron count rates. In the examples given to illustrate sensitivities, none of these sources produce uncertainties in estimated WEH values greater than ~0.4 wt. %. Uncertainties in AEC abundance likely will have the largest effect, followed by (in decreasing order) uncertainty in the regolith density, our formal statistical uncertainties, detector and MMRTG height, diurnal variations, and uncertainties in the GCR environment.

## Results

### *WEH Estimates for Fixed Locations*

WEH is estimated for each fixed location where DAN passive data were acquired during the first 200 sols. As described in Section 2 (Methods), this analysis assumes the composition of the regolith within the sensing volume of the instrument is homogenous both laterally and with depth. Furthermore, the WEH abundances we report from DAN passive measurements at fixed locations make use of AEC abundances derived from DAN active measurements taken at the same locations (Mitrofanov *et al.*, 2014). Shown below (Figure 2.12 and Table 2.2) are the WEH estimates for the 36 fixed locations along *Curiosity's* traverse from Bradbury Landing to John Klein (sols 0 - 200).

During these sols, the rover traversed across two major geological surface units. Prior to the Bathurst Inlet location (just west of the site labeled "Rocknest" in Figure 2.12), the rover was on the hummocky plains unit (HP) and after that it moved onto the bedded fractured unit (BF) (Grotzinger *et al.*, 2014). The BF unit is divided into three members, named Glenelg, Gillespie

## WEH Along Traverse at Fixed Locations

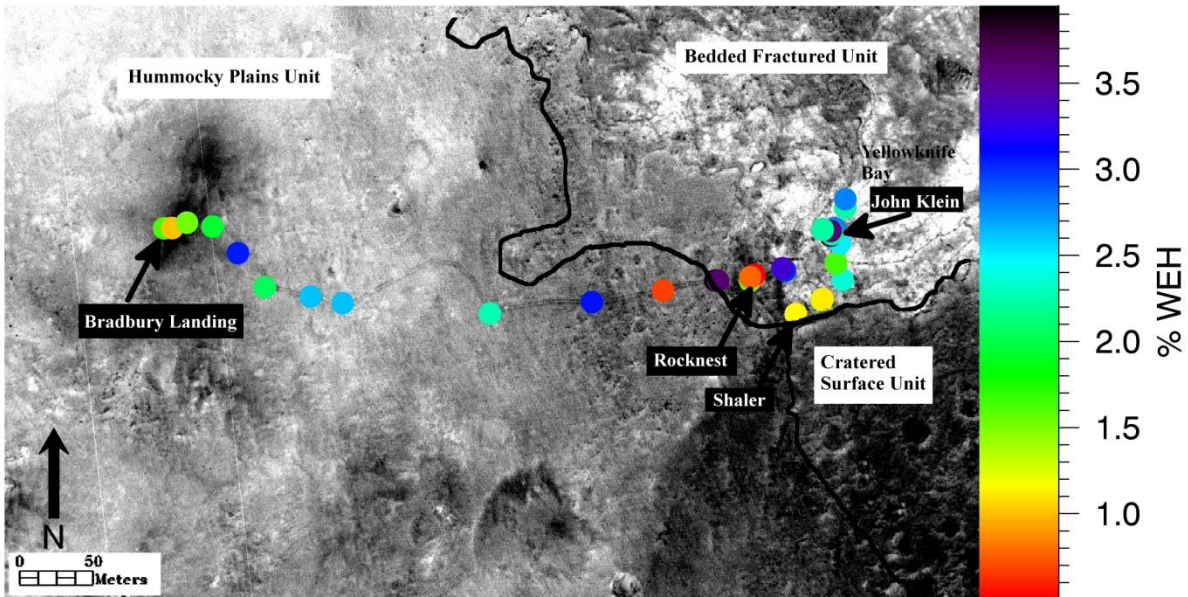


Figure 2.12. WEH estimates along *Curiosity's* traverse from Bradbury Landing to John Klein (sol 0 - 200). Black lines denote surface contacts between geologic units based on Grotzinger *et al.* (2014). White boxes represent the major geologic units, while black boxes represent specific locations along the traverse. Yellowknife Bay is also shown within the Bedded Fractured unit. The Yellowknife Bay formation contains the Sheepbed, Gillespie Lake, and Glenelg members, in ascending stratigraphic order respectively (Grotzinger *et al.*, 2014).

**Table 2.2. WEH estimates for fixed locations along the traverse from Bradbury Landing to John Klein. Locations within the bedded fractured unit are shaded in gray. A comparison between DAN passive and DAN active results is discussed in Section 6.2 and Figure 2.21.**

<b>Sol</b>	<b>Traverse Distance (m)</b>	<b>WEH (wt. %)</b>
0-15	0	1.6 ± 0.2
17-21	7	1.0 ± 0.2
22-23	27	1.5 ± 0.2
24-26	48.5	1.9 ± 0.3
26-29	78.6	3.1 ± 0.2
29-37	109.1	2.0 ± 0.2
38	141.5	2.6 ± 0.3
39	163.2	2.6 ± 0.4
45	293.8	2.3 ± 0.4
49	335.2	3.1 ± 0.4
50	392.3	0.7 ± 0.09
52	453.3	3.9 ± 0.2
54	455	3.6 ± 0.2
55	479.1	1.5 ± 0.2
57	485.1	0.9 ± 0.04
59	486.9	0.9 ± 0.05
59-100	490	0.5 ± 0.06
100-102	491.9	0.8 ± 0.06
102-111	517.2	3.0 ± 0.3
111-120	519.1	3.3 ± 0.3
120-121	553.7	1.2 ± 0.3
121-122	577.9	1.3 ± 0.2
122-123	578.9	1.1 ± 0.3
123-124	598.3	2.4 ± 0.3
124-125	612.3	1.6 ± 0.2
125-127	638.4	2.5 ± 0.4
127-130	671.2	2.2 ± 0.5
130-133	676.8	2.8 ± 0.2
133-147	698.8	2.8 ± 0.3
147-151	701.5	2.1 ± 0.5
151-152	702.2	2.8 ± 0.3

**Table 2.2. Continued.**

<b>Sol</b>	<b>Traverse Distance (m)</b>	<b>WEH (wt. %)</b>
152-159	704.6	3.7 ± 0.2
159-162	705.9	2.2 ± 0.4
162	714.9	3.6 ± 0.3
163-166	716.8	2.1 ± 0.5
166-200	723.4	2.2 ± 0.6

Lake, and Sheepbed, by lithological properties, chemical composition, and attributes observed from orbit (Grotzinger *et al.*, 2014). The surface of the BF unit is characterized by its light tone and meter- to decameter-scale fracture network (Grotzinger *et al.*, 2014). Yellowknife Bay is also within the BF unit and corresponds to the depression seen in Figure 2.12. The HP unit exhibits clast-strewn surfaces with occasional outcrops of pebble conglomerate facies (Grotzinger *et al.*, 2014). DAN did not collect passive data over exposed conglomeritic targets. The average WEH value for the HP unit is 2.3 wt. % with a standard deviation of 0.6 wt. %, whereas it is 2.1 wt. % with a standard deviation of 0.7 wt. % for the BF unit. The WEH estimates for the BF unit range from  $0.5 \pm 0.06$  wt. % to  $3.7 \pm 0.2$  wt. %. Within the HP unit, WEH ranges from  $0.7 \pm 0.09$  wt. % to  $3.9 \pm 0.2$  wt. %. Further discussion on differences between these two units can be seen Section 6.4 (Statistical Distribution of WEH Estimates Within Geologic Units).

### ***WEH Estimates for Traverse Segments***

WEH estimates from traverse segments are based on the thermal neutron counting rate and the assumption of a fixed, average AEC abundance of 1.05 wt. %, and an AEC abundance uncertainty of 0.19 wt. %, as described in Section 2 (Methods). It is admittedly unrealistic that all of these points would have the same AEC abundance, but there is no information available from any experiment on the rover to provide better constraints between the fixed locations. As such, it must be borne in mind that our estimates of WEH for traverse measurements will be too low if the actual AEC abundance at a given location is greater than the average value we used, and vice-versa (see Section 4 (Sources of Uncertainty)). We represent this effect in our results by propagating the AEC uncertainty (which comes from the statistical spread of AEC abundances determined at all fixed locations) into the uncertainties in the traverse segment WEH estimates.

Figure 2.13 shows the WEH estimates derived from all traverse segment DAN passive data over the first 200 sols of the mission. In this figure, uncertainty bars are omitted for clarity, however see Figures 2.14 and 2.15 and the online digital supplement for local expansions of the same results that include uncertainty bars. Thermal neutron count rates that were acquired at the same rover traverse distance location, *e.g.*, when the rover stops during traverses to acquire hazard avoidance images, have been averaged together to reduce counting uncertainties and make one WEH estimate for that location.

The average derived WEH estimate from all traverse segments in sols 0-200 is 2.9 wt. % with a standard deviation of 1.1 wt. %. The average WEH values for the HP unit and the BF unit are 3.4 wt. % with a standard deviation of 1.2 wt. % and 2.4 wt. % with a standard deviation of 0.9 wt. %, respectively. Within the HP unit, WEH estimates range from  $0.8 \pm 0.2$  wt. % to  $7.6 \pm 1.3$  wt. %. WEH estimates within the BF unit range from  $0.6 \pm 0.2$  wt. % to  $5.5 \pm 0.8$  wt. %. There is a large degree of variability in the WEH estimates observed in the traverse data from both units, but the HP unit has a greater average WEH content.

Locally expanded results for the sol 48 traverse are shown in Figure 2.14. These results include the largest WEH estimate ( $7.6 \pm 1.3$  wt. %) identified in the first 200 sols of passive observations. This measurement was made within the HP unit, at a traverse distance of ~ 308 meters. Another interesting localized increase in WEH along a traverse measurement is seen in the sol 102 traverse within the BF unit (Figure 2.15).

The largest WEH estimate identified from a traverse measurement within the BF unit is  $5.5 \pm 0.8$  wt. %, found within Yellowknife Bay during the sol 159 traverse. This can be seen in Figure 2.13 at a traverse distance of ~706 meters. Other interesting areas showing high WEH estimates of greater than or equal to 5 wt. % are those at traverse distances of, ~308, ~310, ~326,



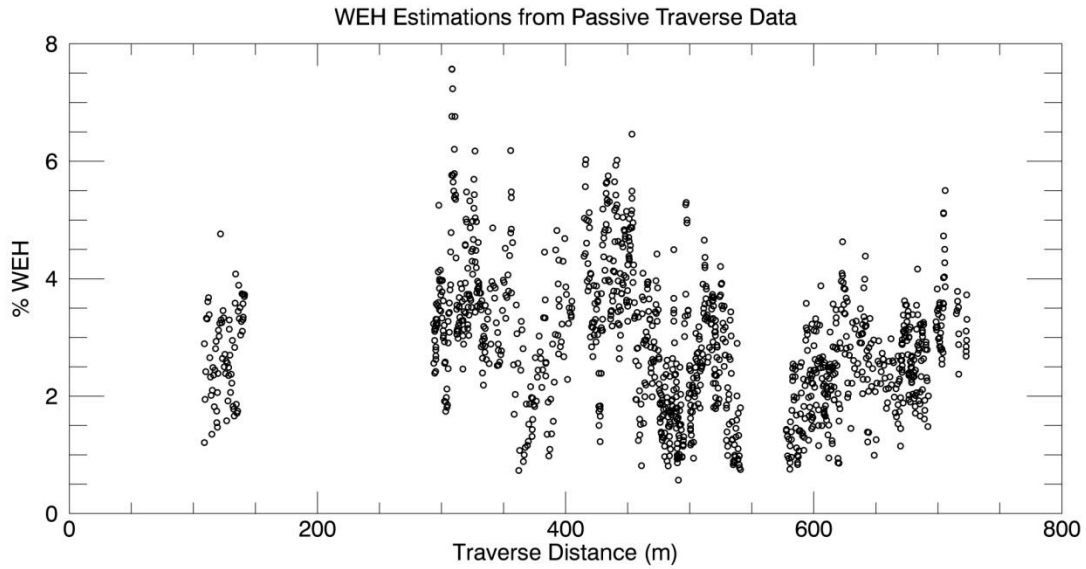


**Figure 2.13. WEH estimates from DAN passive data acquired along all rover traverse segments. Uncertainty bars are omitted for clarity. However, uncertainty bars for the same data from individual daily traverse segments may be seen in Figures 2.14 and 2.15 and the online digital supplement. The contact between the HP and BF units was encountered just prior to the Bathurst Inlet location, which is at a traverse distance of 479.1 m.**

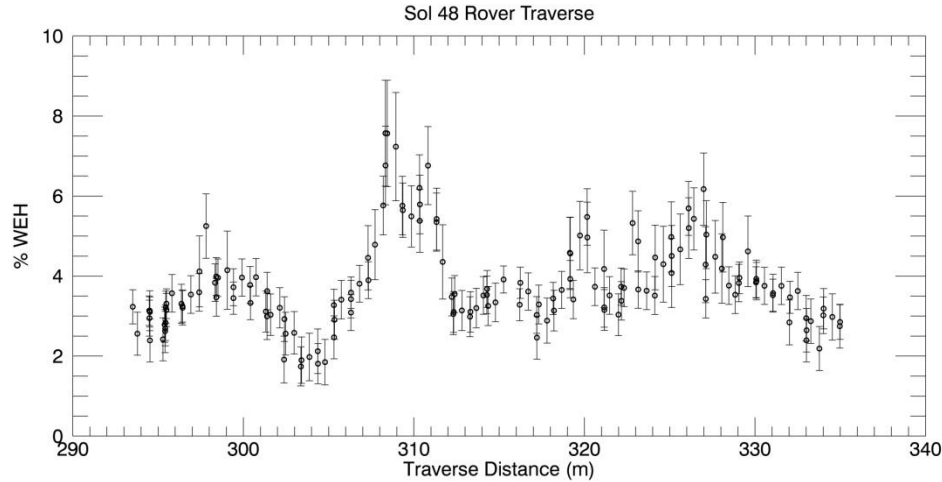


**Figure 2.14. WEH estimates along the sol 48 rover traverse. Uncertainties include counting statistics, simulation uncertainties, GCR uncertainties, and AEC abundance uncertainty of 0.19 wt. %. See Section 4 (Sources of Uncertainty) for a discussion of other potential sources of uncertainty. Uncertainties at some positions along the traverse segment are significantly smaller than others because the rover sometimes pauses mid-traverse, resulting in longer integration times and better counting statistics.**

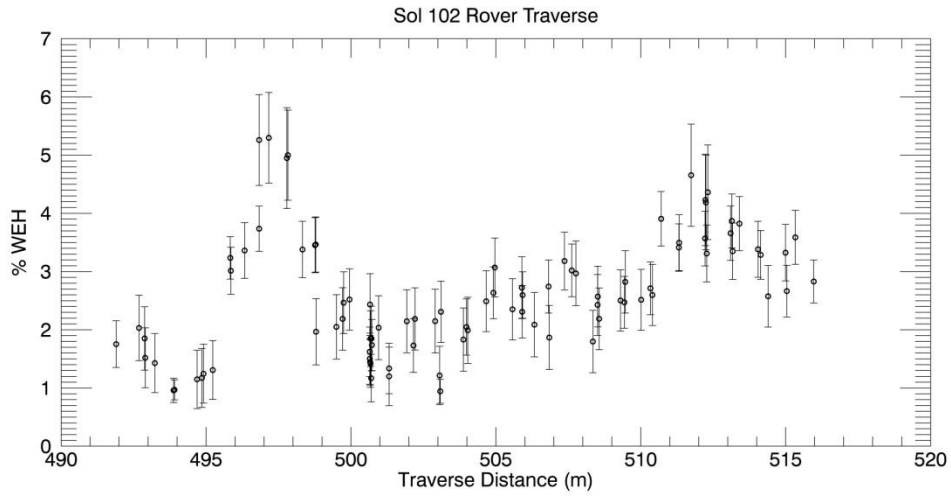


**Figure 2.15. WEH estimates along the sol 102 rover traverse, exiting the Rocknest area.**

**Uncertainties represent the same information as in the preceding figure.**

~356, ~415, ~418, ~430, ~433, ~441, ~453, ~497 and ~705 meters. Many local minima in WEH estimates are also present across the traverse as well. The largest traverse distance range of consistently low estimates of WEH is in the Rocknest area, which can be seen at a traverse distance of 490 meters and contains the low estimate of  $0.6 \pm 0.2$  wt. %. However, upon leaving the Rocknest area, WEH estimates climb to just over 5 wt. % on the sol 102 traverse (Figure 2.15) and then fall back down to between 1 and 2 wt. % before steadily climbing up to estimates greater than 2 wt. % for the rest of the traverse.

As discussed above, the AEC abundance used for analyses of traverse segment DAN passive data is the average abundance from DAN active results from all fixed locations in the first 200 sols of the mission. An alternative assumption would have been to use AEC abundances derived by linearly interpolating between fixed location AEC abundances (from DAN active measurements) at the start and finish of each traverse segment. This method is not necessarily geologically plausible, as it assumes that the AEC abundance varies linearly between locations that are tens of meters apart. However, we have re-estimated WEH values using this method for the traverses on sol 48 and sol 102 and compared them to our original (fixed AEC) abundances as a way of testing the sensitivity of our results to the method employed (Figures 2.16 and 2.17). The comparison shows that the two methods give similar results in most locations. The overall trends in these traverses are preserved and the anomalies pointed out remain anomalies.

In the preceding section we presented WEH estimates from 27 DAN passive traverse measurements. However, only two of those individual traverse segments were expanded to show small-scale variations (Figures 2.14 and 2.15). We provide similar expanded plots of WEH estimates for the other 25 traverse segments in the online supplementary materials section of this manuscript.

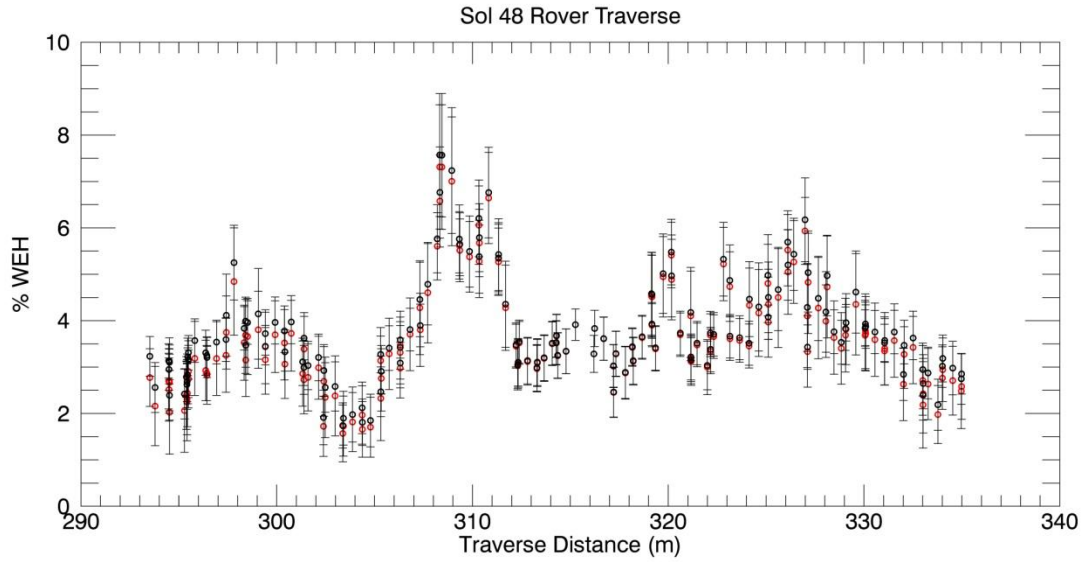


**Figure 2.16. Sol 48 traverse WEH estimates using AEC abundances interpolated from DAN active measurements made at the beginning and end of the traverse (red) and using a fixed, average AEC abundance (black).**

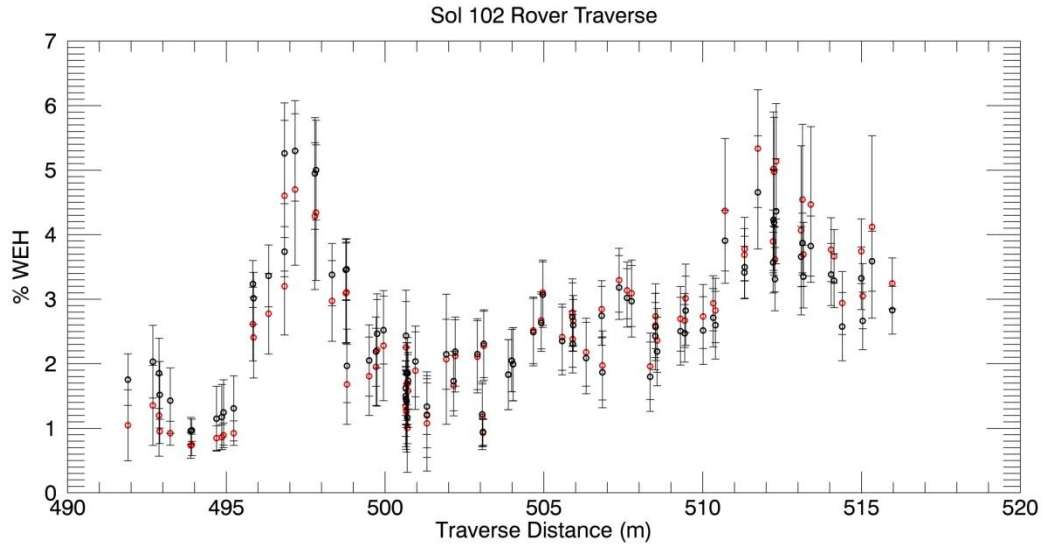


**Figure 2.17. Sol 102 traverse WEH estimates using AEC abundances interpolated from DAN active measurements made at the beginning and end of the traverse (red) and using a fixed, average AEC abundance (black).**

## Discussion

Hydrogen can be incorporated into geologic materials in many ways, including: adsorbed H<sub>2</sub>O, trapped H<sub>2</sub>O, solvation H<sub>2</sub>O (i.e., water that is coordinated with a cation on the exchange sites in the interlayers of phyllosilicates), crystal H<sub>2</sub>O (Ming *et al.*, 2007), or in minerals that contain hydroxyl (OH). The DAN instrument has no means to identify the chemical host(s) of the hydrogen it senses. Inferences can be made, however, by using results from other instruments, previous missions, and modeling. Gale Crater is located in the equatorial region of Mars, where near-surface water ice is not stable (*e.g.*, Schorghofer and Aharonson, 2005). This suggests that DAN hydrogen detections are coming from hydrated and/or OH-bearing phases formed by aqueous processes interacting with solid materials to form alteration minerals earlier in time (Ming *et al.*, 2007). Adsorbed water on the surface of regolith grains, brought about by exchange between the atmosphere and the regolith, is another potential reservoir of H<sub>2</sub>O within the DAN sensing volume. However, DAN passive measurements are not thought to be sensitive to the absolute magnitude of this exchange because it is extremely small compared to the bulk WEH of the regolith and has not been observed in ChemCam hydration experiments (Meslin *et al.*, 2013). These factors lead to the inference that H-bearing minerals are likely the most significant chemical host of the hydrogen detected by DAN within the shallow regolith of Gale crater.

### ***Fixed Locations***

The rover traversed from Bradbury Landing to John Klein during sols 0 to 200 and investigated many locations of interest along the way. Two outcrops within the HP unit, named Link (sol 27) and Hottah (sol 39), have been interpreted as remnants of ancient streambeds that experienced sustained water flow, based on the presence of fluvial conglomerate material

(Williams *et al.*, 2013). In the locations adjacent to these outcrops where DAN passive data were acquired we find above-average WEH estimates. The WEH estimate adjacent to the Link outcrop is  $3.1 \pm 0.2$  wt. %. While DAN passive data were not acquired adjacent to Hottah, the data taken closest to this location (a few meters of rover traverse distance away) indicate a WEH of  $2.6 \pm 0.3$  wt. %. Both of these estimates fall on the high side of the distribution of WEH values found within the HP unit (average WEH 2.3 wt % with a standard deviation of 0.6 wt%). Enhanced hydrogen content near the locations where conglomerate material has been observed is consistent with the interpretation that water flowed over these locations (Williams *et al.*, 2013) for a period of time sufficient to alter primary minerals.

A systematic evaluation was made of potential relationships between local surface geologic properties and WEH estimates along the traverse. The set of MSL Rear Hazcam images from each of the locations of fixed DAN passive measurements was ordered according to their corresponding WEH estimates. This ordered set was then visually inspected in sequence for any trends in observable surface properties (*e.g.*, loose rock abundance, rock size, proportion of bedrock to regolith). No such correlations were revealed. This suggests that the differences in WEH from location to location are due to changes in the subsurface, and that these changes are not necessarily observable at the surface. This result, however, only applies to correlations between WEH and local surface geologic properties at each rover stop. As discussed in Section 6.4 (Statistical Distribution of WEH Estimates Within Geologic Units), correlations do exist at the spatial scale of entire geologic units crossed along the traverse.

The highest WEH measurement for a fixed location within the HP unit was  $3.9 \pm 0.2$  wt. % WEH at a traverse distance of 453.3 meters on sol 52. This location exhibits typical HP surface properties as will be seen in Figure 2.18. The fixed location following this stop, at a



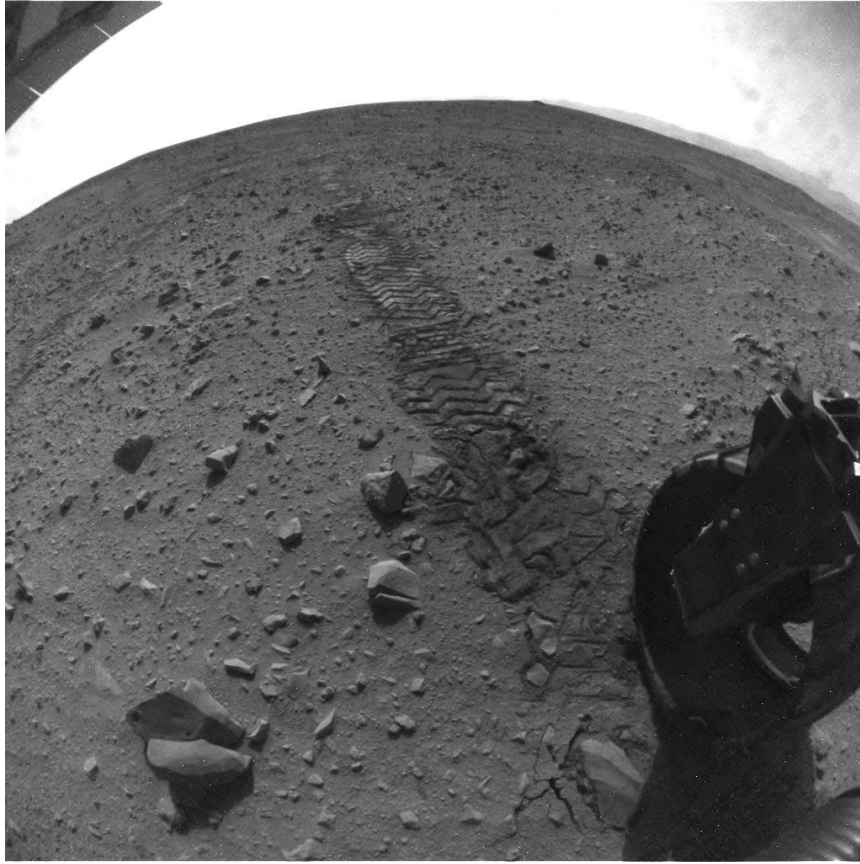


**Figure 2.18. Rear hazard camera photograph of the DAN measurement location on sol 52. This was the fixed location (within the HP unit) with the greatest DAN passive WEH estimate ( $3.9 \pm 0.2$  wt %) in the first 200 sols of the mission. Typical HP unit surface properties are observed here as in other locations in the unit with varying abundances of WEH.**

traverse distance of 455 meters on sol 54, contained  $3.6 \pm 0.2$  wt. % WEH. Slightly more rocks are present within the DAN surface footprint at this location than on sol 52, but, otherwise, the surface properties are very similar to other HP locations. These two locations contain the greatest WEH estimates in the HP unit for fixed locations, but show no surface trends to correlate with the elevated WEH content.

An area of consistently elevated WEH estimates within the BF unit for fixed locations is observed in the Yellowknife Bay area, near the John Klein drill location. WEH estimates show a general rise approaching this area from Shaler onward, and remain elevated in the near vicinity of John Klein (Figure 2.19).

DAN passive analyses at the John Klein location indicated an abundance of  $2.2 \pm 0.6$  wt. % WEH in the same area where phyllosilicates were detected by the Chemistry and Mineralogy experiment (CheMin) (Vaniman *et al.*, 2014). Because of this CheMin detection, we infer that at least some of the hydrogen detected by DAN is contained within both H<sub>2</sub>O in the interlayer of the phyllosilicates and structural OH (Ming *et al.*, 2007; Vaniman *et al.*, 2014; Ming *et al.*, 2014). Just prior to arriving at John Klein, greater WEH estimates of  $2.8 \pm 0.2$  wt. % (sol 130 - 133),  $2.8 \pm 0.3$  wt. % (sols 133 - 147),  $2.8 \pm 0.3$  wt. % (sols 151-152),  $3.7 \pm 0.2$  wt. % (sols 152 - 159), and  $3.6 \pm 0.3$  wt. % (sol 162) were observed. These locations are all within the Sheepbed member of Yellowknife Bay and exhibit the polygonal fractures/mudstones of characteristic of the unit to varying degrees. DAN active-derived results at John Klein indicate a WEH content of  $1.7 \pm 0.4$  wt. % in a top layer of 20 cm thickness and  $2.5 \pm 0.3$  wt. % in a lower layer (Mitrofanov *et al.*, 2014). The bulk WEH content from DAN active results was therefore  $2.2 \pm 0.2$  wt. % (Mitrofanov *et al.*, 2014), which agrees with the DAN passive result of  $2.2 \pm 0.6$  wt. %. The estimates made for locations surrounding John Klein are consistent with the conclusion

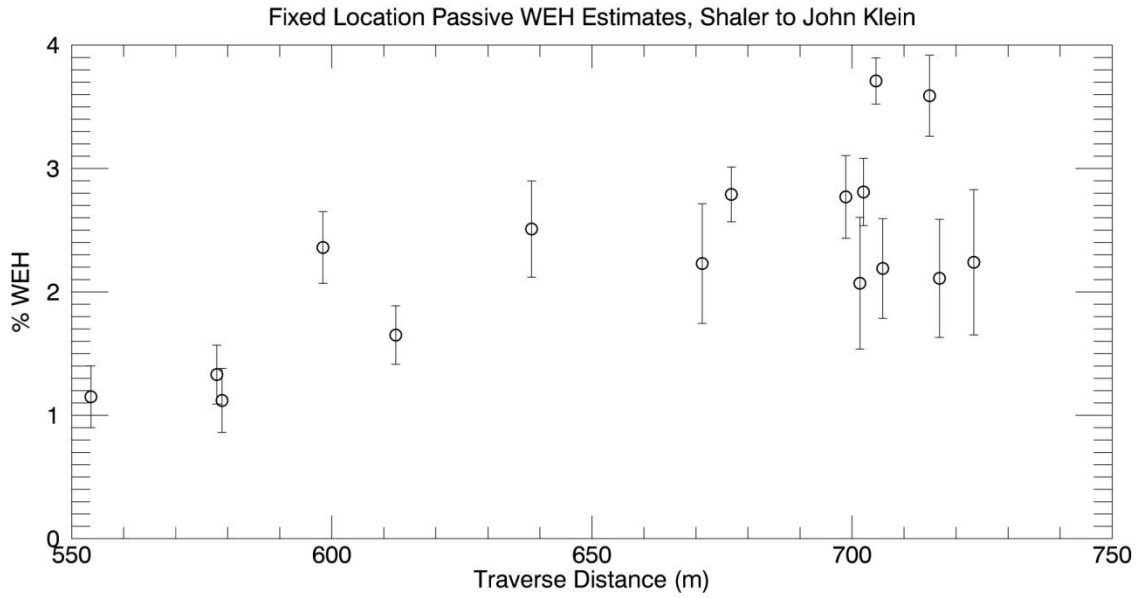


**Figure 2.19. Fixed location WEH estimates from Shaler to John Klein. The Sheepbed member starts at a traverse distance of ~615 meters.**

that sustained aqueous activity occurred there (Grotzinger *et al.*, 2014). Greater DAN WEH estimates in these locations suggest clay minerals may be present in higher abundances than at the John Klein site if the chemical (in this case, mineral) hosts of hydrogen are the same. With similar surface morphology and close proximity to John Klein (i.e., within the Sheepbed member), there is no reason to assume otherwise. The abundance of clay minerals present in these locations, estimated from DAN passive measurements, is provided below (Section 6.5 (Clay Mineral Water Equivalent Hydrogen)).

We observe the lowest of all fixed location WEH estimates ( $0.5 \pm 0.06$  wt. %) at Rocknest on sols 59-100, which was in the bedded fractured unit, specifically within the Glenelg member. This location also displayed the lowest WEH estimate derived from DAN active measurements in the first 200 sols (Mitrofanov *et al.*, 2014), although the active-derived estimate of average bulk WEH was greater at  $0.85 \pm 0.1$  wt. %. The DAN active results report a best fit to a 2-layer model, with  $1.1 \pm 0.5$  wt. % WEH in a 10-cm-thick top layer and  $0.8 \pm 0.1$  wt. % in the bottom layer.

Lastly, we have examined estimates of the relative contributions to thermal neutron counts from the two different sources (GCR and MMRTG) along the traverse. The proportions vary from location to location based on the GCR environment at the time of measurement and the subsurface composition (simulated as a homogeneous subsurface). Because MMRTG-sourced neutrons and GCR-sourced neutrons have slightly different sensing depth profiles (the GCR-sourced neutrons coming from, on average, deeper), the relative proportions of simulated counts from these two groups can be affected by whether a homogeneous subsurface model or a layered subsurface model is employed. Figure 2.20 shows the estimated MMRTG contribution to the thermal neutron count rates at fixed locations along the traverse. These vary from  $41.5 \pm 0.3$

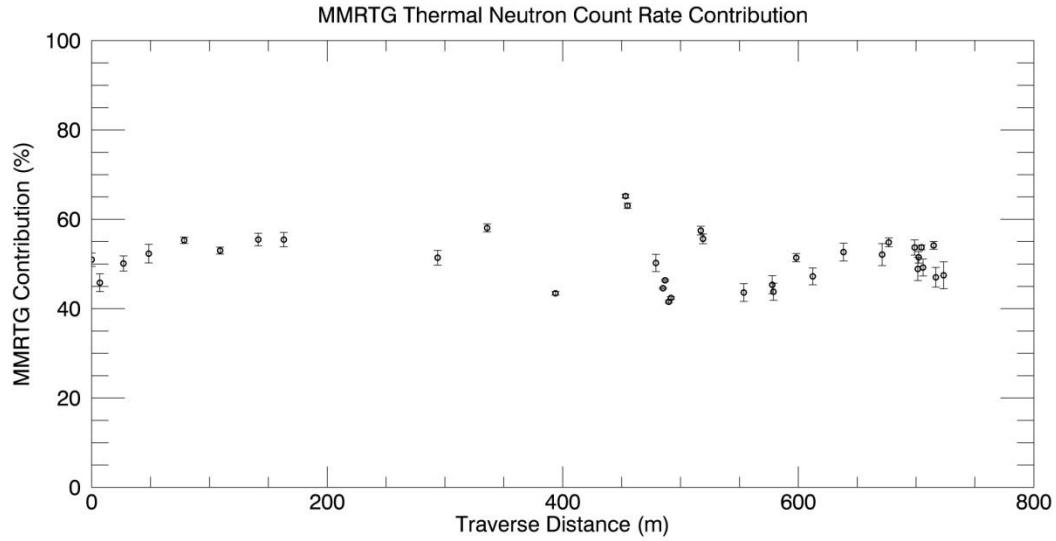


**Figure 2.20. Percentage of thermal neutron count rate attributed to MMRTG-sourced thermal neutrons at fixed locations along the traverse. Estimates are based on a simulated homogeneous subsurface.**

% to  $65.2 \pm 0.5$  % within this time period. Locations with less WEH content have lower proportions of MMRTG-sourced neutrons in the thermal neutron count rates. The MMRTG-sourced contribution to epithermal count rates is greater, varying from  $57.1 \pm 0.6$  % to  $78.2 \pm 1.2$  %.

### ***Comparison with DAN Active Results***

We have compared WEH estimates derived from DAN passive data to those derived from DAN active data (Mitrofanov *et al.*, 2014) for fixed locations where both types of measurements were acquired within the first 200 sols of the surface mission. In locations other than the calibration sites, we reduce the DAN active estimates to an average of the WEH estimate in the best-fit two-layer model, weighted by the relative thicknesses of the layers (surface to interface, and interface to the bottom of the DAN active sensing depth at ~60 cm). This average is crude, considering that the sensitivity of the measurement is not constant with depth, but it is sufficient to make preliminary comparisons with passive data.

Figure 2.21 shows a scatter plot of the two sets of measurements. Overall, there is strong correlation between the two types of measurements ( $R = 0.74$ ) (Dancey and Reidy, 2004). Also, the two types of measurements show slightly better agreement with each other ( $R = 0.81$ ) when only those locations for which the probability of model acceptance for the DAN active results (see Mitrofanov *et al.*, 2014) is high (greater than 70%, represented as solid plot symbols in Figure 2.21). 39% of the fixed locations show very good agreement (i.e., points that plot close to the identity line in Figure 2.21) between the bulk WEH estimates derived from the two types of measurements. Where the WEH estimates from passive and active disagree, the most likely cause is differences in the horizontal and vertical sensing footprints of the two modes. In Figure 2.21, most of the locations for which the derived WEH estimates do not agree plot above the

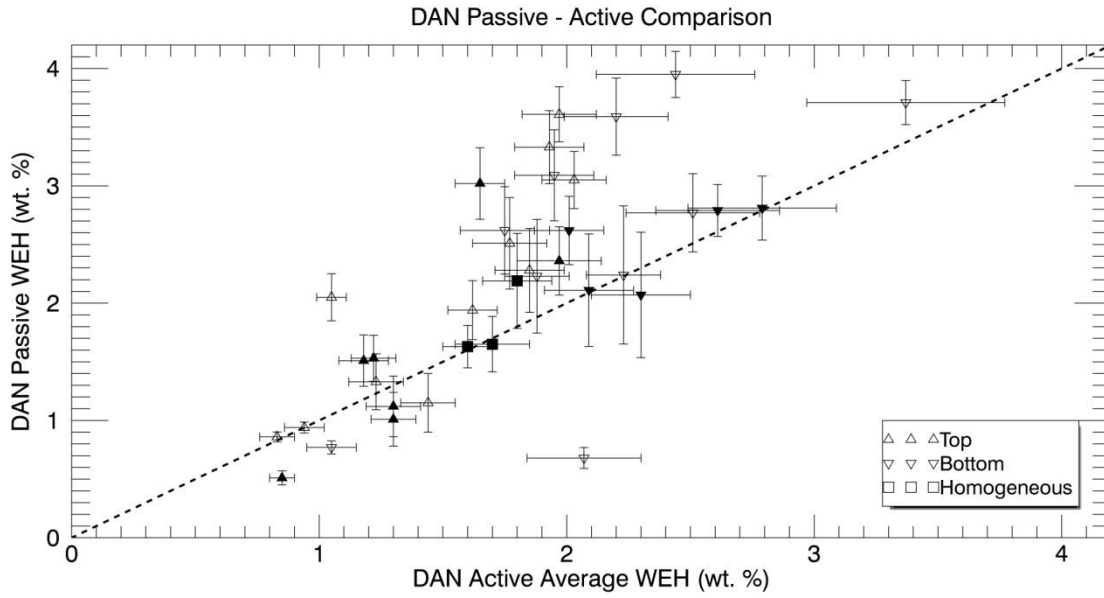


**Figure 2.21. Scatter plot of DAN passive WEH versus DAN active (60 cm weighted average) WEH for co-located, fixed location measurements. Different plot symbols are used to represent different best-fit model types from analyses of the active data (per Mitrofanov *et al.*, 2014): squares represent a homogeneous model; upward-pointing triangles represent a two-layer model with a greater WEH abundance in the top layer; downward-pointing triangles represent a two-layer model with greater WEH abundance in the bottom layer. Solid plot symbols represent locations where the probability of model acceptance for the DAN active results are greater than 70%. Based on uncertainties, there are 17 points above the identity line, 5 points plot below it, and 14 on the identity line.**

identity line, i.e., WEH estimates derived from DAN passive measurements are larger than those derived from DAN active measurements. Previous modeling of DAN active measurements (Mitrofanov *et al.*, 2014) showed that in most locations that were best fit by a two-layer model (down to the ~60 cm sensing depth of DAN's active mode), the lower layer had a greater WEH abundance. Such locations are plotted in Figure 2.21 as downward pointing triangles. The fact that most of the downward pointing triangles fall above the identity line could indicate that the trend of increasing hydrogen abundance with depth continues below the ~60-cm limit of sensitivity for the DAN active mode. The calibration sites, which were chosen (in part) because they are where DAN active results are best-modeled by a homogeneous subsurface, are represented by squares in Figure 2.21.

Some locations plot below the identity line in Figure 2.21, where the DAN passive WEH estimate is less than the DAN active WEH estimate. Mitrofanov *et al.* (2014) showed that some of the DAN active measurements were best fit by a two-layer model with greater WEH abundance in the upper layer than in the lower layer. Some of these locations also plot above the identity line. This would be consistent with a three-layer model that is relatively depleted in hydrogen in the middle layer (a layer extending down to ~60 cm), though such interpretations should be treated with an abundance of caution because the proportion of neutrons detected in passive mode that have scattered at depths between 60 and 100 cm is low.

While there is overall good agreement between WEH estimates obtained from active and passive modes, it is most likely that multiple factors are contributing to the differences that do exist. These include differences in the horizontal and vertical footprints of the modes, differences in the energy spectra of the neutrons generated from different sources, the fact that the PNG is a localized source whereas GCR-induced neutrons are distributed, and the fact that the MMRTG-



sourced neutrons have to traverse both into and out of the surface whereas GCR-induced neutrons produced in the regolith only have to traverse out of it (meaning the latter can come from greater depths). Future work will refine these initial comparisons between active and passive data by employing a more rigorous model of the vertical sensing profiles of the two modes of operation.

### ***Traverse Segments***

Traverse segments display a wider range of WEH estimates than the measurements from fixed locations. This is easily explained, as both the number of measurements and the total area investigated along traverses were much greater than at fixed locations. Traverse measurements can be useful in establishing context for the fixed locations, and they enable nearly continuous along-track monitoring of localized anomalies in the hydrogen or thermal neutron absorbing element content of the subsurface.

In many traverse segments, thermal neutron count rates are statistically the same over distances of up to many meters, however, there are also abrupt changes in the thermal neutron count rates that occur over distances comparable to the 1-m horizontal footprint of DAN, i.e., at the instrument's limit of resolution. For example, within the sol 48 traverse data (Figure 2.9), there is a local maximum in the thermal neutron count rate data that spans a length of ~1 meter in the along-track direction of the rover at a traverse distance of ~308 meters. The thermal neutron count rates can be seen to rise and fall from the local maximum as the rover approaches, crosses, and then drives away from this location. This highly localized maximum ( $77.21 \pm 2.52$  thermal neutrons per second) was the highest thermal neutron count rate observed in the DAN passive measurements from the first 200 sols of the mission. Based on our simulations, which used an assumed traverse-averaged AEC abundance of 1.05 wt. %, this thermal neutron count rate

corresponds to a WEH of  $7.6 \pm 1.3$  wt. % (Figure 2.14), which is also the highest WEH estimate along the traverse during the first 200 sols. The fixed location WEH estimates on either side of the sol 48 traverse are  $2.3 \pm 0.4$  wt. % and  $3.1 \pm 0.4$  wt. %, which agree reasonably well with the DAN passive start- and end-of-drive WEH estimates for this traverse (Figure 2.14). Images of the sol 48 traverse path from MSL navigation cameras and HiRISE reveal nothing anomalous at the approximate location of this measurement. The next highest traverse WEH measurement was on the sol 55 at a traverse distance of  $\sim 453$  meters of  $6.5 \pm 0.9$  wt. %. The corresponding thermal neutron count rate was  $69.08 \pm 2.45$  thermal neutron counts per second, with nothing anomalous in the images of the surface at this location. Likewise, on the sol 102 (Figure 2.10) traverse segment we observe a similar local maximum in the thermal neutron count data at a traverse distance of  $\sim 497$  meters. This thermal neutron count rate ( $65.03 \pm 2.45$  thermal neutron counts per second) corresponds to  $5.3 \pm 0.8$  wt. % WEH (Figure 2.15). This local maximum is interesting because the location of the measurement was just beyond Rocknest, which was identified as particularly hydrogen-poor in analyses of both DAN passive and DAN active (Mitrofanov *et al.*, 2014) measurements. Images of the sol 102 traverse path from the navigation cameras again show nothing anomalous at this location when compared to the rest of the traverse path.

Another interesting localized high value in the passive thermal neutron data is the local maximum on sol 159 at a traverse distance of  $\sim 706$  m. The thermal neutron count rate at this location was  $71.62 \pm 2.50$  thermal neutron counts per second, which corresponds to a WEH estimate of  $5.5 \pm 0.8$  wt. %. This measurement was made in the Yellowknife Bay Sheepbed member over typical light-toned, fractured material on the approach to John Klein. Furthermore, WEH estimates along the traverse from Shaler to John Klein (from both fixed locations and

traverse segment DAN passive measurements) and specifically within the Sheepbed member consistently increase and remain elevated along the approach to the John Klein area. This can be seen in Figures 2.19 and 2.13. These data, combined with the identification of phyllosilicates at John Klein (Vaniman *et al.*, 2014; Ming *et al.*, 2014), suggest that DAN may be seeing the signature of laterally-continuous clay-bearing materials in the approach to John Klein.

There are other locations along the sol 0 to 200 traverse where the thermal neutron count rate is anomalously low. The lowest thermal neutron count rate on any of the traverse segments was  $35.81 \pm 2.08$  thermal neutron counts per second on sol 100 at a traverse distance of  $\sim 491$  meters. This thermal neutron count rate corresponds to a WEH of  $0.6 \pm 0.2$  wt. %. The anomaly was located in the Rocknest area, which also had the lowest WEH estimate derived from a fixed location in both passive and active measurements. In both the fixed location data and the traverse data, the WEH estimates dropped as the rover approached a minimum in WEH at Rocknest. WEH estimates rise again immediately after Rocknest. The Rocknest WEH depression spans a length of a few meters of rover traverse distance.

While most trends we see in the WEH estimates from traverse data occur on the scale of a few meters, we observe three much larger-scale trends. One was the aforementioned rise and consistently elevated WEH estimates seen approaching and surrounding John Klein. The second and largest trend is the consistently elevated WEH abundances in the traverse distance range of  $\sim 290$  m to  $\sim 360$  m (Figure 2.13). Estimates in this region fall between approximately 2 and 7.6 wt. % WEH, with an average value of 3.7 wt. % and a standard deviation of 1.1 wt. %. Two fixed location measurements acquired within this region agree with the range of WEH estimates of  $2.3 \pm 0.4$  wt. % and  $3.1 \pm 0.4$  wt. %. This area was traversed during sols 48, 49, and part of sol 50, and is wholly contained within the HP unit. No textures or surface features are apparent in

images of the region that might be associated with compositional changes or increases in subsurface hydrogen abundance. Another large-scale feature spans the traverse distance ranges of ~428 m to ~456 meters, and shows elevated WEH estimates with an average value of 4.3 wt. % with a standard deviation of 0.8 wt. %. The two highest WEH estimates taken at fixed locations are also within this traverse distance range. This range was traversed over during the sol 52, 53, and 55 traverse. WEH estimates derived from traverse measurements in these areas of large-scale trends and in the more localized WEH depression centered on the Rocknest location all show general agreement with estimates from measurements made at fixed locations within the same areas.

#### ***Statistical Distribution of WEH Estimates within Geologic Units***

A summary of the WEH estimates found within each geologic unit (Grotzinger *et al.*, 2014), from both fixed location and traverse segment measurements, is shown in Table 2.3. Distributions of all WEH estimates (both fixed locations and traverse segments) for the HP unit and the BF unit are shown in Figure 2.22. The boundary between the two units (see Figure 2.12) is near the Bathurst Inlet location, which is west of Rocknest at a traverse distance of 479.1 m per the units presented in Grotzinger *et al.* (2014). To test the hypothesis that the two populations are statistically separable, we have applied a Student's t-test analysis. This test showed that the null hypothesis (that the differences in the populations are random) is rejected at the >95% confidence level. A Kolmogorov-Smirnov test (K-S test), which also tests whether or not the populations are from identical distributions by evaluating the shape of the cumulative distribution functions, has also been applied. The K-S test reveals that there is no significant probability that the populations are from the same distribution. With the distributions expressed in 1 wt. %-wide bins, the BF unit has a peak in its distribution at 2.0 - 3.0 wt. %, whereas the HP

**Table 2.3. Summary of WEH estimates derived from fixed and traverse segment DAN passive data. Minimum, maximum, and unit averages are shown with their uncertainties or standard deviations, respectively. Standard deviations are provided to give an approximate sense of the width of the distributions of values within each population and are not meant to imply that the distributions are formally normal (see histograms in Fig. 2.22).**

Unit	Passive WEH					
	Fixed			Traverse Segments		
	Min	Max	Average (Standard Deviation)	Min	Max	Average (Standard Deviation)
Hummocky Plains	0.7 ± 0.09	3.9 ± 0.2	2.3 (0.6)	0.8 ± 0.2	7.6 ± 1.3	3.4 (1.2)
Bedded Fractured	0.5 ± 0.06	3.7 ± 0.2	2.1 (0.7)	0.6 ± 0.2	5.5 ± 0.8	2.4 (0.9)

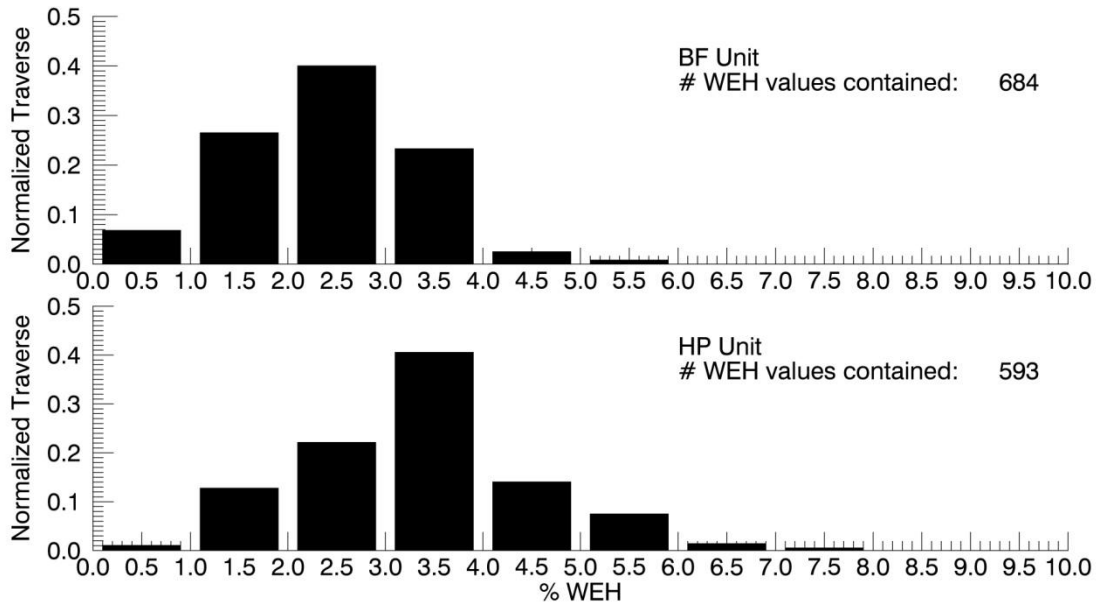


**Figure 2.22. Distribution of all WEH measurements during the first 200 sols of the mission for the hummocky plains unit (bottom) and the bedded fractured unit (top). Normalized traverse refers to the normalized fraction of the traverse sensed by the instrument within both the BF and HP units. The number of WEH measurements taken from each unit is shown.**

unit has its peak at 3.0 - 4.0 wt. %. The distribution of WEH estimates for the HP unit also has a longer tail at greater values. The statistical separability of the distribution of DAN WEH estimates for the two units demonstrates that they possess compositional differences that extend to at least ~1 m depth, in addition to the textural and color properties at the surface that were initially used to define the units. Other measurements made by other experiments on *Curiosity* also support the conclusion that the two units are compositionally distinct (Grotzinger *et al.*, 2014), though DAN is the only instrument in the payload capable of extending this finding significantly into the subsurface.

### ***Clay Mineral Water Equivalent Hydrogen***

Although we typically express the hydrogen estimates detected using DAN passive data as WEH, it is unlikely that the hydrogen is actually present in unbound water molecules. A more geologically plausible host for the hydrogen is in H-bearing minerals and adsorbed H<sub>2</sub>O on particle surfaces. WEH may be recast as the equivalent hydrogen contained in such minerals using assumptions about which minerals are present. Such estimates are subject to error due to the variable hydration states that can exist in some H-bearing minerals as well as uncertainties in the relative proportions of such minerals in the regolith composition. However, even with these uncertainties taken into account, DAN data can be used to provide broad constraints on the abundances of H-bearing minerals, especially if ancillary data on H-bearing mineral compositions and abundances from other instruments, such as SAM and CheMin, are available.

The total water evolved during SAM pyrolysis experiments of the John Klein mudstone ranged from 1.8 to 2.4 wt. % H<sub>2</sub>O (Ming *et al.*, 2014), which agrees well with the DAN WEH estimate from passive mode of  $2.2 \pm 0.6$  wt. % for the John Klein site. The agreement between the two measurements suggests that WEH content may be homogeneous from the top ~6 cm

accessed by the drill sample to the ~1 m sensing depth of the DAN passive measurement in the Sheepbed member at the John Klein site. Furthermore, the proportion of 2:1 phyllosilicate present in John Klein is 15 ( $\pm 4$ ) wt. % based on the assumption that all H<sub>2</sub>O released between 450-835°C during SAM pyrolysis runs resulted from dehydroxylation of Fe-saponite (Ming *et al.*, 2014). CheMin detected a proportion of 22 ( $\pm 11$ ) wt. % 2:1 phyllosilicate in the John Klein sample from XRD semi-quantitative data (Vaniman *et al.*, 2014). The John Klein mudstone also contained about 1 wt. % bassanite and akaganeite, but these abundances are at the CheMin detection limits (Vaniman *et al.*, 2014). Other potential water-bearing phases detected by CheMin and SAM include about 28 wt. % X-ray amorphous material and < 0.5 wt. % oxychlorine phases, *e.g.*, perchlorate and/or chlorate salts (Vaniman *et al.*, 2014; Ming *et al.*, 2014).

Ultimately, this information can be used to estimate clay mineral water equivalent hydrogen (CMWEH) from the SAM and CheMin data sets. Hydrogen in the form of hydroxyls in the octahedral sheet of the Fe-saponite account for 0.6 wt. % WEH based on the high temperature water release (Ming *et al.*, 2014). The WEH of the interlayer can be constrained between 0.4 (Na-exchanged smectite) and 1.4 (Ca-exchanged smectite) wt. % WEH by adopting the experimental results from Bish *et al.* (2003) on the amount of H<sub>2</sub>O retained by those species under Martian conditions. Upper and lower limits on CMWEH for John Klein can then be derived by summing the interlayer and hydroxyl WEH to 1.0 to 2.0 wt. % WEH. These estimates suggest that at least just under one-half of the WEH detected by DAN is in a clay mineral. The upper bound on CMWEH approaches the DAN WEH of 2.2 wt. %, hence, some of the H is likely present in other phases. The WEH of the other known H-bearing phases, *i.e.*, bassanite and akaganeite, only account for <0.2 WEH. It is likely the remaining unexplained WEH (which



would be greater if CMWEH is closer to the lower bound) is bound in the X-ray amorphous component in John Klein.

We can estimate the clay abundances, or CMWEH, at locations other than John Klein within the Sheepbed member by making the assumption that the proportion of WEH attributable to clay minerals is the same throughout the member as it is in the John Klein sample. Upper and lower bounds on the DAN-estimated clay abundances are determined using Ca-exchanged smectite or Na-exchanged smectite, respectively. SAM and CheMin analyses, discussed above, of the John Klein sample (Ming *et al.*, 2014; Vaniman *et al.*, 2014) suggest that Ca-exchanged smectite would account for 90.9% of the DAN WEH present, while Na-exchanged smectite would account for 43.5% of the WEH present. Using these percentages, we can constrain the WEH contained in the smectite at other locations in the Sheepbed member.

The Ca-exchanged smectite equivalent hydrogen (CaSEH) provides an upper bound on the clay mineral contribution to WEH in the regolith. The Na-exchanged smectite equivalent hydrogen (NaSEH) provides a lower bound on the clay mineral contribution to WEH in the regolith. CaSEH ranges from  $1.9 \pm 0.5$  to  $3.4 \pm 0.2$  wt. %, while NaSEH ranges from  $0.9 \pm 0.2$  to  $1.7 \pm 0.1$  wt. % for the locations investigated within the Sheepbed member. The remaining WEH in the regolith at these locations is accounted for by the bassanite, akaganeite, and the X-ray amorphous component described above in amounts that depend on which clay mineral is assumed present. Based on DAN passive measurements, the material in the Sheepbed member appears to contain variable abundances of phyllosilicates and amorphous phases, with some areas having more and other areas having less than John Klein (Figure 2.23). The areas with greater abundance may be places where the primary basaltic minerals have undergone a greater degree of alteration than at John Klein to form the clay minerals and amorphous component.

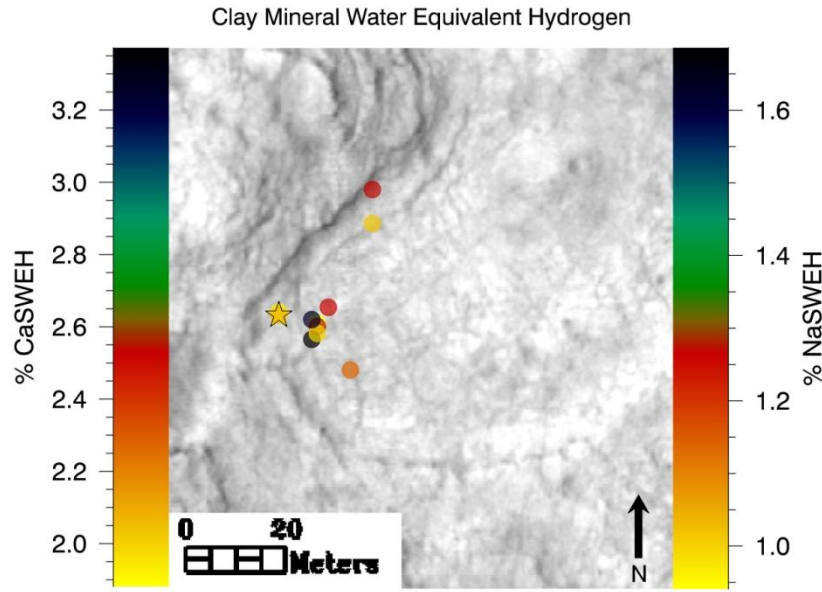


**Figure 2.23. Estimated Na-exchanged and Ca-exchanged saponite water equivalent hydrogen (NaSWEH, CaSWEH) from DAN passive measurements at fixed locations within the Sheepbed member of Yellowknife Bay. The star represents the John Klein location. These values represent the amount of DAN passive WEH that is contained in the phyllosilicates within the Sheepbed member, under the assumptions stated in Section 6.5 (Clay Mineral Water Equivalent Hydrogen). Greater values indicate a greater abundance of phyllosilicate present at that location. CaSWEH and NaSWEH represent the lower and upper limits on the CMWEH present as determined from SAM and CheMin results (Ming *et al.*, 2014; Vaniman *et al.*, 2014). Spot size shown here does not represent actual DAN footprint size.**

DAN has no means to constrain the formation mechanism of these H-bearing minerals, but these results are consistent with results from other instruments, which suggest that the clay minerals are authigenic and derived from aqueous alteration of olivine (McLennan *et al.*, 2014; Vaniman *et al.*, 2014; Bristow *et al.*, 2014).

## Conclusions

There is substantial variability in the DAN passive thermal neutron count rates along *Curiosity's* traverse from sol 0 to 200. Our simulation of these measurements indicates that WEH content in the top ~100 cm beneath the rover's traverse path ranges from  $0.5 \pm 0.06$  wt. % to  $7.6 \pm 1.3$  wt. % WEH for both the 36 fixed locations that are co-located with DAN active measurements and the 27 traverse segments. The majority of our WEH estimates are less than HEND estimates of ~5 wt. % WEH in Gale Crater (Litvak *et al.*, 2013). However, a small percentage (5%) of locations yielded DAN passive WEH estimates equal to or greater than the HEND value. The differences between the orbital WEH estimate and those made from DAN data are easily reconcilable because of the very large difference in the spatial resolution of the measurements. A similar disparity between DAN-active WEH estimates and the HEND orbital WEH measurement was noted by Mitrofanov *et al.* (2014). This is consistent with there being lateral heterogeneity of WEH content within the HEND footprint and an increased sensing depth of HEND and DAN passive mode as compared to DAN active mode, as noted by Mitrofanov *et al.* (2014).

Our estimates for fixed locations are comparable to DAN active results with good overall agreement between the two modes of data collection. The discrepancies are most likely attributable to some combination of differences in the horizontal and vertical sensitivities and the

fact that the two modes sense different proportions of neutrons sourced from point sources (PNG and MMRTG) versus a distributed source (GCR).

Collection of DAN passive data while the rover is traversing allows for localization of compositional variations within the regolith. Results from such measurements over the first 200 sols show localized thermal neutron count anomalies (interpreted as anomalies in estimated WEH abundance) at spatial scales down to ~1 m, which is the lateral limit of resolution of the experiment. Interestingly, no correlation was found between any surface properties observed in image data (*e.g.*, loose rock abundance, rock size, proportion of bedrock to regolith) and the positions of these localized highs and lows in estimated WEH content. These traverse data do, however, reveal statistically meaningful differences in the estimated hydrogen content of large-scale subsurface compositional units which correspond to geologic units mapped at the surface.

The hydrogen sensed in DAN passive data probably is hosted in various alteration minerals, such as clays. WEH estimates from DAN passive data are consistent with evidence for sustained fluvial activity seen by other instruments onboard MSL at locations along the traverse, *i.e.*, Link and Hottah (Williams *et al.*, 2013) and John Klein (Vaniman *et al.*, 2014). Furthermore, the amount of clays that would need to be present to account for the hydrogen observed at the John Klein location by DAN passive observations are consistent with the abundance reported by the SAM experiment for a drill sample from the same location (Ming *et al.*, 2014), with possible greater and lesser clay mineral abundances in the near-vicinity of John Klein within the Sheepbed member.

## **Acknowledgments**

This work was financially supported by J. Moersch's MSL Participating Scientist Award (NASA JPL 1451872). Our computational resources included the University of Tennessee high performance computing cluster "Newton". We would like to thank Mike Malin for productive discussions regarding the effects of regolith density on the results. We would also like to thank the MSL operations and science teams for helping acquire these data.

## References

- Anderson, R. B., and J. F. Bell III (2010), Geologic mapping and characterization of Gale Crater and implications for its potential as a Mars Science Laboratory landing site, *Mars* 5, 76-128, 2010; doi:10.1555/mars.2010.0004.
- Bish, D.L., J. Carey, D. Vaniman, S. Chipera (2003), Stability of hydrous minerals on the martian surface, *Icarus*, 164, 96-103.
- Bristow, T. F., D. L. Bish, D. T. Vaniman, R. V. Morris, D. F. Blake, J. P. Grotzinger, E. B. Rampe, J. A. Crisp, C. N. Achilles, D. W. Ming, B. L. Ehlmann, P. L. King, J. C. Bridges, J. L. Eigenbrode, D. Y. Sumner, S. J. Chipera, J. M. Moorokian, A. H. Treiman, S. M. Morrison, R. T. Downs, J. D. Farmer, D. D. Marais, P. Sarrazin, M. M. Floyd, M. A. Mischna (2014), The origin and implications of clay minerals from Yellowknife Bay, Gale crater, Mars, *American Mineralogist*, doi:10.2138/am-2015-5077, in press.
- Calef, F. J., W. E. Dietrich, L. Edgar, J. Farmer, A. Fraeman, J. Grotzinger, M. C. Palucis, T. Parker, M. Rice, S. Rowland, K. M. Stack, D. Sumner, J. Williams, and the MSL Science Team (2013), Geologic mapping of the Mars Science Laboratory landing ellipse, Lunar and Planetary Science Conference, The Woodlands, Texas.
- Dancey, C., and J. Reidy (2004), *Statistics without Maths for Psychology: using SPSS for Windows*, London: Prentice Hall.
- Drake, D.M., W.C. Feldman, and B.M. Jakosky (1988), Martian Neutron Leakage Spectra, *Journal of Geophysical Research*, 93, 6353-6368.
- Dunford, C. L. (1992), Evaluated Nuclear Data File, ENDF/B-VI, *Nuclear Data for Science and Technology*, Part X, 788-792, doi:10.1007/978-3-642-58113-7\_222.
- Ehresmann, B., C. Zeitlin, D. M. Hassler, R. F. Wimmer-Schweingruber, E. Böhm, S. Böttcher, D. E. Brinza, S. Burmeister, J. Guo, J. Köhler, C. Martin, A. Posner, S. Rafkin, and G. Reitz (2014), Charged particle spectra obtained with the Mars Science Laboratory Radiation Assessment Detector (MSL/RAD) on the surface of Mars, *Journal of Geophysical Research*, 119, 468–479, doi:10.1002/2013JE004547.
- Feldman, W. C., D. M. Drake, R. D. O'Dell, F. W. Brinkley, Jr., and R. C. Anderson (1989), Gravitational effects on planetary neutron flux spectra, *Journal of Geophysical Research*, 94, 513-525.
- Feldman, W.C., S. Maurice, S., Binder, A.B., Barraclough, B.L., Elphic, R.C., and Lawrence, D.J. (1998) Fluxes of Fast and Epithermal Neutrons from Lunar Prospector: Evidence for Water Ice at the Lunar Poles, *Science*, 281:1496-1500.
- Feldman, W. C., W. V. Boynton, R. L. Tokar, T. H. Prettyman, O. Gasnault, S. W. Squyres, R.

- C. Elphic, D. J. Lawrence, S. L. Lawson, S. Maurice, G. W. McKinney, K. R. Moore, and R. C. Reedy (2002), Global distribution of neutrons from Mars: Results from Mars Odyssey, *Science*, 297, 75, doi:10.1126/science.1073541.
- Goldsten, J. O., E. A. Rhodes, W. V. Boynton, W. C. Feldman, D. J. Lawrence, J. I. Trombka, D. M. Smith, L. G. Evans, J. White, N. W. Madden, P. C. Berg, G. A. Murphy, R. S. Gurnee, K. Strohbahn, B. D. Williams, E. D. Schaefer, C. A. Monaco, C. P. Cork, J. Del Eckels, W. O. Miller, M. T. Burks, L. B. Hagler, S. J. DeTeresa, and M. C. Witte (2007), The MESSENGER Gamma-Ray and Neutron Spectrometer, *Space Science Reviews*, 131, 339-391.
- Grotzinger, J. P., J. Crisp, A. R. Vasavada, R. C. Anderson, C. J. Baker, R. Barry, D. F. Blake, P. Conrad, K. S. Edgett, B. Ferdowski, R. Gellert, J. B. Gilbert, M. Golombek, J. Gómez-Elvira, D. M. Hassler, L. Jandura, M. Litvak, P. Mahaffy, J. Maki, M. Meyer, M. C. Malin, I. Mitrofanov, J. J. Simmonds, D. Vaniman, R. V. Welch, and R. C. Weins (2012), Mars Science Laboratory Mission and Science Investigation, *Space Science Reviews*, 170, doi:10.1007/s11214-012-9892-2.
- Grotzinger, J. P., D. Sumner, L. Kah, K. Stack, S. Gupta, L. Edgar, D. Rubin, K. Lewis, J. Schieber, N. Mangold, R. Milliken, P. Conrad, D. DesMarais, J. Farmer, K. Siebach, F. Calef III, J. Hurowitz, S. McLennan, D. Ming, D. Vaniman, J. Crisp, A. Vasavada, K. Edgett, M. Malin, D. Blake, R. Gellert, P. Mahaffy, R. Wiens, S. Maurice, J. Grant, S. Wilson, R. C. Anderson, L. Beegle, R. B. Anderson, T. Bristow, W. Dietrich, G. Dromart, J. Eigenbrode, A. Fraeman, C. Hardgrove, K. Herkenhoff, L. Jandura, G. Kocurek, S. Lee, L. Leshin, R. Leveille, D. Limonadi, J. Maki, S. McCloskey, M. Meyer, M. Minitti, H. Newsom, D. Oehler, A. Okon, M. Palucis, T. Parker, S. Rowland, M. Schmidt, S. Squyres, A. Steele, E. Stolper, R. Summons, A. Treimann, R. Williams, A. Yingst, and MSL Science Team (2014), A Habitable Fluvio-Lacustrine Environment at Yellowknife Bay, Gale Crater, Mars, *Science*, 343(6169), 1242777, doi:10.1126/science.1242777.
- Hardgrove, C., J. Moersch, and D. Drake (2011), Effects of geochemical composition on neutron die-away measurements: Implications for Mars Science Laboratory's Dynamic Albedo of Neutrons experiment, *Nuclear Instruments and Methods in Physics Research A*, 659, 442-455.
- Hardgrove, C., J. Moersch, I. Mitrofanov, M. Litvak, A. Behar, W.V. Boynton, L. DeFlores, D. Drake, F. Fedosov, D. Golovin, I. Jun, K. Harshman, A.S. Kozyrev, A. Malakhov, R. Milliken, R.O. Kuzmin, M. Mischna, M. Mokrousov, S. Nikiforov, A.B. Sanin, C. Tate, A. Varenikov, and the MSL Science Team (2014), Modeling of Mars Science Laboratory Curiosity's Dynamic Albedo of Neutrons Instrument Data Using Elemental Geochemistry, Lunar and Planetary Science Conference, The Woodlands, Texas.
- Hassler, D.M., C. Zeitlin, R.F. Wimmer-Schweingruber, B. Ehresmann, S. Rafkin, J.L. Eigenbrode, D.E. Brinza, G. Weigle, S. Böttcher, E. Böhm, S. Burmeister, J. Guo, J. Köhler, C. Martin, G. Reitz, F.A. Cucinotta, M.-H. Kim, D. Grinspoon, M.A. Bullock, A.

- Posner, J. Gómez-Elvira, A. Vasavada, J.P. Grotzinger, and the MSL Science Team (2014), Mars' surface radiation environment measured with the Mars Science Laboratory's Curiosity rover, *Science*, 343(6169), 1244797, doi:10.1126/science.1244797.
- Jun, I., I. Mitrofanov, M. L. Litvak, A. B. Sanin, W. Kim, A. Behar, W. V. Boynton, L. DeFlores, F. Fedosov, D. Golovin, C. Hardgrove, K. Harshman, A. S. Kozyrev, R. O. Kuzmin, A. Malakhov, M. Mischna, J. Moersch, M. Mokrousov, S. Nikiforov, V. N. Shvetsov, C. Tate, V. I. Tret'yakov, and A. Vostrukhin (2013), Neutron background environment measured by the Mars Science Laboratory's (MSL) Dynamic Albedo of Neutrons Instrument during the first 100 sols, *Journal of Geophysical Research, Planets*, 118(11):2400-2412, 10.1002/2013JE004510, 2013.
- Knoll, G. F. (2000), *Radiation Detection and Measurement*, New York: John Wiley and Sons, Inc.
- Litvak, M.L., I. G. Mitrofanov, Yu. N. Barmakov, A. Behar, A. Bitulev, Yu. Bobrovitsky, E. P. Bogolubov, W. V. Boynton, S. I. Bragin, S. Churin, A. S. Grebennikov, A. Konovalov, A. S. Kozyrev, I. G. Kurdumov, A. Krylov, Yu. P. Kuznetsov, A. V. Malakhov, M. I. Mokrousov, V. I. Ryzhkov, A. B. Sanin, V. N. Shvetsov, G. A. Smirnov, S. Sholeninov, G. N. Timoshenko, T. M. Tomilina, D. V. Tuvakin, V. I. Tretyakov, V. S. Troshin, V. N. Uvarov, A. Varenikov, and A. Vostrukhin (2008), The Dynamic Albedo of Neutrons (DAN) experiment for NASA's 2009 Mars Science Laboratory, *Astrobiology*, 8, 605-613, DOI: 10.1089/ast.2007.0157.
- Litvak, M.L., I. G. Mitrofanov, A. Behar, W. V. Boynton, L. Deflores, F. Fedosov, D. Golovin, C. Hardgrove, K. Harshman, I. Jun, A. S. Kozyrev, A.S. Kozyrev, R.O. Kuzmin, A. Malakhov, R. Milliken, M. Mischna, J. Moersch, M. Mokrousov, S. Nikiforov, A. B. Sanin, V.N.Shvetsov, C. Tate, V. I. Tret'yakov, A. Vostrukhin and MSL Science Team (2013), Estimation of natural neutron emission from the surface of the Gale crater from the ground data from DAN and the orbital data from HEND, Lunar and Planetary Science Conference, The Woodlands, Texas.
- Litvak, M.L., I. G. Mitrofanov, A.B.Sanin, D. Lisov, A. Behar, W. V. Boynton, L. Deflores, F. Fedosov, D. Golovin, C. Hardgrove, K. Harshman, I. Jun, A. S. Kozyrev, A.S. Kozyrev, R.O. Kuzmin, A. Malakhov, R. Milliken, M. Mischna, J. Moersch, M. Mokrousov, S. Nikiforov, V.N.Shvetsov, K. Stack, R. Starr, C. Tate, V. I. Tret'yakov, A. Vostrukhin and MSL Science Team (2014), Local Variations of Bulk Hydrogen and Chlorine Content Measured at the Contact Between the Sheepbed and Gillespie Lake Units in Yellowknife Bay, Gale Crater, Using the DAN Instrument Onboard Curiosity, *Journal of Geophysical Research, Planets*, 119, doi:10.1002/2013JE004556.
- Mashnik, S. G. (2005), CEM03. 01 and LAQGSM03.01 versions of the improved Cascade Exciton Model (CEM) and Los Alamos Quark-Gluon string model (LAQGSM) codes, Report LA-UR-05-2686, Los Alamos National Laboratory, Los Alamos, N. M.



- McKinney, G.W., J.W. Durkee, F.X. Gallmeier, J.S. Hendricks, M.R. James, D.B. Pelowitz, L.S. Waters, "MCNPX Overview", LA-UR-06-6206 (278 KB), Proceedings of the 2006 HSSW, FNAL, IL, September 6-8, 2006.
- McLennan, S.M., R. B. Anderson, J. F. Bell III, J. C. Bridges, F. Calef III, J. L. Campbell, B. C. Clark, S. Clegg, P. Conrad, A. Cousin, D. J. Des Marais, G. Dromart, M. D. Dyar, L. A. Edgar, B. L. Ehlmann, C. Fabre, O. Forni, O. Gasnault, R. Gellert, S. Gordon, J. A. Grant, J. P. Grotzinger, S. Gupta, K. E. Herkenhoff, J. A. Hurowitz, P. L. King, S. Le Mouélic, L. A. Leshin, R. L  veill  , K. W. Lewis, N. Mangold, S. Maurice, D. W. Ming, R. V. Morris, M. Nachon, H. E. Newsom, A. M. Ollila, G. M. Perrett, M. S. Rice, M. E. Schmidt, S. P. Schwenzer, K. Stack, E. M. Stolper, D. Y. Sumner, A. H. Treiman, S. VanBommel, D. T. Vaniman, A. Vasavada, R. C. Weins, R. A. Yingst, and the MSL Science Team (2014), Elemental Geochemistry of Sedimentary Rocks in Yellowknife Bay, Gale Crater, Mars. *Science*, 343(6169), 1244734, doi:10.1126/science.1244734.
- McSween Jr, H.Y., I. O. McGlynn, and A. D. Rogers (2010), Determining the modal mineralogy of martian regoliths, *Journal of Geophysical Research*, 115, E00F12, doi:10.1029/2010JE003582.
- Meslin, P.-Y., O. Gasnault, O. Forni, S. Schr  der, A. Cousin, G. Berger, S.M. Clegg, J. Lasue, S. Maurice, V. Sautter, S. Le Mou  lic, R.C. Wiens, C. Fabre, W. Goetz, D. Bish, N. Mangold, B. Ehlmann, N. Lanza, A.M. Harri, R. Anderson, E. Rampe, T.H. McConnochie, P. Pinet, D. Blaney, R. L  veill  , D. Archer, B. Barraclough, S. Bender, D. Blake, J.G. Blank, N. Bridges, B.C. Clark, L. DeFlores, D. Delapp, G. Dromart, M.D. Dyar, M. Fisk, B. Gondet, J. Grotzinger, K. Herkenhoff, J. Johnson, J.-L. Lacour, Y. Langevin, L. Leshin, E. Lewin, M.B. Madsen, N. Melikechi, A. Mezzacappa, M.A. Mischna, J.E. Moores, H. Newsom, A. Ollila, R. Perez, N. Renno, J.-B. Sirven, R. Tokar, M. de la Torre, L. d'Uston, D. Vaniman, A. Yingst, and MSL Science Team (2013), Soil diversity and hydration as observed by ChemCam at Gale Crater, Mars, *Science*, 341 (6153):1238670, doi:10.1126/science.1238670.
- Milliken, R. E., J. P. Grotzinger, and B. J. Thomson (2010), Paleoclimate of Mars as captured by the stratigraphic record in Gale Crater, *Geophysical Research Letters*, 37, L04201, doi:10.1029/2009GL041870, 2010.
- Ming, D. W., B. C. Clark, and R. V. Morris (2007), Chapter 23: Aqueous alteration on Mars In J.F. Bell III (Ed.), *The Martian Surface: Composition, Mineralogy, and Physical Properties* (pp. 521-540). Cambridge, UK: Cambridge University Press.
- Ming, D. W., P. D. Archer, D. P. Glavin, J. L. Eigenbrode, H. B. Franz, B. Sutter, A. E. Brunner, J. C. Stern, C. Freissinet, A. C. McAdam, P. R. Mahaffey, M. Cabane, P. Coll, J. L. Campbell, S. K. Atreya, P. B. Niles, J. F. Bell III, D. L. Bish, W. B. Brinckerhoff, A. Buch, P. G. Conrad, D. J. Des Marais, B. L. Ehlmann, A. G. Fair  n, K. Farley, G. J., Flesch, P. Francois, R. Gellert, J. A. Grant, J. P. Grotzinger, S. Gupta, K. E. Herkenhoff, J. A. Hurowitz, L. A. Leshin, K. W. Lewis, S. M. McLennan, K. E. Miller, J. Moersch, R. V. Morris, R. Navarro-Gonz  lez, A. A. Pavlov, G. M. Perrett, I. Pradler, S. W. Squyres,

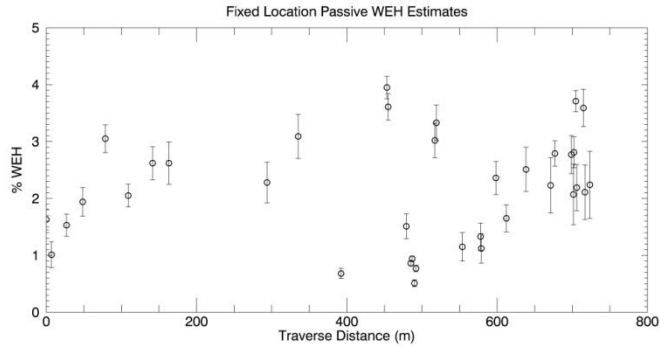
- R. E. Summons, A. Steele, E. M. Stolper, D. Y. Sumner, C. Szopa, S. Teinturier, M. G. Trainer, A., H. Treimann, D. T. Vaniman, A. R. Vasavada, C. R. Webster, J. J. Wray, R. A. Yingst, and the MSL Science Team (2014), Volatile and organic compositions of sedimentary rocks in Yellowknife Bay, Gale Crater, Mars, *Science*, 343(6169), 1245267, doi:10.1126/science.1245267.
- Mitrofanov, I. G., D. Anfimov, A. S. Kozyrev, M. L. Litvak, A. B. Sanin, V. I. Tret'yakov, A. Krylov, V. Shvetsov, W. V. Boynton, C. Shinohara, D. Hamara, and R. S. Saunders (2002), Maps of subsurface hydrogen from the High Energy Neutron Detector, Mars Odyssey, *Science*, 297, 78-81.
- Mitrofanov, I. G., M. L. Litvak, A. B. Varenikov, Y. N. Barmakov, A. Behar, Y. I. Bobrovniksky, E. P. Bogolubov, W. V. Boynton, K. Harshman, E. Kan, A. S. Kozyrev, R. O. Kuzmin, A. V. Malakhov, M. I. Mokrousov, S. N. Ponomareva, V. I. Ryzhkov, A. B. Sanin, G. A. Smirnov, V. N. Shvetsov, G. N. Timoshenko, T. M. Tomilina, V. I. Tret'yakov, and A. A. Vostrukhin (2012), Dynamic Albedo of Neutrons (DAN) experiment onboard NASA's Mars Science Laboratory, *Space Science Review*, 170, 559–582, DOI 10.1007/s11214-012-9924-y.
- Mitrofanov, I. G., M. L. Litvak, A. B. Sanin, R. Starr, D. I. Lisov, R. O. Kuzmin, A. Behar, W. V. Boynton, C. Hardgrove, K. Harshman, I. Jun, R. Milliken, M. A. Mischna, J. E. Moersch, and C. G. Tate (2014), Content of water and chlorine in the martian regolith along the first 1900 meters of the traverse of Curiosity, as measured by DAN instrument onboard the rover, *Journal of Geophysical Research Planets*, 119, 1579-1596, doi:10.1002/2013JE004553.
- Morthekai, P., M. Jain, L. Dartnell, A.S. Murray, L. Bøtter-Jensen, and L. Desorgher (2007), Modelling of the dose-rate variations with depth in the Martian regolith using GEANT4, *Nuclear Instruments and Methods in Physics Research A*, 580, 667-670.
- Mrigakshi, A. I., D. Matthiä, T. Berger, G. Reitz, and R. F. Wimmer-Schweingruber (2012), Assessment of galactic cosmic ray models, *Journal of Geophysical Research*, 117, A08109, doi:10.1029/2012JA017611.
- Prettyman, T. H., W. V. Boynton, W. C. Feldman, S. Karunatillake, D. J. Lawrence, S. Maurice, M. T. Mellon, A. E. Metzger, G. W. McKinney, J. R. Murphy, R. D. Starr, S. W. Squyres, and R. L. Tokar (2004), Composition and structure of the martian surface at high southern latitudes from neutron spectroscopy, *Journal of Geophysical Research*, 109, E05001, doi:10.1029/2003JE002139.
- Prettyman, T. H., W. C. Feldman, H. Y. McSween Jr., R. D. Dingler, D. C. Enemark, D. E. Patrick, S. A. Storms, J. S. Hendricks, J. P. Morgenthaler, K. M. Pitman, and R. C. Reedy (2011), Dawn's Gamma Ray and Neutron Spectrometer, *Space Science Reviews*, 163, doi: 10.1007/s11214-011-9862-0.
- Rao, U. R. (1971), Solar modulation of galactic cosmic radiation, *Space Science Reviews*, 12,

719-809.

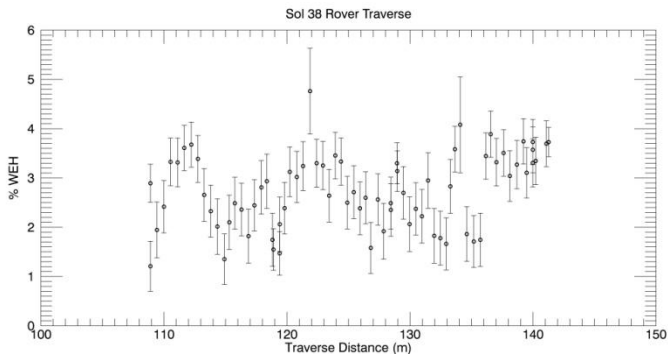
- Rasool, S.I., and C. De Bergh (1970), The Runaway Greenhouse and the Accumulation of CO<sub>2</sub> in the Venus Atmosphere, *Nature*, 226, 1037-1039.
- Schorghofer, N., and O. Aharonson (2005), Stability and exchange of subsurface ice on Mars, *Journal of Geophysical Research*, 110, E05003, doi:10.1029/2004JE002350.
- Simpson, J. A. (1983), Elemental and isotopic composition of the galactic cosmic rays, *Annual Reviews Nuclear Particle Science*, 33, 323-381.
- Tate, C.G., J. Moersch, E. Maclennan, I. Jun, C. Hardgrove, M. Mischna, M. Litvak, A. Varenikov, I. Mitrofanov, A. Behar, W. V. Boynton, L. Deflores, D. Drake, F. Fedosov, D. Golovin, K. Harshman, A. S. Kozyrev, D. Lisov, A. Malakhov, R. Milliken, M. Mokrousov, S. Nikiforov, A. B. Sanin, R. Starr, A. Vostrukhin, B. Ehresmann, F. J. Martin-Torres, and M. P. Zorzano (2015), Estimating Thermal Conductivity from MSL DAN Passive Data, Lunar and Planetary Science Conference, The Woodlands, Texas.
- Thomson, B.J., N.T. Bridges, R. Milliken, A. Baldrige, S.J. Hook, J.K. Crowley, G.M. Marion, C.R. de Souza Filho, A.J. Brown, and C.M. Weitz (2011), Constraints on the origin and evolution of the layered mound in Gale Crater, Mars using Mars Reconnaissance Orbiter data, *Icarus*, 214, 413-432, doi:10.1016/j.icarus.2011.05.002.
- Tylka, A.J., J. H. Adams, Jr., P. R. Boberg, B. Brownstein, W. F. Dietrich, E. O. Flueckiger, E. L. Petersen, M. A. Shea, D. F. Smart, and E. C. Smith (1997), CREME96: A Revision of the Cosmic Ray Effects on Micro-Electronics Code, *IEEE Transactions on Nuclear Science*, 44, 2150-2160.
- Vaniman D.T., D.L. Bish, D.W. Ming, T.F. Bristow, R.V. Morris, D. F. Blake, S. J. Chipera, S.M. Morrison, A.H. Treiman, E.B. Rampe, M. Rice, C.N. Achilles, J. Grotzinger, S.M. McLennan, J. Williams, J. Bell III, H. Newsom, R.T. Downs, S. Maurice, P. Sarrazin, A.S. Yen, J.M. Morookian, J.D. Farmer, K. Stack, R.E. Milliken, B. Ehlmann, D.Y. Sumner, G. Berger, J.A. Crisp, J.A. Hurowitz, R. Anderson, D. DesMarais, E.M. Stolper, K.S. Edgett, S. Gupta, and N. Spanovich (2014), Mineralogy of a Mudstone on Mars, *Science*, 343(6169), 1243480, doi:10.1126/science.1243480.
- Williams, R.M.E, J. Grotzinger, W. Dietrich, S. Gupta, D. Sumner, R. Wiens, N. Mangold, M. Malin, K. Edgett, S. Maurice, O. Forni, O. Gasnault, A. Ollila, H. Newsom, G. Dromart, M. Palucis, R. Yingst, R. Anderson, K. Herkenhoff, S. Mouélic, W. Goetz, M. Madsen, A. Koefoed, J. Jensen, J. Bridges, S. Schwenzer, K. Lewis, K. Stack, D. Rubin, L. Kah, J. Bell, J. Farmer, R. Sullivan, T. Van Beek, D. Blaney, O. Pariser, and R. Deen (2013), Martian Fluvial Conglomerates at Gale Crater, *Science*, 340, 1068-1072, doi:10.1126/science.1237317.

## Appendix

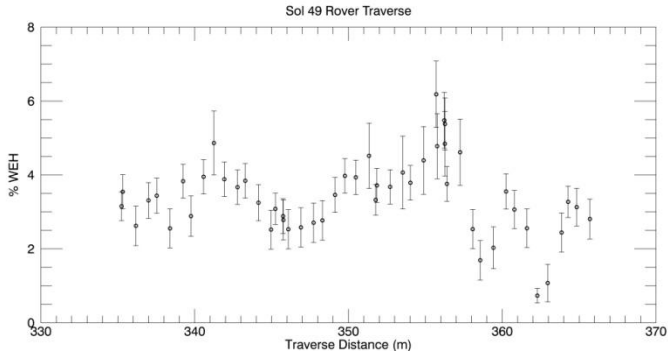
All figures shown here are not included in the manuscript due to space constraints. Supplementary Figure A.2.1 pertains to the WEH estimates of fixed locations during the time period. The results shown in Supplementary Figure A.2.1 are the same results shown in Figure 2.12 in the manuscript, but plotted versus rover traverse distance here. The rest of the figures are individual DAN passive traverse WEH estimates that have not been shown in the manuscript due to space constraints, but are shown here in order for all of our results to be available to the reader. These results, however, are included in the discussion of results section within the manuscript. These figures are analogous to Figures 2.14 and 2.15 in the manuscript, but cover results from different sols/traverses. All of these results are available in the manuscript in a compressed form in Figure 2.13. For WEH estimates from the traverses on sols 48 and 102, see Figures 2.14 and 2.15 in the manuscript.



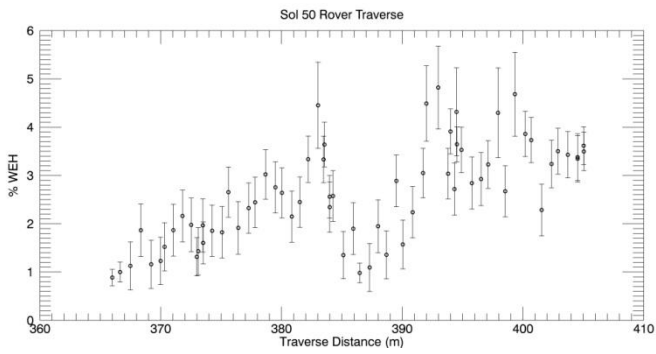
**Supplementary Figure A.2.1. DAN passive WEH estimates for fixed locations plotted as a function of odometry. This figure is complementary to Figure 2.9 in the manuscript.**



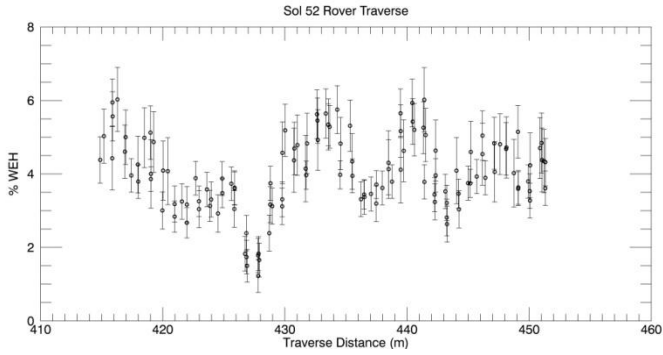
**Supplementary Figure A.2.2. DAN passive WEH estimates for rover traverse on sol 38.**



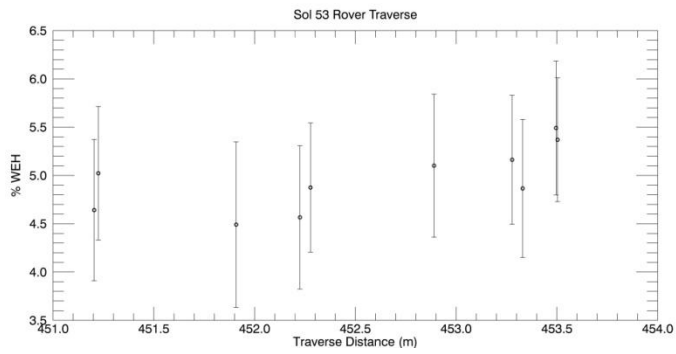
**Supplementary Figure A.2.3. DAN passive WEH estimates for rover traverse on sol 49.**



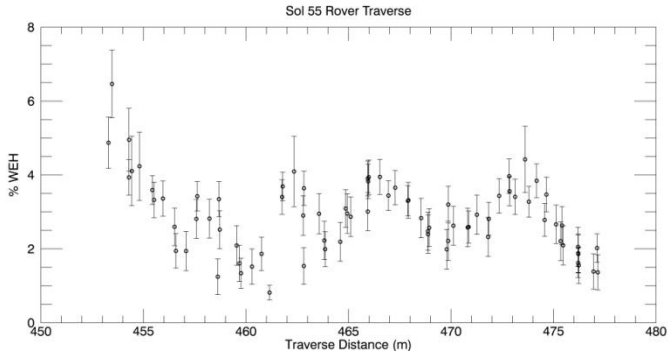
**Supplementary Figure A.2.4. DAN passive WEH estimates for rover traverse on sol 50.**



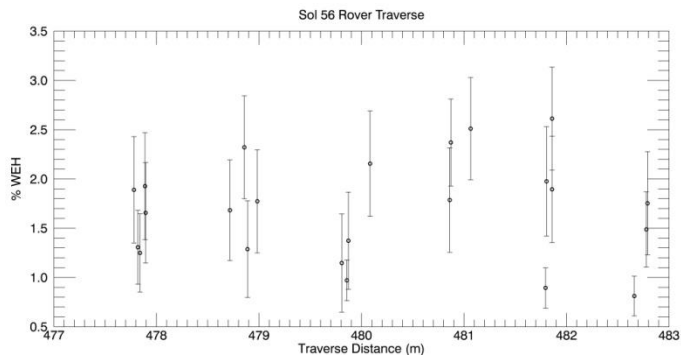
**Supplementary Figure A.2.5. DAN passive WEH estimates for rover traverse on sol 52.**



**Supplementary Figure A.2.6. DAN passive WEH estimates for rover traverse on sol 53.**

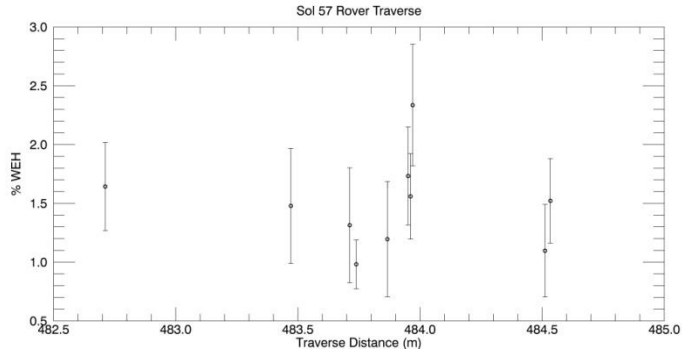


**Supplementary Figure A.2.7. DAN passive WEH estimates for rover traverse on sol 55.**

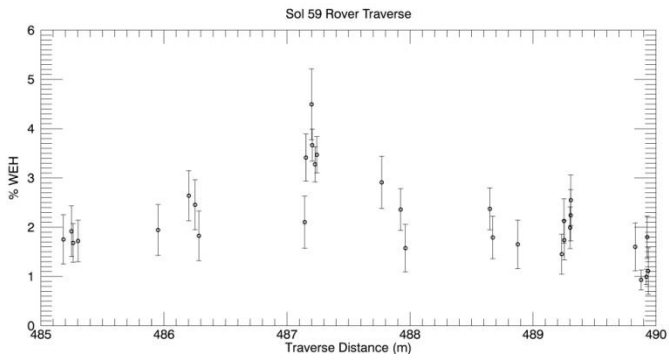


**Supplementary Figure A.2.8. DAN passive WEH estimates for rover traverse on sol 56.**

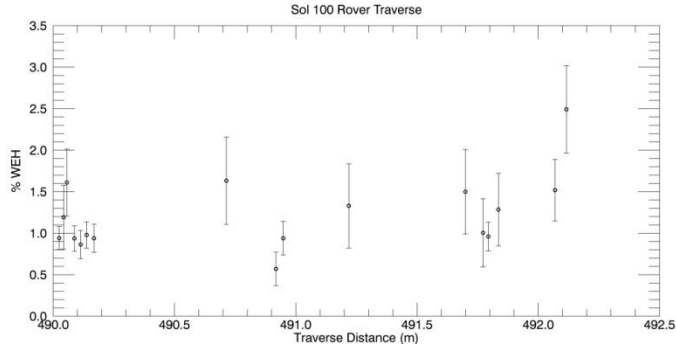




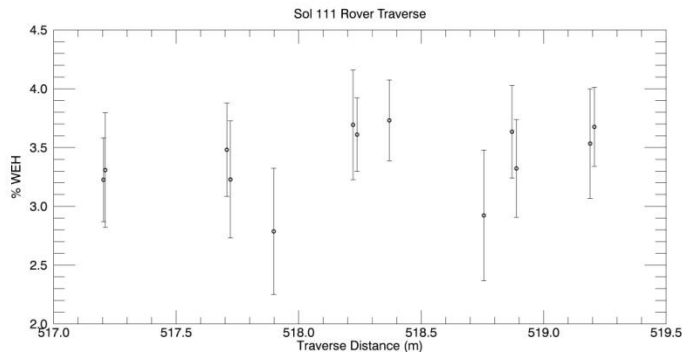
**Supplementary Figure A.2.9. DAN passive WEH estimates for rover traverse on sol 57.**



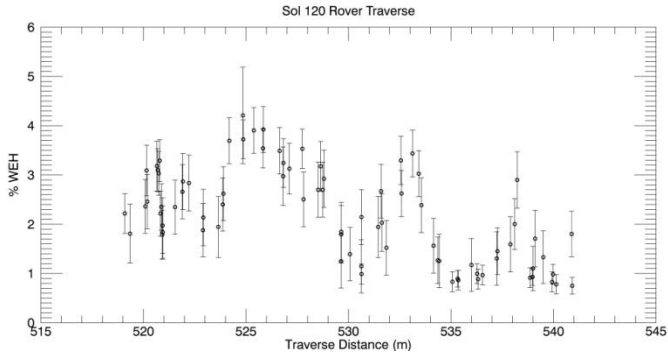
**Supplementary Figure A.2.10. DAN passive WEH estimates for rover traverse on sol 59.**



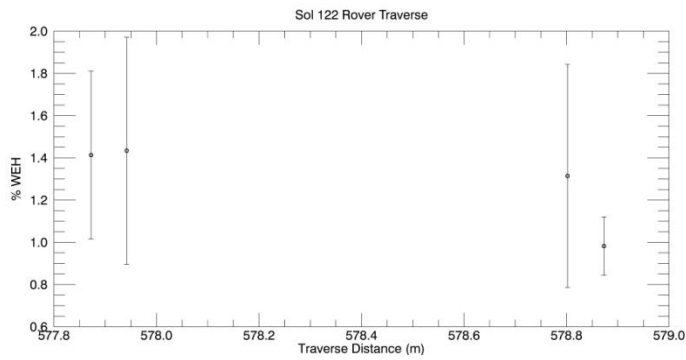
**Supplementary Figure A.2.11. DAN passive WEH estimates for rover traverse on sol 100.**



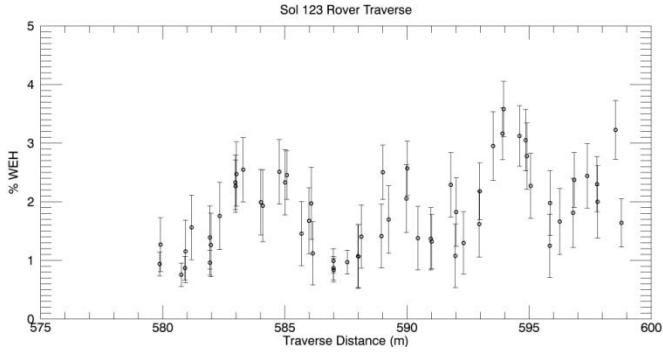
**Supplementary Figure A.2.12. DAN passive WEH estimates for rover traverse on sol 111.**



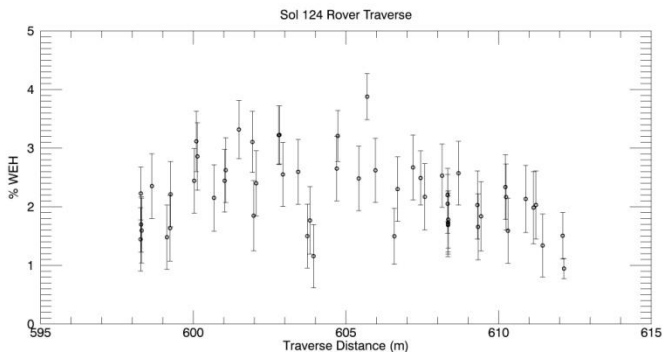
**Supplementary Figure A.2.13. DAN passive WEH estimates for rover traverse on sol 120.**



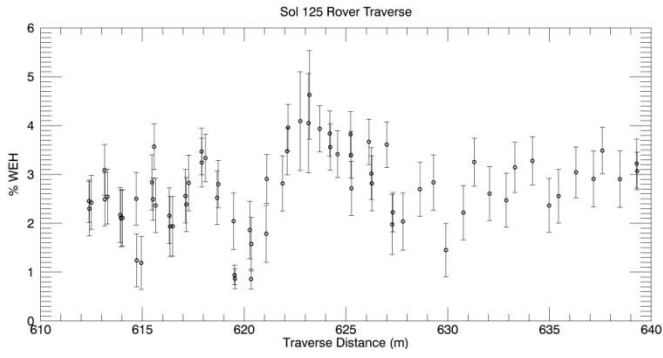
**Supplementary Figure A.2.14. DAN passive WEH estimates for rover traverse on sol 122.**



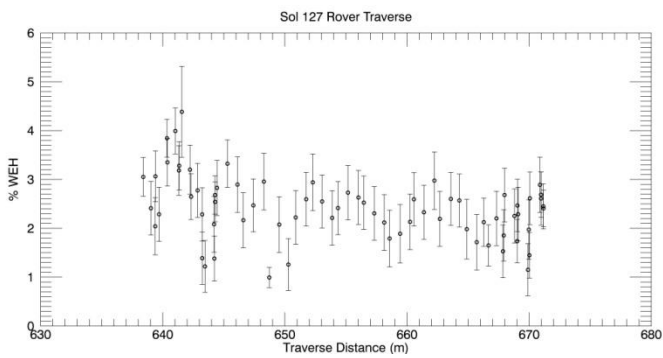
**Supplementary Figure A.2.15. DAN passive WEH estimates for rover traverse on sol 123.**



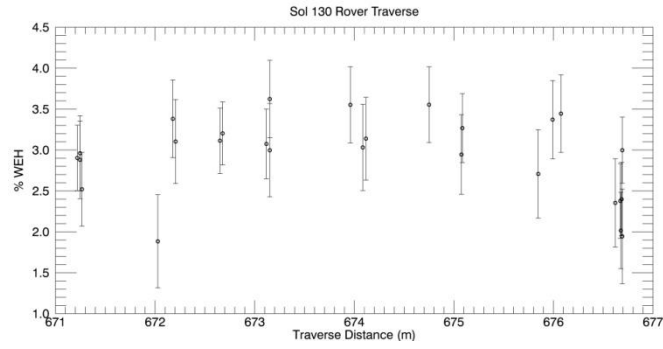
**Supplementary Figure A.2.16. DAN passive WEH estimates for rover traverse on sol 124.**



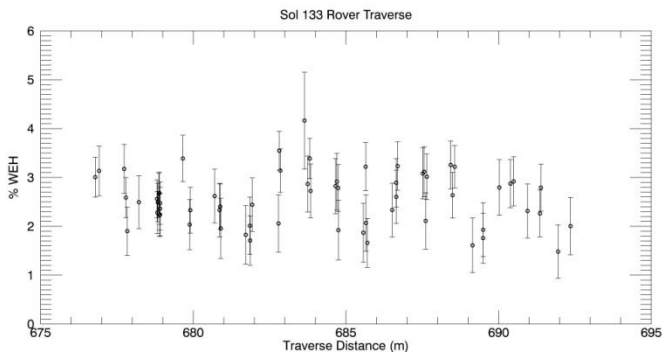
**Supplementary Figure A.2.17. DAN passive WEH estimates for rover traverse on sol 125.**



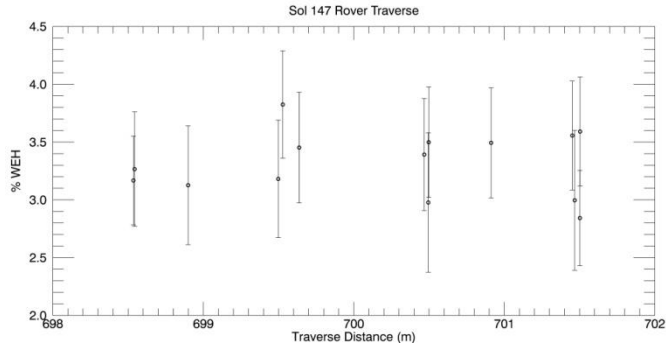
**Supplementary Figure A.2.18. DAN passive WEH estimates for rover traverse on sol 127.**



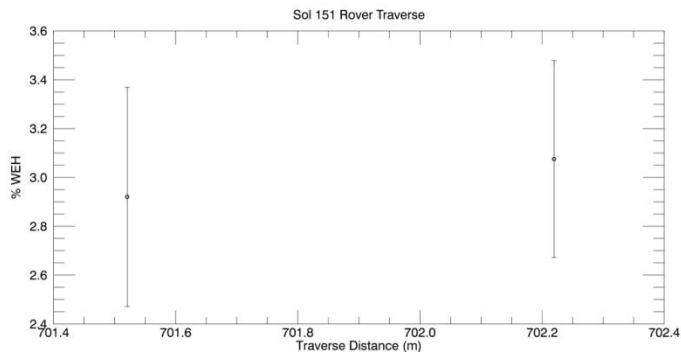
**Supplementary Figure A.2.19. DAN passive WEH estimates for rover traverse on sol 130.**



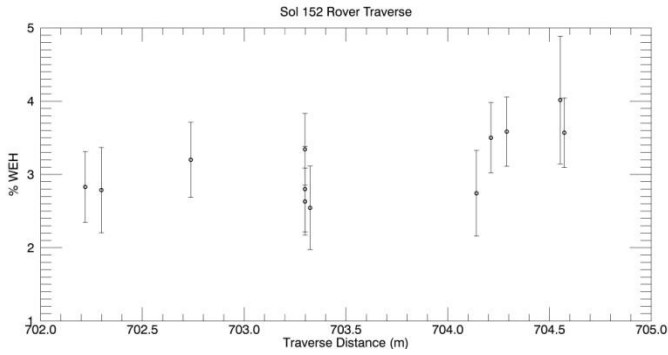
**Supplementary Figure A.2.20. DAN passive WEH estimates for rover traverse on sol 133.**



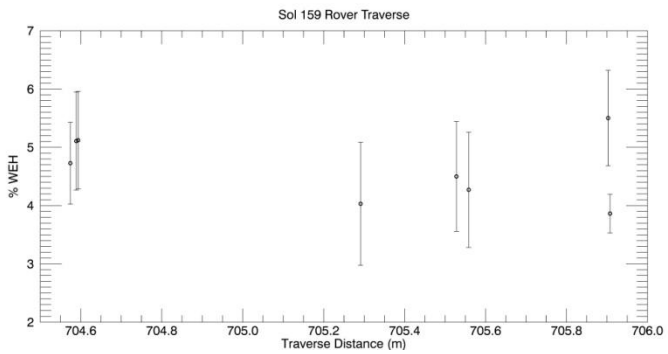
**Supplementary Figure A.2.21. DAN passive WEH estimates for rover traverse on sol 147.**



**Supplementary Figure A.2.22. DAN passive WEH estimates for rover traverse on sol 151.**

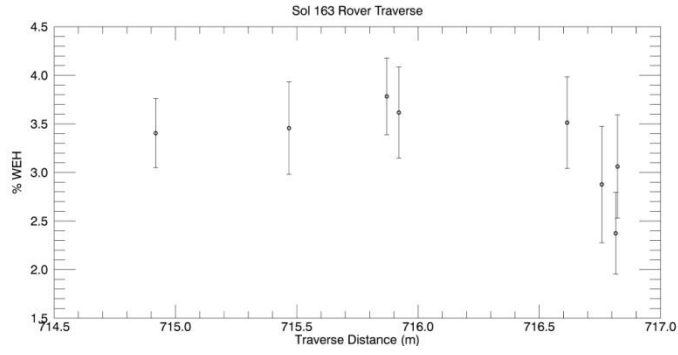


**Supplementary Figure A.2.23. DAN passive WEH estimates for rover traverse on sol 152.**

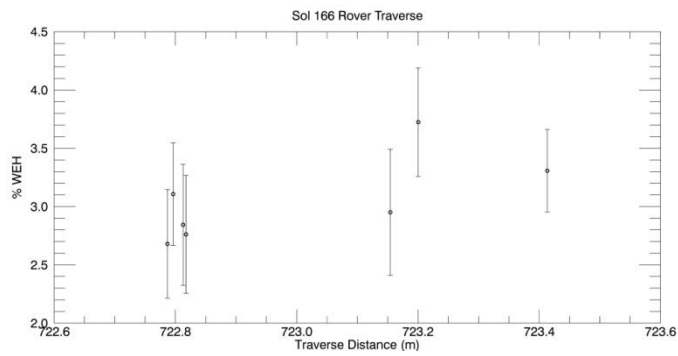


**Supplementary Figure A.2.24. DAN passive WEH estimates for rover traverse on sol 159.**





**Supplementary Figure A.2.25. DAN passive WEH estimates for rover traverse on sol 163.**



**Supplementary Figure A.2.26. DAN passive WEH estimates for rover traverse on sol 166.**

**CHAPTER III**  
**INVESTIGATION OF WATER EQUIVALENT HYDROGEN**  
**ABUNDANCES AND VARIATIONS WITHIN THE SHALLOW**  
**SUBSURFACE OF THE GALE CRATER FLOOR**

A version of this chapter has been submitted by Christopher G. Tate *et al.*:

Tate, C.G., J. Moersch, I. Jun, I. Mitrofanov, M. Litvak, P. Bellutta, W.V. Boynton, D. Drake, B. Ehresmann, F. Fedosov, D. Golovin, C. Hardgrove, K. Harshman, D. M. Hassler, A.S. Kozyrev, R. Kuzmin, D. Lisov, A. Malakhov, R. Milliken, M. Mischna, M. Mokrousov, S. Nikiforov, A.B. Sanin, R. Starr, A. Vostrukhin, and C. Zeitlin (2017), Results from the Dynamic Albedo of Neutrons (DAN) Passive Mode Experiment: Yellowknife Bay to Amargosa Valley (sols 201 - 753), *Icarus*, submitted.

The student (Christopher G. Tate) is the lead author and researcher of this work. This article has been submitted to the journal *Icarus* and is currently under peer review. All co-researchers listed are members of the Mars Science Laboratory Dynamic Albedo of Neutrons team and Radiation Assessment Detector team and have varying levels of involvement in this work. Most co-authors only contributed directly through instrument pre-flight building and testing and or surface operations. J. Moersch, B. Ehresmann, and I. Jun have the most involvement with this project, helping with simulation creation and verification and interpreting results. References to the manuscript in the following chapter and subsequent appendix refer to the main text of Chapter III presented here. The text has not been altered except for formatting changes.

## **Abstract**

The Mars Science Laboratory (MSL) (*Curiosity* rover) Dynamic Albedo of Neutrons (DAN) experiment detects neutrons for the purpose of searching for hydrogen in the shallow subsurface of Mars. DAN has two modes of operation, active and passive. In passive mode, the instrument detects neutrons produced by Galactic Cosmic Ray interactions in the atmosphere and regolith and by the rover's Multi-Mission Radioisotope Thermoelectric Generator. DAN passive data from Yellowknife Bay to Amargosa Valley (sols 201 through 753) are presented and

analyzed here. Water equivalent hydrogen (WEH) estimates from this portion of *Curiosity's* traverse range from 0.0 wt. % up to 15.3 wt. %. Typical uncertainties on these WEH estimates are ~0.5 wt. % but in some cases can be as high as ~4.0 wt. % depending on the specific circumstances of a given measurement. Here we also present a new way of reporting results from the passive mode of the experiment, the DAN passive geochemical index (DPGI). This index is sensitive to some key geochemical variations, but it does not require assumptions about the abundances of high thermal neutron absorption cross section elements, which are needed to estimate WEH. DPGI variations in this section of the traverse indicate that the shallow regolith composition is changing on both the local (~meters) and regional (~100s of meters) scales. This variability is thought to be representative of the diverse composition of source regions for sediments within the crater floor, which is consistent with results from other MSL instruments (Thompson *et al.*, 2016). Kolmogorov-Smirnov Tests on the populations of WEH estimates and DPGI values demonstrate there are statistically significant differences between nearly all of the geologic units investigated along the rover's traverse. We also present updated previous DAN passive results from Bradbury Landing to John Klein that make use of revised DAN active mode results for calibration, however, no qualitative changes in the interpretations made in Tate *et al.* (2015b) are incurred.

## Introduction

The Dynamic Albedo of Neutrons experiment (DAN) on the Mars Science Laboratory (MSL) rover *Curiosity* has been operating successfully on the surface of Mars since landing in Gale Crater on August 6<sup>th</sup>, 2012. In that time, DAN has contributed to the mission's success in completing one of its primary mission objectives of finding a habitable environment (Grotzinger *et al.*, 2012; Grotzinger *et al.*, 2014). DAN measurements constrain the bulk composition of the shallow regolith of Gale crater, specifically, the amount of water equivalent hydrogen (WEH) and absorption equivalent chlorine (AEC) (Mitrofanov *et al.*, 2014; Tate *et al.*, 2015b). For a discussion of results from the DAN active experiment, see Mitrofanov *et al.* (2014), Mitrofanov *et al.* (2016a), Litvak *et al.* (2014), and Litvak *et al.* (2016). Tate *et al.* (2015b) present DAN passive results and WEH estimates from the start of the surface mission at Bradbury Landing (sol 0 of the mission) to John Klein sol (200), and the present work extends this analysis of DAN passive data to Amargosa Valley (sol 753). Also of interest, Jun *et al.* (2013) discuss DAN passive measurements in relation to the martian radiation environment.

In its active mode of operation, the DAN experiment utilizes a pulse neutron generator (PNG) and two  $^3\text{He}$  proportional counters called the detector element (DE), to constrain the abundance of subsurface hydrogen. The DE detects neutrons via the reaction  $n + ^3\text{He} \rightarrow ^3\text{H} + ^1\text{H} + 0.764 \text{ MeV}$  (Batchelor *et al.*, 1955). One of the counters in the DE, known as the counter of total neutrons (CTN), is capable of detecting neutrons over a broad spectrum of energies ( $< 0.1 \text{ MeV}$ ), however, its detection efficiency above 1 keV is very low (Litvak *et al.*, 2008). The other counter in the DE, known as the counter of epithermal neutrons (CETN), is covered with a thin (1 mm-thick) jacket of cadmium that absorbs neutrons with energies below  $\sim 0.4 \text{ eV}$  and therefore only counts neutrons with energies above this "Cd cutoff" (Litvak *et al.*, 2008). The

count rates in each detector are differenced to produce thermal neutron count rates, which in the context of the DAN instrument refers to neutrons below the Cd cutoff energy.

The DAN passive mode of operation does not make use of the PNG, but rather relies on signal from two lower-intensity, continuous sources of neutrons: the MSL Multi-Mission Radioisotope Thermoelectric Generator (MMRTG), which produces neutrons as a byproduct of its plutonium fuel decay, and galactic cosmic rays (GCR), which spallate neutrons through nuclear interactions in the atmosphere and subsurface. The DE detects the leakage flux of neutrons, which is used (along with models of the bulk geochemical composition) to infer the water equivalent hydrogen (WEH) content of the shallow regolith. Although DAN is the first neutron remote sensing experiment on the surface of Mars, the High Energy Neutron Detector (HEND) (Mitrofanov *et al.*, 2002) and Neutron Spectrometer (NS) onboard Mars Odyssey (Feldman *et al.*, 2002) have produced global maps of WEH from orbit. As will be discussed, there are salient differences between the analysis of neutron remote sensing data acquired from orbit versus those acquired by DAN on the surface including the spatial footprint, the contribution of neutrons from the MMRTG, and the associated characteristics of the epithermal neutron population (Tate *et al.*, 2015b).

After leaving John Klein, *Curiosity* drove a long distance (just under 9 km) to reach the lower units of Aeolis Mons (Mount Sharp), a primary mission goal, along a path referred to as the Rapid Traverse Route (RTR), seen in Figure 3.1 (Grotzinger *et al.*, 2015). On sol 753, *Curiosity* reached the proximal edge of the Pahrump Hills from within Amargosa Valley (Grotzinger *et al.*, 2015). This is the location of an exposed contact between the Bradbury group (Aeolis Palus) and the lower units of Mount Sharp, specifically the Murray formation, which represent different depositional environments (Grotzinger *et al.*, 2015). The MSL Science

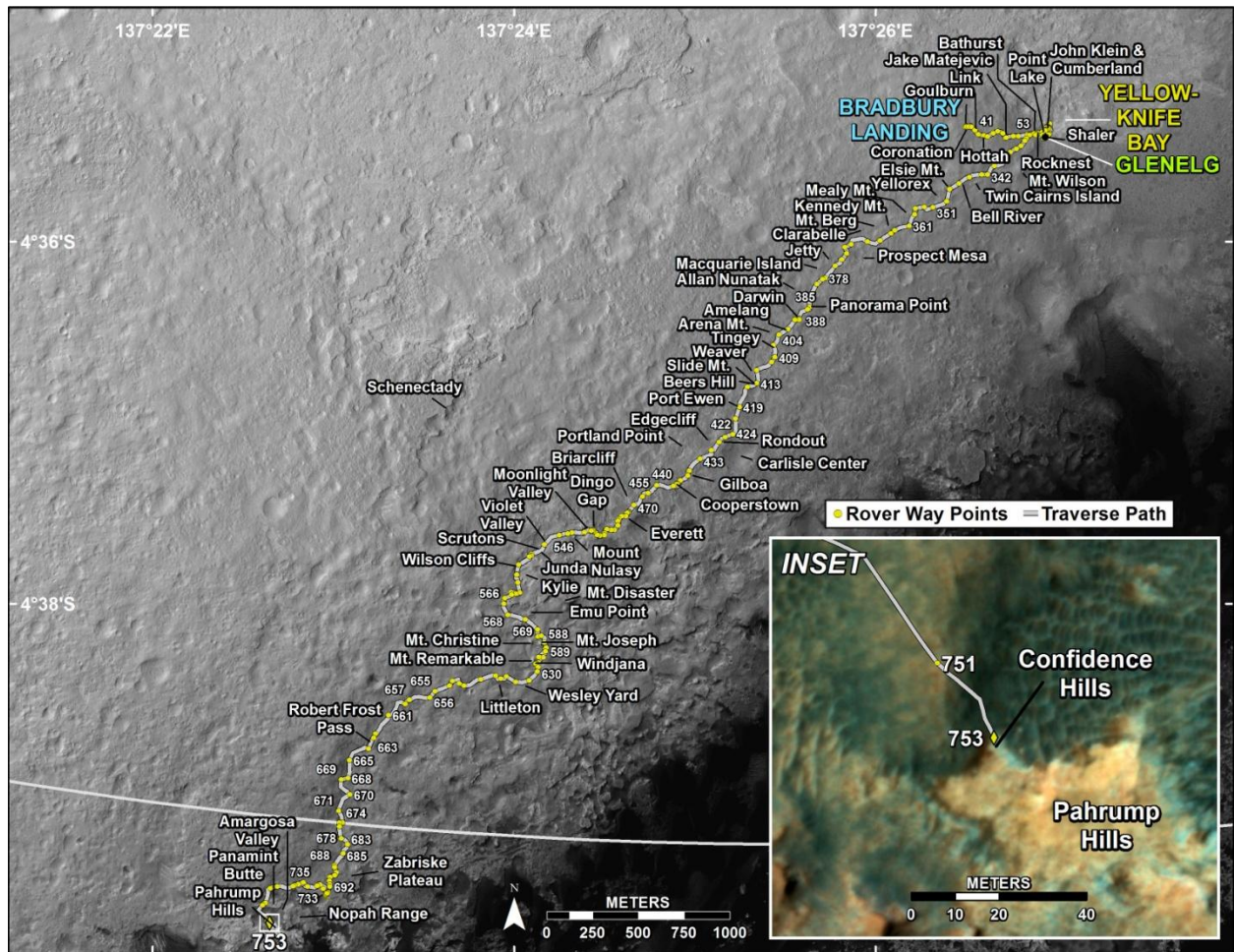


Figure 3.1. The focus of this paper is on DAN passive data along the RTR, which covers locations between Yellowknife Bay and Amargosa Valley. The white line is the lower extent of MSL's landing ellipse. Image Credit: NASA/JPL-Caltech/University of Arizona.

Team's focus on arriving at Pahrump Hills as quickly as possible resulted in fewer in-depth, multi-experiment investigations at waypoints along the traverse than in the preceding portion of the mission. Nevertheless, because the traverse took a long time and only a few geologic units observed in orbital data sets were crossed along the RTR, these units were well-sampled and characterized by *Curiosity's* payload. The units investigated with DAN passive measurements during this portion of the traverse were (as mapped by Calef *et al.* (2013)) the Smooth Hummocky Unit, the Bedded, Fractured Unit, the Eolian Unit, the Striated Light-toned Unit, and the Rugged Unit. In addition to presenting the first analyses of DAN passive results from Yellowknife Bay to Amargosa valley, we also present an update of DAN passive results from Bradbury Landing to John Klein that make use of revised DAN active mode results for calibration, though no qualitative changes in the interpretations of Tate *et al.* (2015b) are incurred.

## Methods

The DAN passive data analysis methods used here are the same as those described in Tate *et al.* (2015b), but with the addition of new DAN active calibration sites from the additional sols investigated. We have also applied corrections to the thermal neutron count rate data to account for changes in the geometry of the MMRTG and DAN DE relationship to the ground. As stated in Tate *et al.* (2015b), this is typically a small effect on WEH estimates and the methods used are described in the appendix to this manuscript. Our approach is to model the martian neutron leakage flux and the DAN detectors' response to it using different regolith compositions, and then compare these model results to DAN passive data in order to find the best



compositional fit. We model the martian neutron leakage flux in the vicinity of the DAN detectors using the Monte Carlo Neutron Particle eXtended code (MCNPX) (McKinney *et al.*, 2006) for transport and interactions of high energy protons and neutrons. We independently model the neutrons sourced from the MMRTG and those sourced from the GCR in order to understand the different contributions to the final neutron leakage flux and to simplify individual computational processes.

The GCR component of the model is further broken down into two scales; a global-scale model that includes the bulk of the atmosphere and a local-scale model, in the near vicinity of the rover that includes atmosphere, regolith, a rover mass model, and DAN DE. This is necessary because the volumes of the DAN detectors are extremely small compared to the volume of Mars and its atmosphere. A single model combining both scales would result in very poor statistics for predicted neutron count rates in the DAN detectors. The global-scale model includes transport and interactions of primary GCR protons and resulting secondary particles that can contribute to the neutron flux, specifically keeping track of the energy and directional distributions of the particles in question. The flux of particles exiting the lower boundary of the global-scale model are used as the particle source for the local-scale model. This model provides an estimate of the GCR-sourced neutron leakage flux at the DAN detectors and their response. The model that estimates the neutron leakage flux due to the presence of the MMRTG utilizes the same geometry as the GCR local-scale model described above, however this model uses the MMRTG neutron spectrum as its source. A full description of the MCNPX models utilized can be found in Tate *et al.* (2015b) and a description of the MMRTG source and rover mass model can be found in Jun *et al.* (2013).

The composition of the regolith can be systematically varied within these models in order

to build a library of model results to compare to the data. The regolith within the model is assumed to be homogenous in composition both vertically and laterally. While more complicated geometries can be modeled, we compare to the simplest assumptions to obtain a bulk regolith composition because DAN passive measurements lack sufficient free parameters to differentiate between simple and complicated geometries. All of our compositional models use the same "background" composition meant to represent the martian regolith, but with varying amounts of hydrogen (WEH) and chlorine. Following the convention adopted in previous DAN analyses (Mitrofanov *et al.*, 2014; Tate *et al.*, 2015b), all absorbers are represented in bulk by the AEC quantity. Also, following the precedent established in prior work, the generic martian regolith composition for elements other than hydrogen and chlorine was taken from the Mars Exploration Rovers (MER) Alpha Particle X-ray Spectrometer (APXS) Gusev average soil composition (McSween *et al.*, 2010). WEH content and AEC are systematically varied against this background composition in order to build a suite of model results for comparison to the data when estimating WEH content.

MCNPX provides its results as fractional probabilities per source particle. Thus when combining model results from multiple sources, scale factors must be applied to account for differences in the intensities of these sources. The scale factor for the MMRTG model was calculated pre-launch by Jun *et al.* (2013) to be  $1\text{E}+7$  neutrons per second. This is modified based on degradation of the MMRTG neutron output using its radioactive half-life, however, the half-life of  $^{238}\text{Pu}$  is 87.7 years and thus this is a nearly negligible effect as of sol 753 in the mission.

Scaling the GCR model is more complicated because it requires an accurate description of the radiation environment reaching the surface of Mars which is not constant in time and

difficult to constrain due to inherent uncertainties in the free space GCR environment at Mars (Mrigakshi *et al.*, 2012; Ehresmann *et al.*, 2014). In order to produce applicable DAN GCR scale factors for any time in the mission, we use both *in situ* calibrations from other MSL results and Radiation Assessment Detector (RAD) penetrating counter data which are sensitive to high energy GCRs reaching the martian surface. In our previous work (Tate *et al.*, 2015b), this scaling was performed using results from calibration locations visited during the first 200 sols of the mission. The scaling determines the overall magnitude of the GCR-sourced neutrons at the calibration locations. Using the known RAD penetrating counter measurements for these locations, a conversion factor between the DAN GCR scale factors and RAD penetrating counter data is calculated, which can be used to calculate GCR scale factors for any given time based on the associated RAD penetrating counter data.

In the present work, we have included additional DAN active results in our calibration scheme. The additional DAN active measurement locations that met our criteria for calibration sites (described in Tate *et al.*, 2015b) were measured on sols 455- 465, sol 568, sol 663, sol 677, and sol 735. We derived a DAN GCR scale factor and a corresponding RAD-DAN conversion factor at each of these sites using the method described above. Using the calibration scheme and the 8 calibration sites throughout the mission, we compute the average RAD-DAN conversion factor from RAD penetrating counter data to the GCR scale factors. The relationship between the GCR scale factor and the RAD penetrating counter data is represented by the equation

$$F_{GCR,RAD} = A * R_S, \tag{1}$$

where  $A$  is the aforementioned conversion factor calculated through the calibration,  $R_S$  is the time varying RAD penetrating counter measurement, and  $F_{GCR,RAD}$  is the corresponding DAN GCR scale factor. Note that the form of equation 1 is different from that used in Tate *et al.*,

2015b, where the RAD-DAN conversion factor was estimated with a linear fit across the three calibration sites. In the present work, we simply take the average of all 8 calibration sites because no linear trends were observed in the larger sets of calibration sites.

Using Equation 1 with the calculated RAD-DAN conversion factor and associated RAD penetrating counter data captures the temporal variations in the primary GCR environment that affect the production of neutrons within the martian regolith and allows one to scale simulation results according to those changes to accurately predict DAN passive count rates. Figure 3.2 shows the RAD penetrating counter data and the generated DAN GCR scale factors ( $F_{GCR,RAD}$ ) from sols 0 to 753 of the mission.

It is worth noting that our scaling strategy could still be used in the event that the DAN PNG fails (Litvak *et al.*, 2008) and no further DAN active calibration sites are available. If this happens, the 8 existing calibration sites combined with ongoing RAD penetrating counter measurements can be used to characterize the effect of the time variable GCR environment on DAN passive WEH estimates. Thus, DAN passive mode data will continue to have scientific value even after the DAN PNG ceases to function (Litvak *et al.*, 2008).

Lastly, obtaining DAN passive WEH estimates requires an estimate of the AEC abundance within the regolith for a given location. Here we use the most recent DAN active derived results for AEC abundances (Mitrofanov *et al.*, in prep) when analyzing the co-located DAN passive measurement. In order to analyze DAN passive data between these co-located measurements where we have no DAN active results or data from any other instrument to provide measured abundances of the relevant absorbing elements, we must also place reasonable constraints on the AEC abundance. In our previous work (Tate *et al.*, 2015b), we used a single AEC value at these locations that was the average of all DAN active AEC results acquired during

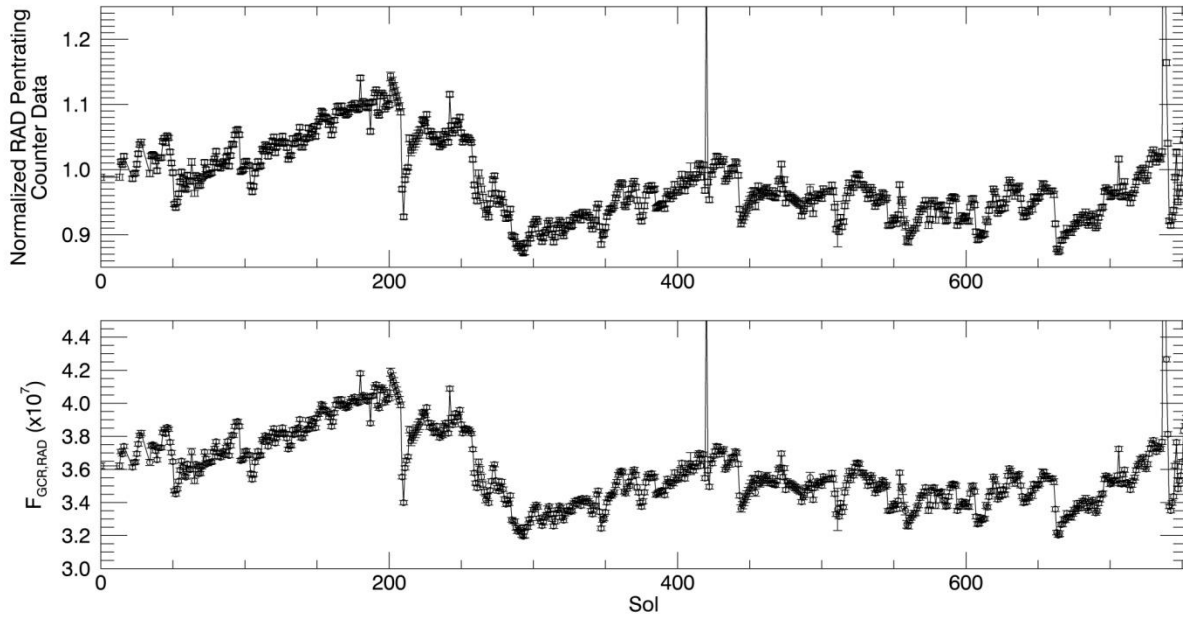


**Figure 3.2. Normalized RAD penetrating counter data from the start of the mission up through sol 753 are shown on the top panel. Calculated  $F_{\text{GCR,RAD}}$  scale factors from Equation 1 for use in analyzing DAN passive data are shown on the bottom panel. Plotted uncertainties are derived from RAD counting statistics only.**

the first 200 sols of the traverse (Mitrofanov *et al.*, 2014). In the present work, we have instead used AEC values along the traverse that are computed by interpolating between AEC abundances derived from the nearest DAN active measurements. The reason we have not used a single average value for the traverse data in the present work is that it is simply too large of a region with too much variability in the AEC abundances. Previously, in Tate *et al.* (2015b) the traverse distance (less than 1 km) and the variability of AEC ( $0.65 \pm 0.04$  to  $1.60 \pm 0.11$  wt %) were both relatively small compared to the length of the traverse (~9.5 km) and the variability of AEC ( $0.05 \pm 0.02$  to  $2.45 \pm 0.33$  wt %) for the traverse section analyzed here.

## Data

DAN passive measurements are separated into two categories for this analysis, referred to as “fixed location” measurements and “traverse” measurements. Fixed location measurements take place at locations where the rover has stopped and acquired measurements with other instruments, including DAN active mode measurements. Traverse measurements are acquired continuously during rover traverse segments between the fixed locations, and are not complemented by co-located compositional measurements from other instruments. Fixed location measurements have the advantage that other, co-located measurements can provide constraints on their interpretation, whereas traverse measurements are useful in that they provide some insight into compositional variations along the traverse where there are few other measurements to draw upon. Traverse measurements actually make up the bulk of the DAN passive data set with 23,183 distinct locations investigated with traverse measurements versus 234 separate fixed locations investigated.

### ***Fixed Location Data***

DAN acquires data in both the CTN and CETN counters in 20-second integration bins. The count rates from each of the counters are differenced to produce thermal neutron count rates. The thermal neutron count rates measured at fixed locations for sols 0 to 753 are shown in Figure 3.3 and their averages by location are shown in Figure 3.4. Table 3.1 shows the observational circumstances, measurements, and results used in further analysis for these locations including the average thermal neutron count rate, average epithermal neutron count rate, AEC wt. %, and the average  $F_{GCR,RAD}$  for a given location. *Curiosity* has investigated 234 separate fixed locations from sol 0 to 753 with a total integration time at all of these locations of 9,535,740 seconds. *Curiosity's* primary task after leaving John Klein was to drive toward Mount Sharp nearly every sol, so the typical cadence of DAN passive observations at fixed locations was to acquire measurements upon arriving at a location in the afternoon and then again shortly prior to departing that location the following morning. For fixed locations beyond John Klein (sols 273 and higher), total integration times ranged from 2,040 seconds (sol 297) to 402,340 seconds (sols 609-630).

Substantial variation occurs in the thermal neutron count rates. On the other hand very little variation occurs in the epithermal neutron count rates (Jun *et al.*, 2013; Tate *et al.*, 2015b). As shown by Jun *et al.* (2013), the epithermal neutron population is constantly replenished by MMRTG-produced high-energy neutrons down-scattering into the epithermal energy range creating a dynamic equilibrium. It is also shown that the epithermal neutrons are dominated by MMRTG-produced neutrons and many of these epithermal neutrons interact directly with the detectors or the rover body before being detected, without ever reaching the regolith such that these neutrons can carry no signature of the regolith composition (Jun *et al.*, 2013). While the GCR-induced epithermal neutrons behave as expected with respect to varying WEH abundance

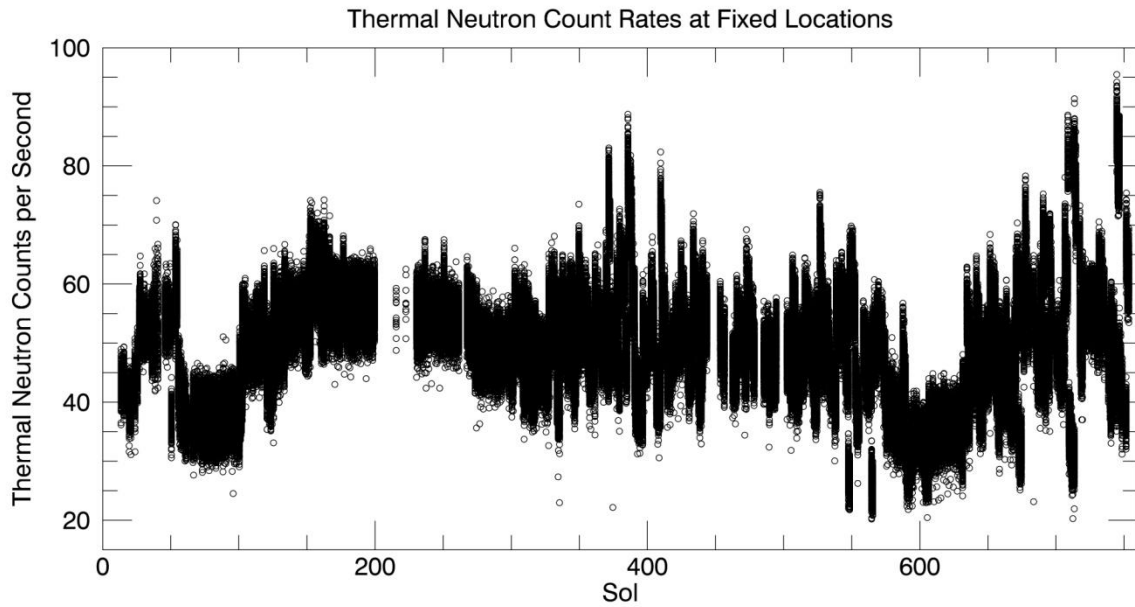


**Figure 3.3. DAN thermal neutron count rates acquired at fixed locations for sols 0 through 753. Thermal neutron count rates are produced by differencing the CTN and CETN neutron count rates. Uncertainties in count rates are calculated from Poisson statistics and are not shown here for clarity, but are calculated by the square root of the count rate.**



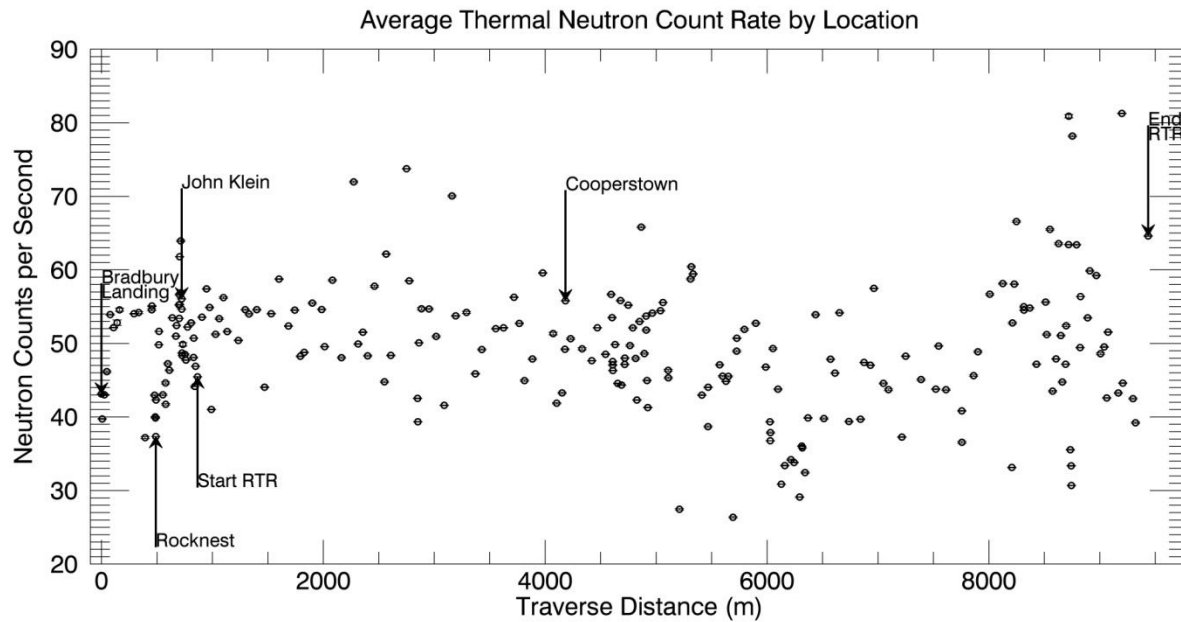


**Figure 3.4. DAN thermal neutron count rates are shown for fixed locations, averaged by location and plotted versus traverse distance in meters. Shown uncertainties are calculated from Poisson statistics, but are small because of the long duration of the integration times at these locations. Key reference locations are indicated with arrows.**

**Table 3.1. The observational circumstances, DAN passive measurements, and constraints from other measurements used in further analysis of fixed locations where the rover acquired DAN passive data between Bradbury Landing (sol 0) and Amargosa Valley (sol 753).**

Observational Circumstances				DAN Passive Measurements		Constraints from other Measurements		Comments
Sols	Traverse Distance (m)	Latitude (S) (deg)	Longitude (E) (deg)	Average Thermal Neutron Count Rate (n/s)	Average Epithermal Neutron Count Rate (n/s)	Absorption Equivalent Chlorine from DAN Active (wt. %)	Location-averaged $F_{GCR,RAD}$ (source particles/ second)	
0-15	0	-4.589467	137.441633	43.13±.06	23.17±.03	1.30±0.05	3.64E+07±3.09E+06	Bradbury Landing
17-21	7	-4.589465	137.441734	39.73±.08	24.4±.04	1.35±0.06	3.67E+07±4.42E+05	
22-23	27	-4.589403	137.441892	43.01±.09	24.89±.05	1.25±0.06	3.64E+07±1.31E+05	
24-26	48.5	-4.589447	137.442181	46.16±.12	24.63±.06	1.35±0.03	3.69E+07±1.34E+05	
26-29	78.6	-4.589750	137.442476	53.93±.08	25.99±.04	1.05±0.05	3.78E+07±9.26E+04	Near Link
29-37	109.1	-4.590137	137.442786	52.15±.04	25.74±.02	0.85±0.03	3.73E+07±2.13E+05	CAP2
38	141.5	-4.590244	137.443302	52.81±.37	25.55±.19	0.65±0.04	3.71E+07±1.33E+05	Near Hottah
39	163.2	-4.590319	137.443663	54.56±.2	25.08±.1	0.80±0.05	3.69E+07±9.23E+04	
45	293.8	-4.590435	137.445348	54.04±.05	24.75±.03	0.85±0.05	3.82E+07±6.55E+04	
49	335.24	-4.590306	137.446506	54.2±.14	24.66±.07	0.80±0.04	3.70E+07±1.29E+05	
50	392.3	-4.590176	137.447304	37.19±.14	24.11±.07	0.75±0.08	3.65E+07±1.28E+05	Forbush decrease in GCR
52	453.3	-4.590062	137.4479	54.57±.14	24.86±.07	1.05±0.06	3.48E+07±1.25E+05	
54	455	-4.590066	137.44794	55.09±.06	25.92±.03	1.05±0.04	3.54E+07±7.23E+04	
55	479.1	-4.590063	137.448297	42.96±.09	25.48±.05	1.05±0.07	3.62E+07±8.93E+04	Near Bathurst
57	485.1	-4.590017	137.448351	40.01±.06	24.36±.03	1.05±0.02	3.63E+07±8.94E+04	
59	486.9	-4.590020	137.448339	39.87±.04	24.62±.02	1.05±0.06	3.58E+07±7.24E+04	

**Table 3.1. Continued.**

Sols	Traverse Distance (m)	Latitude (S) (deg)	Longitude (E) (deg)	Average Thermal Neutron Count Rate (n/s)	Average Epithermal Neutron Count Rate (n/s)	Absorption Equivalent Chlorine from DAN Active (wt. %)	Location-averaged $F_{GCR,RAD}$ (source particles/ second)	Comments
59-100	490	-4.589996	137.448342	37.34±.01	24.49±.01	1.05±0.03	3.69E+07±2.13E+04	Rocknest
100-102	491.9	-4.590022	137.44831	42.31±.04	26.19±.02	0.80±0.05	3.70E+07±7.41E+04	
102-111	517.2	-4.589948	137.448695	49.81±.03	25.3±.02	1.55±0.02	3.65E+07±4.03E+04	Near Point Lake
111-120	519.1	-4.589922	137.448676	51.64±.02	25.66±.01	1.60±0.11	3.79E+07±4.34E+04	Near Point Lake
120-121	553.7	-4.590442	137.448828	43.01±.1	25.36±.05	1.40±0.13	3.80E+07±9.33E+04	Near Shaler
121-122	577.9	-4.590282	137.449107	44.63±.13	26.61±.07	1.30±0.16	3.78E+07±9.18E+04	
122-123	578.9	-4.590275	137.44912	41.72±.09	24.56±.05	1.60±0.15	3.80E+07±9.26E+04	
123-124	598.3	-4.590054	137.449349	47.24±.11	24.73±.06	1.60±0.07	3.81E+07±9.39E+04	
124-125	612.3	-4.589866	137.449277	46.35±.07	24.44±.03	1.05±0.1	3.82E+07±9.39E+04	
125-127	638.4	-4.589637	137.449331	53.48±.04	25.98±.02	0.85±0.06	3.83E+07±7.59E+04	
127-130	671.2	-4.589231	137.449383	50.99±.04	25.33±.02	0.95±0.01	3.79E+07±6.48E+04	
130-133	676.8	-4.589137	137.449388	52.44±.04	25.61±.02	0.95±0.08	3.76E+07±6.46E+04	
133-147	698.8	-4.589463	137.449258	55.23±.03	25.29±.01	0.95±0.02	3.84E+07±3.36E+04	
147-151	701.5	-4.589506	137.449235	53.4±.03	24.82±.01	0.85±0.06	3.90E+07±5.88E+04	
151-152	702.2	-4.589516	137.449231	56.64±.07	27.22±.04	0.95±0.03	3.94E+07±9.39E+04	

**Table 3.1. Continued.**

Sols	Traverse Distance (m)	Latitude (S) (deg)	Longitude (E) (deg)	Average Thermal Neutron Count Rate (n/s)	Average Epithermal Neutron Count Rate (n/s)	Absorption Equivalent Chlorine from DAN Active (wt. %)	Location-averaged $F_{GCR,RAD}$ (source particles/ second)	Comments
152-159	704.6	-4.589552	137.449223	61.79±.02	26.32±.01	0.95±0.04	3.96E+07±4.67E+04	
159-162	705.9	-4.589535	137.449238	55.28±.04	25.59±.02	0.80±0.05	3.91E+07±6.57E+04	
162	714.9	-4.589497	137.449218	63.94±.1	26.87±.05	0.85±0.06	3.94E+07±1.30E+05	
163-166	716.8	-4.589476	137.44912	56.89±.04	25.96±.02	0.75±0.03	4.00E+07±6.65E+04	
166-272	723.4	-4.589485	137.449129	56.06±.01	26.14±.01	0.90±0.03	4.03E+07±2.29E+04	John Klein
272-274	726.49	-4.589467	137.449116	48.7±.07	23.87±.04	0.80±0.06	3.59E+07±8.06E+04	
275-294	727.16	-4.589479	137.449112	48.36±.02	23.81±.01	0.85±0.05	3.35E+07±3.62E+04	Cumberland
297	733.46	-4.589502	137.449112	49.87±.22	25.46±.11	0.95±0.04	3.30E+07±1.36E+05	
297-298	753.27	-4.589571	137.449275	48.49±.08	25.6±.04	0.95±0.04	3.29E+07±9.52E+04	
299-301	761.70	-4.589661	137.449168	47.73±.06	26.44±.03	1.55±0.07	3.35E+07±8.16E+04	
302-307	776.46	-4.589779	137.448964	52.23±.03	26.52±.02	1.90±0.08	3.32E+07±5.53E+04	Point Lake Area
307-308	808.23	-4.590148	137.449275	52.8±.07	27.34±.04	2.05±0.06	3.30E+07±9.58E+04	
308-309	830.23	-4.590378	137.44905	48.09±.06	27.47±.03	1.35±0.08	3.32E+07±9.62E+04	
309-313	832.04	-4.590374	137.449024	50.72±.03	27.53±.02	1.60±0.1	3.34E+07±6.69E+04	
313-317	841.29	-4.590455	137.44891	44.15±.03	24.06±.01	1.50±0.13	3.31E+07±6.13E+04	Shaler
317-324	848.12	-4.590507	137.448813	46.89±.03	26.59±.01	1.50±0.16	3.34E+07±4.85E+04	Shaler

**Table 3.1. Continued.**

Sols	Traverse Distance (m)	Latitude (S) (deg)	Longitude (E) (deg)	Average Thermal Neutron Count Rate (n/s)	Average Epithermal Neutron Count Rate (n/s)	Absorption Equivalent Chlorine from DAN Active (wt. %)	Location-averaged $F_{GCR,RAD}$ (source particles/ second)	Comments
324-327	866.14	-4.590203	137.448728	45.45±.04	25.25±.02	1.0±0.09	3.36E+07±6.91E+04	Start of Driving Campaign to Mt. Sharp
327-329	906.16	-4.590189	137.448117	53.57±.05	27.38±.02	0.80±0.06	3.39E+07±8.09E+04	
329-331	947.28	-4.590202	137.447535	57.41±.06	26.3±.03	1.10±0.05	3.40E+07±8.15E+04	
331-333	975.29	-4.590515	137.447213	54.89±.06	27.52±.03	1.55±0.09	3.40E+07±8.06E+04	
333-335	990.82	-4.590705	137.447088	41.02±.05	26.55±.03	1.50±0.18	3.40E+07±8.09E+04	
335-336	1029.01	-4.591184	137.446737	51.24±.09	28.75±.04	1.20±0.11	3.41E+07±1.01E+05	
336-337	1061.95	-4.591452	137.446288	53.37±.09	26.95±.05	1.10±0.08	3.42E+07±1.00E+05	
337-338	1099.63	-4.591769	137.44574	56.23±.11	27.14±.05	0.65±0.05	3.42E+07±1.00E+05	
338-340	1133.75	-4.592082	137.44529	51.61±.06	26.31±.03	1.30±0.13	3.38E+07±8.09E+04	
340-342	1234.02	-4.593047	137.44425	50.4±.06	26.61±.03	1.30±0.11	3.35E+07±8.07E+04	
342-343	1296.43	-4.593831	137.443652	54.59±.09	26.9±.04	0.95±0.06	3.38E+07±1.01E+05	
343-344	1330.09	-4.593837	137.443104	54.01±.11	26.85±.06	0.95±0.07	3.41E+07±1.01E+05	
344-345	1400.18	-4.594072	137.441967	54.59±.08	26.78±.04	1.10±0.07	3.46E+07±1.01E+05	
345-347	1470.33	-4.594665	137.440999	44.04±.05	24.52±.03	0.90±0.1	3.35E+07±8.10E+04	
347-349	1530.45	-4.595182	137.440156	54.04±.06	26.87±.03	0.90±0.04	3.28E+07±7.99E+04	

**Table 3.1. Continued.**

Sols	Traverse Distance (m)	Latitude (S) (deg)	Longitude (E) (deg)	Average Thermal Neutron Count Rate (n/s)	Average Epithermal Neutron Count Rate (n/s)	Absorption Equivalent Chlorine from DAN Active (wt. %)	Location-averaged $F_{GCR,RAD}$ (source particles/ second)	Comments
349-351	1600.61	-4.596308	137.439878	58.75±.06	26.7±.03	0.75±0.05	3.35E+07±8.09E+04	
351-354	1685.73	-4.596859	137.438602	52.37±.04	26.17±.02	1.10±0.07	3.43E+07±7.04E+04	
354-356	1742.82	-4.596819	137.43828	54.53±.07	25.85±.04	0.75±0.05	3.45E+07±8.22E+04	
356-358	1792.85	-4.596951	137.43701	48.26±.06	26.49±.03	1.0±0.06	3.50E+07±8.33E+04	
358-361	1827.88	-4.597514	137.436924	48.78±.05	26.75±.02	1.30±0.08	3.57E+07±7.30E+04	
361-363	1900.95	-4.598564	137.436402	55.49±.11	28.11±.05	0.95±0.07	3.55E+07±8.42E+04	
363-365	1985.52	-4.598978	137.435081	54.61±.07	26.15±.04	0.75±0.04	3.47E+07±8.25E+04	
365-369	2011.97	-4.599240	137.43473	49.56±.04	25.92±.02	1.0±0.02	3.53E+07±6.40E+04	
369-370	2082.09	-4.599891	137.43374	58.6±.08	26.38±.04	0.95±0.03	3.59E+07±1.03E+05	
370-371	2163.67	-4.600005	137.43256	48.06±.1	26.52±.05	1.0±0.07	3.58E+07±1.03E+05	
371-372	2273.82	-4.600243	137.431071	71.96±.1	27.13±.05	0.75±0.04	3.53E+07±1.02E+05	
372-374	2313.93	-4.600518	137.430491	49.93±.06	25.91±.03	0.85±0.06	3.45E+07±8.26E+04	
374-376	2356.80	-4.601090	137.430643	51.52±.07	26.05±.04	0.85±0.07	3.39E+07±8.22E+04	
376-377	2399.81	-4.601642	137.430208	48.31±.09	26.38±.04	0.65±0.04	3.43E+07±1.04E+05	
377-378	2461.11	-4.602228	137.429607	57.78±.12	26.42±.06	1.20±0.09	3.49E+07±1.04E+05	

**Table 3.1. Continued.**

Sols	Traverse Distance (m)	Latitude (S) (deg)	Longitude (E) (deg)	Average Thermal Neutron Count Rate (n/s)	Average Epithermal Neutron Count Rate (n/s)	Absorption Equivalent Chlorine from DAN Active (wt. %)	Location-averaged $F_{GCR,RAD}$ (source particles/ second)	Comments
378-379	2551.22	-4.603365	137.428661	44.78±.09	24.6±.05	1.0±0.1	3.54E+07±1.03E+05	
379-383	2566.33	-4.603459	137.428428	62.15±.05	26.23±.02	0.75±0.04	3.56E+07±6.49E+04	
383-385	2608.77	-4.603925	137.427912	48.37±.05	25.25±.03	1.0±0.05	3.52E+07±8.44E+04	
385-388	2750.26	-4.606005	137.427272	73.75±.05	26.04±.02	0.25±0.	3.46E+07±7.12E+04	
388-390	2774.54	-4.606251	137.427059	58.51±.06	25.61±.03	0.45±0.03	3.47E+07±8.33E+04	Panorama Point
390-391	2849.72	-4.607074	137.426279	42.53±.05	26.11±.03	1.05±0.09	3.46E+07±1.02E+05	
392-396	2852.46	-4.607115	137.426291	39.35±.05	25.88±.03	1.05±0.11	3.52E+07±6.38E+04	Darwin
396-402	2862.26	-4.607217	137.426275	50.08±.04	26.72±.02	1.0±0.04	3.55E+07±5.46E+04	
402-403	2885.05	-4.607204	137.425896	54.71±.16	27.92±.08	1.05±0.08	3.62E+07±1.05E+05	
403-404	2952.97	-4.608044	137.425251	54.69±.08	24.78±.04	0.25±0.02	3.61E+07±1.05E+05	
404-406	3017.24	-4.608585	137.424417	50.95±.1	26.22±.05	1.20±0.09	3.57E+07±8.39E+04	Amelang target
406-409	3089.88	-4.609542	137.42391	41.58±.04	26.54±.02	0.70±0.07	3.61E+07±1.77E+05	Tingey Target
409-410	3160.45	-4.610645	137.424049	70.05±.12	26.87±.06	0.10±0.03	3.63E+07±3.39E+05	
410-412	3193.38	-4.611086	137.423736	53.75±.07	26.29±.04	0.75±0.05	3.61E+07±8.43E+04	
412-413	3290.69	-4.611823	137.422374	54.22±.13	26.04±.06	0.85±0.09	3.63E+07±1.04E+05	

**Table 3.1. Continued.**

Sols	Traverse Distance (m)	Latitude (S) (deg)	Longitude (E) (deg)	Average Thermal Neutron Count Rate (n/s)	Average Epithermal Neutron Count Rate (n/s)	Absorption Equivalent Chlorine from DAN Active (wt. %)	Location-averaged $F_{GCR,RAD}$ (source particles/ second)	Comments
414-417	3370.48	-4.613046	137.422372	45.87±.05	25.15±.03	1.10±0.1	3.66E+07±6.54E+04	
418-419	3428.99	-4.613358	137.421488	49.17±.07	26.16±.04	0.90±0.06	3.62E+07±1.02E+05	
420-422	3554.78	-4.615214	137.420769	52.01±.06	25.82±.03	1.0±0.06	4.00E+07±9.60E+04	Sol 420 SEP Event
422-424	3624.73	-4.616304	137.420416	52.12±.05	26.76±.03	1.10±0.12	3.60E+07±8.40E+04	
424-426	3719.17	-4.617718	137.420161	56.27±.06	26.34±.03	1.0±0.07	3.68E+07±7.99E+04	
426-429	3767.01	-4.618001	137.419445	52.72±.07	24.53±.03	0.90±0.09	3.72E+07±7.33E+04	
429-431	3813.39	-4.618455	137.418884	44.94±.1	25.29±.05	1.10±0.11	3.70E+07±1.04E+05	
431-433	3884.94	-4.619215	137.41818	47.89±.09	26.06±.04	1.60±0.1	3.68E+07±8.51E+04	
433-436	3978.33	-4.619987	137.417152	59.58±.05	27.68±.03	1.20±0.09	3.62E+07±7.28E+04	
436-437	4071.82	-4.621081	137.416146	51.34±.18	28.15±.09	1.65±0.2	3.65E+07±1.05E+05	
437-438	4103.73	-4.621534	137.416014	41.87±.09	25.14±.05	1.0±0.1	3.67E+07±1.05E+05	
438-439	4152.58	-4.621985	137.415335	43.27±.1	25.73±.05	1.75±0.16	3.67E+07±1.04E+05	
439-440	4178.10	-4.622291	137.415058	49.2±.06	27.13±.03	2.10±0.17	3.69E+07±1.04E+05	
440-453	4182.79	-4.622335	137.415	55.8±.04	29.17±.02	1.85±0.16	3.50E+07±6.32E+04	Cooperstown outcrop
453	4229.66	-4.622509	137.414675	50.65±.11	28.43±.06	1.25±0.28	3.54E+07±1.97E+05	



**Table 3.1. Continued.**

Sols	Traverse Distance (m)	Latitude (S) (deg)	Longitude (E) (deg)	Average Thermal Neutron Count Rate (n/s)	Average Epithermal Neutron Count Rate (n/s)	Absorption Equivalent Chlorine from DAN Active (wt. %)	Location-averaged $F_{GCR,RAD}$ (source particles/ second)	Comments
454-455	4332.99	-4.622435	137.413126	49.27±.14	28.8±.07	1.25±0.07	3.46E+07±2.19E+05	
455-465	4420.15	-4.623129	137.41236	47.65±.04	26.39±.02	2.0±0.08	3.54E+07±5.42E+04	
465-470	4470.47	-4.623464	137.411841	52.13±.04	25.83±.02	0.60±0.07	3.53E+07±5.84E+04	
470-472	4544.45	-4.624251	137.411061	48.52±.06	28.15±.03	2.20±0.14	3.64E+07±8.42E+04	
473-474	4594.47	-4.624878	137.410566	56.67±.08	27.6±.04	0.85±0.06	3.62E+07±8.42E+04	
474-477	4603.15	-4.624881	137.410477	53.51±.05	26.05±.03	1.40±0.13	3.53E+07±7.20E+04	
477-488	4608.44	-4.624957	137.41043683	47.54±.03	26.12±.02	2.15±0.14	3.48E+07±4.98E+04	
488-490	4608.96	-4.624948	137.41044387	47.07±.06	25.88±.03	1.90±0.11	3.47E+07±8.28E+04	
490-494	4610.22	-4.624968	137.41043721	46.32±.04	26.34±.02	2.15±0.14	3.49E+07±8.45E+04	
494-504	4630.44	-4.625259	137.4102843	49.84±.04	28.85±.02	1.85±0.17	3.51E+07±4.38E+04	Sol 504 SEP Event
504-506	4653.90	-4.625275	137.40992254	44.56±.06	24.58±.03	1.05±0.08	3.54E+07±8.47E+04	Sol 504 SEP Event
506-508	4678.96	-4.625550	137.4096246	55.83±.05	27.25±.03	1.30±0.1	3.55E+07±9.36E+04	
508-511	4688.46	-4.625699	137.4095748	44.34±.05	27.02±.03	2.30±0.22	3.42E+07±3.26E+05	
511-513	4717.01	-4.626121	137.40956802	47.15±.06	25.08±.03	1.10±0.11	3.36E+07±4.30E+05	
513-515	4718.25	- 4.6261425 1	137.409561	48.01±.06	26.32±.03	1.55±0.12	3.37E+07±8.17E+04	

**Table 3.1. Continued.**

Sols	Traverse Distance (m)	Latitude (S) (deg)	Longitude (E) (deg)	Average Thermal Neutron Count Rate (n/s)	Average Epithermal Neutron Count Rate (n/s)	Absorption Equivalent Chlorine from DAN Active (wt. %)	Location-averaged $F_{GCR,RAD}$ (source particles/ second)	Comments
515-518	4748.60	-4.626535	137.40922991	55.2±.05	27.16±.03	1.05±0.09	3.47E+07±7.15E+04	
518-519	4764.31	-4.626539	137.4089666	49.71±.11	26.21±.06	1.55±0.1	3.57E+07±1.03E+05	
519-520	4789.57	-4.626482	137.40855305	52.12±.1	27.18±.05	1.20±0.09	3.56E+07±1.04E+05	
520-521	4815.52	-4.626841	137.40832275	47.96±.12	28.93±.06	1.05±0.1	3.56E+07±1.03E+05	
521-524	4826.75	-4.627014	137.40828769	42.3±.05	26.77±.02	1.40±0.12	3.60E+07±7.21E+04	
524-526	4850.90	-4.627050	137.40788096	52.98±.06	25.88±.03	0.95±0.06	3.64E+07±8.41E+04	
526-527	4865.95	-4.626986	137.4076658	65.81±.1	27.46±.05	0.50±0.03	3.61E+07±1.03E+05	
527-528	4894.14	-4.626670	137.40736233	48.62±.08	26.41±.04	1.25±0.11	3.58E+07±1.02E+05	
528-532	4909.81	-4.626551	137.40726257	53.72±.04	26.77±.02	1.05±0.1	3.56E+07±6.38E+04	
532-533	4910.85	-4.626539	137.40727869	51.81±.12	25.47±.06	1.40±0.15	3.51E+07±1.01E+05	Dingo Gap
533-535	4917.97	-4.626598	137.40721439	44.96±.08	26.88±.04	0.95±0.12	3.55E+07±8.24E+04	Dingo Gap
535-538	4924.98	-4.626590	137.40709447	41.28±.05	25.1±.03	0.95±0.09	3.50E+07±7.04E+04	Dingo Gap
538-540	4966.12	-4.626746	137.40649189	54.12±.07	26.92±.03	1.40±0.14	3.49E+07±8.74E+04	Moonlight Valley
540-542	5039.18	-4.626792	137.40531799	54.45±.05	27.65±.03	1.55±0.11	3.51E+07±8.20E+04	Moonlight Valley
542-545	5061.93	-4.626894	137.40494907	55.56±.04	26.38±.02	1.35±0.08	3.52E+07±7.10E+04	

**Table 3.1. Continued.**

Sols	Traverse Distance (m)	Latitude (S) (deg)	Longitude (E) (deg)	Average Thermal Neutron Count Rate (n/s)	Average Epithermal Neutron Count Rate (n/s)	Absorption Equivalent Chlorine from DAN Active (wt. %)	Location-averaged $F_{GCR,RAD}$ (source particles/ second)	Comments
545-546	5108.96	-4.627012	137.40417628	46.34±.13	27.02±.06	1.55±0.15	3.43E+07±9.97E+04	Violet Valley
546-547	5110.19	-4.627025	137.40416361	45.32±.1	27.14±.05	1.75±0.14	3.35E+07±9.88E+04	Violet Valley
547-548	5210.45	-4.627868	137.40279713	27.45±.09	25.05±.05	1.30±0.09	3.35E+07±9.85E+04	
548-549	5310.51	-4.628784	137.40157624	58.75±.11	27.1±.05	1.35±0.12	3.37E+07±9.87E+04	
549-550	5317.48	-4.628889	137.40158557	60.43±.08	28.69±.04	1.50±0.13	3.39E+07±9.90E+04	
550-552	5333.34	-4.628981	137.40140136	59.44±.06	27.6±.03	1.20±0.14	3.38E+07±8.05E+04	
552-553	5412.50	-4.629728	137.40042634	42.97±.08	25.2±.04	1.30±0.11	3.39E+07±9.90E+04	Kylie
553-554	5467.72	-4.630632	137.40023814	38.68±.09	26.54±.05	1.05±0.09	3.50E+07±1.00E+05	Kylie
554-559	5468.91	-4.630652	137.40023632	44.04±.06	24.93±.03	1.05±0.13	3.42E+07±9.77E+04	Kylie
559-560	5572.83	-4.632302	137.40052492	47.09±.09	25.78±.04	1.30±0.11	3.26E+07±1.42E+05	
560-561	5599.12	-4.632410	137.40013044	45.55±.08	25.94±.04	1.30±0.11	3.28E+07±1.08E+05	
561-563	5629.62	-4.632288	137.39972155	44.85±.06	26.14±.03	0.80±0.08	3.31E+07±7.98E+04	
563-564	5651.03	-4.632515	137.39978076	45.52±.07	26.5±.04	2.20±0.14	3.33E+07±1.10E+05	
564-565	5692.89	-4.632799	137.39914891	26.35±.08	26.17±.05	1.60±0.19	3.33E+07±1.10E+05	
565-566	5726.11	-4.633312	137.39903959	48.95±.1	25.82±.05	1.35±0.18	3.35E+07±1.13E+05	

**Table 3.1. Continued.**

Sols	Traverse Distance (m)	Latitude (S) (deg)	Longitude (E) (deg)	Average Thermal Neutron Count Rate (n/s)	Average Epithermal Neutron Count Rate (n/s)	Absorption Equivalent Chlorine from DAN Active (wt. %)	Location-averaged $F_{GCR,RAD}$ (source particles/ second)	Comments
566-568	5727.48	-4.633321	137.39906086	50.7±.07	26.32±.03	1.05±0.08	3.39E+07±8.87E+04	
568-569	5795.73	-4.634360	137.39941601	51.91±.13	27.03±.06	1.75±0.09	3.44E+07±9.96E+04	
569-572	5898.68	-4.634771	137.40104868	52.74±.08	26.68±.04	1.05±0.07	3.46E+07±7.41E+04	
572-574	5988.09	-4.635697	137.40217379	46.78±.07	25.95±.03	1.15±0.09	3.43E+07±9.35E+04	
574-581	6026.21	-4.636341	137.40217222	39.34±.03	26.29±.02	1.35±0.18	3.44E+07±5.27E+04	Start of Kimberley campaign
581-586	6029.10	-4.636386	137.40218228	36.77±.03	25.78±.01	1.85±0.22	3.43E+07±5.72E+04	Kimberley, Smooth Hummocky
586-587	6030.74	-4.636361	137.40218485	37.88±.07	26.06±.04	1.80±0.13	3.38E+07±9.89E+04	Kimberley, Smooth Hummocky
587-588	6053.05	-4.636269	137.40249879	49.31±.12	26.78±.06	1.80±0.13	3.41E+07±9.93E+04	Kimberley, Smooth Hummocky
588-589	6098.62	-4.636899	137.40279243	43.78±.09	26.87±.05	2.20±0.24	3.46E+07±1.00E+05	Kimberley, Smooth Hummocky
589-593	6128.66	-4.637361	137.40296669	30.86±.03	25.67±.02	2.45±0.33	3.50E+07±6.36E+04	Kimberley, Smooth Hummocky
593-595	6159.91	-4.637730	137.40289626	33.39±.05	25.64±.03	2.05±0.21	3.41E+07±8.16E+04	Kimberley, Smooth Hummocky
595-597	6215.79	-4.638249	137.40266381	34.2±.08	25.15±.04	1.70±0.19	3.38E+07±8.11E+04	Kimberley, Smooth Hummocky
597-603	6243.34	-4.638223	137.40226811	33.81±.05	24.21±.03	1.50±0.24	3.40E+07±5.41E+04	Kimberley, Square Top member
603-606	6293.99	-4.638727	137.40224913	29.11±.04	22.94±.02	1.60±0.3	3.48E+07±7.63E+04	Kimberley, Square Top member
606-609	6313.13	-4.638860	137.40203313	36.04±.04	25.73±.02	1.30±0.12	3.33E+07±6.91E+04	Kimberley, Dillinger member

**Table 3.1. Continued.**

Sols	Traverse Distance (m)	Latitude (S) (deg)	Longitude (E) (deg)	Average Thermal Neutron Count Rate (n/s)	Average Epithermal Neutron Count Rate (n/s)	Absorption Equivalent Chlorine from DAN Active (wt. %)	Location-averaged $F_{GCR,RAD}$ (source particles/ second)	Comments
609-630	6317.95	-4.638843	137.40201003	35.8±.01	24.97±.01	1.15±0.03	3.43E+07±3.02E+04	Kimberley Drill Target, Dillinger member
630-631	6342.47	-4.639160	137.40220082	32.44±.08	23.73±.04	0.95±0.07	3.60E+07±1.02E+05	End of Kimberley Campaign
631-634	6369.10	-4.639572	137.40214478	39.87±.05	24.98±.03	0.95±0.1	3.55E+07±7.98E+04	
634-635	6437.81	-4.640390	137.40136182	53.91±.09	26.97±.05	1.60±0.16	3.54E+07±1.16E+05	
635-636	6512.94	-4.640521	137.40015056	39.79±.08	26.58±.05	2.0±0.19	3.56E+07±1.02E+05	
636-637	6572.21	-4.640005	137.39930003	47.85±.08	26.69±.04	1.25±0.23	3.57E+07±1.01E+05	
637-641	6612.65	-4.640230	137.39876146	45.96±.04	25.29±.02	1.10±0.13	3.47E+07±6.30E+04	
641-643	6652.98	-4.639947	137.39827925	54.17±.06	26.18±.03	1.30±0.1	3.42E+07±8.81E+04	
643-644	6738.20	-4.640294	137.39691579	39.38±.08	25.31±.04	1.20±0.18	3.43E+07±1.13E+05	
644-646	6842.44	-4.640884	137.39538279	39.7±.05	25.15±.03	1.40±0.12	3.45E+07±8.93E+04	
646-649	6874.24	-4.640664	137.39493171	47.42±.05	24.99±.03	1.65±0.13	3.49E+07±7.63E+04	
649-651	6931.43	-4.6404341 8	137.3943025	47.03±.06	25.72±.03	2.0±0.16	3.51E+07±8.26E+04	
651-655	6963.27	-4.640872	137.39403092	57.49±.05	24.97±.02	1.30±0.13	3.55E+07±8.32E+04	
655-656	7048.82	-4.641378	137.39271222	44.57±.07	25.29±.04	0.95±0.11	3.56E+07±1.02E+05	
656-657	7094.51	-4.641963	137.3922351	43.71±.12	25.8±.06	2.0±0.23	3.55E+07±1.02E+05	

**Table 3.1. Continued.**

Sols	Traverse Distance (m)	Latitude (S) (deg)	Longitude (E) (deg)	Average Thermal Neutron Count Rate (n/s)	Average Epithermal Neutron Count Rate (n/s)	Absorption Equivalent Chlorine from DAN Active (wt. %)	Location-averaged $F_{GCR,RAD}$ (source particles/ second)	Comments
657-658	7215.47	-4.642161	137.39033902	37.26±.07	25.12±.04	1.95±0.17	3.54E+07±1.02E+05	
658-661	7249.55	-4.642553	137.38996359	48.26±.05	25.75±.02	1.55±0.13	3.54E+07±7.59E+04	
661-662	7388.35	-4.643583	137.38842777	45.09±.11	25.23±.06	1.30±0.12	3.44E+07±1.13E+05	
662-663	7521.30	-4.645296	137.38722631	43.78±.08	25.45±.04	2.0±0.24	3.29E+07±9.79E+04	
663-664	7546.56	-4.645663	137.38705246	49.65±.07	25.46±.04	1.0±0.04	3.21E+07±9.64E+04	Robert Frost Pass
664-665	7613.08	-4.646649	137.38657384	43.71±.08	23.12±.04	0.85±0.04	3.21E+07±1.07E+05	
665-667	7755.58	-4.647737	137.38482894	40.83±.07	25.9±.04	1.55±0.27	3.25E+07±8.47E+04	
667-668	7756.77	-4.647737	137.38482894	36.55±.13	25.±.07	1.85±0.22	3.28E+07±9.79E+04	
668-669	7862.01	-4.649367	137.38468007	45.62±.09	26.04±.05	0.60±0.07	3.30E+07±9.82E+04	
669-670	7900.81	-4.649497	137.38404897	48.86±.1	26.21±.05	1.35±0.12	3.31E+07±1.06E+05	
670-671	8007.96	-4.650872	137.38485883	56.69±.11	26.83±.05	1.05±0.13	3.32E+07±1.07E+05	
671-672	8124.73	-4.652372	137.3838113	58.14±.08	26.05±.04	0.75±0.1	3.31E+07±1.07E+05	
672-674	8206.88	-4.653536	137.38418296	33.14±.05	24.47±.03	1.15±0.09	3.32E+07±9.03E+04	
674-676	8212.19	-4.653448	137.3841709	52.79±.1	25.36±.05	1.15±0.08	3.35E+07±8.01E+04	
676-677	8228.57	-4.653496	137.38389916	58.07±.09	25.96±.04	0.90±0.07	3.37E+07±9.87E+04	

**Table 3.1. Continued.**

Sols	Traverse Distance (m)	Latitude (S) (deg)	Longitude (E) (deg)	Average Thermal Neutron Count Rate (n/s)	Average Epithermal Neutron Count Rate (n/s)	Absorption Equivalent Chlorine from DAN Active (wt. %)	Location-averaged $F_{GCR,RAD}$ (source particles/ second)	Comments
677-678	8248.17	-4.653823	137.38389984	66.57±.1	26.36±.04	0.45±0.04	3.38E+07±9.91E+04	
678-679	8314.66	-4.654926	137.38404876	54.99±.1	26.64±.05	1.0±0.05	3.37E+07±1.09E+05	
679-683	8315.89	-4.654926	137.38407016	54.52±.08	26.54±.04	1.0±0.07	3.40E+07±8.57E+04	
683-685	8368.29	-4.655472	137.38464127	54.81±.1	25.58±.05	1.05±0.08	3.38E+07±8.82E+04	
685-688	8428.73	-4.656308	137.38423634	47.17±.06	25.24±.03	1.05±0.1	3.39E+07±6.97E+04	
688-689	8511.11	-4.657405	137.38345626	55.62±.07	25.43±.04	1.40±0.08	3.40E+07±1.09E+05	
689-690	8520.74	-4.657560	137.38345592	51.21±.09	24.56±.05	1.30±0.09	3.36E+07±1.09E+05	
690-691	8550.28	-4.658036	137.38361051	65.51±.1	25.36±.05	0.20±0.03	3.34E+07±9.86E+04	
691-692	8574.16	-4.658331	137.38345428	43.51±.1	24.69±.05	2.0±0.18	3.37E+07±9.85E+04	
692-695	8605.16	-4.658484	137.38304636	47.89±.05	25.29±.03	1.0±0.08	3.43E+07±7.89E+04	
695-696	8628.52	-4.658824	137.3829746	63.57±.11	25.33±.05	0.20±0.05	3.50E+07±1.01E+05	
696-702	8648.39	-4.659146	137.38300311	51.07±.06	25.77±.03	1.35±0.09	3.54E+07±5.57E+04	
702-703	8661.57	-4.659361	137.3830145	44.75±.1	23.87±.05	0.95±0.06	3.53E+07±1.01E+05	
703-705	8691.20	-4.659819	137.38282886	47.17±.04	25.27±.02	1.35±0.08	3.54E+07±8.34E+04	
705-706	8696.13	-4.659866	137.38284499	52.4±.13	27.06±.06	1.30±0.07	3.64E+07±1.03E+05	

**Table 3.1. Continued.**

Sols	Traverse Distance (m)	Latitude (S) (deg)	Longitude (E) (deg)	Average Thermal Neutron Count Rate (n/s)	Average Epithermal Neutron Count Rate (n/s)	Absorption Equivalent Chlorine from DAN Active (wt. %)	Location-averaged $F_{GCR,RAD}$ (source particles/ second)	Comments
706-708	8718.38	-4.660075	137.38266726	63.43±.06	24.57±.03	0.25±0.03	3.58E+07±8.29E+04	
708	8719.55	-4.660180	137.38268618	80.89±.22	27.12±.1	0.25±0.	3.51E+07±1.43E+05	
709-710	8733.90	-4.660284	137.3827051	35.54±.06	25.7±.03	1.0±0.06	3.58E+07±1.02E+05	
710-711	8741.68	-4.660157	137.38266812	33.36±.07	24.77±.04	0.85±0.08	3.56E+07±1.02E+05	
711-713	8743.59	-4.660138	137.38266338	30.69±.04	21.56±.02	0.30±0.04	3.52E+07±8.26E+04	
713-714	8752.41	-4.660020	137.38269375	78.2±.1	26.62±.04	0.05±0.02	3.49E+07±1.01E+05	
714-717	8789.96	-4.659548	137.38239347	63.41±.08	24.79±.04	0.25±0.	3.52E+07±7.14E+04	
717-719	8822.14	-4.659935	137.38273472	49.43±.04	24.05±.02	1.10±0.07	3.59E+07±8.36E+04	
719-729	8825.74	-4.659959	137.38274963	56.37±.03	24.63±.01	1.10±0.07	3.66E+07±4.39E+04	Bonanza King Drill Target
729-731	8889.83	-4.659190	137.38210494	53.48±.06	24.48±.03	0.80±0.07	3.75E+07±8.54E+04	
731-733	8909.64	-4.659285	137.38184267	59.87±.07	25.52±.04	1.0±0.06	3.72E+07±8.48E+04	
733-735	8968.33	-4.659364	137.3809408	59.23±.08	25.91±.04	0.50±0.03	3.73E+07±8.54E+04	
735-738	9006.30	-4.658964	137.38055273	48.6±.12	27.08±.06	2.20±0.11	4.58E+07±8.21E+04	Sol 737 SEP Event
738-739	9039.33	-4.659144	137.38010138	49.53±.08	24.86±.04	1.70±0.11	4.61E+07±1.17E+05	Sol 738 SEP Event
739-740	9062.29	-4.659233	137.37973541	42.58±.06	24.8±.03	1.60±0.11	4.04E+07±1.09E+05	Sol 739 SEP Event



**Table 3.1. Continued.**

Sols	Traverse Distance (m)	Latitude (S) (deg)	Longitude (E) (deg)	Average Thermal Neutron Count Rate (n/s)	Average Epithermal Neutron Count Rate (n/s)	Absorption Equivalent Chlorine from DAN Active (wt. %)	Location-averaged $F_{GCR,RAD}$ (source particles/ second)	Comments
740-742	9074.00	-4.659319	137.37959575	51.53±.05	25.±.03	1.75±0.09	3.51E+07±8.22E+04	
743-744	9166.63	-4.659342	137.37816602	43.26±.09	25.31±.05	0.75±0.06	3.42E+07±1.00E+05	
744-746	9198.55	-4.659468	137.37764367	81.27±.05	25.38±.02	0.25±0.	3.61E+07±8.36E+04	
746-747	9206.69	-4.659534	137.37752809	44.6±.08	25.38±.04	1.25±0.16	3.62E+07±1.03E+05	
747-748	9298.76	-4.660861	137.37707605	42.49±.1	27.11±.05	1.60±0.2	3.51E+07±1.01E+05	
748-751	9321.39	-4.661054	137.37677878	39.21±.09	24.04±.04	0.70±0.06	3.64E+07±7.29E+04	
751-753	9435.74	-4.662413	137.37724479	64.61±.06	26.53±.03	0.50±0.1	3.87E+07±8.68E+04	End of RTR in Amargosa Valley

(Tate *et al.*, 2015b), the MMRTG-produced epithermals do not (Jun *et al.*, 2013; Tate *et al.*, 2015b). Because the epithermal neutron count rate is essentially invariant with position, here we follow the strategy (also used in Tate *et al.*, 2015b) of using only the thermal neutron count rate in estimating WEH from DAN passive measurements.

The lowest measured thermal neutron count rate for all fixed locations is  $26.35 \pm 0.08$  thermal neutrons counts per second at a traverse distance of 5692.89 m during sols 564 - 565. Other low thermal neutron count rates were measured at traverse distances of 5210.44 m, 6128.65 m, 6159.91 m, 6243.33 m, 6293.99 m, 6342.46 m, 8147.88 m, 8206.88 m, and 8743.59 m. There is also a widespread minimum in the thermal neutron count rates centered around sol 600. The rover was investigating the Kimberley outcrop from different locations during this time period (sols 574-631) at a traverse distance of ~6000 m to ~6342 m. During sol 272 to 753, the rover did not stay at any other location longer than it did at the Kimberley outcrop.

The highest thermal neutron count rate,  $81.27 \pm 0.05$  counts per second, was measured at a traverse distance of 9198.55 m, corresponding to sols 744-746. Other high thermal neutron count rates were found at traverse distance locations of 8719.54 m and 8752.41 m.

### ***Traverse Data***

Continuously-acquired DAN passive traverse data are shown in Figure 3.5. These data were acquired while the rover was driving between fixed locations. Because *Curiosity* moves very slowly and periodically stops to take imaging data and make updates to its navigation systems, many DAN passive measurements are co-located along individual traverses. Such stops are contained within daily traverses and are not considered “fixed locations” in our analyses because no other compositional measurements are typically acquired at them. We average the count rates at these points together to improve counting statistics for individual locations within

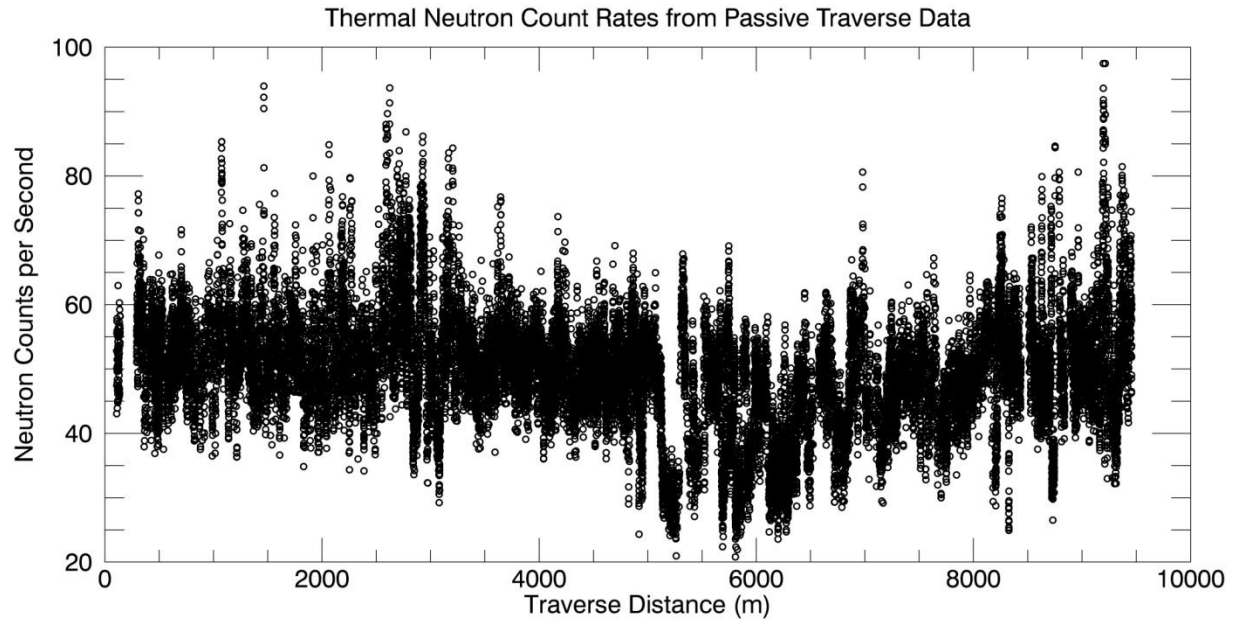


**Figure 3.5. DAN passive thermal neutron count rates from traverse measurements acquired along *Curiosity's* ~9.5 km route from Bradbury Landing to Amargosa Valley. Uncertainties on individual measurements are calculated by the square root of the count rates, but are not shown here for clarity.**

the traverse. A total of 23,183 measurements at individual locations were acquired along the traverse route. Substantial variation occurs in the thermal neutron count rates (Figure 3.5).

Greater variability in thermal neutron count rates is observed in the traverse data compared to the fixed location data, which is to be expected because the number of points measured is much greater in the traverse data station. The highest measurement is  $97.47 \pm 2.74$  thermal neutron counts per second at a traverse distance of ~9195 m. There are 78 traverse measurements, which show thermal neutron count rates greater than or equal to 80 thermal neutron counts per second and only twelve of which exhibit count rates greater than or equal to 90 thermal neutron counts per second. These high measurements typically show a rise in the thermal neutron count rates leading up to the highest values and then a decrease upon moving away, suggesting that the characteristic length scale for the local geochemical anomalies that produce the enhanced counts are larger than the ~tens of centimeters the rover would typically traverse over several DAN passive measurements. An example of one of these enhancements is shown in Figure 3.6. Similar localized increases in the thermal neutron count rates are observed around traverse distances of ~1075 m, ~1350 m, ~1465 m, ~2065 m, ~2605 m, ~2625 m, ~2710 m, ~2930 m, ~2990 m, ~3205 m, ~5840 m, ~6980 m, ~9215 m, and ~9370 m.

The minimum thermal neutron count rate observed in the traverse measurements is  $20.80 \pm 1.91$  counts per second at a traverse distance of ~5807 m. There are 405 measurements that exhibit thermal neutron count rates less than or equal to 30 thermal neutron counts per second, and only 29 of those are less than or equal to 25 counts per second. Most of those 405 measurements are within the traverse distance range of ~5140 m to ~6303 m. A general decrease in thermal neutron count rates is observed in this area of the traverse in both the traverse data (Figure 3.5) and the fixed location data (Figures 3.3 and 3.4). This area corresponds roughly to

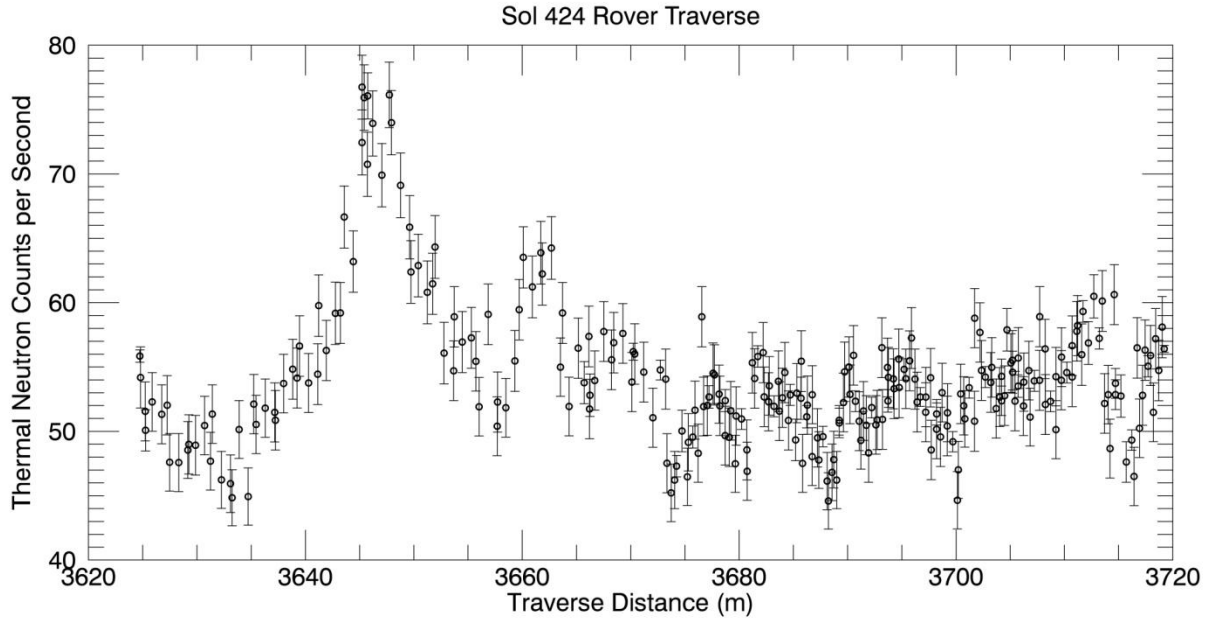


**Figure 3.6.** DAN passive thermal neutron count rates acquired during *Curiosity's* traverse on sol 424.

the Kimberley outcrop investigated on sols 574 - 631 at traverse distances of ~6000 m through ~6342 m. However, the most noticeable widespread depression in the traverse measurement thermal neutron count rates is seen at ~5142 m to ~5300 m traversed on sols 547 and 548, in the region of Violet Valley, which was passed shortly before reaching the Kimberley area. This area is striking not only because it contains many low thermal neutron count rates, but also because it is nearly devoid of any greater count rates, unlike any other regions of the crater floor observed. This region is within the Smooth Hummocky unit and no changes are noted in the surface properties at the locations with greater thermal neutron count rates bookending this area.

### ***Ancillary Data***

Many ancillary data sets were used in this analysis of DAN passive data. In addition to the constraining measurements from DAN active mode and the RAD experiment discussed in Section 2 (Methods), orbital imaging from the High Resolution Imaging Science Experiment (HiRISE) and surface imaging from MSL Rear Hazcam and Environment Camera experiments have been used to investigate any correlations between DAN passive results and local surface properties. Surface properties include such things as rock density, sand density, and mudstone density. MSL telemetry data have been used in constructing correction factors for MMRTG/DAN DE to ground relationships. Geologic maps of Gale Crater (Calef *et al.*, 2013) have also been used to search for any correlations between geologic units and DAN passive measurements. Lastly, results from other MSL instruments have also been used to search for correlations and consistencies with DAN passive results at specific locations and these are noted where applicable. These results include those from MSL APXS (Thompson *et al.*, 2016), the Chemistry and Mineralogy experiment (CheMin) (Treiman *et al.*, 2016), and the Sample Analysis at Mars experiment (SAM) (McAdam *et al.*, 2015).

## Sources of Uncertainties

The formal uncertainties included in our analysis are Poisson statistics on thermal neutron count rates, uncertainties on RAD penetrating counter data propagated through our scale factor calculations, uncertainties in simulated count rates used to interpret the measurements, and AEC abundance uncertainties from DAN active measurements. These uncertainties are propagated through all calculations and presented as uncertainties on our WEH estimates.

There are other contributions to uncertainty in our results that are more difficult to quantify. These include uncertainty in the density of the regolith used for simulations and small diurnal variations in the thermal neutron count rates not associated with regolith composition (Tate *et al.*, 2015a). We have previously shown that the sensitivity of our final WEH estimates to reasonable variations in these parameters is no greater than ~0.4 wt. % (Tate *et al.*, 2015b).

On specific sols there were also uncertainties introduced by the occurrence of solar energetic particle (SEP) events. These events were detected by RAD (Hassler *et al.*, 2014), but corresponding increases were not observed in DAN passive count rates. A lack of event-specific SEP spectra and particle fluxes makes it impossible to rigorously assess the effect of the SEP events on DAN passive count rates. The sols affected by SEP events were sols 242, 420, 504, 737, 738, and 739, though no data are available for the sol 504 event. WEH estimates made on these sols should be viewed with caution.

In summary, there are both formal uncertainties and non-formal uncertainties inherent in our analysis. Formal uncertainties are used to calculate the uncertainty in our WEH estimates. The non-formal uncertainties have been studied in order to understand how they affect our measurements and WEH estimates. It is shown in Tate *et al.* (2015b) that for reasonable variations in these sources uncertainties in our WEH estimates are no greater than ~0.4 wt. %.

This upper limit on uncertainty excludes the rare instances of sols on which SEP events occur. Tate *et al.* (2015b) also showed that the order of significance of the uncertainties discussed here in decreasing order is: AEC uncertainties, uncertainty in the regolith density, our formal statistical uncertainties, diurnal variations, and uncertainties in the GCR environment. In our WEH estimates reported below, Section 5 (Results), the uncertainties quoted for a given WEH estimate are only those calculated from formal sources because they can be readily quantified. However instances in which the formal uncertainties are less than 0.4 wt. % should be interpreted with caution because of the non-formal uncertainties that are not captured in the calculation.

## Results

### *Fixed Location WEH Estimates*

WEH estimates for fixed locations investigated during sols 0 to 753 are shown in Figure 3.7 and Table 3.2. WEH estimates for fixed locations range from 0.0 wt. % to  $6.2 \pm 0.4$  wt. % WEH. The average WEH content measured at fixed locations is 2.4 wt. % with a standard deviation of 1.2 wt. %.

A special note is required regarding the meaning of the WEH estimate of 0.0 wt. % on sols 711 through 713. In certain cases the thermal neutron count rate data is below what can be simulated by the parameters of our grid for the used AEC abundances. The data acquired during sols 711-713 is an example of this. While the WEH content at these locations such as this may not be exactly 0.0 wt. %, our models for the given set of parameters cannot distinguish between the actual WEH content and 0.0 wt. %. Ultimately, the conclusion is the same in that the WEH



### WEH Along Traverse at Fixed Locations

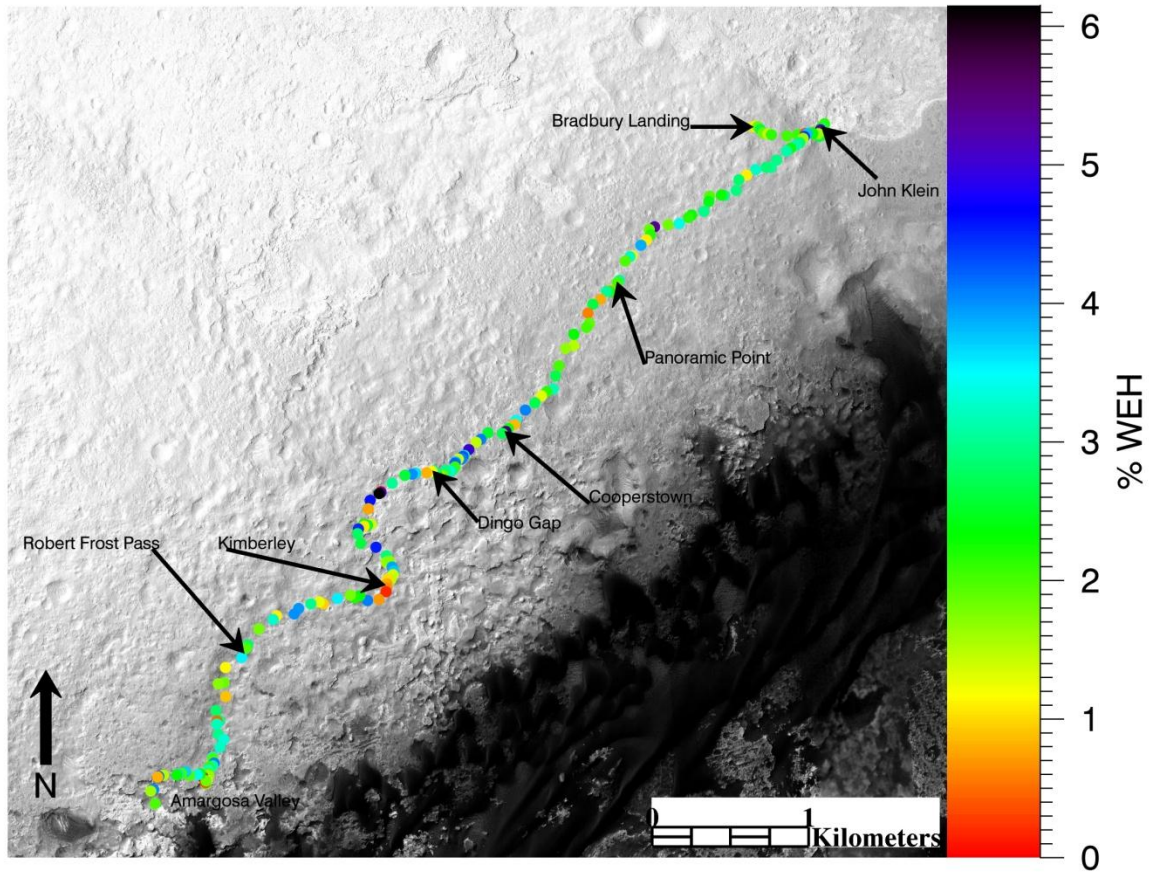


**Figure 3.7. WEH estimates derived from DAN passive data acquired at fixed locations along *Curiosity's* traverse from Bradbury Landing to Amargosa Valley.**

**Table 3.2. WEH estimates for fixed locations derived from DAN passive data. The uncertainties shown here represent those from formal sources and estimates from reasonable variations in non-formal sources are not greater than 0.4 wt. %. \*See text for special note regarding interpretation of 0.0 wt. %.**

<b>Sols</b>	<b>Traverse Distance (m)</b>	<b>WEH (wt. %)</b>
<b>0-15</b>	0.00	1.4 ± 0.3
<b>17-21</b>	7.00	1.0 ± 0.1
<b>22-23</b>	27.00	1.3 ± 0.2
<b>24-26</b>	48.50	1.9 ± 0.1
<b>26-29</b>	78.60	2.7 ± 0.2
<b>29-37</b>	109.10	1.9 ± 0.1
<b>38</b>	141.50	1.4 ± 0.2
<b>39</b>	163.20	2.1 ± 0.3
<b>45</b>	293.80	2.1 ± 0.4
<b>49</b>	335.24	2.1 ± 0.3
<b>50</b>	392.30	0.3 ± 0.1
<b>52</b>	453.30	3.1 ± 0.2
<b>54</b>	455.00	3.1 ± 0.2
<b>55</b>	479.10	1.0 ± 0.1
<b>57</b>	485.10	0.8 ± 0.1
<b>59</b>	486.90	0.8 ± 0.1
<b>59-100</b>	490.00	0.6 ± 0.1
<b>100-102</b>	491.90	0.7 ± 0.1
<b>102-111</b>	517.20	2.9 ± 0.2
<b>111-120</b>	519.10	3.2 ± 0.4
<b>120-121</b>	553.70	1.4 ± 0.3
<b>121-122</b>	577.90	1.5 ± 0.3
<b>122-123</b>	578.90	1.5 ± 0.3
<b>123-124</b>	598.30	2.4 ± 0.3
<b>124-125</b>	612.30	1.3 ± 0.3
<b>125-127</b>	638.40	2.0 ± 0.2
<b>127-130</b>	671.20	1.9 ± 0.1
<b>130-133</b>	676.80	2.2 ± 0.5
<b>133-147</b>	698.80	2.5 ± 0.2
<b>147-151</b>	701.50	1.9 ± 0.2
<b>151-152</b>	702.20	2.7 ± 0.2
<b>152-159</b>	704.60	3.5 ± 0.2

**Table 3.2. Continued.**

<b>Sols</b>	<b>Traverse Distance (m)</b>	<b>WEH (wt. %)</b>
<b>159-162</b>	705.90	2.0 ± 0.3
<b>162</b>	714.90	3.4 ± 0.3
<b>163-166</b>	716.80	2.0 ± 0.3
<b>166-272</b>	723.40	2.3 ± 0.3
<b>272-274</b>	726.49	1.3 ± 0.3
<b>275-294</b>	727.16	1.7 ± 0.2
<b>297</b>	733.46	2.3 ± 0.3
<b>297-298</b>	753.27	2.1 ± 0.4
<b>299-301</b>	761.70	2.9 ± 0.3
<b>302-307</b>	776.46	5.3 ± 0.2
<b>307-308</b>	808.23	5.6 ± 0.1
<b>308-309</b>	830.23	2.6 ± 0.2
<b>309-313</b>	832.04	3.6 ± 0.3
<b>313-317</b>	841.29	2.2 ± 0.3
<b>317-324</b>	848.12	2.6 ± 0.3
<b>324-327</b>	866.14	1.6 ± 0.3
<b>327-329</b>	906.16	2.3 ± 0.3
<b>329-331</b>	947.28	3.8 ± 0.2
<b>331-333</b>	975.29	4.5 ± 0.9
<b>333-335</b>	990.82	1.6 ± 0.3
<b>335-336</b>	1029.01	2.9 ± 0.2
<b>336-337</b>	1061.95	3.1 ± 0.2
<b>337-338</b>	1099.63	2.3 ± 0.2
<b>338-340</b>	1133.75	3.1 ± 0.3
<b>340-342</b>	1234.02	2.9 ± 0.2
<b>342-343</b>	1296.43	3.0 ± 0.4
<b>343-344</b>	1330.09	2.9 ± 0.2
<b>344-345</b>	1400.18	3.3 ± 0.2
<b>345-347</b>	1470.33	1.1 ± 0.4
<b>347-349</b>	1530.45	2.8 ± 0.1
<b>349-351</b>	1600.61	2.9 ± 0.2
<b>351-354</b>	1685.73	2.9 ± 0.3
<b>354-356</b>	1742.82	2.3 ± 0.2
<b>356-358</b>	1792.85	2.0 ± 0.2
<b>358-361</b>	1827.88	2.4 ± 0.2
<b>361-363</b>	1900.95	3.0 ± 0.2
<b>363-365</b>	1985.52	2.3 ± 0.2
<b>365-369</b>	2011.97	2.1 ± 0.4

**Table 3.2. Continued.**

<b>Sols</b>	<b>Traverse Distance (m)</b>	<b>WEH (wt. %)</b>
<b>369-370</b>	2082.09	3.4 ± 0.2
<b>370-371</b>	2163.67	1.8 ± 0.2
<b>371-372</b>	2273.82	5.3 ± 0.2
<b>372-374</b>	2313.93	1.9 ± 0.2
<b>374-376</b>	2356.80	2.2 ± 0.3
<b>376-377</b>	2399.81	1.1 ± 0.2
<b>377-378</b>	2461.11	3.9 ± 0.2
<b>378-379</b>	2551.22	1.3 ± 0.4
<b>379-383</b>	2566.33	3.2 ± 0.3
<b>383-385</b>	2608.77	2.0 ± 0.1
<b>385-388</b>	2750.26	3.0 ± 0.2
<b>388-390</b>	2774.54	2.0 ± 0.3
<b>390-391</b>	2849.72	1.1 ± 0.3
<b>392-396</b>	2852.46	0.8 ± 0.1
<b>396-402</b>	2862.26	2.2 ± 0.4
<b>402-403</b>	2885.05	3.0 ± 0.3
<b>403-404</b>	2952.97	0.8 ± 0.1
<b>404-406</b>	3017.24	2.7 ± 0.2
<b>406-409</b>	3089.88	0.6 ± 0.1
<b>409-410</b>	3160.45	1.9 ± 0.2
<b>410-412</b>	3193.38	2.0 ± 0.3
<b>412-413</b>	3290.69	2.3 ± 0.4
<b>414-417</b>	3370.48	1.5 ± 0.3
<b>418-419</b>	3428.99	1.7 ± 0.2
<b>420-422</b>	3554.78	2.0 ± 0.6
<b>422-424</b>	3624.73	2.7 ± 0.3
<b>424-426</b>	3719.17	3.2 ± 0.4
<b>426-429</b>	3767.01	2.2 ± 0.5
<b>429-431</b>	3813.39	1.3 ± 0.3
<b>431-433</b>	3884.94	2.7 ± 0.3
<b>433-436</b>	3978.33	4.1 ± 0.6
<b>436-437</b>	4071.82	3.5 ± 0.7
<b>437-438</b>	4103.73	0.9 ± 0.1
<b>438-439</b>	4152.58	2.3 ± 0.5
<b>439-440</b>	4178.10	4.8 ± 0.8
<b>440-453</b>	4182.79	5.7 ± 0.3
<b>453</b>	4229.66	2.7 ± 0.4
<b>454-455</b>	4332.99	2.6 ± 0.2

**Table 3.2. Continued.**

<b>Sols</b>	<b>Traverse Distance (m)</b>	<b>WEH (wt. %)</b>
455-465	4420.15	4.1 ± 0.8
465-470	4470.47	1.5 ± 0.3
470-472	4544.45	5.0 ± 0.2
473-474	4594.47	2.7 ± 0.2
474-477	4603.15	3.5 ± 0.3
477-488	4608.44	4.8 ± 0.6
488-490	4608.96	3.7 ± 0.4
490-494	4610.22	4.3 ± 0.6
494-504	4630.44	4.1 ± 1.3
504-506	4653.90	1.4 ± 0.3
506-508	4678.96	3.7 ± 0.2
508-511	4688.46	4.2 ± 0.8
511-513	4717.01	2.1 ± 0.3
513-515	4718.25	2.9 ± 0.3
515-518	4748.60	3.3 ± 0.2
518-519	4764.31	3.0 ± 0.3
519-520	4789.57	2.9 ± 0.2
520-521	4815.52	1.9 ± 0.4
521-524	4826.75	1.5 ± 0.2
524-526	4850.90	2.5 ± 0.3
526-527	4865.95	2.8 ± 0.1
527-528	4894.14	2.3 ± 0.3
528-532	4909.81	3.0 ± 0.3
532-533	4910.85	3.2 ± 0.4
533-535	4917.97	1.2 ± 0.5
535-538	4924.98	0.8 ± 0.1
538-540	4966.12	3.6 ± 0.3
540-542	5039.18	4.0 ± 0.4
542-545	5061.93	3.8 ± 0.2
545-546	5108.96	2.6 ± 0.4
546-547	5110.19	3.0 ± 0.5
547-548	5210.45	0.1 ± 0.1
548-549	5310.51	5.1 ± 0.7
549-550	5317.48	6.2 ± 0.4
550-552	5333.34	4.6 ± 0.6
552-553	5412.50	1.7 ± 0.2
553-554	5467.72	0.8 ± 0.1
554-559	5468.91	1.4 ± 0.3

**Table 3.2. Continued.**

<b>Sols</b>	<b>Traverse Distance (m)</b>	<b>WEH (wt. %)</b>
<b>559-560</b>	5572.83	2.5 ± 0.2
<b>560-561</b>	5599.12	2.2 ± 0.3
<b>561-563</b>	5629.62	1.1 ± 0.3
<b>563-564</b>	5651.03	4.5 ± 0.6
<b>564-565</b>	5692.89	0.2 ± 0.2
<b>565-566</b>	5726.11	2.8 ± 0.3
<b>566-568</b>	5727.48	2.6 ± 0.2
<b>568-569</b>	5795.73	4.5 ± 0.7
<b>569-572</b>	5898.68	2.9 ± 0.3
<b>572-574</b>	5988.09	2.0 ± 0.3
<b>574-581</b>	6026.21	1.1 ± 0.3
<b>581-586</b>	6029.10	1.6 ± 0.4
<b>586-587</b>	6030.74	1.8 ± 0.3
<b>587-588</b>	6053.05	3.9 ± 0.4
<b>588-589</b>	6098.62	3.7 ± 0.5
<b>589-593</b>	6128.66	1.4 ± 0.3
<b>593-595</b>	6159.91	1.5 ± 0.2
<b>595-597</b>	6215.79	1.0 ± 0.4
<b>597-603</b>	6243.34	0.8 ± 0.2
<b>603-606</b>	6293.99	0.4 ± 0.3
<b>606-609</b>	6313.13	0.8 ± 0.1
<b>609-630</b>	6317.95	0.6 ± 0.1
<b>630-631</b>	6342.47	0.2 ± 0.1
<b>631-634</b>	6369.10	0.7 ± 0.1
<b>634-635</b>	6437.81	4.1 ± 1.4
<b>635-636</b>	6512.94	2.4 ± 0.7
<b>636-637</b>	6572.21	2.2 ± 0.4
<b>637-641</b>	6612.65	1.8 ± 0.3
<b>641-643</b>	6652.98	3.6 ± 0.2
<b>643-644</b>	6738.20	0.9 ± 0.1
<b>644-646</b>	6842.44	1.3 ± 0.3
<b>646-649</b>	6874.24	3.0 ± 0.4
<b>649-651</b>	6931.43	4.0 ± 0.5
<b>651-655</b>	6963.27	4.0 ± 0.2
<b>655-656</b>	7048.82	1.1 ± 0.5
<b>656-657</b>	7094.51	3.3 ± 0.8
<b>657-658</b>	7215.47	1.8 ± 0.3
<b>658-661</b>	7249.55	2.8 ± 0.4

**Table 3.2. Continued.**

<b>Sols</b>	<b>Traverse Distance (m)</b>	<b>WEH (wt. %)</b>
<b>661-662</b>	7388.35	2.0 ± 0.2
<b>662-663</b>	7521.30	3.6 ± 0.8
<b>663-664</b>	7546.56	2.6 ± 0.2
<b>664-665</b>	7613.08	1.2 ± 0.3
<b>665-667</b>	7755.58	1.9 ± 0.5
<b>667-668</b>	7756.77	1.7 ± 0.4
<b>668-669</b>	7862.01	0.9 ± 0.1
<b>669-670</b>	7900.81	2.8 ± 0.2
<b>670-671</b>	8007.96	3.7 ± 0.2
<b>671-672</b>	8124.73	2.9 ± 0.3
<b>672-674</b>	8206.88	0.5 ± 0.1
<b>674-676</b>	8212.19	3.2 ± 0.2
<b>676-677</b>	8228.57	3.4 ± 0.3
<b>677-678</b>	8248.17	3.0 ± 0.1
<b>678-679</b>	8314.66	3.3 ± 0.3
<b>679-683</b>	8315.89	3.2 ± 0.4
<b>683-685</b>	8368.29	3.4 ± 0.2
<b>685-688</b>	8428.73	2.0 ± 0.4
<b>688-689</b>	8511.11	4.1 ± 0.8
<b>689-690</b>	8520.74	3.1 ± 0.3
<b>690-691</b>	8550.28	2.1 ± 0.2
<b>691-692</b>	8574.16	3.4 ± 0.6
<b>692-695</b>	8605.16	2.0 ± 0.6
<b>695-696</b>	8628.52	1.7 ± 0.2
<b>696-702</b>	8648.39	3.0 ± 0.2
<b>702-703</b>	8661.57	1.2 ± 0.4
<b>703-705</b>	8691.20	2.3 ± 0.2
<b>705-706</b>	8696.13	3.0 ± 0.3
<b>706-708</b>	8718.38	1.7 ± 0.2
<b>708</b>	8719.55	4.2 ± 0.4
<b>709-710</b>	8733.90	0.5 ± 0.1
<b>710-711</b>	8741.68	0.2 ± 0.1
<b>711-713</b>	8743.59	0.0*
<b>713-714</b>	8752.41	2.9 ± 0.2
<b>714-717</b>	8789.96	1.8 ± 0.1
<b>717-719</b>	8822.14	2.3 ± 0.3
<b>719-729</b>	8825.74	3.4 ± 0.2
<b>729-731</b>	8889.83	2.0 ± 0.2

**Table 3.2. Continued.**

<b>Sols</b>	<b>Traverse Distance (m)</b>	<b>WEH (wt. %)</b>
<b>731-733</b>	8909.64	$3.7 \pm 0.3$
<b>733-735</b>	8968.33	$2.1 \pm 0.3$
<b>735-738</b>	9006.30	$3.6 \pm 0.3$
<b>738-739</b>	9039.33	$2.3 \pm 0.4$
<b>739-740</b>	9062.29	$1.5 \pm 0.3$
<b>740-742</b>	9074.00	$4.2 \pm 0.8$
<b>743-744</b>	9166.63	$0.8 \pm 0.1$
<b>744-746</b>	9198.55	$4.1 \pm 0.5$
<b>746-747</b>	9206.69	$1.6 \pm 0.3$
<b>747-748</b>	9298.76	$2.0 \pm 0.4$
<b>748-751</b>	9321.39	$0.4 \pm 0.1$
<b>751-753</b>	9435.74	$2.5 \pm 0.3$



content at locations such as this is extremely low.

The largest WEH estimate for fixed locations ( $6.2 \pm 0.4$  wt. %) was measured on sols 549-550 at a traverse distance of 5317.48 m. This location is in the Smooth Hummocky unit. The WEH estimates are elevated in the measurements near this point as well, with the nearest locations yielding estimates of  $5.1 \pm 0.7$  wt. % (sols 548-549),  $4.6 \pm 0.6$  wt. % (sols 550-552). The surface properties at these locations exhibit nothing noteworthy and are typical of the Smooth Hummocky unit.

The highest average thermal neutron count rate ( $81.27 \pm 0.05$ ) measured for a fixed location corresponds to a WEH content of  $4.1 \pm 0.5$  wt. %. This location was investigated on sol 744 - 746 at a traverse distance of 9198.55 m and had a particularly low AEC abundance (derived from a DAN active measurement, Mitrofanov *et al.*, in prep) of  $0.25 \pm 0.00$  wt. %. This location has a surface that is typical of the Smooth Hummocky unit, but other locations on this unit display the full range of WEH estimates seen throughout the traverse.

The lowest average WEH estimate for fixed locations is the aforementioned 0.0 wt. % on sols 711-713 at a traverse distance of 8743.6 m. Other fixed location measurements within the area are low as well at  $0.45 \pm 0.1$  wt. % measured on sols 709-710 and  $0.2 \pm 0.1$  wt. % measured on sols 710-711. The surface properties in this location were somewhat atypical of the rest of the traverse in that the surface was covered with sandy ripples.

Another measurement of note is the WEH estimate of  $0.2 \pm 0.1$  wt. % measured on sols 630-631 at a traverse distance of 6342.5 m. The AEC abundance at this location was  $0.95 \pm 0.07$  wt. %. This location is located near the Kimberley outcrop, which is characterized by generally low thermal neutron count rates in the DAN passive data. The Kimberley outcrop is composed of member units Square Top, Dillinger, and Mount Remarkable (Grotzinger *et al.*, 2015). Not all

measurements in the Kimberley area are on Kimberley members, so some of the WEH estimates are much higher. However, the DAN passive fixed location measurements closest to specific examples of Kimberley members, such as Square Top and Dillinger, exhibit relatively depleted WEH contents. These are  $0.8 \pm 0.2$  wt. % (sols 597-603),  $0.4 \pm 0.3$  wt. % (sols 603-606),  $0.8 \pm 0.1$  wt. % (sols 606-609),  $0.6 \pm 0.1$  wt. % (sols 609-630), and  $0.7 \pm 0.1$  wt. % (sols 631-634).

The lowest thermal neutron count rate measured,  $26.35 \pm 0.08$  thermal neutron counts per second, corresponds to a WEH estimate of  $0.2 \pm 0.2$  wt. %. This measurement was taken during sols 564-565 at a traverse distance of 5692.9 m and had an AEC abundance of  $1.6 \pm 0.19$  wt. %. This location is in the Smooth Hummocky unit, and it displays no unusual surface properties that suggest an anomalous bulk subsurface composition.

### ***Traverse WEH Estimates***

WEH estimates derived from DAN passive continuously-acquired traverse data are shown in Figure 3.8. WEH estimates from measurements acquired during rover traverses show greater variability than what is observed in the fixed location estimates. These estimates range from 0.0 wt. % WEH to  $15.3 \pm 1.1$  wt. % WEH. The average value is 2.5 wt. % WEH with a standard deviation of 1.4 wt. %. While the range of observed values is greater, this is likely due to the much larger number of locations measured because the statistical distribution of all traverse WEH estimates agrees very well that of the fixed location WEH estimates.

The highest WEH estimate is  $15.3 \pm 1.1$  wt. %, occurring at a traverse distance of 9214 m on sol 747. There are many other instances of these local-scale anomalies in the WEH estimates along the traverse. These typically have very high point to point correlation over a scale of meters to 10s of meters. An example is shown in Figure 3.9, where a local anomaly can be seen at ~3660 m as the WEH estimates increase to approximately 7.5 wt. % WEH and then return to

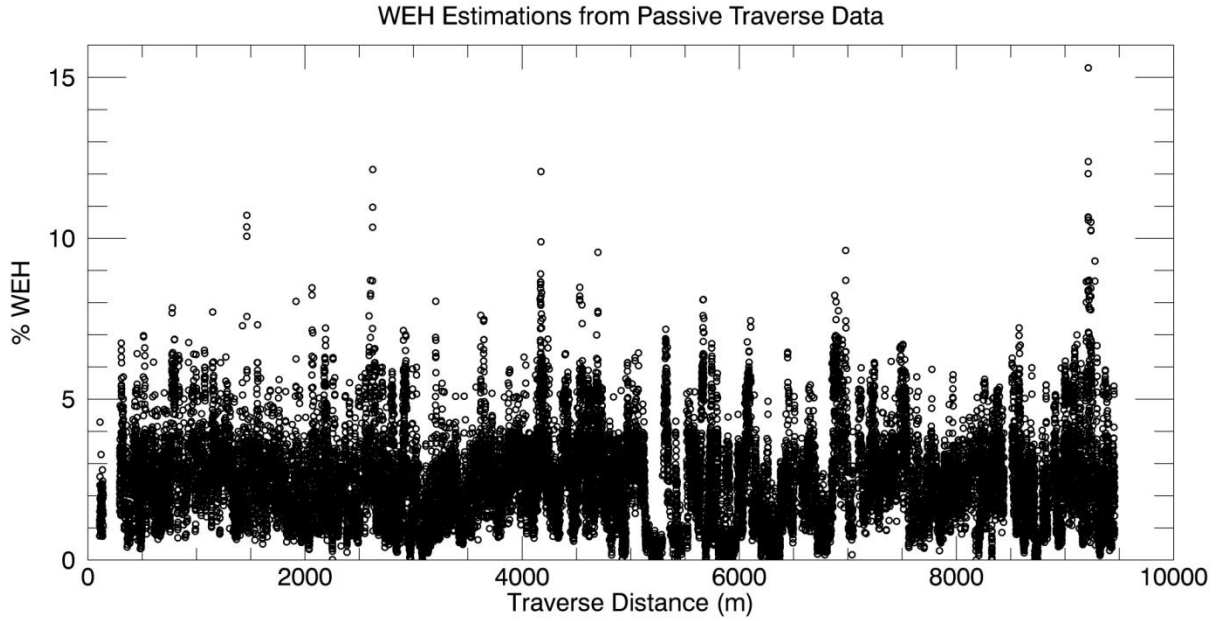


**Figure 3.8. WEH estimates along Curiosity's traverse from Bradbury Landing (traverse distance 0 m) to Amargosa Valley (traverse distance ~9435 m). Uncertainties are not shown for clarity, but the magnitude of typical traverse WEH estimates can be seen in Figure 3.9.**

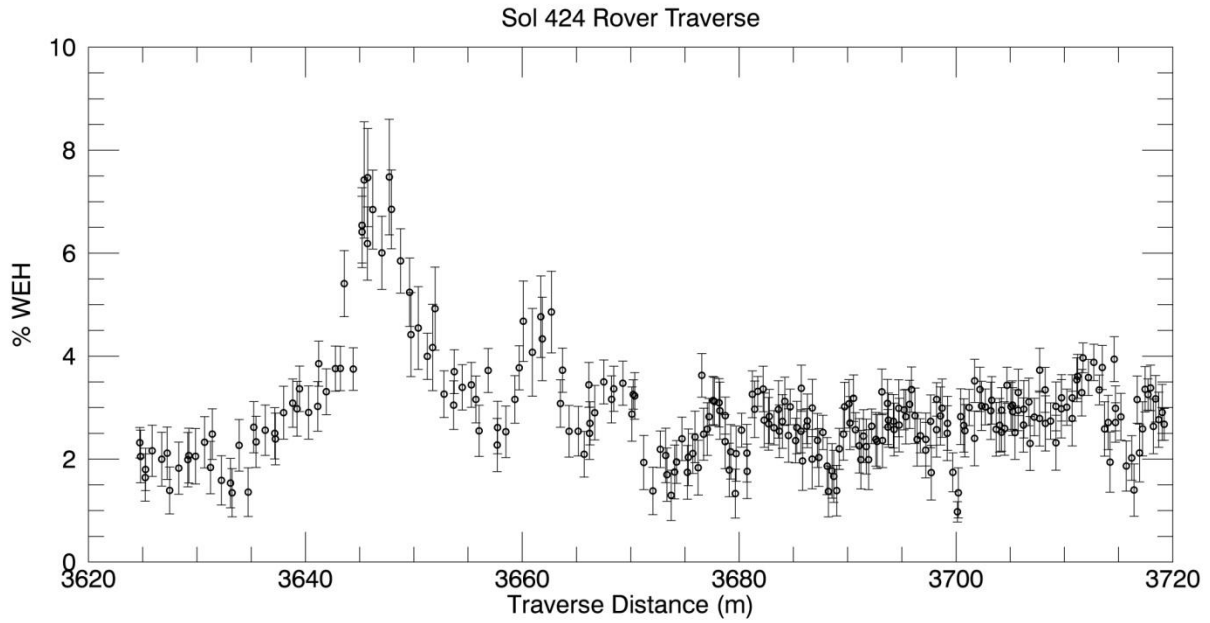


**Figure 3.9. WEH estimates from sol 424 traverse showing an example of the small-scale anomalies observed in the continuously-acquired DAN passive traverse data.**

more typical values.

Some other interesting examples of local anomalies can be seen on individual traverses on sols 403, 404, 406, 409, 412, 419, 424, 453, 470, 569, 572, 655, 657, 664, 665, 717, 746, 747, and 751. MSL drive direction images, which show the path of the rover on particular traverses, were examined in conjunction with DAN passive traverse WEH estimates, however, no strong correlations were found between variations in surface properties and variations in WEH estimates.

There are two large-scale elevated WEH regions along the traverse. These are at traverse distances ~4160 m to ~4210 m and ~6850 m to ~6950 m and can be seen in Figure 3.8. The average WEH estimates in these regions is 4.9 wt. % with a standard deviation of 1.7 wt. % and 4.7 wt. % with a standard deviation of 1.5 wt. %, respectively. The region from ~4160 to ~4210 is Ridged unit and exhibits exposures of mudstones. The region from ~6850 to ~6950 is a mixture of Ridged unit and Smooth Hummocky unit and exhibits a typical Smooth Hummocky surface throughout.

The lowest WEH estimates are 0.0 wt. % WEH, and the same caveats about the meaning of this value apply as for fixed locations discussed in Section 5.1 (Fixed Location WEH Estimates). There are 106 such measurements. These measurements generally occur in a few different traverse regions among other measurements of consistently low WEH. The two largest regions of low WEH estimates are observed at traverse distances of ~5150 m to ~5300 m and ~6120 m to ~6342 m (Kimberley outcrop). The average WEH estimate in these regions is 0.4 wt. % with a standard deviation of 0.3 wt. %, and 1.2 wt. % with a standard deviation of 0.8 wt. % for the two regions, respectively. The region from ~5150 m to 5300 m consist of typical Smooth Hummocky surfaces. The Kimberley outcrop region is also within the Smooth Hummocky unit.

Two smaller regions of low WEH estimates occur at ~4920 m to ~4925 m and ~8733 m to ~8752 m. The average WEH estimates in these regions is 0.4 wt. % with a standard deviation of 0.3 wt. %, and 0.4 wt. % with a standard deviation of 0.6 wt. %, respectively. The WEH depression at ~4920 m to ~4925 m corresponds with the Dingo Gap megaripple area, which is a sandy area. The region at a traverse distance ~8733 m to ~8752 m is a sandy region the rover crossed twice during these sols, which also includes some of the aforementioned megaripples. The fixed location measurements in these areas are in agreement with the continuously-acquired traverse measurements, with both yielding low WEH estimates.

## **Discussion**

### ***Fixed Location WEH Estimates***

DAN passive fixed location WEH estimates are strongly correlated with DAN active WEH estimates. This is not surprising, as these measurements are co-located along the traverse. Figure 3.10 shows the DAN passive WEH estimates plotted versus the DAN active WEH estimates.

The correlation coefficient between the two measurements is 0.79. The correlation coefficient increases to 0.91 if the correlation coefficient is calculated using only locations where the probability of model acceptance from DAN active results is greater than or equal to 70%. The average values between the co-located measurements of the two modes of operations compare very well, with 2.7 wt. % and a standard deviation of 0.6 wt. % WEH for DAN active measurements versus 2.4 wt. % and a standard deviation of 1.2 wt.% WEH for DAN passive measurements. Both of these data sets show depleted WEH content relative to HEND

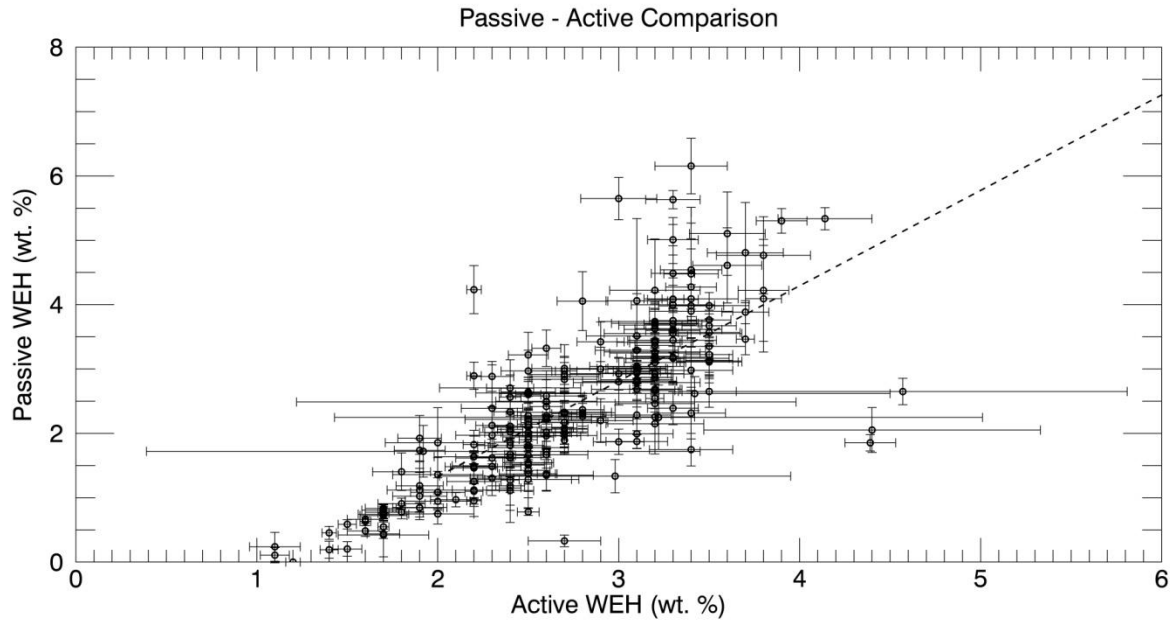


**Figure 3.10. DAN Passive WEH estimates versus DAN Active WEH estimates. The dashed line is line of best fit. The correlation coefficient is 0.79.**

measurements of the Gale crater region onboard Mars Reconnaissance Orbiter average (~5 wt.%). Interestingly, DAN passive WEH estimates do show a few regions and isolated areas that have WEH contents comparable to the HEND measurements or greater. However, the overall disagreement between the surface and orbital data sets is not entirely unexpected because of the large spatial resolution of the orbital measurements (Litvak *et al.*, 2013).

We have examined MSL Rear Hazard Camera images from the fixed locations to look for correlations between local surface properties, such as the amount of rocks, sand, or mudstones within the sensing footprint, and WEH estimates. Unfortunately, no specific surface type was observed to correlate with elevated or depleted WEH content. This is not unexpected, however, as previous work from earlier in the mission (Tate *et al.*, 2015b) also showed no such correlations. DAN passive measurements are simply not sensitive to surficial changes unless those changes extend to depths of 10s of centimeters.

The Kimberley outcrop region is one of the only locations where we have DAN passive data and co-located results from other MSL instruments. This is because the goal of driving to Mount Sharp required abbreviated science campaigns at most of the rover's stops along the RTR. DAN passive WEH estimates are consistently low within this region on Kimberley members Square Top and Dillinger. MSL CheMin results show that the Windjana sample, which was drilled from the Dillinger member, contains much less phyllosilicate material than what has previously been observed at the locations John Klein and Cumberland (Treiman *et al.*, 2016). MSL SAM results also show that the H<sub>2</sub>O abundance in the Windjana sample is less than what is observed at other sampling locations, *e.g.*, Rocknest, John Klein, and Cumberland (McAdam *et al.*, 2015). DAN passive WEH estimates from the fixed locations closest to the Dillinger member are therefore consistent with these results from the CheMin and SAM instruments.



### ***Traverse WEH Estimates***

The large range of WEH estimates derived from the DAN passive traverse data from sols 0 to 753 (Figure 3.8) is reasonable in the context of other compositional results. The APXS experiment has identified seven distinct and diverse classes of rocks in the same portion of the overall traverse (Thompson *et al.*, 2016). These diverse rock compositions are inferred to be indicative of diverse geologic histories, including hydrothermal alteration, in the crater rim source regions of the sediments filling the crater. The diverse history of these sediments would naturally lead to a large range of DAN passive WEH estimates.

There are local anomalies observed in the WEH estimates inferred from DAN passive traverse measurements ranging in lateral scale from a few meters to hundreds of meters. The strongest of these anomalies are identified in Section 5.2 (Traverse WEH Estimates). While some local negative anomalies in WEH are associated with the occurrence of sand accumulations on the surface, not all occurrences of sand are associated with negative anomalies in our WEH estimates. This indicates that surface properties are not always indicative of the subsurface composition. The large areal coverage of the DAN passive data set, however, allows us to investigate statistical differences in the WEH content of the large-scale geologic units traversed (Section 6.4 (Geologic Units)).

Localized positive and negative WEH anomalies (e.g., Figure 3.9) are most likely caused by elevated abundances or depletions of hydrated minerals, respectively. The locations of these anomalies appear scattered within the alluvial deposits that Curiosity traversed. Based on MSL APXS results, Thompson *et al.* (2016) suggested that some locations in the sediment source regions experienced very localized hydrothermal alteration prior to being dispersed across the crater floor through alluvial processes. Thus, the present day locations of these altered materials are scattered and not directly related to the locations where the alteration took place. The local

positive WEH anomalies seen in the DAN passive data may also be signatures of such deposits of hydrothermally altered materials. Because DAN cannot determine how hydrogen is bound within the subsurface and because there are no other compositional data from these locations, it is difficult to speculate further on the origin of these localized anomalies.

The traverse WEH estimates for the Kimberley outcrop region are consistently low, which agrees with the fixed location WEH estimates in this region. They are also consistent with results from the CheMin and SAM instruments that also show low phyllosilicate and H<sub>2</sub>O abundances (Treiman *et al.*, 2016; McAdam *et al.*, 2015). APXS results for the sediments around the Kimberley region lead to the conclusion that the environment these sediments formed in was neither warm nor wet (Thompson *et al.*, 2016). DAN passive WEH estimates are consistent with this conclusion.

The large range of WEH estimates seen from sols 0 to 753 is reasonable in the context of results from other instruments. For example, the APXS experiment has identified seven distinct and diverse classes of rocks in the same portion of the overall traverse (Thompson *et al.*, 2016). Assuming these diverse rock compositions are related to the source regions of the sediments filling the crater, the large range of DAN Passive WEH estimates is consistent with the diverse history of surfaces and sediments observed within Gale crater. This assumption is reasonable because of the presence of alluvial fans leading inward from the crater rim (Anderson and Bell, 2010) and possible glacial/periglacial erosion, transport, and deposition within the crater (Thompson *et al.*, 2016), both of which processes could transport sediment and material from the source regions to within the crater.

A few localized negative WEH anomalies along the traverse coincide with regions that contain sandy, aeolian ripples. These areas are the Rocknest area, the Dingo Gap area, and the

area investigated between sols 709-713. These specific examples of low WEH estimates corresponding to sandy ripples could be indicative of active saltation of the sand grains leading to the loss of any adsorbed surface water. There may also be a deficit of H-bearing clay minerals in these ripples because such minerals tend to break down into particle sizes much smaller than sand grains.

### ***DAN Passive Geochemical Index***

Inferring WEH estimates from DAN passive thermal neutron measurements – particularly traverse measurements – is inherently challenging because of the ambiguity associated with the unknown abundances of neutron-absorbing elements (represented as AEC) at any particular location. The analysis method described above uses reasonable assumptions about AEC values along traverses based on nearby DAN active measurements, but the reported WEH estimates must always carry the caveat that any differences between the actual AEC abundances and those assumed would introduce error in the WEH estimates. This being said, there is no doubt that most variations in the thermal neutron signal along the traverse are associated with geochemical variations in the regolith of some sort. For example, a particularly high thermal neutron count rate at a given location could be caused by a locally-enhanced WEH content *or* a local depletion in AEC (or both), but either way it represents the detection of a local geochemical anomaly. To capture this sensitivity to geochemical anomalies without incurring the ambiguities associated with estimating WEH abundances, we have devised a new metric called the DAN passive geochemical index (DPGI). This index makes no assumptions about the specific compositional nature of geochemical anomalies, it only flags where they occur.

In order to compare measurements taken at different locations and different times during the mission, the DPGI is calculated by removing systematic temporal variations from the

measured thermal neutron count rates that are caused by variations in the GCR, and then normalizing the corrected count rates at each location to the mean of all temporally-corrected count rates taken over the entire period from sols 0 to 753. Temporally-corrected thermal neutron count rates are determined by the equation

$$CR_S^{TC} = \gamma(t) * CR_S^{Meas}, \quad (2)$$

where  $CR_S^{TC}$  is the temporally-corrected thermal neutron count rate for a given location S,  $\gamma(t)$  is a time dependent correction factor given by equation 3 (below), and  $CR_S^{Meas}$  is the DAN passive measured thermal neutron count rate for a given location S. The correction factor,  $\gamma(t)$ , is given by the equation

$$\gamma(t) = CR_{t_0}^{Mod} / CR_{t_S}^{Mod}, \quad (3)$$

where  $CR_{t_0}^{Mod}$  is the modeled thermal neutron count rate using the GCR environment at the start of the mission and  $CR_{t_S}^{Mod}$  is the modeled thermal neutron count rate using the appropriate GCR environment for the time that the rover is at a given location S for the same regolith composition parameters as  $CR_{t_0}^{Mod}$ . These modeled counts rates incorporate the time-varying-nature of the GCR environment, calculated using RAD penetrating counter data as discussed in Section 2 (Methods).

In calculating  $\gamma(t)$ , we use a composition of 2 wt. % WEH and 1 wt. % AEC for both  $CR_{t_0}^{Mod}$  and  $CR_{t_S}^{Mod}$  so that  $\gamma(t)$  is only sensitive to variations in the GCR environment. The time-corrected thermal neutron count rates are then normalized to the mean time-corrected thermal neutron count rate from the entire period from sols 0 to 753 by the equation

$$CR_{NORM}^{TC} = CR_S^{TC} / CR_{MEAN}^{TC}, \quad (4)$$

where  $CR_{MEAN}^{TC}$  is the mean temporally-corrected thermal neutron count rate for sols 0 to 753.

The final DPGI metric is calculated by adjusting the  $CR_{NORM}^{TC}$  values so that they are distributed about the mean by the equation

$$DPGI \equiv (CR_{NORM}^{TC} - \overline{CR_{NORM}^{TC}}) / \sigma_{CR_{NORM}^{TC}}, \quad (5)$$

where  $\overline{CR_{NORM}^{TC}}$  is the mean of  $CR_{NORM}^{TC}$  and  $\sigma_{CR_{NORM}^{TC}}$  is the standard deviation of  $CR_{NORM}^{TC}$ .

A DPGI value of 1 thus corresponds to 1 standard deviation from the mean DPGI value. Figure 3.11 shows the value of the DGPI along the entire traverse from sol 0 to 753, and Figure 3.12 shows a histogram of these values. The  $\pm 3\sigma$  lines from the mean are also marked on Figures 3.11 and 3.12.

Any given DPGI value corresponds to a suite of allowable pairs of WEH and AEC values. Thus, if a potential user of DAN results disagrees with the assumptions about AEC we have used in Section 5.2 (Traverse WEH Estimates) to estimate WEH values, they may make an alternative choice for AEC and find the resulting WEH estimate using the DGPI and information presented in Figure 3.13. Note that the simulations used to generate this figure assume the “generic Mars” background regolith composition of McSween *et al.* (2010), as discussed in Section 2 (Methods). Locations with exceptionally anomalous background compositions (*e.g.*, the high silica deposits encountered after sol 753 at Marias Pass – see Jun *et al.* (2015)) require a different set of simulations using a different background composition.

DPGI values less than 0 generally represent compositions with low WEH and/or high AEC abundances, whereas DPGI values greater than 0 generally represent the opposite. Pathologic cases of high WEH combined with high AEC, or low WEH combined with low AEC could “cancel out” to produce DPGI values of close to 0, and thus would go unnoticed by this

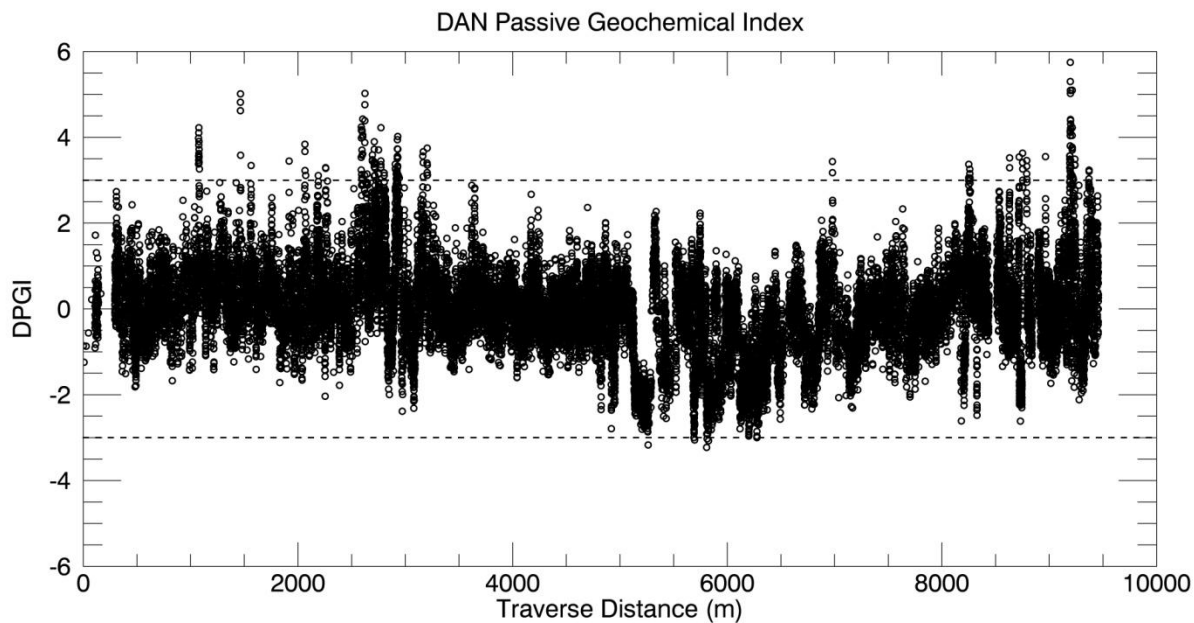


**Figure 3.11. DAN passive geochemical indices (DPGI) for all fixed and traverse measurement locations. Clusters of DPGI values greater than  $\pm 3\sigma$  from the mean are observed at traverse distances of ~1080 m, ~2070 m to 3218 m, ~5816 m, and ~8270 m to ~9205 m. The  $\pm 3\sigma$  lines are marked with the dashed lines.**

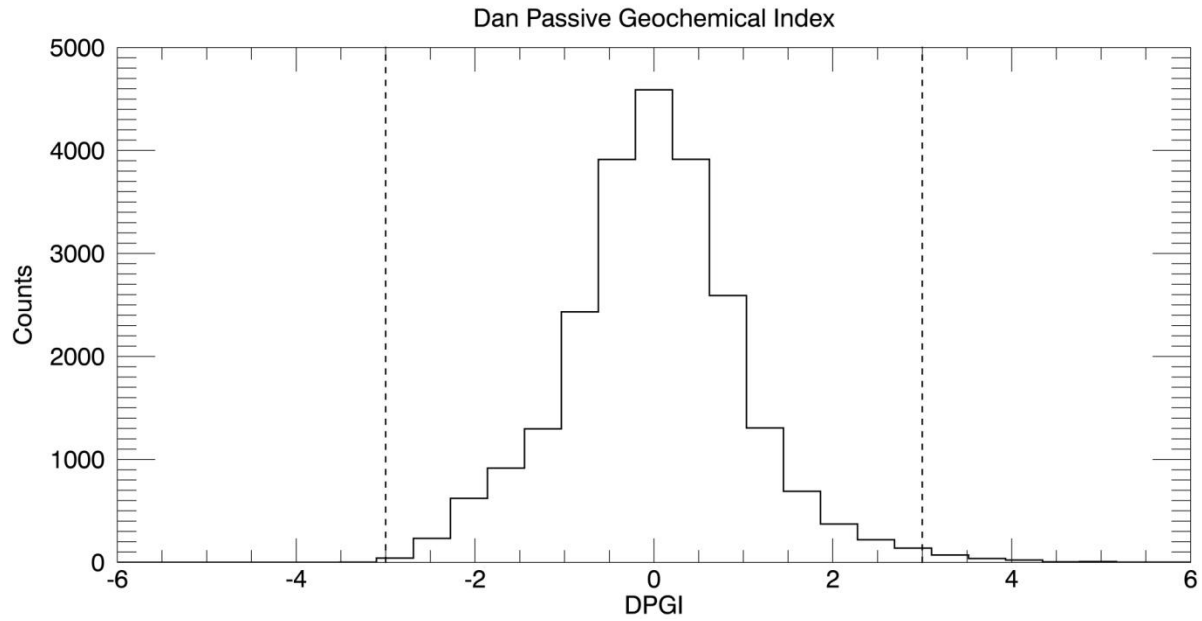


**Figure 3.12. Histogram of DAN passive geochemical index (DPGI) values derived from measurements acquired during sols 0 to 753 of the mission. The  $\pm 3\sigma$  lines are marked with the dashed lines.**

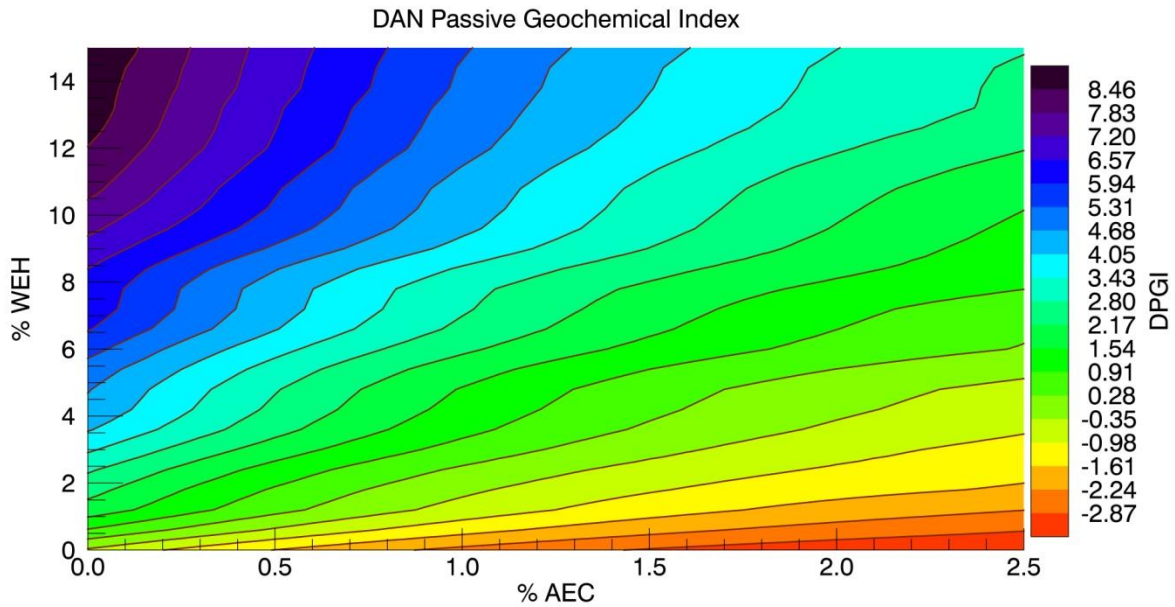


**Figure 3.13. Simulated DPGI values are calculated using the assumed “generic Mars” background regolith composition of McSween *et al.* (2010). For a given DPGI value, the suite of allowable WEH-AEC pairings may be found on this figure. Contours were calculated using spline fits across a grid of simulation results modeled at intervals of 0.5 wt. % in AEC and 1.0 wt. % in WEH. However, imperfect simulations, *i.e.* uncertainties in simulation results, leads to contours that are not perfectly smooth.**



by this index, so it cannot be considered as being sensitive to all possible anomalies in those parameters. On the other hand, locations with very low or high DPGI values are unambiguously anomalous.

As with our WEH estimates, the DPGI values show variability along the traverse and appear to be distributed normally (Figure 3.12), which agrees well our WEH estimates (Section 5 (Results)). The maximum DPGI value of  $5.75 \pm 0.88$  is observed at a traverse distance of 9195 m. This was on the Smooth Hummocky unit that is typical of Aeolis Palus in a location that did not exhibit anomalies in its visible surface geology. Other values greater than  $3\sigma$  from the mean are seen on Figure 3.11, but the corresponding anomalous areas along the traverse are much smaller in size.

The minimum DPGI value  $-3.23 \pm 0.28$  is observed at a traverse distance of 5807 m in a low DPGI region at ~5800 m, which is prior to, but approaching the Kimberley outcrop, where other low DPGI values and low WEH estimates can be seen. This area is classified as a part of the Smooth Hummocky unit. Corresponding WEH estimates in this region are very low.

The Kimberley outcrop region also has an extended traverse segment (~150 m) of generally low DPGI values, including values  $3\sigma$  below the mean. This suggests a bulk composition that is very different from the typical observed regolith composition along the traverse. The low DPGI values here are consistent with the low H<sub>2</sub>O measurements from SAM (McAdam *et al.*, 2015). They are also consistent with the measurements from APXS and CheMin, which indicate the region is enhanced in potassium (Thompson *et al.*, 2016; Treiman *et al.*, 2016) and other elements with non-negligible thermal neutron absorption cross sections, such as Fe, Mn, Cl, and Br (Thompson *et al.*, 2016). DAN active measurements are consistent with these measurements as well, showing the area to be generally enhanced in AEC and depleted in

WEH (Litvak *et al.*, 2016).

An added benefit of the DPGI is that it will provide for continued utility of the DAN experiment after its active mode ceases to function. Unfortunately, the PNG has a limited lifetime (Litvak *et al.*, 2008). As described in Section 2 (Methods), our method of estimating WEH requires the use of AEC values from DAN active mode measurements, but DPGI values do not have this dependence. Thus the DAN experiment will be able to provide utility beyond the lifetime of its active mode.

### ***Geologic Units***

During sols 0 to 753, MSL traversed 5 different geologic units on the crater floor. These units have been identified and mapped based on geomorphic, textural, and physical properties observed from orbit (Calef *et al.*, 2013; Grotzinger *et al.*, 2014). The large areal coverage of the DAN passive dataset allows for investigation of compositional differences between these units. Figure 3.14 shows the histograms of WEH estimates for each unit normalized to the number of measurements in those units.

In order to determine if statistically significant differences between the units exist, we have performed two-sample Kolmogorov-Smirnov Tests between the WEH populations of each unit for each possible pairing of units. The two-sample Kolmogorov-Smirnov Test compares the empirical distribution functions of two samples of data in order to determine whether the two samples came from the same distribution. All possible permutations between pairings of different units have been examined. Results from our testing show that these unit populations are statically different from each other at the 95% confidence interval. Furthermore, we also performed the same set of Kolmogorov-Smirnov Tests on the populations of DPGI values for each unit. The results are that the units are still distinguishable in their DPGI populations at the

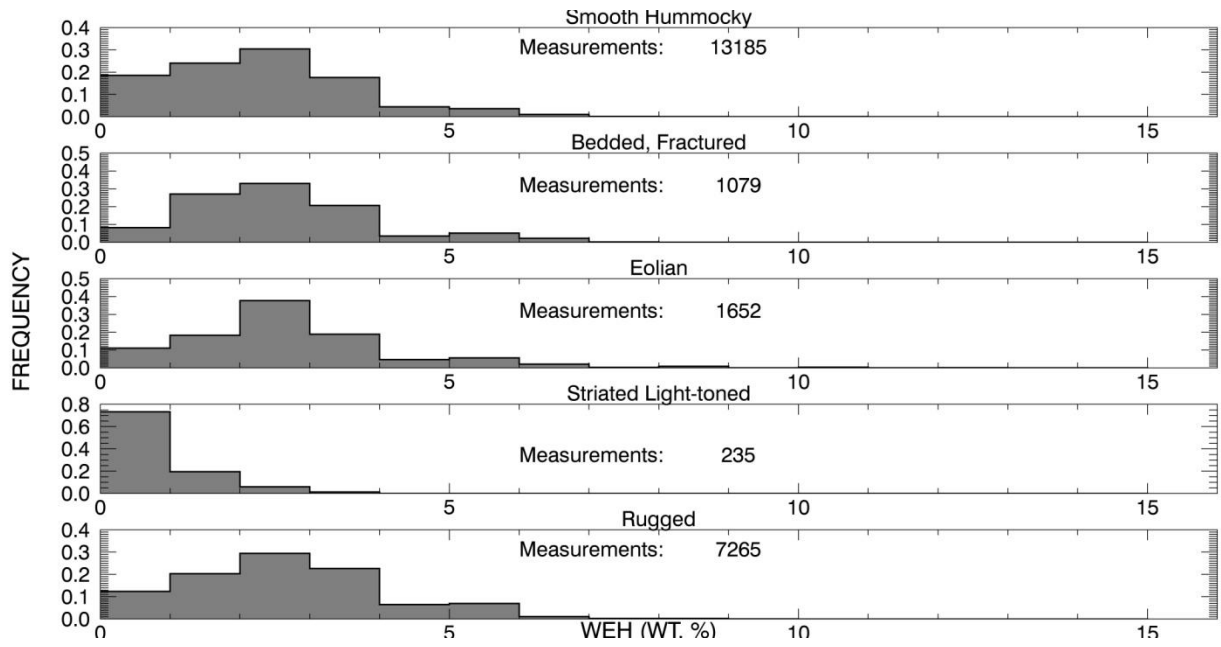


**Figure 3.14. Normalized histograms of WEH estimates from each unit traversed over during sols 0 to 753. Frequency is on the y-axis. WEH in 1.0 wt. % bins are on the x-axis. The number of measurements acquired in each unit is also shown.**

95% confidence interval. Furthermore, we also performed the same set of Kolmogorov-Smirnov Tests on the populations of DPGI values for each unit. The results are that the units are still distinguishable in their DPGI populations at the 95% confidence interval, with the exception of the Bedded, Fractured and the Rugged units. This result supports the conclusion that the statistically different units mapped within Aeolis Palus have compositional differences, and that those differences extend into the subsurface.

## Conclusions

There is a large range of thermal neutron count rates ( $20.80 \pm 0.62$  to  $97.47 \pm 2.76$ ) measured by the DAN passive experiment between sols 0 and 753. The analysis presented above shows that there is a correspondingly large range of WEH estimates (0.0 wt. % up to  $15.3 \pm 1.1$  wt. % ) at locations along the Rapid Traverse Route in Gale Crater. This diversity in WEH estimates is consistent with a complex and varied source region of sediments that have been transported and deposited in the location of the rover's traverse between sols 0 and 753 of the mission. Heterogeneity within the HEND instrument sensing footprint (~300 km) is apparent. The average DAN passive WEH content for the crater floor is less than the HEND average (Litvak *et al.*, 2013) for the region (2.5 wt. % versus ~5 wt. %), however, this is not surprising given the large difference in spatial resolution between the two experiments. DAN passive mode data agree well with DAN active mode results in terms of average WEH content (~2.7 wt. %) and spatial variations. DAN passive results are also consistent with measurements from other instruments, particularly within the Kimberley outcrop region, where there is general agreement about low water content. Most geologic units identified from orbital data are also distinguishable

in the DAN passive data, indicating that large-scale compositional differences extend into the subsurface for these units.

Finally, we have developed a new method for characterizing the DAN passive thermal neutron count rates (DPGI) as discussed in Section 6.4 (Geologic Units). The DPGI will also be useful for DAN passive data analysis after the PNG ceases to function. It will be especially interesting as *Curiosity* continues its investigations onto the units of Mount Sharp, which are thought to be members of stratigraphic and depositional environments different from Aeolis Palus (Grotzinger *et al.*, 2015) and contain hydrated minerals that have been observed from orbit (Milliken *et al.*, 2010). Comparing the DAN passive WEH/DPGI populations for differences between the Aeolis Palus units and Mt. Sharp units should help in understanding how different these units are and how the shallow regolith is changing as *Curiosity* traverses from the crater floor up the slopes of Mount Sharp.

## **Acknowledgements**

This work was financially supported by J. Moersch's MSL Participating Scientist Award (NASA JPL 1451872). We would also like to thank the MSL operations and science teams for helping acquire these data.

## References

- Anderson, R. B. and J. F. Bell III (2010), Geologic mapping and characterization of Gale Crater and implications for its potential as a Mars Science Laboratory landing site, *Mars* 5, 76-128, 2010; doi:10.1555/mars.2010.0004.
- Ardvison, R. E., K. D. Iagnemma, M. Maimone A. A. Fraeman, F. Zhou, M. C. Heverly, P. Belluta, D. Rubin, N. T. Stein, J. P. Grotzinger, and A. R. Vasavada (2016), Mars Science Laboratory Curiosity Rover Megaripple Crossings up to sol 710 in Gale Crater, *Journal of Field Robotics*, doi: 10.1002/rob.21647.
- Batchelor, R., R. Aves, and T. H. R. Skyrme (1955), Helium-3 Filled Proportional Counter for Neutron Spectroscopy, *Review of Scientific Instruments*, 26, 1037-1047.
- Calef, F. J., W. E. Dietrich, L. Edgar, J. Farmer, A. Fraeman, J. Grotzinger, M. C. Palucis, T. Parker, M. Rice, S. Rowland, K. M. Stack, D. Sumner, J. Williams, and the MSL Science Team (2013), Geologic mapping of the Mars Science Laboratory landing ellipse, Lunar and Planetary Science Conference, The Woodlands, Texas.
- Feldman, W. C., W. V. Boynton, R. L. Tokar, T. H. Prettyman, O. Gasnault, S. W. Squyres, R. C. Elphic, D. J. Lawrence, S. L. Lawson, S. Maurice, G. W. McKinney, K. R. Moore, and R. C. Reedy (2002), Global Distribution of Neutrons from Mars: Results from Mars Odyssey, *Science*, 297, DOI: 10.1126/science.1073541.
- Grotzinger, J. P., J. Crisp, A. R. Vasavada, R. C. Anderson, C. J. Baker, R. Barry, D. F. Blake, P. Conrad, K. S. Edgett, B. Ferdowski, R. Gellert, J. B. Gilbert, M. Golombek, J. Gómez-Elvira, D. M. Hassler, L. Jandura, M. Litvak, P. Mahaffy, J. Maki, M. Meyer, M. C. Malin, I. Mitrofanov, J. J. Simmonds, D. Vaniman, R. V. Welch, and R. C. Weins (2012), Mars Science Laboratory Mission and Science Investigation, *Space Science Reviews*, 170, doi:10.1007/s11214-012-9892-2.
- Grotzinger, J. P., D. Sumner, L. Kah, K. Stack, S. Gupta, L. Edgar, D. Rubin, K. Lewis, J. Schieber, N. Mangold, R. Milliken, P. Conrad, D. DesMarais, J. Farmer, K. Siebach, F. Calef III, J. Hurowitz, S. McLennan, D. Ming, D. Vaniman, J. Crisp, A. Vasavada, K. Edgett, M. Malin, D. Blake, R. Gellert, P. Mahaffy, R. Wiens, S. Maurice, J. Grant, S. Wilson, R. C. Anderson, L. Beegle, R. B. Anderson, T. Bristow, W. Dietrich, G. Dromart, J. Eigenbrode, A. Fraeman, C. Hardgrove, K. Herkenhoff, L. Jandura, G. Kocurek, S. Lee, L. Leshin, R. Leveille, D. Limonadi, J. Maki, S. McCloskey, M. Meyer, M. Minitti, H. Newsom, D. Oehler, A. Okon, M. Palucis, T. Parker, S. Rowland, M. Schmidt, S. Squyres, A. Steele, E. Stolper, R. Summons, A. Treiman, R. Williams, A. Yingst, and MSL Science Team (2014), A Habitable Fluvio-Lacustrine Environment at Yellowknife Bay, Gale Crater, Mars, *Science*, 343(6169), 1242777, doi:10.1126/science.1242777.
- Grotzinger, J.P., S. Gupta, D. Rubin, J. Schieber, D. Y. Sumner, K. Stack, A. Vasavada, R.

- Ardvison, F. Calef III, L. Edgar, W.F. Fischer, J.A. Grant, L.C. Kah, M.P. Lamb, K. Lewis, N. Mangold, M. Minitti, M. Palucis, M. Rice, K. Siebach, R. Williams, A. Yingst, D. Blake, D. Blaney, P. Conrad, J. Crisp, W.E. Dietrich, G. Dromart, K.S. Edgett, R. Ewing, R. Gellart, J. Griffes, J. Hurowitz, G. Kocurek, P. Mahaffy, M. Malin, S.M. McLennan, M. Mischna, D. Ming, R. Milliken, H. Newsom, D. Oehler, D. Vaniman, R. Wiens, and S. Wilson (2015), Deposition, Exhumation, and Paleoclimatology of an Ancient Lake Deposit, Gale Crater, Mars, *Science*, 350, doi: 10.1126/science.aac7575.
- Hassler, D.M., C. Zeitlin, R.F. Wimmer-Schweingruber, B. Ehresmann, S. Rafkin, J.L. Eigenbrode, D.E. Brinza, G. Weigle, S. Böttcher, E. Böhm, S. Burmeister, J. Guo, J. Köhler, C. Martin, G. Reitz, F.A. Cucinotta, M.-H. Kim, D. Grinspoon, M.A. Bullock, A. Posner, J. Gómez-Elvira, A. Vasavada, J.P. Grotzinger, and the MSL Science Team (2014), Mars' surface radiation environment measured with the Mars Science Laboratory's Curiosity rover, *Science*, 343(6169), 1244797, doi:10.1126/science.1244797.
- Jun, I., I. Mitrofanov, M. L. Litvak, A. B. Sanin, W. Kim, A. Behar, W. V. Boynton, L. DeFlores, F. Fedosov, D. Golovin, C. Hardgrove, K. Harshman, A. S. Kozyrev, R. O. Kuzmin, A. Malakhov, M. Mischna, J. Moersch, M. Mokrousov, S. Nikiforov, V. N. Shvetsov, C. Tate, V. I. Tret'yakov, and A. Vostrukhin (2013), Neutron background environment measured by the Mars Science Laboratory's (MSL) Dynamic Albedo of Neutrons Instrument during the first 100 sols, *Journal of Geophysical Research: Planets*, 118, 2400-2412, doi: 10.1002/2013JE004510.
- Jun, I., I. Mitrofanov, M. L. Litvak, A. B. Sanin, L. M. M. Sierra, J. Frydenvang, F. Fedosov, D. Golovin, C. Hardgrove, K. Harshman, A. S. Kozyrev, A. Malakhov, M. Mischna, J. Moersch, M. Mokrousov, S. Nikiforov, C. G. Tate, and the MSL Science Team, Observation of very high passive mode thermal neutron counts by the MSL DAN Instrument at Marias Pass in Gale Crater, American Geophysical Union Fall Meeting, San Francisco, California.
- Litvak, M.L., I. G. Mitrofanov, Yu. N. Barmakov, A. Behar, A. Bitulev, Yu. Bobrovniksky, E. P. Bogolubov, W. V. Boynton, S. I. Bragin, S. Churin, A. S. Grebennikov, A. Kononov, A. S. Kozyrev, I. G. Kurdumov, A. Krylov, Yu. P. Kuznetsov, A. V. Malakhov, M. I. Mokrousov, V. I. Ryzhkov, A. B. Sanin, V. N. Shvetsov, G. A. Smirnov, S. Sholeninov, G. N. Timoshenko, T. M. Tomilina, D. V. Tuvakin, V. I. Tret'yakov, V. S. Troshin, V. N. Uvarov, A. Varenikov, and A. Vostrukhin (2008), The Dynamic Albedo of Neutrons (DAN) experiment for NASA's 2009 Mars Science Laboratory, *Astrobiology*, 8, 605-613, DOI: 10.1089/ast.2007.0157.
- Litvak, M.L., I. G. Mitrofanov, A. Behar, W. V. Boynton, L. Deflores, F. Fedosov, D. Golovin, C. Hardgrove, K. Harshman, I. Jun, A. S. Kozyrev, A.S. Kozyrev, R.O. Kuzmin, A. Malakhov, R. Milliken, M. Mischna, J. Moersch, M. Mokrousov, S. Nikiforov, A. B. Sanin, V.N.Shvetsov, C. Tate, V. I. Tret'yakov, A. Vostrukhin and MSL Science Team (2013), Estimation of natural neutron emission from the surface of the Gale crater from the ground data from DAN and the orbital data from HEND, *Lunar and Planetary Science*

Conference, The Woodlands, Texas.

- Litvak, M. L., I. G. Mitrofanov, A. B. Sanin, D. Lisov, A. Behar, W. V. Boynton, L. DeFlores, F. Fedosov, D. Golovin, C. Hardgrove, K. Harshman, I. Jun, A. S. Kozyrev, R. O. Kuzmin, A. Malakhov, R. Milliken, M. Mischna, J. Moersch, M. Mokrousov, S. Nikiforov, V. N. Shvetsov, K. Stack, R. Starr, C. Tate, V. I. Tret'yakov, A. Vostrukhin, and the MSL Science Team (2014), Local variations of bulk hydrogen and chlorine-equivalent neutron absorption content measured at the contact between Sheepbed and Gillespie Lake units in Yellowknife Bay, Gale Crater, using the DAN instrument onboard Curiosity, *Journal of Geophysical Research: Planets*, 119, 1259-1275, doi:10.1002/2013JE004556.
- Litvak, M. L., I. G. Mitrofanov, C. Hardgrove, K. M. Stack, A. B. Sanin, D. Lisov, W. V. Boynton, F. Fedosov, D. Golovin, K. Harshman, I. Jun, A. S. Kozyrev, R. O. Kuzmin, A. Malakhov, R. Milliken, M. Mischna, J. Moersch, M. Mokrousov, S. Nikiforov, R. Starr, C. Tate, V. I. Tret'yakov, and A. Vostrukhin (2016), Hydrogen and Chlorine Abundances in the Kimberley Formation of Gale Crater Measured by the DAN Instrument Onboard the Mars Science Laboratory Curiosity Rover, *Journal of Geophysical Research: Planets*, 121, doi: 0.1002/2015JE004960.
- McAdam, A. C., P. D. Archer Jr., B. Sutter, H. B. Franz, J. L. Eigenbrode, D. W. Ming, R. V. Morris, P. B. Niles, J. C. Stern, C. Freissinett, D. P. Glavin, S. K. Atreya, D. L. Bish, D. F. Blake, P. R. Mahaffy, R. Navarro-Gonzalez, C. P. McKay, M. B. Wilhelm, and the MSL science team (2015), Major Volatiles From MSL SAM Evolved Gas Analysis: Yellowknife Bay Through Lower Mount Sharp, Lunar and Planetary Science Conference, The Woodlands, Texas.
- McKinney, G.W., J.W. Durkee, F.X. Gallmeier, J.S. Hendricks, M.R. James, D.B. Pelowitz, L.S. Waters, "MCNPX Overview", LA-UR-06-6206 (278 KB), Proceedings of the 2006 HSSW, FNAL, IL, September 6-8, 2006.
- McSween Jr, H.Y., I. O. McGlynn, and A. D. Rogers (2010), Determining the modal mineralogy of martian regoliths, *Journal of Geophysical Research*, 115, E00F12, doi:10.1029/2010JE003582.
- Milliken, R. E., J.P. Grotzinger, and B. J. Thomson (2010), Paleoclimate of Mars as captured by the stratigraphic record in Gale Crater, *Geophysical Research Letters*, 37, L04201, doi:10.1029/2009GL041870.
- Mitrofanov, I. G., D. Anfimov, A. S. Kozyrev, M. L. Litvak, A. B. Sanin, V. I. Tret'yakov, A. Krylov, V. Shvetsov, W. V. Boynton, C. Shinohara, D. Hamara, and R. S. Saunders (2002), Maps of subsurface hydrogen from the High Energy Neutron Detector, Mars Odyssey, *Science*, 297, 78-81.
- Mitrofanov, I. G., M. L. Litvak, A. B. Varenikov, Y. N. Barmakov, A. Behar, Y. I. Bobrovniksky, E. P. Bogolubov, W.V. Boynton, K. Harshman, E. Kan, A. S. Kozyrev, R. O. Kuzmin, A. V. Malakhov, M. I. Mokrousov, S. N. Ponomareva, V. I. Ryzhkov, A. B.



- Sanin, G. A. Smirnov, V. N. Shvetsov, G. N. Timoshenko, T. M. Tomilina, V. I. Tret'yakov, and A. A. Vostrukhin (2012), Dynamic Albedo of Neutrons (DAN) experiment onboard NASA's Mars Science Laboratory, *Space Science Review*, 170, 559–582, DOI 10.1007/s11214-012-9924-y.
- Mitrofanov, I. G., M. L. Litvak, A. B. Sanin, R. Starr, D. I. Lisov, R. O. Kuzmin, A. Behar, W. V. Boynton, C. Hardgrove, K. Harshman, I. Jun, R. Milliken, M. A. Mischna, J. E. Moersch, and C. G. Tate (2014), Content of water and chlorine in the martian regolith along the first 1900 meters of the traverse of Curiosity, as measured by DAN instrument onboard the rover, *Journal of Geophysical Research: Planets*, 119, 1579-1596, doi:10.1002/2013JE004553.
- Mitrofanov, I. G., A. S. Kozyrev, D. I. Lisov, A. A. Vostrukhin, D. V. Golovin, M. L. Litvak, A. V. Malakhov, M. I. Mokrousov, S. Yu. Nikiforov, and A. B. Sanin (2016a), Active Neutron Sensing of the Martian Surface with the DAN Experiment Onboard the NASA "Curiosity" Mars Rover: Two Types of Soil with Different Water Content in the Gale Crater, *Astronomy Letters*, 42, 251-259, doi: 10.1134/S1063773716040058.
- Mitrofanov, I. G., A. S. Kozyrev, D. I. Lisov, A. A. Vostrukhin, D. V. Golovin, M. L. Litvak, A. V. Malakhov, M. I. Mokrousov, S. Yu. Nikiforov, and A. B. Sanin (2016b), Active Neutron Sensing of the Martian Surface with the DAN Experiment Onboard the NASA "Curiosity" Mars Rover: Water Content in the Gale Crater, in prep.
- Tate, C.G., J. Moersch, I. Jun, C. Hardgrove, M. Mischna, M. Litvak, A. Varenikov, I. Mitrofanov, W.V. Boynton, L. Deflores, D. Drake, F. Fedosov, D. Golovin, K. Harshman, A.S. Kozyrev, D. Lisov, A. Malakhov, R. Milliken, M. Mokrousov, S. Nikiforov, A.B. Sanin, R. Starr, A. Vostrukhin, F. J. Martin-Torres, María-Paz Zorzano (2015a), Thermal conductivity of the near-surface martian regolith derived from variations in MSL passive neutron count and ground temperature measurements, Lunar and Planetary Science Conference, The Woodlands, Texas.
- Tate, C.G., J. Moersch, I. Jun, D. W. Ming, I. Mitrofanov, M. Litvak, A. Behar, W.V. Boynton, L. Deflores, D. Drake, B. Ehresmann, F. Fedosov, D. Golovin, C. Hardgrove, K. Harshman, D. M. Hassler, A.S. Kozyrev, R. Kuzmin, D. Lisov, A. Malakhov, R. Milliken, M. Mischna, M. Mokrousov, S. Nikiforov, A.B. Sanin, R. Starr, A. Varenikov, A. Vostrukhin, and C. Zeitlin (2015b), Water Equivalent Hydrogen Estimates from the first 200 sols of *Curiosity's* Traverse (Bradbury Landing to Yellowknife Bay): Results from the Dynamic Albedo of Neutrons (DAN) Passive Mode Experiment, *Icarus*, 262, 102-123, doi:10.1016/j.icarus.2015.09.002.
- Thompson, L. M., M. E. Schmidt, J. G. Spray, J. A. Berger, A. Faréin, J. L. Campbell, G. M. Perret, N. Boyd, R. Gellert, I. Pradler, and S. J. VanBommel (2016), Potassium-rich sandstones within the Gale impact crater, Mars: The APXS perspective, *Journal of Geophysical Research: Planets*, 121, 1981-2003, doi:10.1002/2016JE005055.
- Treiman, A. H., D. L. Bish, D. T. Vaniman, S. J. Chipera, D. F. Blake, D. W. Ming, R.V. Morris,

T. F. Bristow, S. H. Morrison, M. B. Baker, E. B. Rampe, R. T. Downs, J. Filiberto, A. F. Glazner, R. Gellert, L. M. Thompson, M. E. Schmidt, L. Le Deit, R. C. Weins, A. C. McAdam, C. N. Achilles, K. S. Edgett, J. D. Farmer, K. V. Fendrich, J. P. Grotzinger, S. Gupta, J. M. Morookian, M. E. Newcombe, M. S. Rice, J. G. Spray, E. M. Stopler, D. Y. Sumner, A. R. Vasavada, and A. S. Yen (2016), Mineralogy, provenance, and diagenesis of a potassic basaltic sandstone on Mars: CheMin X-ray diffraction of the Windjana sample (Kimberley area, Gale Crater), *Journal of Geophysical Research: Planets*, 121, 75-106, doi:10.1002/2015JE004932.

## Appendix

As stated in Section 2 (Methods), an empirically-derived geometric correction that compensates for the effects of varying positions of the MMRTG and DAN DE relative to the ground has been applied to the thermal neutron count rates before estimating WEH contents. Extreme variations in the distance between the DAN DE and the ground are unusual due to the fact that the rover typically drives over relatively benign surfaces. As a result, this correction is very small relative to the magnitude of variations in thermal neutron counts caused by regolith compositional variability. There are, however, a few instances of the rover driving over individual features that could affect the tilt of the rover (and other geometric factors) enough to significantly affect the thermal neutron count rates. In the first 753 sols of the mission, these features were all sandy mega-ripples as described in detail in Ardvison *et al.* (2016). DAN measurements acquired during the traversal of two of these features, one encountered on sol 535 and the other on sol 683, showed correlated decreases in the thermal and epithermal neutron count rates. The data acquired on sol 683 indicated the largest effect as evidenced by the large decrease in the epithermal neutron count rates at the position of the ripple as indicated by the position of the extrema around the SCLK time of  $4.58123 \times 10^8$  seconds in Figure A.3.1. Such correlations had not been observed in the data until these times.

The epithermal neutron count rates have been shown to be relatively invariant with respect to composition over the traverse (Jun *et al.*, 2013; Tate *et al.*, 2015b) and thus the abrupt decrease in this instance, which is much larger than the typical scatter observed in the epithermal neutron count rates, is inferred to be the result of geometric factors. While the thermal neutron count rates experience a larger magnitude decrease around the ripple, the majority of the

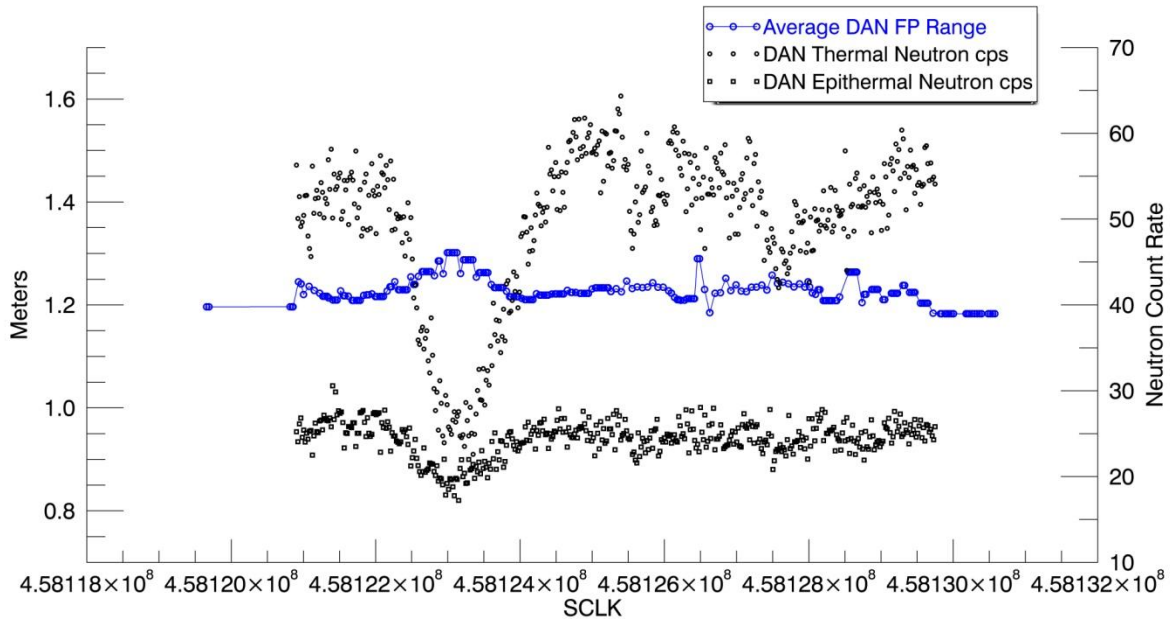


**Figure A.3.1. Uncorrected thermal and epithermal neutron count rates acquired during the sol 683 traverse of a large, sandy ripple. These neutron count rates have been averaged by odometry position. Also, shown is the average DAN to ground range within an assumed DAN footprint.**

decrease is most likely caused by non-geometric factors. The composition cannot be assumed to be constant because the presence of the sand is constrained to the ripple itself. Furthermore, similar decreases in thermal neutron count rates have been observed elsewhere in sandy areas that don't correlate with a ripple or a similar epithermal neutron count rate decrease. This implies very low hydrogen content for such sands which has the similar effect of drastically lowering the thermal neutron count rates. Lastly, simple simulations of varying DAN DE height show that unrealistic variations in height would be required to produce the observed changes in the measured thermal neutron count rates if the composition is fixed.

While the MMRTG occupies a well-defined space, it is not a point source of fast neutrons. Furthermore, simulations show that MMRTG-sourced neutrons interact with the MMRTG itself on their way "out", resulting in an even more extended effective source volume for those neutrons. Neutrons from this extended source interact with the rover and the ground. Again, simulations show that the random scattering of these neutrons within the regolith results in an extended surface area from which the neutrons are leaking back toward the detectors. If both the MMRTG and the surface area that neutrons leak out of were point sources, a  $1/r^4$  dependence of count rates on the height of the MMRTG and detectors ( $1/r^2$  for the neutrons traveling from the MMRTG to ground and then another  $1/r^2$  for the neutrons traveling from the ground to detectors) would be expected, but the strength of the dependence is greatly lessened because of the extended nature of these elements. Lastly, the MMRTG and DAN DE heights do not simply increase and decrease vertically with respect to the ground because they are attached to the rover body. These heights are ultimately a function of the rover tilt as controlled by the local (on order of the size of the rover's wheelbase) topography and the response of the suspension system to that topography. Rover tilt, local topography, and possibly shielding of the

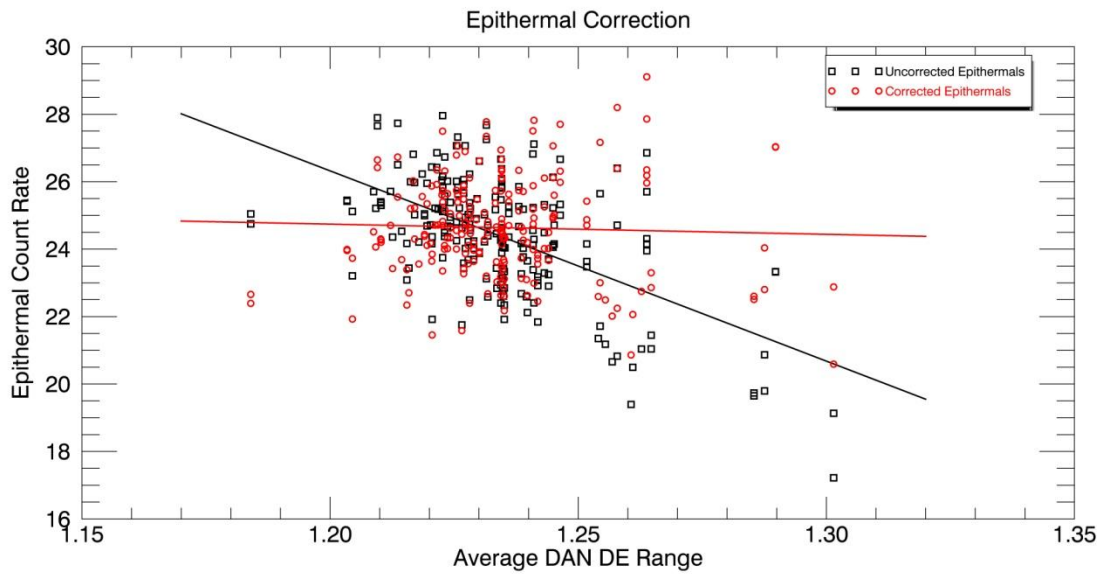
ground by the body of the rover will affect the measured neutron count rate dependence. Simulating such effects is difficult and would have to be performed at the position of every DAN passive measurement using the actual local topography involved, and more importantly, the rover suspension system response. Ultimately, the implication is there is not a simple relationship between detector height and the measured count rates. For these reasons we have used the epithermal neutron count rates and the geometry derived from rover telemetry data around this ripple to derive an empirical correction to apply to the epithermal and thermal neutron count rates.

MSL telemetry data have been investigated to find the strongest correlation between different geometric factors and epithermal neutron count rates while crossing the sol 683 ripple. It was found that the strongest correlation between the epithermal neutron count rates and geometry of the detector to the ground was observed when using an average DAN DE to ground range taken within an assumed ground footprint of 1.5 meter radius centered beneath the DAN DE. This is also shown in Figure A.3.1. We infer that there must also be a detector-ground geometric effect on the thermal neutron count rates, even though the dominant reason for the observed dip is likely to be compositional.

The average range is calculated by reconstructing an approximate ground surface using MSL telemetry data. These data include the 3-dimensional locations of the wheels and the DAN DE and MMRTG at discrete positions along the traverse in the "site" reference frame, which uses a fixed position on the ground as its origin. The approximate shape of the ground surface is reconstructed by fitting a plane to the four rear wheels of the rover at each telemetry position. Each plane is filled with points at a constant density to build a point cloud of the surface. Spatially overlapping segments between the current plane and the ground surface point cloud are

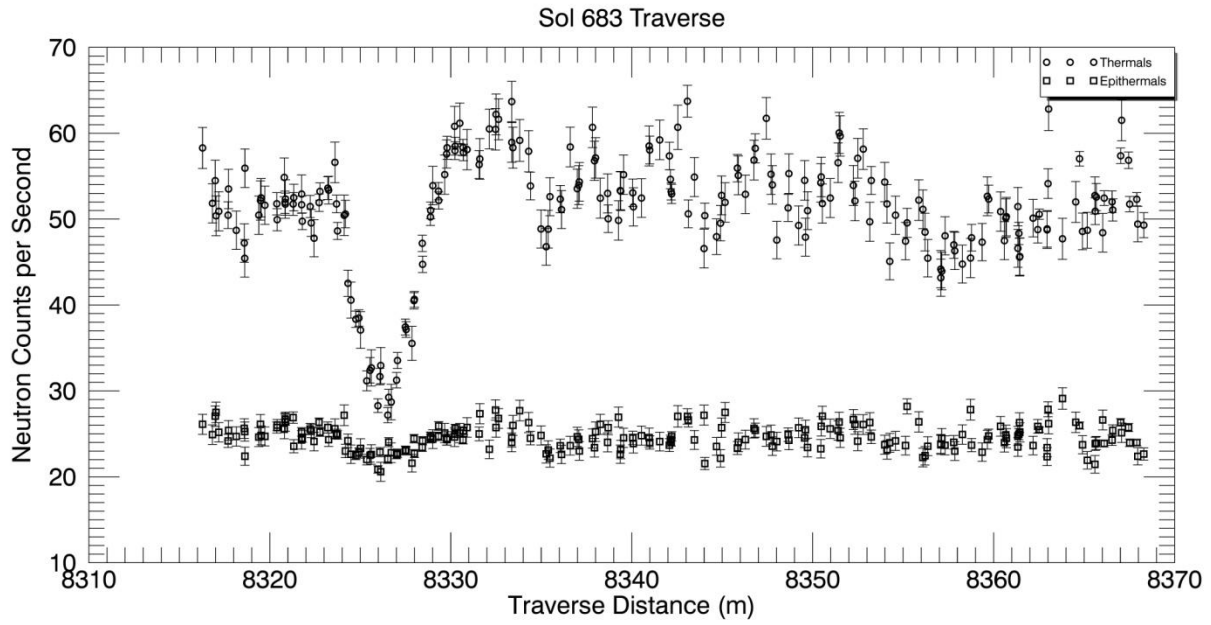
removed through the construction of a convex hull around the ground surface points and comparing it to the generated points for the current plane. The non-overlapping points can then be added to the ground surface point cloud. The DAN DE range on a nominal flat surface is calculated in the same manner. This range, combined with the nominal average range calculated from the surface topography can be used to construct a correction for each point along the traverse as follows: We make the assumption that epithermal neutron count rates are only affected by geometric factors and fit a linear relationship between the average DAN DE range values and the epithermal neutron count rates encountered while traversing the ripple on sol 683. The correction factor as a function of the average DAN DE range is defined as the epithermal neutron count rate at the nominal average DAN DE range divided by the predicted epithermal neutron count rate for the average DAN DE range at every position along the traverse. The measured epithermal and thermal neutron count rates are then multiplied by this correction factor to produce corrected epithermal and thermal neutron count rates. The uncorrected and corrected epithermal neutron count rates from sol 683 in the vicinity of the ripple are shown in Figure A.3.2.

Figure A.3.3 shows the corrected thermal and epithermal neutron count rates from sol 683. The epithermals in this case are not perfectly flat as the correction is based on the fit seen in Figure A.3.2, which involves inherent scatter in our epithermal neutron count rate measurements and telemetry data, resulting in a less-than-perfect fit to the data. The magnitude of the correction to the thermal neutron count rates around the minimum during the sol 683 traverse is ultimately ~5 thermal neutron counts per second. In this specific case, the WEH estimates are raised from 0.0 wt. % to ~0.3 wt. %, which is within the extreme case of WEH variations induced by vertical height variations estimated by Tate *et al.* (2015b).



**Figure A.3.2. Averaged uncorrected and corrected epithermal neutron count rates versus average DAN DE range acquired on sol 683 in the vicinity of the ripple. The corresponding lines of best fit for each quantity are shown in their respective colors.**





**Figure A.3.3. Corrected thermal and epithermal neutron count rates from sol 683 as a function of traverse distance and averaged by odometry location.**

Fortunately, this correction is small. The effect on the count rates observed on sol 683 is the largest such departure from nominal encountered during sols 0 through 753 of the mission based on examination of the data. However WEH estimates, rather than count rates, are ultimately what are important, and larger deviations in WEH estimates can occur. This is due to the sensitivity of the neutron leakage flux to changes within the parameter space (*i.e.*, WEH and AEC) with respect to the thermal neutron count rates, but such deviations are not common.

The method of constructing the surface topography can produce spurious points in places where the rover telemetry data is sparse, missing, and/or circling in place. The average DAN DE range throughout the traverse has been filtered for such points and these have been removed. A histogram showing the distribution of the filtered average DAN DE range as has been applied in this analysis is shown in Figure A.3.4.

Lastly, a comparison has been made between the WEH estimates with no geometric correction applied and WEH estimates with the geometric correction applied. A histogram of the induced differences in WEH estimates ( $\Delta$ WEH) is shown in Figure A.3.5 showing that the vast majority of our results are only negligibly affected by this correction, while about 10% are affected by amounts greater than  $\pm 0.4$  wt. % , which is the approximate total uncertainty for DAN passive WEH estimates described in Tate *et al.* (2015b).

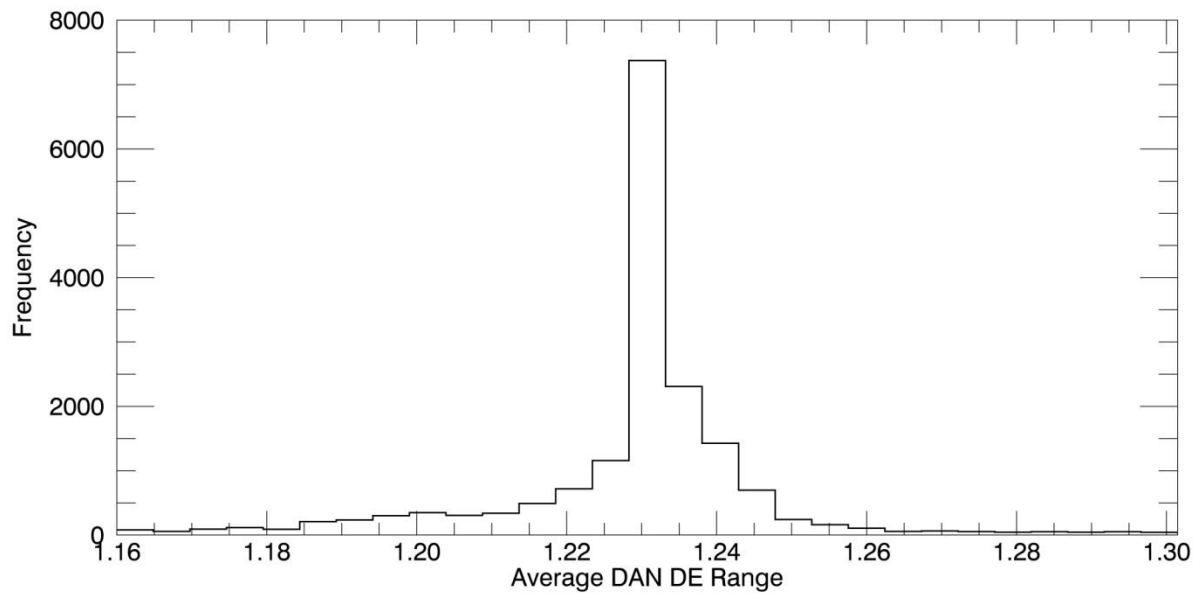


**Figure A.3.4. Histogram of the calculated average DAN DE ranges for the mission through sol 753.**

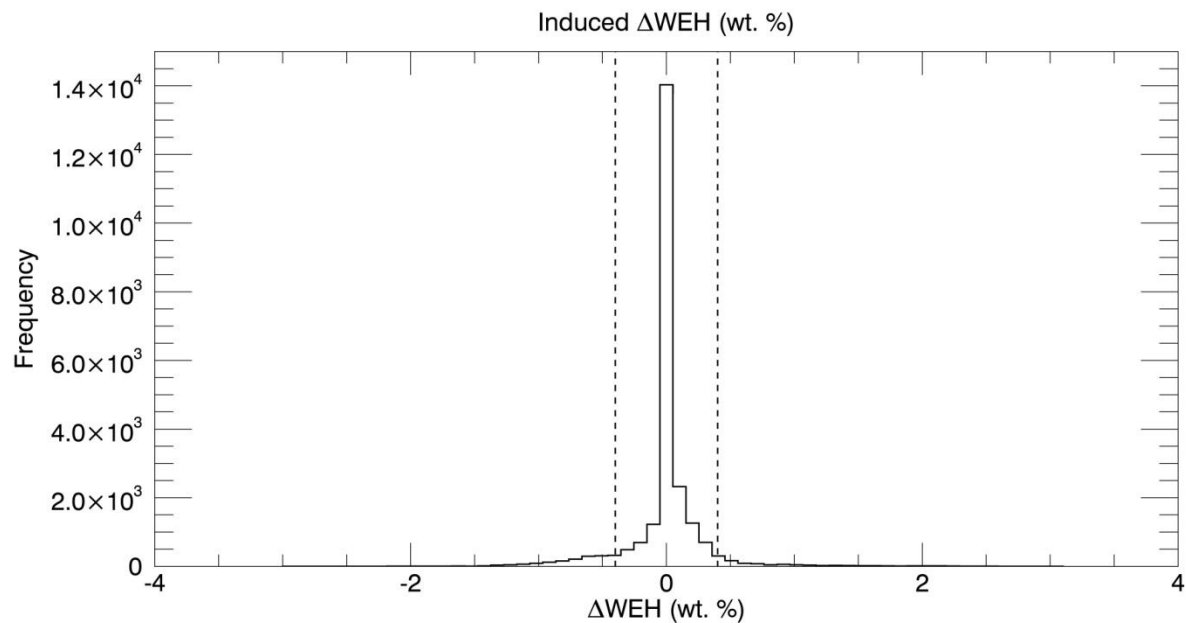


**Figure A.3.5. Histogram of induced  $\Delta$ WEH values between WEH estimates produced with the geometric correction applied and not applied. The dashed lines represent  $\pm 0.4$  wt. % WEH variations.**

**CHAPTER IV**  
**OBSERVED DIURNAL VARIATIONS IN MSL DYNAMIC ALBEDO OF**  
**NEUTRONS PASSIVE MODE DATA**

A version of this chapter will be submitted by Christopher G. Tate *et al.*:

Tate, C.G., J. Moersch, I. Jun, I. Mitrofanov, M. Litvak, W.V. Boynton, D. Drake, F. Fedosov, D. Golovin, C. Hardgrove, K. Harshman, A.S. Kozyrev, R. Kuzmin, D. Lisov, A. Malakhov, R. Milliken, M. Mischna, M. Mokrousov, S. Nikiforov, A.B. Sanin, R. Starr, and A. Vostrukhin (2017), Observed Diurnal Variations in MSL Dynamic Albedo of Neutrons Passive Mode Data, in prep.

The student (Christopher G. Tate) is the lead author and researcher of this work. This article will be submitted to the journal *Nuclear Instruments and Methods*. All co-researchers listed are members of the Mars Science Laboratory Dynamic Albedo of Neutrons team and have varying levels of involvement in this work. Most co-authors only contributed directly through instrument pre-flight building and testing and or surface operations. J. Moersch has the most involvement with this project, helping with simulation creation and verification and interpreting results.

### **Abstract**

The Mars Science Laboratory Dynamic Albedo of Neutrons experiment (DAN) measures the martian neutron leakage flux in order to estimate the amount of water equivalent hydrogen present in the shallow regolith. When DAN is operating in passive mode, it is sensitive to neutrons produced through the interactions of galactic cosmic rays (GCR) with the regolith and atmosphere and neutrons produced by the rover's Multi-Mission Radioisotope Thermoelectric Generator (MMRTG). During the mission, DAN passive mode data were collected over the full diurnal cycle at the locations known as Rocknest (sols 60-100) and John Klein (sols 166-272). A weak, but unexpected, diurnal variation was observed in the neutron count rates reported at these locations. We investigate different hypotheses that could be causing these observed variations. These hypotheses are variations in subsurface temperature, atmospheric pressure, the exchange

of water vapor between the atmosphere and regolith, and instrumental effects on the neutron count rates. Our investigation suggests the most likely factors contributing to the observed diurnal variations in DAN passive data are instrumental effects and time-variable preferential shielding of alpha particles, with other environmental effects only having small contributions.

## Introduction

The Dynamic Albedo of Neutrons instrument (DAN) onboard the Mars Science Laboratory (MSL) rover *Curiosity* has been acquiring data from the surface of Mars since August, 2012. The mission has been successful in finding a habitable environment for life (Grotzinger *et al.*, 2014) and expanding our understanding of Mars history and the role water has played in that history (Grotzinger *et al.*, 2015). The DAN instrument has contributed to this understanding by making measurements that are sensitive to local variations of hydrogen and chlorine content within the shallow regolith (Mitrofanov *et al.*, 2016; Litvak, *et al.*, 2016; Tate *et al.*, 2015).

DAN measures the martian neutron leakage flux. It utilizes two  $^3\text{He}$  proportional counters, one of which is unshielded and detects neutrons of energies up to  $\sim 100$  keV (Litvak *et al.*, 2008). This counter is known as the counter of total neutrons (CTN). The second counter, known as the counter of epithermal neutrons (CETN), is shielded with a cadmium jacket, which absorbs thermal neutrons below  $\sim 0.4$  eV, the cadmium cutoff (Litvak *et al.*, 2008). This allows for detection of only neutrons at epithermal energies above the cadmium cutoff. By differencing the count rates produced by the two counters, DAN is sensitive to the thermal neutron population. DAN can operate in two modes, an active mode and a passive mode. Active mode involves the use of a pulse neutron generator (PNG) to produce high intensity pulses of high energy neutrons (Litvak *et al.*, 2008). Results from DAN active mode operations are presented in Mitrofanov *et al.* (2014), Mitrofanov *et al.* (2016), Litvak *et al.* (2014), and Litvak *et al.* (2016). In passive mode, the instrument acquires neutron counting data without the use of the PNG. There are two sources of neutrons that DAN is sensitive to in passive mode: the Multi-Mission Radioisotope Thermoelectric Generator (MMRTG) and galactic cosmic rays (GCR). For further



discussion of DAN's passive mode of operation, specifically in relation to the radiation environment, see Jun *et al.* (2013). For DAN passive results and water equivalent hydrogen estimates, see Tate *et al.* (2015) and Tate *et al.* (submitted). This work will focus on the DAN passive data acquired from two specific locations early in the mission.

An unexpected observation from DAN passive data is the presence of a weak diurnal variation in the martian neutron leakage fluxes measured at the locations Rocknest and John Klein, which the rover was stationary at for multiple weeks. The purpose of this work is to test proposed hypotheses for the cause of the observed variations. We will show the diurnal variations as detected in the data, present multiple working hypotheses for the cause of the variations, and describe the methods used to test each hypothesis. This will be followed by an evaluation of the results that leads to the conclusion that the most reasonable explanation for the variations is a combination of instrumental effects and effects due to variations in the local environment of which an increase in neutron production in the regolith due to time-variable preferential shielding of primary GCR alpha particles by the martian atmosphere is the largest.

## **Data**

### ***DAN Passive Data***

Though *Curiosity* is nearly always on the move and investigating new locales, there were two sites early in the mission that the rover stayed at for particularly extended durations. These locations are known as Rocknest (sols 59-100) and John Klein (sols 166-272). Staying at the same locations for multiple weeks allowed the DAN instrument to acquire data over many diurnal cycles with nearly complete time-of-sol coverage and no changes in the non-volatile

composition of the regolith. When these data are examined, however, an increase is observed in the CTN and thermal neutron count rates and a decrease is observed in the CETN neutron count rates that coincides roughly with the middle of the sol and peaking in early to mid afternoon hours. Figures 4.1 and 4.2 show the data from the two locations. There is no reason to suppose that there is anything unique about these locations that would produce the observed diurnal variations in neutron count rates. The amplitudes of the variations are simply too weak to be noticeable against the statistical noise in the count rates from locations where the rover had shorter stays, and it is far smaller than the changes in count rates associated with compositional variations encountered by the rover along its traverse.

The amplitudes and phases of the variations in measured neutron count rates can be seen in Figures 4.1 and 4.2. CTN and thermal neutron count rates at each location increase in the afternoon, while CETN count rates decrease. Rocknest average CTN count rates show a peak to peak 3.3% increase. Average thermal neutron count rates increase by 9.5% and average CETN neutron count rates decrease by 6.7%. At John Klein, average CTN neutron count rates increase by 2.7%. Average thermal neutron count rates increase by 5.7%. Average CETN neutron count rates decrease by 4.1%. Furthermore, CETN neutron count rates typically do not vary with compositional changes (Jun *et al.*, 2013; Tate *et al.*, 2015) and thus it is interesting that the epithermal population in these cases is responding to some other factor, which is possibly instrumental.

In order to verify that the observed variations are occurring on a diurnal time scale with a one sol periodicity, we have performed Fourier analyses on the thermal neutron count rates from each location. Figures 4.3 and 4.4 show the power spectra from the Fourier analysis at each location. These results show a large increase in the power at a frequency of 1/sol confirming the

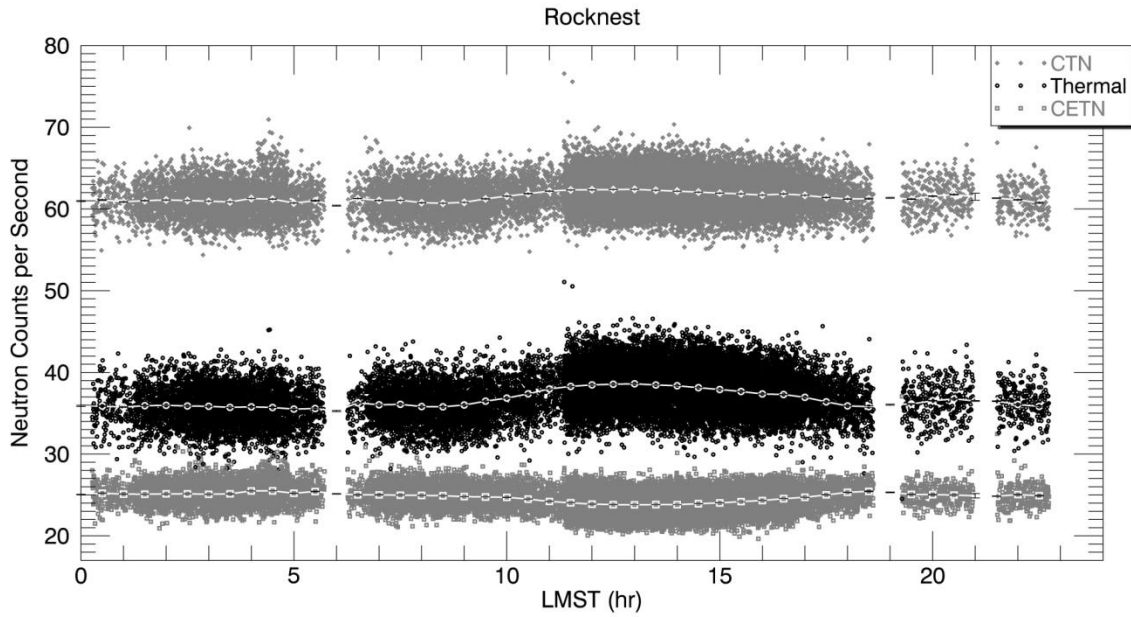


**Figure 4.1. DAN passive data from Rocknest acquired over sols 60 through 99, plotted as a function of Local Mean Solar Time (irrespective of sol number). Averaged count rates for 30-minute bins are overlaid in white symbols. Shown uncertainties for these averaged count rates are on the order of the symbol size.**

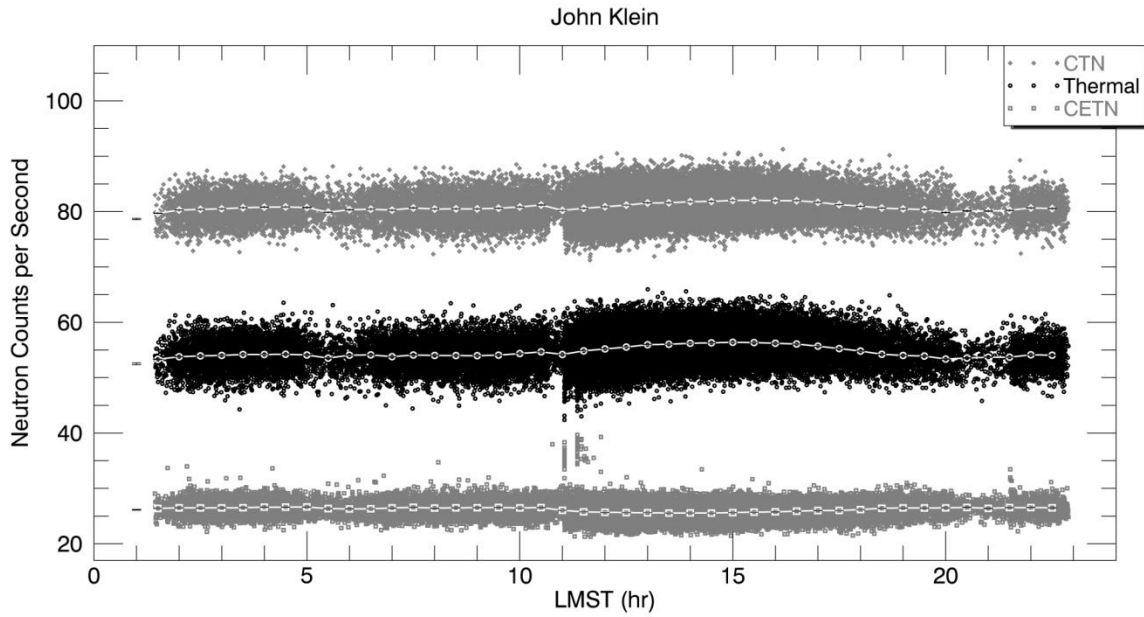


**Figure 4.2. DAN passive data from John Klein acquired over sols 166 through 271, plotted as a function of Local Mean Solar Time (irrespective of sol number). Averaged count rates for 30-minute bins are overlaid in white symbols. Shown uncertainties for these averaged count rates are on the order of the symbol size.**

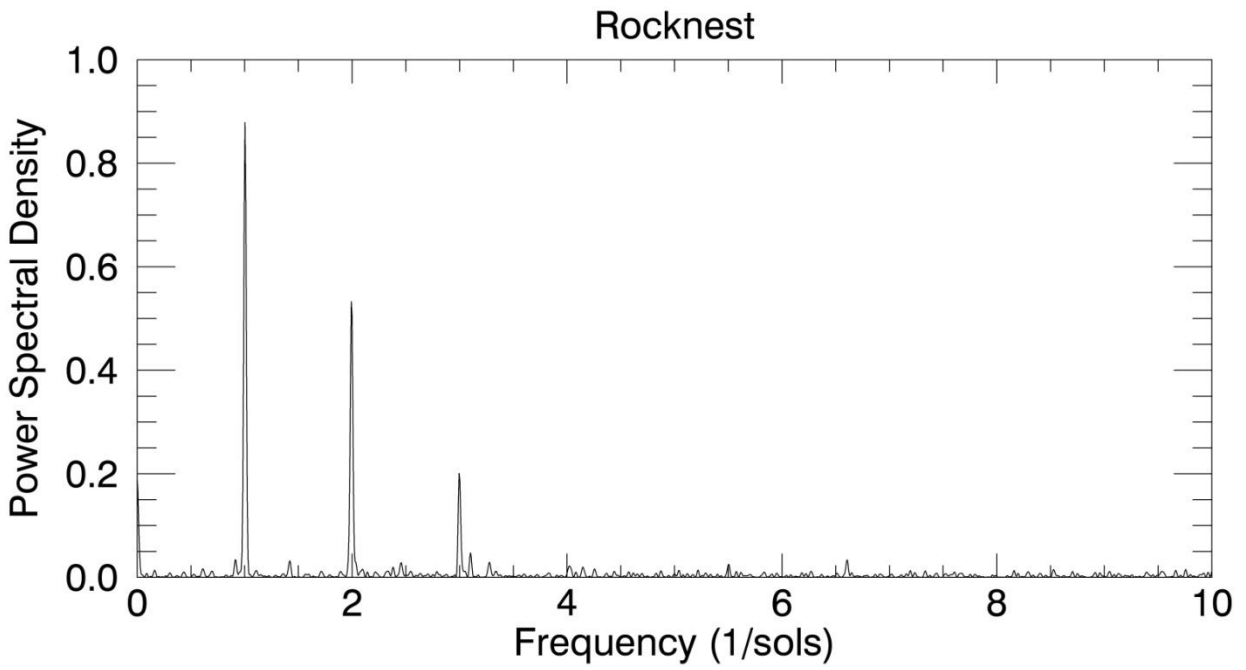


**Figure 4.3. Rocknest power spectrum of DAN passive measured thermal neutron count rates from Fourier analysis showing 1 sol periodicity.**

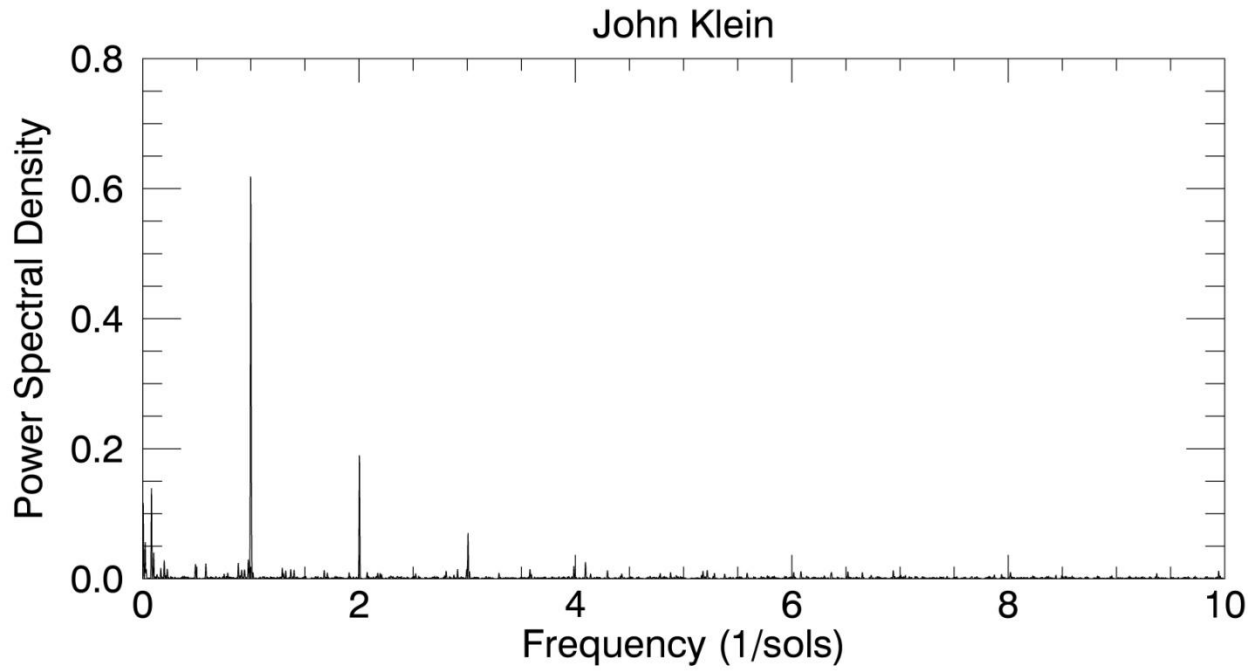


**Figure 4.4. John Klein power spectrum of DAN passive measured thermal neutron count rates from Fourier analysis showing 1 sol periodicity.**

diurnal nature of the variations observed in the DAN passive measurements.

### ***Data From Other MSL Instruments***

The MSL Rover Environmental Monitoring Station (REMS) experiment measured surface temperature and atmospheric pressure, which also vary with diurnal periodicity (Gómez-Elvira *et al.*, 2012). REMS measures surface temperature within a patch of ground 100 m<sup>2</sup> adjacent to the rover (Gómez-Elvira *et al.*, 2012). We have used REMS surface temperature and atmospheric pressure data to model the response of neutron leakage fluxes to variations in those quantities. The average atmospheric pressures and surface temperatures measured by REMS at Rocknest and John Klein are shown in Figures 4.5 and 4.6.

We have also used data and results from the MSL Radiation Assessment Detector (RAD) (Rafkin *et al.*, 2014). We use RAD penetrating counter data in our analysis to constrain the variations in the energetic particle environment at the surface per Tate *et al.* (2015). We have also used results of investigations into diurnal particle fluxes as measured by RAD during the first 350 sols of the mission (Rafkin *et al.*, 2014).

### ***Engineering Data***

Engineering data sets have also been used in the work presented here. MSL telemetry data, specifically DAN detector temperatures, have been used to investigate the relationship between detector temperature and DAN passive measurements.

## **Hypotheses Tested**

In order to investigate the diurnal variations in the measured neutron count rates, it is necessary to develop multiple hypotheses which might be contributing to the variations and investigate each individually. This is done by modeling each of the hypotheses with real data or

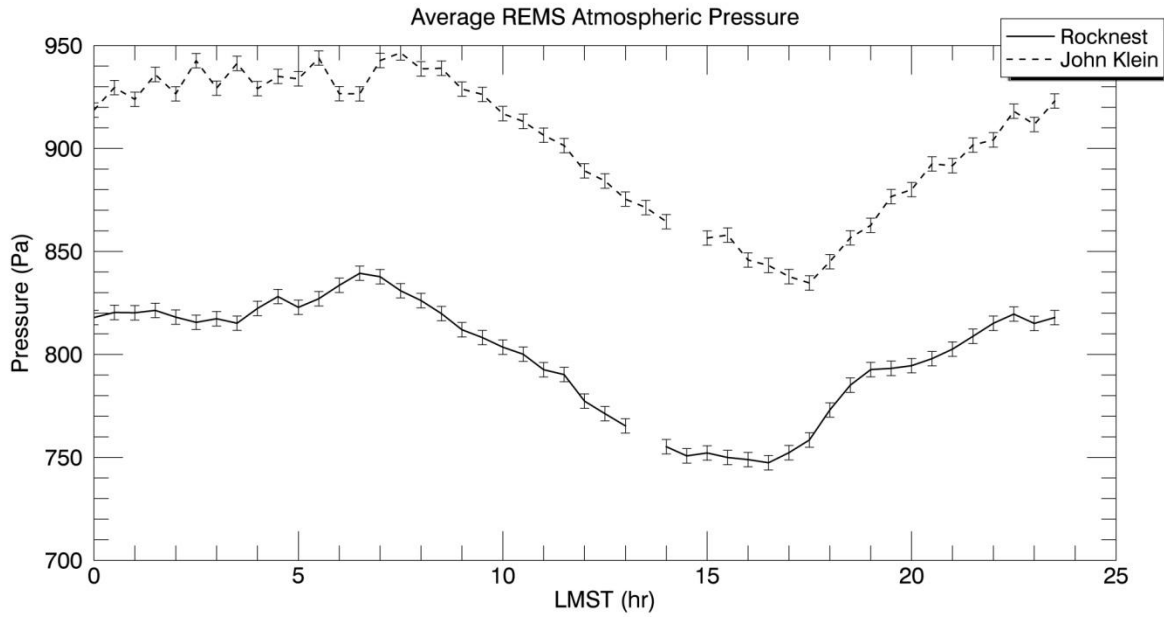


**Figure 4.5. Average atmospheric pressure at Rocknest (solid line) and John Klein (dashed line), plotted as a function of Local Mean Solar Time. Diurnal variations in pressure are on the order of ~100 Pa, while John Klein absolute pressures are ~100 Pa greater than pressures at Rocknest.**



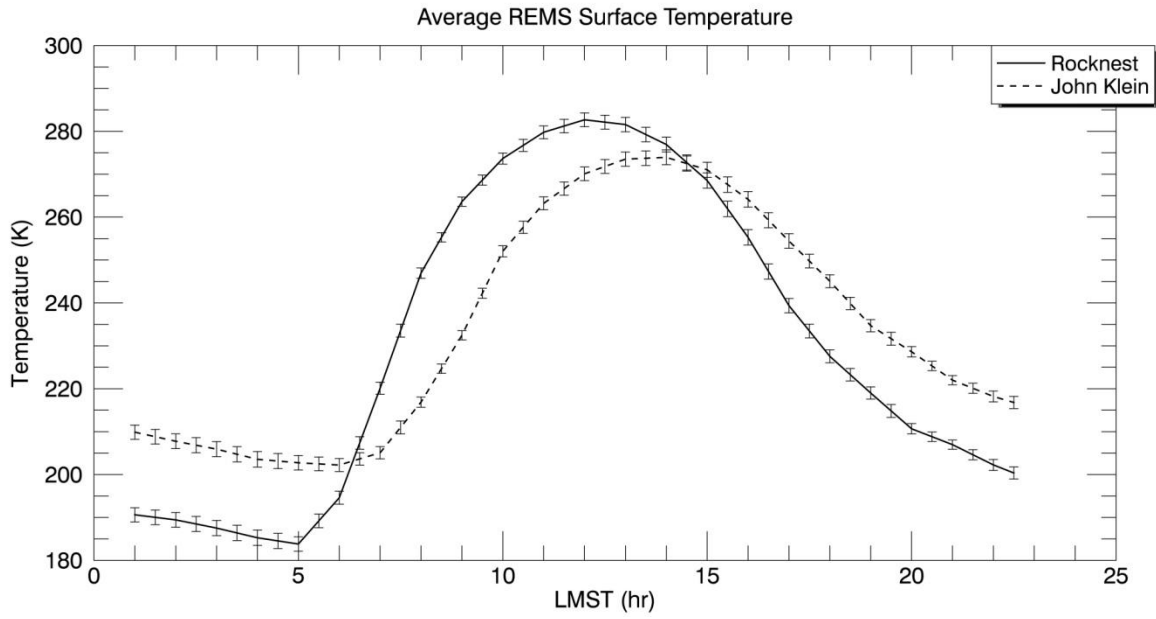


**Figure 4.6. Average REMS surface temperature measured at Rocknest (solid line) and John Klein (dashed line), plotted as a function of Local Mean Solar Time.**

constraints on the modeling placed by real data in combination with MCNPX and then comparing the modeled amplitude and phase of the induced variations on the neutron leakage flux to what is observed in the DAN passive data . This allows for elimination of most of the proposed hypotheses as the dominant sources of the observed variations. The hypotheses investigated and discussed in detail below are variations in subsurface temperature, variations in atmospheric pressure which leads to variations in secondary neutron production in the atmosphere and variations in neutron production in the regolith due to preferential shielding of alpha particles by the martian atmosphere, variations in detector temperature, and diurnal water vapor exchange between the regolith and the atmosphere.

### ***Subsurface Temperature***

#### **Methods**

The first environmental property that we have explored as a possible cause of the diurnal neutron variations is subsurface temperature. As neutrons propagate through a moderating medium, the neutron population loses energy through interactions with the nuclei of the moderator. These neutrons will come into an equilibrium in which the neutron energies are equal to the thermal energy of the moderating nuclei and have a Maxwellian-Boltzmann distribution of velocities. Thus neutrons within the medium can only lose energy until their energies are equal to the thermal energies of the moderating nuclei. In this way, the temperature of the medium can affect the final neutron energy distribution.

We have performed extensive modeling to test the magnitude of the effect that subsurface temperature has on the neutron leakage fluxes. Because the bulk regolith has thermal properties that control how quickly the surface temperature wave propagates into the subsurface and the amount of damping of the amplitude of the diurnal temperature swing, we have modeled

subsurface temperature profiles at different times throughout the sol for different thermal skin depths using the average REMS surface temperature as the initial boundary condition within a finite difference model. Estimated thermal skin depths for Mars are typically  $\sim < 10$  cm (Putzig and Mellon, 2007) and so we have modeled subsurface temperature profiles for thermal skin depths between 0 cm and 20 cm. Next, we modified the Monte Carlo Neutral Particle eXtended radiation transport code (MCNPX) (McKinney *et al.*, 2006) models developed for DAN passive modeling and data analysis in Tate *et al.* (2015) to account for the modeled subsurface temperature profiles throughout a sol. We do this in the same way that previous work by Little *et al.* (2003) used to study the effect of temperature on lunar neutron leakage fluxes. This allows for MCNPX to use a free-gas approximation, in order to adjust for temperature dependent cross sections and interactions within the transport model based on the temperature of the medium, or model regolith in our case. We have also gone one step further and tested the use of thermal scattering libraries,  $S(\alpha, \beta)$ , for neutron-hydrogen interactions with the hydrogen bound in water when simulating neutrons with energies below a few eV (McKinney *et al.*, 2006).

## Results

Results from our simulations are consistent with previous work by Little *et al.* (2003) in that, within the temperature ranges investigated ( $\sim 150$  K to  $\sim 300$  K), the thermal and epithermal neutron leakage fluxes increase with temperature. However, the magnitude of the effect is controlled by the ratio of the scattering cross section to the macroscopic thermal neutron absorption cross section ( $\delta$ ) (Little *et al.*, 2003) and the size of the diurnal thermal wave envelope at depth (Little *et al.*, 2003) which is controlled by the magnitude of the thermal skin depth. The larger  $\delta$  is, the smaller the effect temperature has on the neutron leakage fluxes (Little *et al.*, 2003). Smaller thermal skin depths as well have smaller magnitude effect on the neutron leakage

fluxes. Values of  $\delta$  calculated for our regolith compositions are comparable to the largest values investigated by Little *et al.* (2003), meaning that the effect produced should be small. Little *et al.* (2003), also show that on the diurnal time scale, the temperature envelope in the lunar regolith does not penetrate far enough to significantly impact the neutron leakage fluxes. That is, the GCR penetration depth is much deeper than the thermal skin depth and thus the majority of neutron interactions are occurring below the temperature variations making variations in neutron fluxes due to diurnal temperature variations negligible (Little *et al.*, 2003). While applying these methods to martian compositions and including MMRTG-induced neutrons, which do not penetrate as deep as GCR-induced neutrons, our results are still consistent, albeit for Mars, that the neutron leakage fluxes are not greatly affected by martian diurnal temperature variations. We are only examining the diurnal temperature penetration in our models because the neutron count rate variations we are seeking to understand also have a 1-sol periodicity. The penetration depth of the GCR-induced neutrons is  $\sim 1$  m, while the penetration depth of the MMRTG-induced neutrons is  $\sim 60$  cm. Both of these neutron populations penetrate well below the diurnal thermal wave envelope for the thermal parameters used in this study, which involved thermal skin depths ranging from 0 cm to 20 cm. The peak to peak variations in the CTN modeled count rates for the example 10 cm thermal skin depth curve are 0.5% and 0.9% for Rocknest and John Klein, respectively. The peak to peak variations in the modeled thermal neutron count rates for Rocknest and John Klein for the example 10 cm thermal skin depth curve such as shown below are, respectively 0.86 % and 1.3 %. The time of the peak at Rocknest in both CTN counts and thermal neutron counts produced is 16:30 LMST and 17:30 LMST at John Klein. Furthermore, the modeled diurnal variations in epithermal neutron counts that are produced by this effect do not match the phase that is observed in the data. These simulations show (Figure 4.7) that

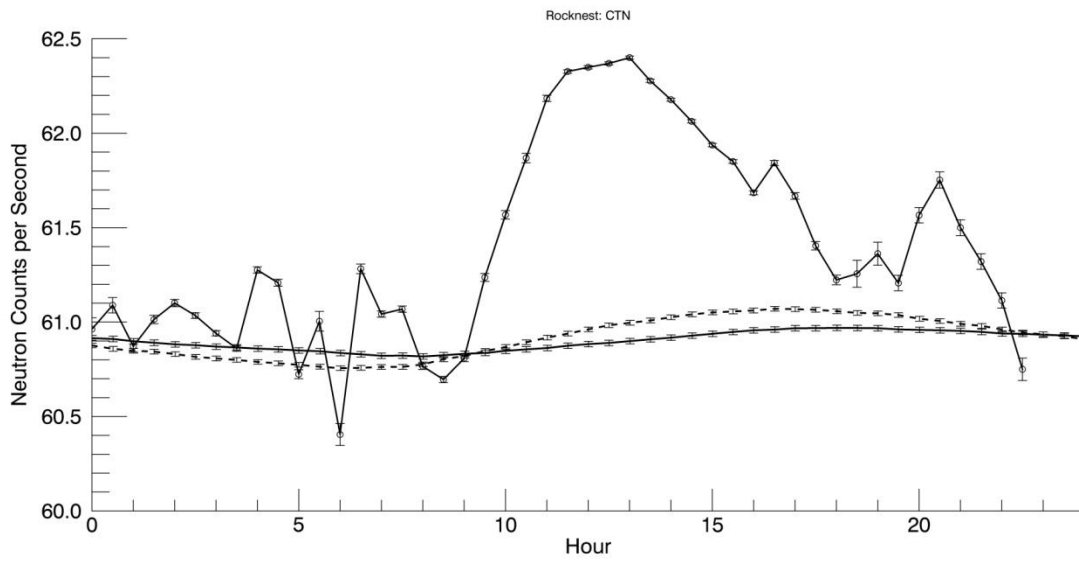


**Figure 4.7. Simulation results for Rocknest showing the effect that subsurface temperature profiles for thermal skin depths of 6 cm and 10 cm have on total neutron count rates. The average Rocknest CTN count rates through the sol are shown for comparison. Results are similar for other thermal skin depths and John Klein-based simulations.**

variations in subsurface temperature, while inducing a small effect are not the dominant source of the observed variations in the neutron leakage fluxes.

### ***Atmospheric Pressure Variations***

#### **Methods**

There are two effects that variations in atmospheric pressure cause in relation to the neutron leakage flux. The first effect is varying production of secondary neutrons in the atmosphere in response to variations in atmospheric pressure. Secondary neutron production occurs through interactions of GCRs with the nuclei of the atmosphere and is positively correlated with atmospheric pressure. Another effect of the martian atmosphere, observed by MSL RAD, is the preferential shielding of alpha particles by the martian atmosphere throughout the diurnal cycle, which is anticorrelated with atmospheric pressure (Rafkin *et al.*, 2014). Changes in martian atmospheric pressure are driven by heating and cooling and thus expansion and contraction of the atmosphere during the diurnal cycle (Rafkin *et al.*, 2014). Because of lateral migration of atmospheric mass during the heating and cooling cycle, the net amount of mass in the atmospheric column changes with pressure, leading to lower atmospheric column density at pressure minimum (Rafkin *et al.*, 2014). Lower atmospheric column density provides less shielding of GCRs, specifically alpha particles and heavier ions, that penetrate the atmosphere and reach the martian surface. This shielding is mass dependent on the primary GCR particle (Rafkin *et al.*, 2014). Specifically, higher  $z$  particles, *i.e.* alpha particles and heavier ions, are preferentially shielded versus the GCR protons because of nuclear fragmentation in the atmosphere (Rafkin *et al.*, 2014). GCR alpha particles and heavier ion fluxes are observed by RAD to undergo a ~20% peak to peak variation from pressure maximum to pressure minimum throughout a sol (Rafkin *et al.*, 2014). Because the RAD data were only examined in bulk for the

first 350 sols of the mission to determine the magnitude of the preferential shielding on GCR alpha particles and heavier ions, there are not individual estimates of the magnitude of variation for alpha particles due to the shielding for differing times/locations during the mission (*e.g.*, Rocknest and John Klein). However, we have used the result of ~20% peak to peak alpha particle flux variation to estimate how the DAN passive neutron count rates can vary throughout a sol in response to this phenomenon.

Starting with our MCNPX simulations as described in Tate *et al.* (2015), we perform full-scale martian atmosphere simulations tracking primary GCRs, including alpha particles and secondary neutrons. We vary the atmospheric pressure which is based on the half-hourly average REMS pressure data taken from each location over the entire duration throughout the sol, which leads to changes in the column density of the atmosphere. A scale height of 11 km is used when calculating the mass ( $\text{g}/\text{cm}^2$ ) of each atmosphere shell within the MCNPX model similar to work done by Prettyman *et al.* (2004). Results from these models are then used in conjunction with the local-scale models of the regolith and DAN detectors (Tate *et al.*, 2015) to simulate measured count rates by the DAN detectors. We use the same initial GCR spectrum for the alpha particles as for protons because they are very similar (Masarik and Reedy, 1996). Simulating transport through the martian atmosphere for differences in column density allows us to characterize how the alpha particles' spectrum and distribution changes between pressure maximum and minimum. We can then use these results in the local-scale simulations, which involves the corresponding estimated regolith compositions at Rocknest and John Klein (Tate *et al.*, 2015) to estimate the DAN passive neutron count rates. The contribution from secondary neutron production in the atmosphere is inherently involved in this simulation strategy.

Estimating count rates involves scaling simulation results to count rates as discussed in

Tate *et al.* (2015) because MCNPX simulation results are normalized per source particle. The scale factor necessary to perform this scaling includes all GCR source particles relevant to our simulations. A 20% increase in alpha particles must be accounted for both in this scale factor and within the simulation itself. Within our models, we nominally assume that alpha particles make up 12% of the initial GCR flux (Simpson, 1983). We use the global-scale atmosphere simulation results, at pressure maximum for the case of Rocknest, which reports alpha particles making up 3.16% of the source particle environment for the local-scale simulations. Local-scale simulations are run with the alpha particles making up 3.16% of the source particles. Based on what is observed in RAD data, we also increase this factor from 3.16% to 3.79% to account for the 20% increase of GCR alpha particles reaching the surface within our simulations. Local-scale simulations are also run with alpha particles making up 3.79% of the source particles to bracket the entire range. This 20% increase must also be recreated within the GCR simulation scale factors used to convert the simulation results to count rates. Since the scale factor is based on the source particles relevant to our local-scale simulation, which we have simulated to show alpha particles make up 3.16% of at pressure maximum, we can compute the corresponding 20% increase to 3.16 % of the scale factor at pressure maximum. The initial scale factors for both Rocknest and John Klein simulations are created by the use of RAD penetrating counter data calibrated to DAN passive measurements as discussed in Tate *et al.* (2015). Because these initial scale factors are created from daily averages of RAD penetrating counter data over the duration of stay at a particular location, we have fine-tuned the initial scale factor to the first time bin of the average count rate at each location in order for simulation results to be directly comparable to the data. These scale factors are the source particles per second necessary to convert the simulation results to count rates. From the simulations discussed above, 3.16% of these source



particles can be attributed to alpha particles at pressure maximum and then a 20% increase to this at pressure minimum based on RAD observations (Rafkin *et al.*, 2014). Converting simulation results to count rates through the use of the corresponding scale factors estimates the simulated DAN passive count rates for pressure maximum and minimum. The same procedure is performed for simulating and normalizing the set of simulations containing the relevant John Klein parameters. The effect the increase in alpha particles reaching the martian surface has is to increase the neutron production in the regolith at pressure minimum, which should lead to greater neutron count rates as measured by DAN. This effect is only applied to the GCR-induced neutrons. MMRTG-sourced neutrons are unaffected by variations in atmospheric pressure.

## **Results**

The modeling described above allows us to characterize the magnitude of the effect that temporally-variable preferential shielding of alpha particles and secondary neutron production in the atmosphere has on DAN passive measurements. However, if there are nuances in the response and timing of changes in the alpha particles due to atmospheric pressure variations and these are accompanied by changes in the neutron leakage flux, they are not captured in this analysis due to the lack of high temporal resolution RAD data for the alpha particles fluxes that are used in our models. The modeled CTN count rates accounting only for this effect are shown in Figures 4.8 and 4.9. Modeled CTN neutron count rate peak to peak variations for Rocknest and John Klein are, respectively, 2.7% and 1.0%. The peak times are, respectively, 16:30 LMST and 17:30 LMST.

The thermal neutron count rate response can be produced by differencing the modeled CTN count rates with the measured CETN count rates. This is shown in Figures 4.10 and 4.11. Modeled thermal neutron count rate peak to peak variations for Rocknest and John Klein are,

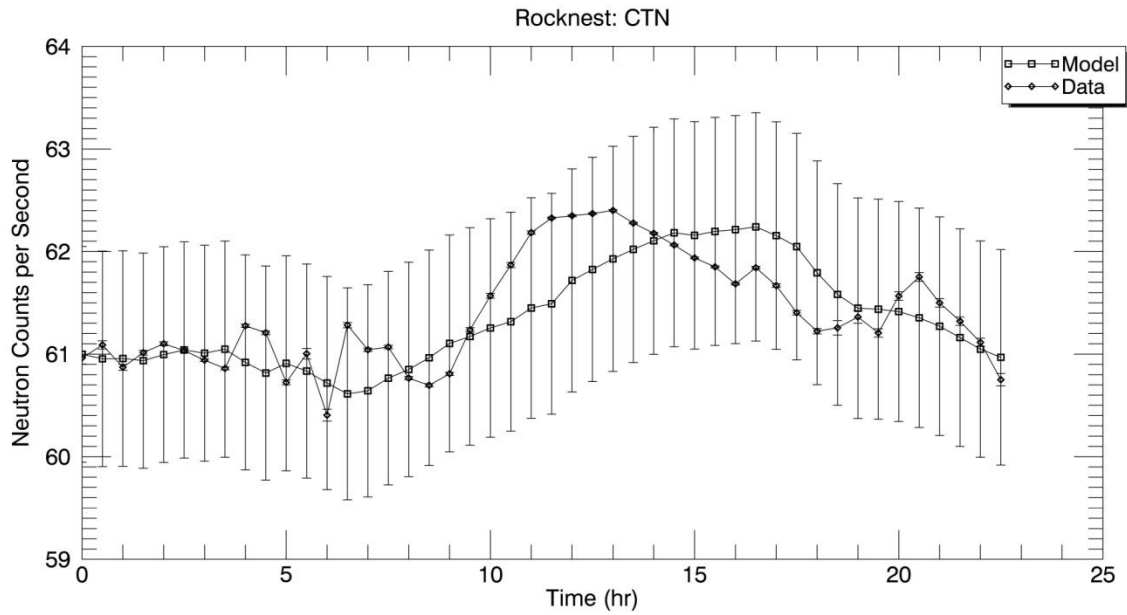


**Figure 4.8. Modeled CTN count rates for the Rocknest location showing the effect that pressure variations in the martian atmosphere have on the measured count rates. Uncertainties in the modeled count rates are calculated from simulation uncertainties. Shown uncertainties for the averaged count rates are on the order of the symbol size.**

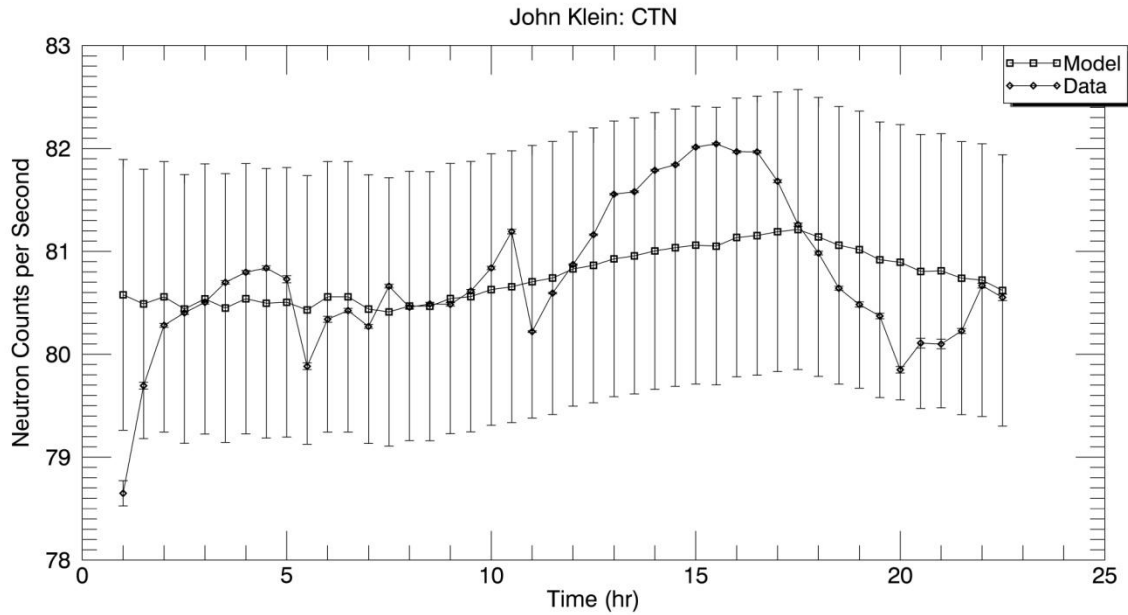


**Figure 4.9. Modeled CTN measured count rates for the John Klein location showing the effect that pressure variations in the martian atmosphere have on the measured count rates. Uncertainties in the modeled count rates are calculated from simulation uncertainties. Shown uncertainties for the averaged count rates are on the order of the symbol size.**

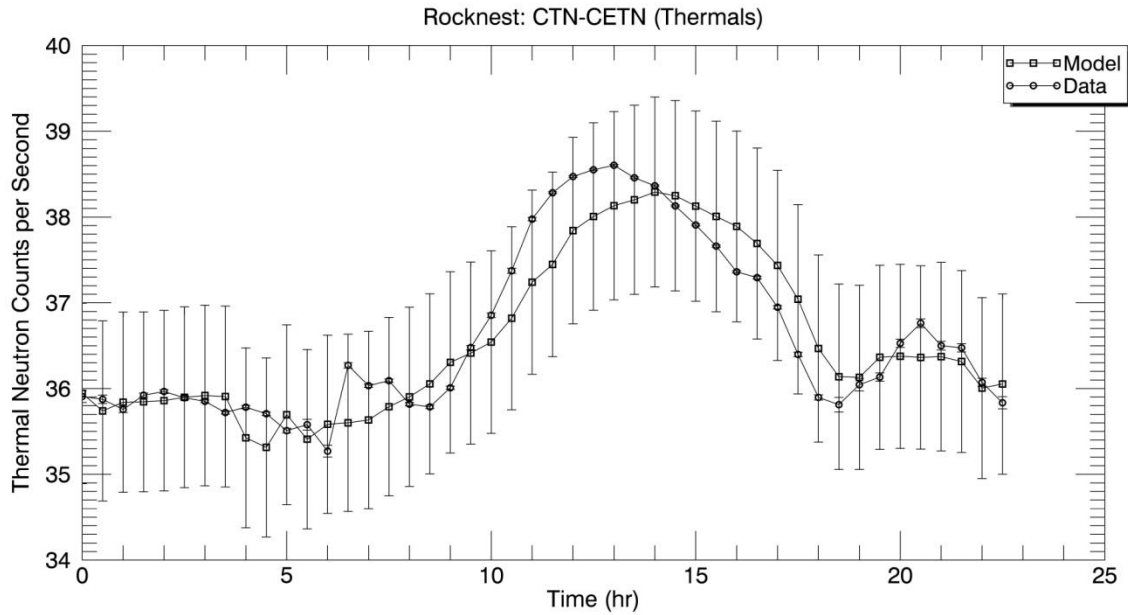


**Figure 4.10. Modeled thermal neutron measured count rates for the Rocknest location showing the effect that pressure variations in the martian atmosphere have on the measured count rates. These count rates are produced through differencing the modeled CTN count rates and the measured CETN count rates. Uncertainties in the modeled count rates are calculated from combining in quadrature the uncertainties from the CTN modeled count rates with the Poisson statistical uncertainties of the CETN count rates. Shown uncertainties for the averaged count rates are on the order of the symbol size.**

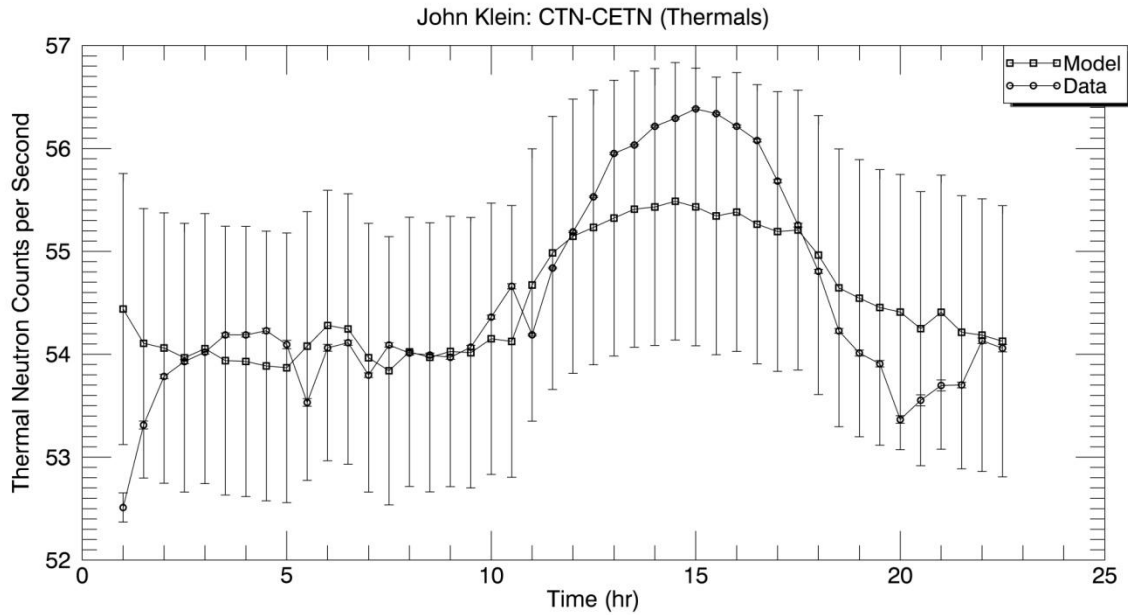


**Figure 4.11. Modeled thermal neutron measured count rates for the John Klein location showing the effect that pressure variations in the martian atmosphere have on the measured count rates. These count rates are produced through differencing the modeled CTN count rates and the measured CETN count rates. Uncertainties in the modeled count rates are calculated from combining in quadrature the uncertainties from the CTN modeled count rates with the Poisson statistical uncertainties of the CETN count rates. Shown uncertainties for the averaged count rates are on the order of the symbol size.**

respectively, 8.4% and 3.1%. The peak times are, respectively, 14:00 LMST and 14:30 LMST. The variations seen in these results are driven by the variations in shielding of alpha particles because the variations induced by varying secondary neutron production in the atmosphere are 180° out of phase with the modeled variations and previous work has shown such secondary neutron production variations to be small (<1%) (Tate *et al.*, 2015).

### ***Instrumental Effects***

Another possible source of variation are instrumental effects of the DAN detectors, CTN and CETN. Telemetry data from the rover allow for monitoring the temperature of the detectors throughout the sol and these data have been down linked and averaged for the same time period and 30-minute binning that is used for the neutron count rate data. The average detector temperature and average CTN, thermal, and CETN neutron count rates for Rocknest and John Klein are shown in Figures 4.12 and 4.13. The correlations and anticorrelations between the DAN passive data and the detector temperature are the strongest among all of the explored sources of the diurnal variations. The timing of the maximum of detector temperature also has the closest match to the relative timing of the maxima/minima observed in the data.

While we do not have a first principles based simulation to test this specific hypothesis, none of the other proposed sources of variation tested can reproduce a diurnal decrease in the CETN-measured count rates. Detector temperature or some other internal engineering factor appears to be the only source of variation remaining for the diurnal variations observed in the CETN.

Pulse height spectra from the DAN DE are down linked from the rover in 16 channels that are a linear combination of the ~150 channels of the DAN multichannel analyzer. Channels 4 through 15 of the down linked channels are used in calculating reported count rates. These

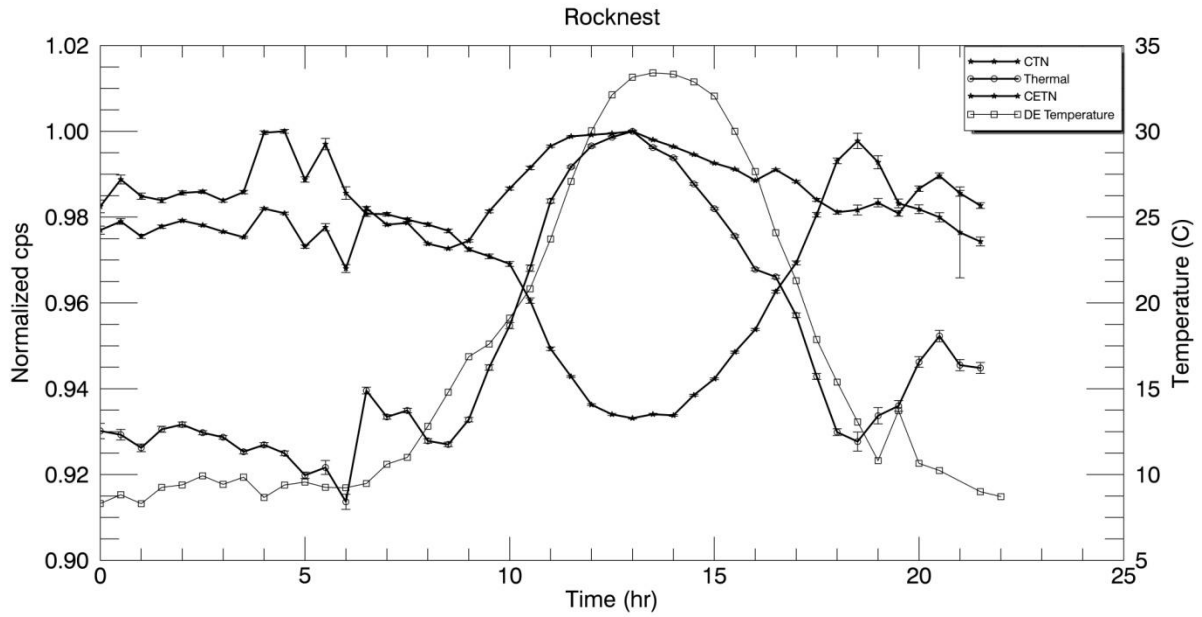


**Figure 4.12. Average Rocknest detector temperature through sol. Average CTN, thermal, and CETN count rates are shown as well.**

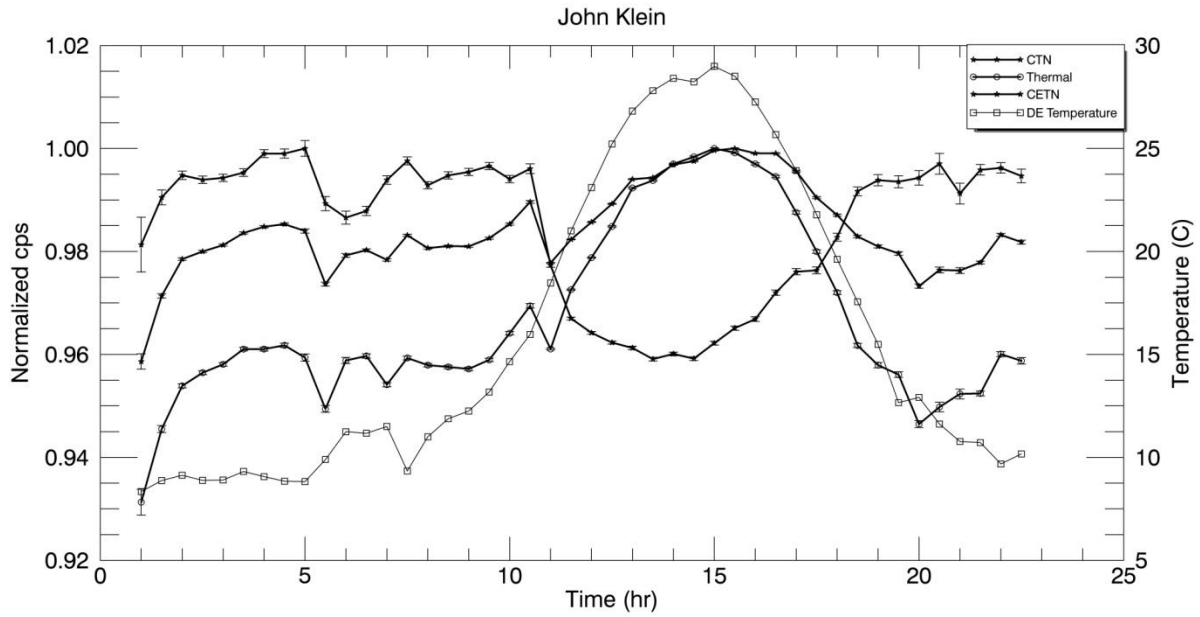


**Figure 4.13. Average John Klein detector temperature throughout sol. Average CTN, thermal, and CETN count rates are shown as well.**



channels and their behavior have been examined throughout the sol cycle. Interestingly, the decrease in neutron count rates in the afternoon hours measured by the CETN, which is the diurnal variation for the CETN in particular, is almost entirely contained in channel 13 for both Rocknest and John Klein data sets as shown in Figures 4.14 and 4.15. This is consistent with the cause of the decrease in the DAN CETN being one or more non-environmental factors. If the epithermal neutron leakage flux itself was experiencing a decrease, one would expect to see all CETN channels affected in a similar way because it is not physically plausible that all of the neutron capture reactions in the CETN associated with the diurnal variation would produce pulse heights in such a narrow range. A hardware malfunction of some kind, which itself may or may not be related to detector temperature, possibly in the multi-channel analyzer (MCA) of the instrument, for this detector is more plausible because of the channel-specific nature of this effect.

Similarly, the increases in the CTN neutron count rates when viewed in the 16 channel pulse height spectra are greatest in the lowest bins, however, smaller increases in the channel count rate do occur in the later bins. Spectra for the CTN neutron count rates are shown in Figures 4.16 and 4.17. As seen in Figures 4.14, 4.15, 4.16, and 4.17, channel 3 in both the CTN and CETN experience a large increase in neutron count rates during the afternoon hours. This concentration in the lowest bins could be indicative of an instrumental effect because such increases should not be localized in a specific channel of the instrument. It is possible this is an increase in noise of the instrument from a component such as the pre-amplifier that increases with temperature. The lowest channels would be most affected by such an increase in noise levels and could cause smaller such increases in noise in the adjacent channels, which is possibly seen in channels 3 through 5. The small increases in higher bins in the afternoon hours, however,

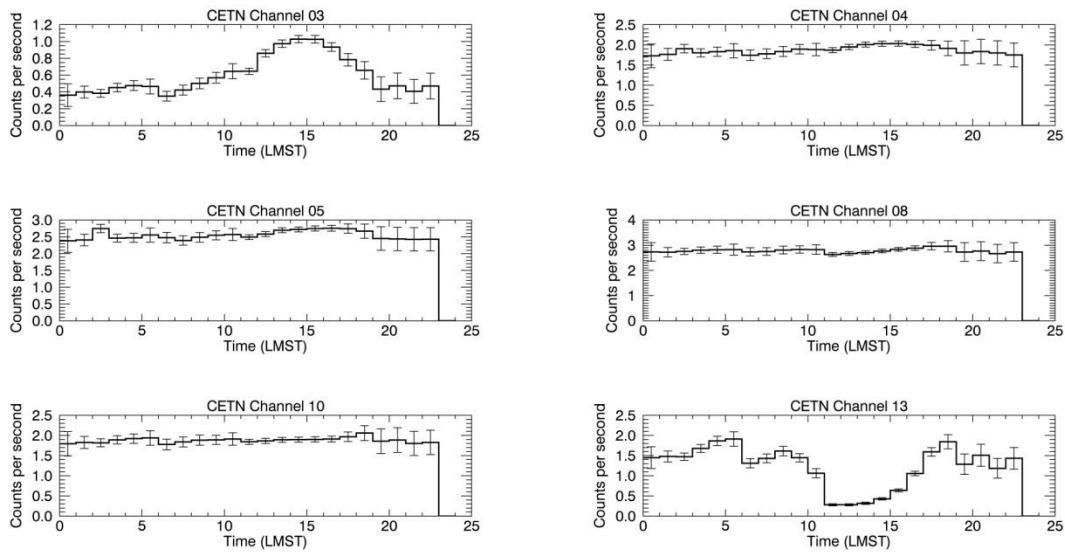


**Figure 4.14. Average CETN channel hourly count rate for channels 3, 4, 5, 8, 10, and 13 measured at Rocknest. Uncertainties are calculated from Poisson statistics. Uncertainties are lowest between the hours of 10 to 15 LMST because the majority of measurements are acquired during these hours.**

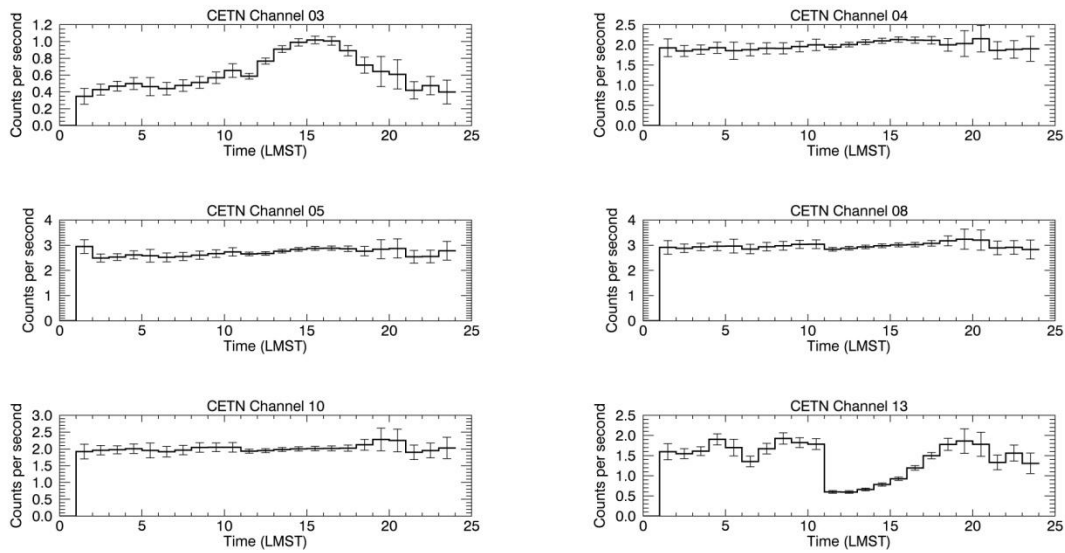


**Figure 4.15. Average CETN channel hourly count rate for channels 3, 4, 5, 8, 10, and 13 measured at John Klein. Uncertainties are calculated from Poisson statistics. Uncertainties are lowest between the hours of 10 to 15 LMST because the majority of measurements are acquired during these hours.**

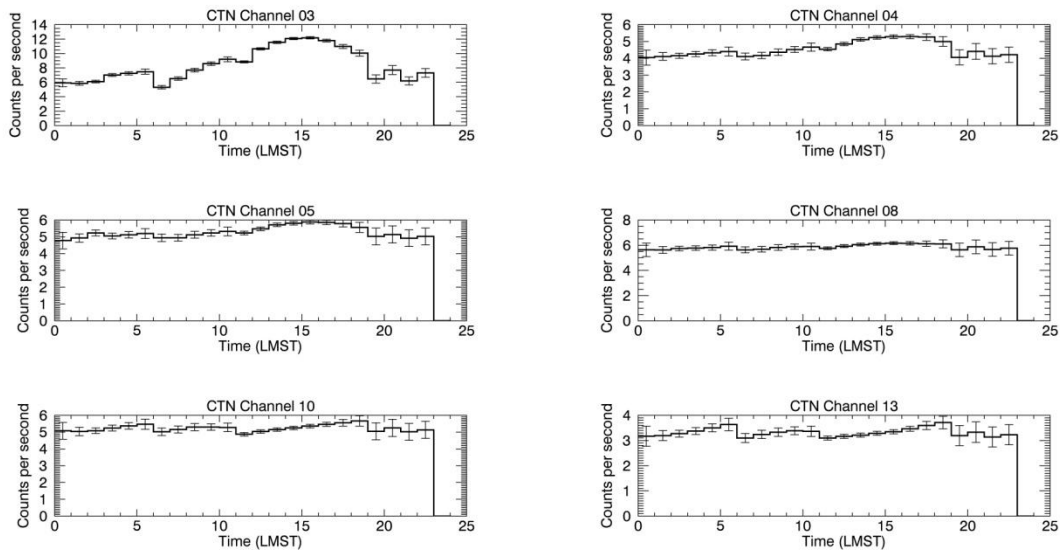


**Figure 4.16. Average CTN channel hourly count rate for channels 3, 4, 5, 8, 10, and 13 measured at Rocknest. Uncertainties are calculated from Poisson statistics. Uncertainties are lowest between the hours of 10 to 15 LMST because the majority of measurements are acquired during these hours.**

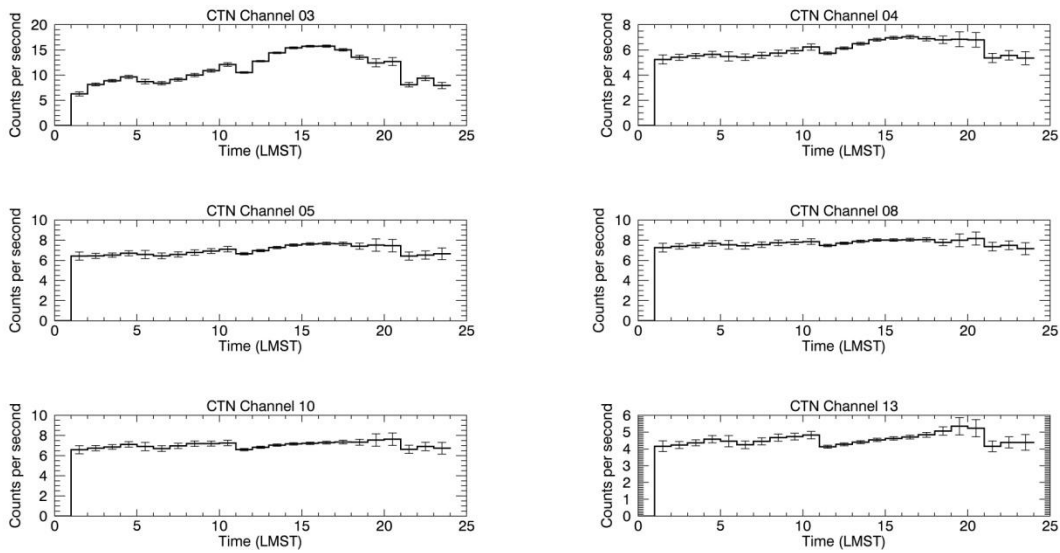


**Figure 4.17. Average CTN channel hourly count rate for channels 3, 4, 5, 8, 10, and 13 measured at John Klein. Uncertainties are calculated from Poisson statistics. Uncertainties are lowest between the hours of 10 to 15 LMST because the majority of measurements are acquired during these hours.**

could be indicative of the increasing neutron leakage flux due to environmental factors, most notably, an increase in the alpha particles. Separating possible effects from detector noise increase with temperature or other temperature-related effect and possible environmental effects will likely require testing of flight spares (or other analogous hardware) under controlled conditions.

A similar  $^3\text{He}$  neutron spectrometer, the Lunar Prospector Neutron Spectrometer (LP-NS), has shown diurnal variations in the measured epithermal neutron count rates (Teodoro *et al.*, 2015). A decrease in the measured epithermal neutron count rates was sourced to an increase in detector temperature (Teodoro *et al.*, 2015) and is of a similar magnitude to that which is observed in the DAN CETN. However, no explanations on the actual source of the variations are hypothesized (Teodoro *et al.*, 2015).

One possible explanation for the sensitivity of the CETN to detector temperature besides a hardware malfunction is the temperature dependence of the cadmium absorption cross sections of the cadmium shield. Cadmium in its natural isotopic abundance has neutron absorption resonances in the low keV energy region, which is at the high end of the sensitivity of the CETN detector, even though detection efficiency is low in this region. The cadmium cutoff absorption feature is also affected by this phenomenon. As the cadmium temperature increases, the resonances undergo Doppler broadening, which increases the resonance integral and leads to greater absorption (Solbrig, 1961). For similar temperature variations to what is observed in the DAN detectors ( $\sim 30^\circ\text{C}$ ), this effect would be small, however, would lead to less neutrons counted per second by the CETN as the detector temperature increases.

The CTN-measured count rates on the other hand are positively correlated with detector temperature, but the magnitude is estimated to be less than the magnitude of the effect on the

CETN. The mechanism of increase is unknown, but possibilities are discussed below.

### ***Diurnal Water Cycle***

Another proposed hypothesis that could affect the DAN passive measured neutron leakage fluxes diurnally would be the presence of a diurnal water cycle in Gale crater. Such a cycle would involve water vapor in the atmosphere being exchanged with the regolith. While this type of water exchange cycle has been proposed for Gale crater based on REMS data (Savijärvi *et al.*, 2016; Martín-Torres *et al.*, 2015), we find that it is insufficient to explain the observed variations in the DAN passive measurements.

As shown by Savijärvi *et al.* (2016), the relative humidity increases during the night because of lower ambient ground temperature and this is compatible with the adsorption of water onto the uppermost layer of the regolith during the night. The precipitable water content during the time of the investigation at Rocknest is  $\sim 8 \mu\text{m}$  (Savijärvi *et al.*, 2016). It should be noted that the vertical sensing footprint of DAN passive measurement extends to  $\sim 1$  m depth because of the penetration depth of GCRs. For such a small amount of water spread over such a small subset of the sensing volume of the DAN experiment, it is not expected to be possible to sense such a change with DAN passive measurements. Furthermore, the derived time of maximum water content of the regolith is during the night because of decreasing ambient temperature and increasing relative humidity (Savijärvi *et al.*, 2016). The timing of the variations observed in the DAN passive data is out of phase with what would be expected in the neutron leakage flux response to such a phenomenon. One would expect the thermal neutron count rates to increase and subsequently the epithermal neutron count rates to decrease during the night when the water is expected to be absorbed by the regolith through deliquescence, if in fact the epithermal neutron population were sensitive to this phenomenon. This, however, is inconsistent with the

variations observed in the DAN passive data when the thermal neutron count rates increase and the epithermal neutrons decrease in the afternoon hours. If there is a diurnal exchange of water vapor between the regolith and atmosphere as proposed by Savijärvi *et al.* (2016), DAN passive measurements are not sensitive to such an exchange.

## Discussion

It can be seen from the discussion above concerning the different hypotheses tested that none of the explored hypotheses alone can correctly reproduce the variations observed in the DAN passive data at Rocknest and John Klein. The closest reproduction of the observed variations comes from modeling the preferential shielding of alpha particles penetrating the atmosphere and including an effect based on the temperature of the detectors, which causes the observed decrease in the CETN-measured count rates and a similar, increase in the CTN-measured count rates. While simulations show that the DAN instrument should be sensitive to variations in atmospheric pressure variations due to the preferential shielding of alpha particles, it cannot be completely ruled out that the instrumental effects are dominating the signal of this variation.

While the external effects investigated did not produce the variations originally noted in the data, they are likely to be affecting the measurements since they are rooted in first principles, however the effects are not necessarily large enough to be noticed. Still, we can combine all of the effects that we have modeled insofar to produce modeled diurnal neutron count rates. This includes the effects of subsurface temperature, secondary neutron production in the atmosphere, preferential shielding of alpha particles, and an assumed temperature dependence of the detectors



inferred from the shape of the variation in the CETN measured count rates. In the case of the Rocknest composition and atmospheric parameters, the CTN count rates are modeled to show an increase of 3.7% through the sol, similar to the observed 3.3% variation. However, the phase of this increase is still later in the sol when compared to the observed variation in the data as shown in Figure 4.18. This is because this effect is intimately tied to the atmospheric pressure and the pressure minimum is later in the sol. In the case of the John Klein composition and atmospheric parameters, the CTN count rates are modeled to show an increase of 1.8% through the sol, versus the observed 2.7% variation. This is shown in Figure 4.19.

Lastly, subtracting the measured CETN count rates from the modeled CTN count rates to produce the thermal neutron count rates throughout the sol produces a close match between the amplitude, shape, and timing of our model results versus the data. The modeled thermal neutron count rates show a closer phase match than the CTN count rates because of the earlier timing of the minimum in the CETN count rates. The modeled thermal neutron count rates for Rocknest and John Klein parameters are shown in Figures 4.20 and 4.21. Modeled Rocknest thermal neutron count rates show an increase of 11.2%, versus the variation in the data of 9.5%. Modeled John Klein thermal neutron count rates show an increase of 4.5% versus the 5.7% observed in the data. The peak times of the Rocknest modeled thermal neutron count rates and average thermal neutron count rates are 14:00 LMST and 13:00 LMST, respectively. The peak times of the John Klein modeled thermal neutron count rates and average thermal neutron count rates are 15:00 LMST and 14:30 LMST, respectively.

The most likely cause of the observed diurnal variations in DAN passive data is some combination of the hypotheses explored above. Table 4.1 shows the hypotheses tested and the associated results and conclusions. The strongest correlations of the environmental factors tested

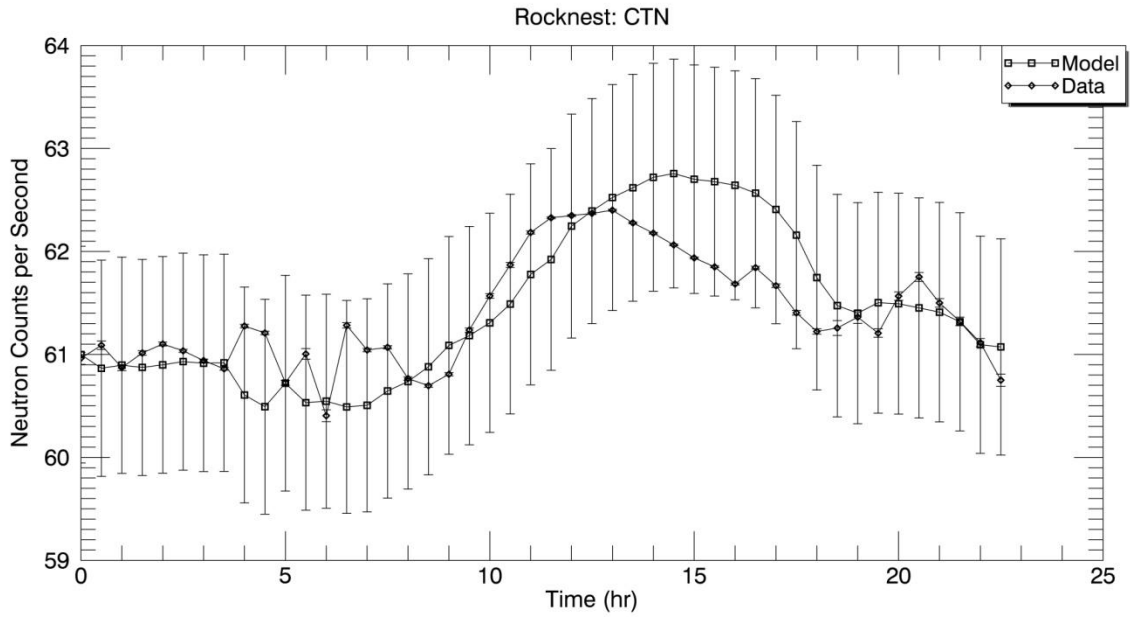


**Figure 4.18. Modeled CTN count rates for the Rocknest location combining effects due to subsurface temperature variations, atmospheric pressure variations, and an empirically-derived correction for instrumental effects. Uncertainties in modeled count rates are calculated from simulation uncertainties.**

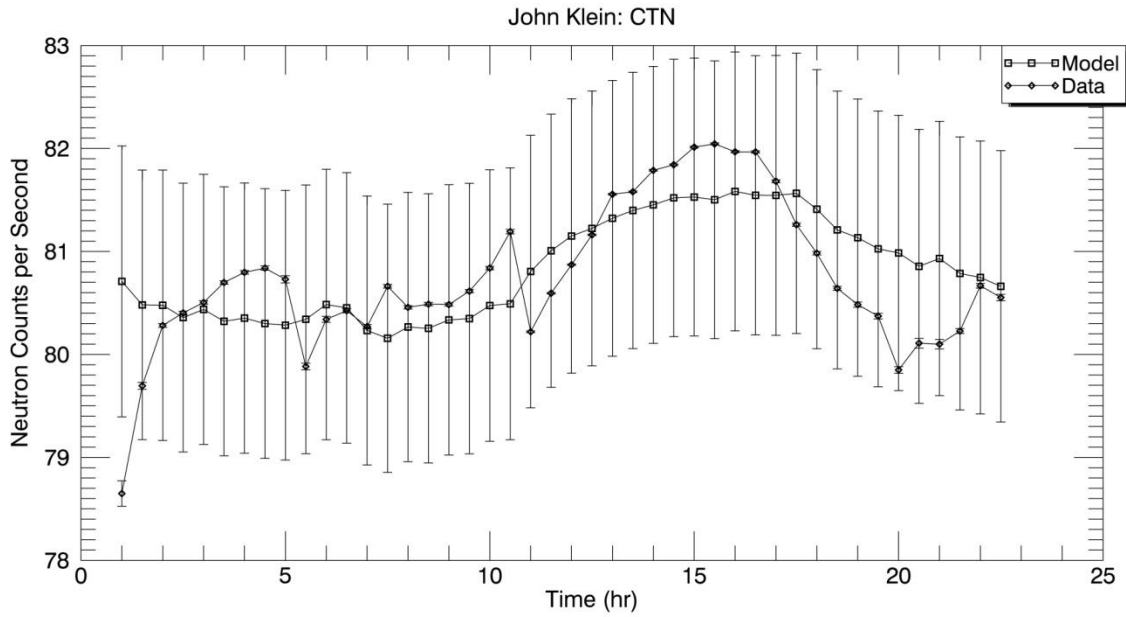


**Figure 4.19. Modeled CTN count rates for the John Klein location combining effects due to subsurface temperature variations, atmospheric pressure variations, and detector temperature variations. Uncertainties in modeled count rates are calculated from simulation uncertainties.**

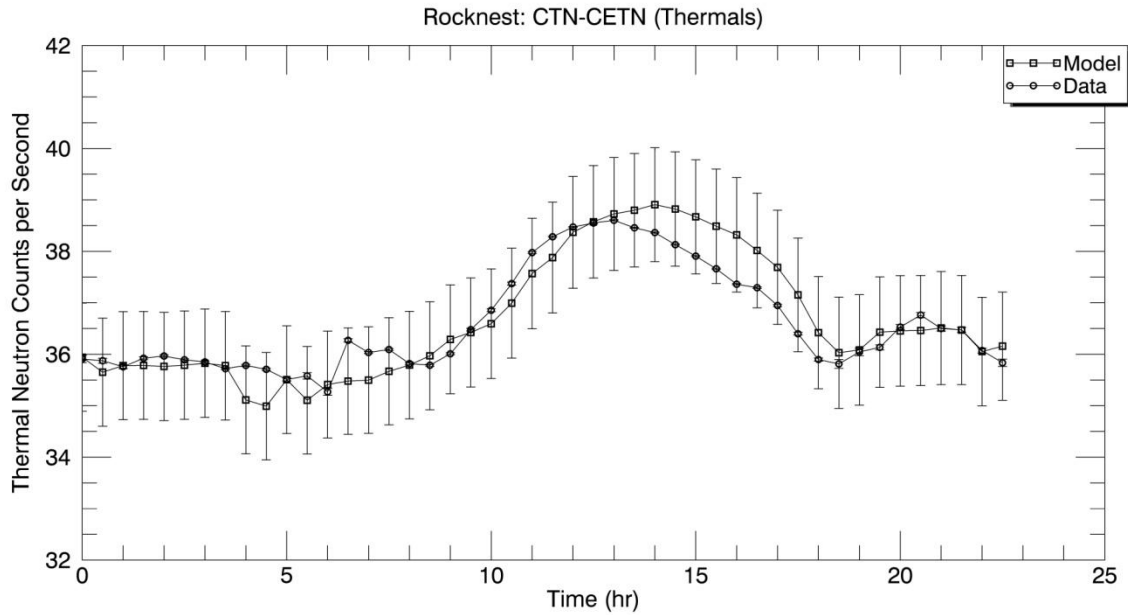


**Figure 4.20. Modeled thermal neutron count rates (squares) throughout the sol at Rocknest. Average thermal neutron count rate data (circles) are shown for comparison. The primary cause of the increase in thermal neutron count rates is the combination of the increase in alpha particles at pressure minimum due to preferential shielding of the martian atmosphere and the decrease in the CETN-measured count rates. Uncertainties are calculated by combining the uncertainties in the modeled CTN count rates and the uncertainties in the CETN count rates.**

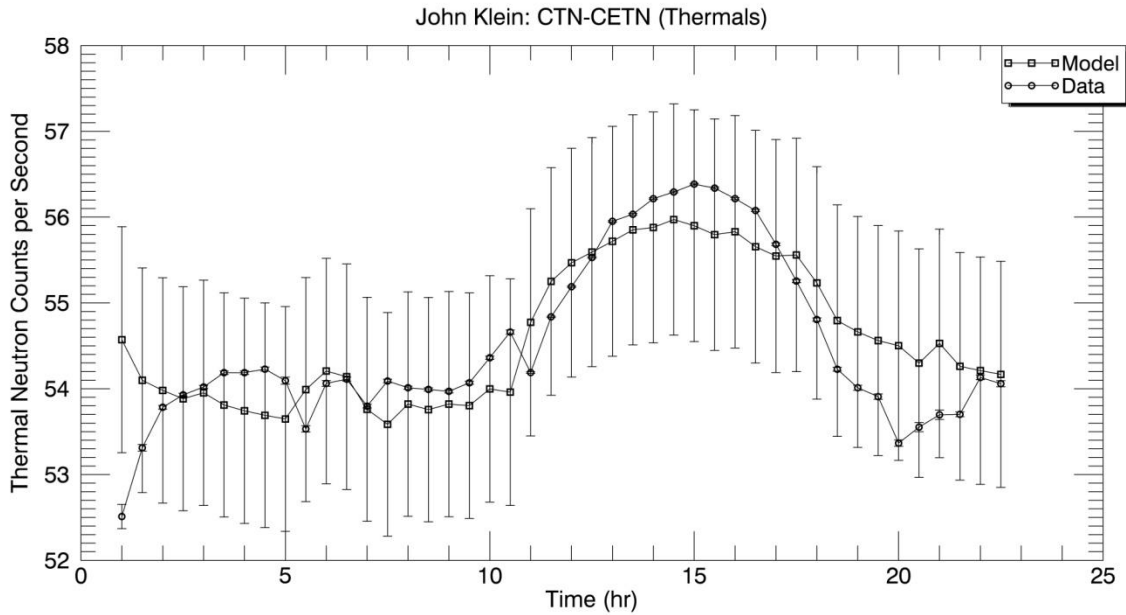


**Figure 4.21. Modeled thermal neutron count rates (squares) throughout the sol at John Klein. Average thermal neutron count rate data (circles) are shown for comparison. The primary cause of the increase in thermal neutron count rates is the combination of the increase in alpha particles at pressure minimum due to preferential shielding of the martian atmosphere and the decrease in the CETN-measured count rates. Uncertainties are calculated by combining the uncertainties in the modeled CTN count rates and the uncertainties in the CETN count rates.**

**Table 4.1. Table of hypotheses investigated showing the modeled peak to peak amplitude in CTN count rates, modeled time of extrema in the CTN count rates, the correlation coefficients between the modeled CTN count rates and the data, and the amount of contribution to the observed diurnal variations. Numbers listed in cells are for Rocknest on the left and John Klein on the right. Blank cells represent hypotheses that do not have models to predict their characteristic induced variations.**

<b>Hypothesis Investigated</b>	<b>Modeled Peak to Peak Amplitude (CTN)</b>		<b>Modeled Time of Extrema (CTN)</b>		<b>Correlation Between Model &amp; Data (CTN)</b>		<b>Contribution to Observed Variations</b>
<b>Subsurface Temperature</b>	<b>0.5%</b>	<b>0.9%</b>	<b>16:30</b>	<b>17:30</b>	<b>0.62</b>	<b>0.48</b>	<b>Small</b>
<b>Atmospheric Pressure</b>	<b>2.7%</b>	<b>1.0%</b>	<b>16:30</b>	<b>17:30</b>	<b>0.75</b>	<b>0.73</b>	<b>Small/Noticeable</b>
<b>Instrumental Effects</b>							<b>Significant</b>
<b>Diurnal Water Cycle</b>							<b>Negligible</b>

are observed between the modeled CTN count rates for atmospheric pressure variations and the data.

As shown above, modeled diurnal neutron count rate curves can be produced by combining all of the effects we have investigated. The largest contributors to the amplitude and shape of the variations are the preferential shielding of alpha particles and the instrumental effects. Other effects from subsurface temperature and secondary neutron production in the atmosphere are small, but included here because they are physical.

Based on the simulations of preferential shielding of alpha particles by the martian atmosphere, we conclude that DAN passive measurements are, in fact, sensitive to this phenomenon. This was certainly unexpected, but if true it provides an independent verification of the (also unexpected) result observed by the RAD instrument (Rafkin *et al.*, 2014).

As stated, an observed diurnal effect attributed to detector temperature has also been observed in LP-NS epithermal neutron count rate data that is on the order of  $\sim 1$  neutron count per second. The effect in the DAN CETN is slightly larger, but the DAN CETN is mostly measuring MMRTG-produced epithermal neutrons. If the effect is coming from the temperature dependence of the cadmium shield then it is expected that the temperature dependence will be larger for the DAN CETN. This is because a significant proportion of MMRTG-induced neutrons do not interact with the regolith before reaching the detectors, thus the DAN CETN is subject to a greater intensity of higher energy neutrons (having no moderating interactions in the regolith) and thus these neutrons are more amenable to being captured by the cadmium absorption resonances.

It is, however, also very possible that this is simply a hardware malfunction, possibly coming from the MCA because it is channel specific, which is unexpected given the nature of

$^3\text{He}$  proportional counters. An increase in noise in both detectors can also lead to slight increases in the count rates in the afternoon of the sols. The combination of these two effects on both the CTN and CETN can possibly explain most of the diurnal variation observed in the DAN passive data, with the exception of the fact that the CTN count rates do have small increases in the higher pulse height spectra bins in the afternoon. Some combination of effects from the external factors of atmospheric pressure variation and subsurface temperature variations are needed to account for this shift in the peak of the CTN count rates to a later time of sol and to explain the increases spread over the higher bins of pulse height spectra.

## Conclusions

We have observed unexpected weak diurnal variations in the DAN passive measurements acquired at Rocknest and John Klein. These variations are manifested as a slight increase in the CTN-measured count rates and thermal neutron count rates and a slight decrease in the CETN-measured count rates in the afternoon of a sol and then a return to lower count rates in the case of the CTN and thermals and greater count rates in the case of the CETN overnight. We have investigated the different hypotheses of subsurface temperature variations, atmospheric pressure variations, and water vapor exchange between the atmosphere and regolith. Diurnal subsurface temperature variations are shown to not to be the dominant cause of these variations, but may have some small contribution and this result is consistent with previous work by Little *et al.* on lunar neutron leakage fluxes (2003). A diurnal water cycle is also shown to not be the cause of the observed variations. We have also shown that variations in atmospheric pressure leading to preferential shielding of alpha particles produces the largest effect on CTN count rates



suggesting this phenomenon is contributing the most out of the environmental factors considered to the observed DAN diurnal variations as well. Investigations into the pulse height spectra of the DAN instrument indicate potential instrumental effects as well. However, the exact proportions of instrumental effects to sensitivity to environmental factors are unknown, but instrumental effects are thought to be significant. The CETN detector has strange behavior in its down linked pulse height spectra throughout the sol which indicates some instrumental effect or glitch possibly originating in the MCA. Still, a combination of instrumental effects and environmental factors is most likely necessary to explain all of the nuances of the CTN diurnal variations. Laboratory testing with flight hardware will be necessary to attempt to discern the magnitude of the instrumental effect and ultimately, untangle the instrumental and environmental effects.

The RAD diurnal variations in energetic particles, specifically the preferential shielding of alpha particles and heavier ions, were not expected or considered in previous studies (Rafkin *et al.*, 2014). The model results presented here indicate that DAN passive measurements are sensitive to the effect of preferential shielding of alpha particles by the atmosphere and this provides a verification of the RAD observation.

A diurnal dependence such as that observed in DAN CETN passive data has been observed in the similar neutron detector LP-NS, which experiences a decrease with detector temperature (Teodoro *et al.*, 2015). This decrease cannot be related to atmospheric variations because the moon has no atmosphere. Ultimately, the variations observed in the DAN CTN and thermal neutron passive data are small relative to the variations caused by changes in the composition of the regolith and have been shown to not have a large impact on WEH estimates (Tate *et al.*, 2015). In the case of orbital instruments, such as the Neutron Spectrometer (NS) on

Mars Odyssey, it may be necessary to reexamine the data to search for a signature of the preferential shielding of alpha particles, as it could potentially be a significant effect due to the fact that this instrument only measures GCR-induced neutrons. It may also be necessary to determine if the measured epithermal neutron count rates are decreasing with detector temperature as is seen in both the DAN CETN and LP-NS. Because instruments such as LP-NS and the Mars Odyssey NS rely on epithermal neutron count rates for WEH estimations, unlike DAN passive data analysis, the implications of such a temperature dependent correction would be of a larger magnitude to such instruments.

### **Acknowledgements**

This work was financially supported by J. Moersch's MSL Participating Scientist Award (NASA JPL 1451872). We would also like to thank the MSL operations and science teams for helping acquire these data.

## References

- Drake, D.M., W.C. Feldman, and B.M. Jakosky (1988), Martian Neutron Leakage Spectra, *Journal of Geophysical Research*, 93, 6353-6368.
- Gómez-Elvira, J., C. Armiens, L. Castañer, M. Domínguez, M. Genzer, F. Gómez, R. Haberle, A.M. Harri, V. Jiménez, H. Kahanpää, L. Kowalski, A. Lepinette, J. Martín, J. Martínez-Frías, I. McEwan, L. Mora, J. Moreno, S. Navarro, M.A. de Pablo, V. Peinado, A. Peña, J. Polkko, M. Ramos, N.O. Renno, J. Ricart, M. Richardson, J. Rodríguez-Manfredi, J. Romeral, E. Sebastián, J. Serrano, M. de la Torre Juárez, J. Torres, F. Torrero, R. Urquí, L. Vázquez, T. Velasco, J. Verdasca, M. P. Zorzano, and J. Martín-Torres (2012), REMS: The Environmental Sensor Suite for the Mars Science Laboratory Rover, *Space Science Reviews*, 170, 583-640, doi:10.1007/s11214-012-9921-1.
- Grotzinger, J. P., D. Sumner, L. Kah, K. Stack, S. Gupta, L. Edgar, D. Rubin, K. Lewis, J. Schieber, N. Mangold, R. Milliken, P. Conrad, D. DesMarais, J. Farmer, K. Siebach, F. Calef III, J. Hurowitz, S. McLennan, D. Ming, D. Vaniman, J. Crisp, A. Vasavada, K. Edgett, M. Malin, D. Blake, R. Gellart, P. Mahaffy, R. Wiens, S. Maurice, J. Grant, S. Wilson, R. C. Anderson, L. Beegle, R. B. Anderson, T. Bristow, W. Dietrich, G. Dromart, J. Eigenbrode, A. Fraeman, C. Hardgrove, K. Herkenhoff, L. Jandura, G. Kocurek, S. Lee, L. Leshin, R. Leveille, D. Limonadi, J. Maki, S. McCloskey, M. Meyer, M. Minitti, H. Newsom, D. Oehler, A. Okon, M. Palucis, T. Parker, S. Rowland, M. Schmidt, S. Squyres, A. Steele, E. Stolper, R. Summons, A. Treimann, R. Williams, A. Yingst, and MSL Science Team (2014), A Habitable Fluvio-Lacustrine Environment at Yellowknife Bay, Gale Crater, Mars, *Science*, 343(6169), 1242777, doi:10.1126/science.1242777.
- Grotzinger, J. P., S. Gupta, D. Rubin, J. Schieber, D. Y. Sumner, K. Stack, A. Vasavada, R. Ardivison, F. Calef III, L. Edgar, W.F. Fischer, J.A. Grant, L.C. Kah, M.P. Lamb, K. Lewis, N. Mangold, M. Minitti, M. Palucis, M. Rice, K. Siebach, R. Williams, A. Yingst, D. Blake, D. Blaney, P. Conrad, J. Crisp, W.E. Dietrich, G. Dromart, K.S. Edgett, R. Ewing, R. Gellart, J. Griffes, J. Hurowitz, G. Kocurek, P. Mahaffy, M. Malin, S.M. McLennan, M. Mischna, D. Ming, R. Milliken, H. Newsom, D. Oehler, D. Vaniman, R. Wiens, and S. Wilson (2015), Deposition, Exhumation, and Paleoclimatology of an Ancient Lake Deposit, Gale Crater, Mars, *Science*, 350, doi: 10.1126/science.aac7575.
- Jun, I., I. Mitrofanov, M. L. Litvak, A. B. Sanin, W. Kim, A. Behar, W. V. Boynton, L. DeFlores, F. Fedosov, D. Golovin, C. Hardgrove, K. Harshman, A. S. Kozyrev, R. O. Kuzmin, A. Malakhov, M. Mischna, J. Moersch, M. Mokrousov, S. Nikiforov, V. N. Shvetsov, C. Tate, V. I. Tret'yakov, and A. Vostrukhin (2013), Neutron background environment measured by the Mars Science Laboratory's (MSL) Dynamic Albedo of Neutrons Instrument during the first 100 sols, *Journal of Geophysical Research, Planets*, 118(11):2400-2412, 10.1002/2013JE004510, 2013.
- Knoll, G. F. (2000), Radiation Detection and Measurement, New York: John Wiley and Sons, Inc.

- Little, R. C., W. C. Feldman, S. Maurice, I. Genetay, D. J. Lawrence, S. L. Lawson, O. Gasnault, B. L. Barraclough, R. C. Elphic, T. H. Prettyman, and A. B. Binder (2003), Latitude variation of subsurface lunar temperature: Lunar Prospector thermal neutrons, *Journal of Geophysical Research*, 108, doi:10.1029/2001JE001497.
- Litvak, M.L., I. G. Mitrofanov, Yu. N. Barmakov, A. Behar, A. Bitulev, Yu. Bobrovniksky, E. P. Bogolubov, W. V. Boynton, S. I. Bragin, S. Churin, A. S. Grebennikov, A. Konovalov, A. S. Kozyrev, I. G. Kurdumov, A. Krylov, Yu. P. Kuznetsov, A. V. Malakhov, M. I. Mokrousov, V. I. Ryzhkov, A. B. Sanin, V. N. Shvetsov, G. A. Smirnov, S. Sholeninov, G. N. Timoshenko, T. M. Tomilina, D. V. Tuvakin, V. I. Tretyakov, V. S. Troshin, V. N. Uvarov, A. Varenikov, and A. Vostrukhin (2008), The Dynamic Albedo of Neutrons (DAN) experiment for NASA's 2009 Mars Science Laboratory, *Astrobiology*, 8, 605-613, DOI: 10.1089/ast.2007.0157.
- Litvak, M. L., I. G. Mitrofanov, A. B. Sanin, D. Lisov, A. Behar, W. V. Boynton, L. DeFlores, F. Fedosov, D. Golovin, C. Hardgrove, K. Harshman, I. Jun, A. S. Kozyrev, R. O. Kuzmin, A. Malakhov, R. Milliken, M. Mischna, J. Moersch, M. Mokrousov, S. Nikiforov, V. N. Shvetsov, K. Stack, R. Starr, C. Tate, V. I. Tretyakov, A. Vostrukhin, and the MSL Science Team (2014), Local variations of bulk hydrogen and chlorine-equivalent neutron absorption content measured at the contact between Sheepbed and Gillespie Lake units in Yellowknife Bay, Gale Crater, using the DAN instrument onboard Curiosity, *Journal of Geophysical Research: Planets*, 119, 1259-1275, doi:10.1002/2013JE004556.
- Litvak, M. L., I. G. Mitrofanov, C. Hardgrove, K. M. Stack, A. B. Sanin, D. Lisov, W. V. Boynton, F. Fedosov, D. Golovin, K. Harshman, I. Jun, A. S. Kozyrev, R. O. Kuzmin, A. Malakhov, R. Milliken, M. Mischna, J. Moersch, M. Mokrousov, S. Nikiforov, R. Starr, C. Tate, V. I. Tretyakov, and A. Vostrukhin (2016), Hydrogen and Chlorine Abundances in the Kimberley Formation of Gale Crater Measured by the DAN Instrument Onboard the Mars Science Laboratory Curiosity Rover, *Journal of Geophysical Research: Planets*, 121, doi: 10.1002/2015JE004960.
- MacFarlane, R. E. and D. W. Muir (1994), *The NJOY nuclear data processing system, version 91*, 7, Los Alamos, NM: LA-12740-M.
- Martín-Torres, F. J., M. Zorzano, P. Valentín-Serrano, A. Harri, M. Genzer, O. Kempainen, E. G. Rivera-Valentin, I. Jun, J Wray, M. B. Madsen, W. Goetz, A. S. McEwen, C. Hardgrove, N. Renno, V. F. Chevrier, M. Mischna, R. Navarro-González, J. Martínez-Frías, P. Conrad, T. McConnochie, C. Cockell, G. Berger, A. R. Vasavada, D. Sumner, and D. Vaniman (2015), Transient liquid water and water activity at Gale crater on Mars, *Nature Geoscience*, 8, 357-361, doi:10.1038/ngeo2412.
- McKinney, G.W., J.W. Durkee, F.X. Gallmeier, J.S. Hendricks, M.R. James, D.B. Pelowitz, L.S. Waters, "MCNPX Overview", LA-UR-06-6206 (278 KB), Proceedings of the 2006 HSSW, FNAL, IL, September 6-8, 2006.
- Mitrofanov, I. G., M. L. Litvak, A. B. Sanin, R. Starr, D. I. Lisov, R. O. Kuzmin, A. Behar, W.

- V. Boynton, C. Hardgrove, K. Harshman, I. Jun, R. Milliken, M. A. Mischna, J. E. Moersch, and C. G. Tate (2014), Content of water and chlorine in the martian regolith along the first 1900 meters of the traverse of Curiosity, as measured by DAN instrument onboard the rover, *Journal of Geophysical Research: Planets*, 119, 1579-1596, doi:10.1002/2013JE004553.
- Mitrofanov, I. G., A. S. Kozyrev, D. I. Lisov, A. A. Vostrukhin, D. V. Golovin, M. L. Litvak, A. V. Malakhov, M. I. Mokrousov, S. Yu. Nikiforov, and A. B. Sanin (2016), Active Neutron Sensing of the Martian Surface with the DAN Experiment Onboard the NASA "Curiosity" Mars Rover: Two Types of Soil with Different Water Content in the Gale Crater, *Astronomy Letters*, 42, 251-259, doi: 10.1134/S1063773716040058.
- Masarik, J. and R.C. Reedy (1996), Gamma ray production and transport in Mars, *Journal of Geophysical Research*, 101, 891-912, doi:10.1029/96JE01563.
- Pater, I. de and J. L. Lissauer (2010), Planetary Sciences 2nd Edition, New York, NY, Cambridge University Press.
- Prettyman, T.H. et al., 2004. Composition and structure of the martian surface at high southern latitudes from neutron spectroscopy. *J. Geophys. Res.* 109, E05001, doi:10.1029/2003JE002139.
- Putzig, N. E. and M. T. Mellon (2007), Apparent thermal inertia and the surface heterogeneity of Mars, *Icarus*, 191, 68-94, doi:10.1016/j.icarus.2007.05.013.
- Rafkin, S. C. R., C. Zeitlin, B. Ehresmann, D. Hassler, J. Guo, J. Köhler, R. Wimmer-Schweingruber, J. Gomez-Elvira, A. Hatti, H. Kahanpää, D. E. Brinza, G. Weigle, S. Böttcher, E. Böhm, S. Burmeister, C. Martin, G. Reitz, F. A. Cucinotta, M. Kim, D. Grinspoon, M. A. Bullock, A. Posner, and the MSL Science Team (2014), Diurnal variations of energetic particle radiation at the surface of Mars as observed by the Mars Science Laboratory Radiation Assessment Detector, *Journal of Geophysical Research: Planets*, 119, 1345-1358, doi:10.1002/2013JE004525.
- Savijärvi, H., H. Ari-Matti, and O. Kemppinen (2016), The diurnal water cycle at Curiosity: Role of exchange with the regolith, *Icarus*, 265, 63-69.
- Simpson, J. A. (1983), Elemental and isotopic composition of the galactic cosmic rays, *Annual Reviews Nuclear Particle Science*, 33, 323-381.
- Solbrig, A. W., Jr. (1961), Doppler Effect in Neutron Absorption Resonances, *American Journal of Physics*, 29, 257-261, doi:10.1119/1.1937737.
- Tate, C.G., J. Moersch, I. Jun, D. W. Ming, I. Mitrofanov, M. Litvak, A. Behar, W.V. Boynton, L. Deflores, D. Drake, B. Ehresmann, F. Fedosov, D. Golovin, C. Hardgrove, K. Harshman, D. M. Hassler, A.S. Kozyrev, R. Kuzmin, D. Lisov, A. Malakhov, R. Milliken, M. Mischna, M. Mokrousov, S. Nikiforov, A.B. Sanin, R. Starr, A. Varenikov,

A. Vostrukhin, and C. Zeitlin (2015), Water Equivalent Hydrogen Estimates from the first 200 sols of *Curiosity's* Traverse (Bradbury Landing to Yellowknife Bay): Results from the Dynamic Albedo of Neutrons (DAN) Passive Mode Experiment, *Icarus*, 262, 102-123, doi:10.1016/j.icarus.2015.09.002.

Tate, C.G., J. Moersch, I. Mitrofanov, M. Litvak, W.V. Boynton, D. Drake, B. Ehresmann, F. Fedosov, D. Golovin, C. Hardgrove, K. Harshman, D. M. Hassler, I. Jun, A.S. Kozyrev, R. Kuzmin, D. Lisov, A. Malakhov, R. Milliken, M. Mischna, M. Mokrousov, S. Nikiforov, A.B. Sanin, R. Starr, A. Vostrukhin, and C. Zeitlin (2017), Results from the Dynamic Albedo of Neutrons (DAN) Passive Mode Experiment: Yellowknife Bay to Amargosa Valley (Sols 201 - 753), *Icarus*, submitted.

Teodoro, L. F. A., D. J. Lawrence, R. C. Elphic, V. R. Eke, W. C. Feldman, S. Maurice, M. Siegler, and D. Paige (2015), The Quest for a Diurnal Effect in Lunar Hydrogen Abundance, Lunar and Planetary Science Conference, The Woodlands, Texas.

**CHAPTER V**  
**CONCLUSION**

Remote neutron spectroscopy is a proven method of acquiring remote sensing data about the composition of bodies within the solar system. Typically, such instruments have been based on orbital platforms and as such have large spatial resolutions on the body being investigated. However, the DAN instrument on MSL is the first rover-based neutron spectrometer to investigate a body in the solar system, specifically Mars, and thus has greatly increased spatial resolution. It is also the first of such instruments to be placed in close proximity to a MMRTG. As such, we developed new simulation strategies in order to analyze and interpret DAN passive data from the surface of Mars. This involved separating the contributions to the martian neutron leakage flux by the source from which the neutrons originated and further breaking down the GCR simulations by global versus local scale. Those sources are production of neutrons through the interactions of GCRs with nuclei of the planetary regolith and atmosphere if present and the interactions of the alpha particles, which are a product of the decay of the  $^{238}\text{Pu}$  fuel of the MMRTG, with the oxides present within the fuel. We also performed the novel idea of using *in situ* radiation data from the surface of Mars in order to constrain the GCR environment at the time of DAN passive measurements. Furthermore, using the *in situ* radiation data, we decoupled the passive mode of the DAN instrument from the active mode of the instrument for future use when the active mode is no longer viable.

Using the methods developed in the work presented here, we estimated the amount of WEH present in the shallow regolith of Gale crater along the traverse route of the rover. WEH is shown to be heterogeneous within the spatial footprint of orbital instruments that have investigated the Gale crater region and ranges from 0.0 wt. % to  $15.3 \pm 1.1$  wt. %. This heterogeneity is indicative of the many different source regions that sediments and materials within the crater floor were sourced from and further that some of these source regions



underwent localized aqueous alteration. We also show that geologic units mapped from orbital data sets are nearly all statistically distinguishable in both WEH estimates and DPGI values, indicating that the differences in the compositions of these units extends to at least ~ 1 m depth in the subsurface.

We have also shown that the average contribution from the MMRTG is ~50% of the measured thermal neutron population. The remaining ~50%, or the GCR contribution, is what is relevant to manned missions to the surface of Mars when characterizing the radiation environment and potential dose contributions. Future work based off of these analyses and results will allow for the characterization of the GCR-induced low energy neutron radiation environment. This will be done through Monte Carlo modeling and will allow for both verification of such radiation transport codes through comparison to *in situ* data and dose contribution estimations for potential manned missions.

Lastly, we have characterized unexpected diurnal variations observed in the martian neutron leakage fluxes in Gale crater. These are thought to arise from a combination of instrumental effects and variations in atmospheric pressure which lead to preferential shielding of alpha particles reaching the surface and secondary neutron production in the atmosphere and possibly small contributions from subsurface temperature variations. These variations in the neutron leakage flux do not have a large impact on derived results from DAN passive data, however, orbital neutron spectrometers that are acquiring data at the same location over a diurnal cycle will most likely need to take this effect into account to accurately assess the WEH content. The work presented here provides a basic framework that can be applied to orbital neutron spectroscopy data analysis methods in order to characterize and account for the effect due to preferential shielding of alpha particles by the martian atmosphere.

There are many avenues of future work pertaining to DAN passive neutron spectroscopy and neutron spectroscopy in general to pursue starting from what has been presented here. Refinements to the simulations used are useful as new information becomes available. DAN-specific refinements will include updated base regolith composition models corresponding to Gale crater, updated rover mass models, and accurate GCR spectra for the time periods investigated. Another possibility of further investigation is the MMRTG-sourced neutron leakage flux. Specifically, calculating a highly accurate neutron leakage flux response of the epithermal neutron population with regards to DAN passive data could allow for another method of estimating WEH from the data. This would involve systematically removing the MMRTG epithermal neutron background from the data, which would then allow for WEH estimates to be performed in the traditional way of using GCR-induced epithermal neutron count rates, which would have the advantage of not relying on constraints placed on the AEC abundance of the regolith. However, this is a difficult problem and a more complete understanding of the MMRTG-induced epithermal neutron population is necessary for such an endeavor. In a more general sense, such Monte Carlo radiation transport codes as MCNPX are continually updated and this can lead to higher fidelity simulations to be applied to data analysis techniques, leading to improved neutron flux estimates and thus WEH estimates. Extending simulation techniques to other transport codes, for example GEANT4, can also allow for the possibility of increasing computational throughput for such problems and the ability to compare and contrast simulation results of multiple transport codes. Corrections to WEH estimates made using DAN passive data and orbital neutron data based on the diurnal variations observed by DAN passive is another avenue of future work. Further investigation is necessary, however, to constrain the magnitude of the effect on orbital neutron spectrometers as it will be instrument specific.

The successes and shortcomings of the DAN experiment will also provide insight into how future rover-based neutron spectrometers will be designed and implemented on the surface of a planetary body. One of the greatest strengths of the DAN instrument is the ability to collect data nearly continuously as a rover traverses across the surface, giving insight into how the regolith of the body is changing on a small scale that other instruments cannot detect. This type of use allows scientists to find interesting geochemical anomalies in the subsurface and then perform further investigations with other instruments, for example, drilling into the subsurface and taking samples at such a location could prove very insightful. On the other hand, one of the greatest weaknesses of this instrument is the fact that the data, specifically the thermal neutron count rates, are under constrained. The developed DPGI helps alleviate some of this problem by presenting the data without the compositional assumptions used in WEH estimates, but new methods of analyzing this type of data set will be useful in removing some of those constraints if possible. Mitigating these and other weaknesses can help guide the development of future neutron spectrometers and missions using them. For example, a rover containing both a neutron spectrometer and a MMRTG might attempt to increase the separation between the two by placing the neutron spectrometer on the opposite end of the rover from the MMRTG, which also allows for some small amount of shielding of the spectrometer by the rover body.

Neutron spectroscopy will continue to be an important technique in planetary science investigations throughout the solar system. While this work is just one example of new methods and techniques of modeling and data analysis being developed, other techniques and new detector technologies are being developed as well. In this context, this work has shown that passive neutron spectroscopy from a rover-based platform is essential in characterizing the shallow regolith of mission landing sites in a way that other remote sensing instruments cannot.

The framework and methods developed here will be used in conjunction with and expanded upon for future rover-based neutron spectrometers at bodies within the solar system and possibly beyond.

## **VITA**

Christopher Gayle Tate was born in Murfreesboro, Tennessee. He completed high school in 2005 and then moved to Knoxville, Tennessee to attend the University of Tennessee where he obtained a degree of Bachelor of Science in physics in 2010. Afterwards, he would elect to stay at the University of Tennessee to pursue a graduate degree in physics. He obtained his Master of Science in physics in 2012 and later in 2012 started conducting research as a member of the Mars Science Laboratory Dynamic Albedo of Neutrons instrument team.